Light Transport in Polymers for Optical Sensing and Photopolymerization

Yin-Chu Chen
B.S., Physics, National Taiwan University, Taipei, Taiwan (1995)
M.S., Electrical Engineering, National Taiwan University, Taipei, Taiwan (1998)

A dissertation presented to the faculty of the
OGI School of Science & Engineering
at Oregon Health & Science University
in partial fulfillment of the
requirements for the degree
Doctor of Philosophy
in
Electrical Engineering

February 2005

The dissertation "Light Transport in Polymers for Optical Sensing and Photopolymerization" by Yin-Chu Chen has been examined and approved by the following Examination Committee:

Scott A. Prahl
Assistant Professor
Thesis Research Advisor

Steven L. Jacques
Professor

Sean J. Kirkpatrick
Associate Professor

Mingdi Yan
Associate Professor
Department of Chemistry, PSU

Jack L. Ferracane
Professor
Division of Biomaterials & Biomechanics,
OHSU

Dedication

To my parents,

Chen, Chung-Yi and Yu, Jao-Yuan

Acknowledgements

I would like to express all my gratitude to the many people who have supported me in so many ways during my Ph.D. study.

First I would like to thank my advisor, Dr. Scott Prahl, for his guidance and support. Scott has taught me the essentials of being a successful researcher. Thanks for his training, for his education, and for showing me the skills of scientific writing and presentation. His intuitive approach to physics has always inspired me. I also thank Dr. Steve Jacques for revealing the state of the art biomedical optics research and motivating me to become a scientist. Without him, I would not have experienced the joy of science study.

I thank Dr. Sean Kirkpatrick, who initiated both the optical sensor and the dental composite projects. Sean always has cool ideas and always knows what is new in the world. He always gave me the momentum when I was stuck. I also thank Dr. Mingdi Yan for her full support on my MIP project and for sharing her knowledge of chemistry. Many thanks to Dr. Jack Ferracane for his great help on my dental composite project. Jack's expertise in dental materials helped move the project along faster than ever. This thesis would not have been possible without his help. A special thank to Dr. Zheming Wang at Pacific Northwest National Laboratory for his help and discussion on the anisotropy study.

I also want to thank my fellow students in my research group, both past and present members: Dr. Paulo Bargo for his help with many experiments and cheerful conversations, Dr. Jessica Roman for her helpful and interesting discussion, Ted Moffitt, who has been a great companion at school, Kirstin for being a caring friend to me, Dan, who has brought many laughters, and Jon, Lian, Jongji, and David for their great support and understanding.

My great gratitude goes to the colleagues at the Oregon Medical Laser Center for their

friendship. They have been so kind and helpful.

Many thanks to the friends from Taiwan for their warm and unconditional support.

Finally, I must thank my parents, Chung-Yi Chen and Jao-Yuan Yu, and my two brothers, Ying-Chuan and Ying-Ray, for accompanying me through the ups and downs of my graduate life. Studying abroad would not have been possible without their full support and encouragement.

Contents

List of Tables

List of Figures

Abstract

Light Transport in Polymers for Optical Sensing and Photopolymerization

Yin-Chu Chen
Oregon Health & Science University, 2005

Supervising Professor: Scott A. Prahl

This thesis studied light-polymer interaction in fluorescent-based molecularly imprinted polymer (MIP) sensors and photopolymerized dental composites. Through the optical property characterization of the polymers and the light transport modeling in the polymers, an optical MIP sensor design strategy and an optimal photo-cured system for dental composites may be explored.

A MIP is a biomimetic sensing element that is robust and stable in a harsh environment and cheap to produce when compared to immunoassay methods. This thesis investigated the sensitivity factors of MIP sensors consisting of highly cross-linked polyurethane containing anthracene binding sites. Two types of transducers were designed and examined with respect to their fluorescence collection efficiency. The optical properties of MIPs, the fluorescence quantum yield of anthracene in MIPs, and the fluorescence anisotropy property of anthracene and polyurethane were studied. Polyurethane would be an effective waveguide but the high background absorption in the spectrometric regions of interest was a serious problem for sensor sensitivity. The MIP rebinding capacity measured by bath batch was about one micromole/g and was six times more than that of non-imprinted polymers. The fluorescence anisotropy study suggests that anthracene rebinds with MIPs

tightly and closely. The detection limit of the MIP sensor was about 15 ppm of anthracene, which is about 0.1 micromole/g.

Photocured composites are commonly used as dental restoratives. Due to the large variety of composite formulations and curing-unit types, it is difficult to test the light curing efficiency of all possible combinations. This thesis sought to provide guidelines for optimization of a photopolymerized system based on the light transport model. The quantum yield of photoinitiator conversion and the composite's dynamic optical properties (as curing) were measured. The photoinitiator conversion (as well as the composite's optical properties, or the composite extent of cure) as a function of radiant exposure was found to fit an exponential model and obey a reciprocity rule for irradiance and illumination time. A dynamic Monte Carlo model to predict the radiant exposure distribution in a medium with dynamic optical properties was constructed and validated. This model will improve understanding of how composite formulations and the spectrum and power of curing units affect curing efficiency.

Chapter 1

Introduction

This dissertation treat 1) how polymers affect photons, which is particularly useful for optical biochemical sensing with molecularly imprinted polymers, and 2) how photons affect polymers, which is particularly useful for photopolymerization processes.

The optical properties of polymers affect how light is transported inside the polymers. This becomes an issue when the polymers are incorporated into optical devices. The required optical qualities will differ or have different emphasis for different applications. For example, a polymer's intrinsic absorption and scattering properties are the two major causes for transmission loss in polymer optical fibers [3–5]. Another example is that in some chromatographic processes optically transparent polymers are required [6]. For polymeric light emitting diode devices, light transport in multilayer structures has been investigated to study the light coupling efficiency [7–10]. In optical biochemical-sensor applications, the absorption and fluorescence characteristics of the sensing elements are critical to the sensors' sensitivity [11].

Biosensors have been used in a wide variety of applications. The increasing rate of obesity and diabetes demand biosensors to monitor diabetic patients' glucose levels. Pharmaceutical researchers need rapid assay biosensors to speed the progress of drug discovery. The war on terrorism demands new detection techniques against biowarfare agents for military and civil defense applications. Biosensors help monitor food safety and detect environmental pollution.

Since almost any given chemical compound will have a unique spectrum when examined by spectroscopy, optical biosensors provide better specificity than electrical sensors. However, in most situations, the molecule of interest (i.e., the analyte) is not present alone in

the sample but is part of a chemical mixture. All these different molecules contribute their spectral features (in proportion to their concentrations) to the overall measured spectrum of the sample, thereby decreasing the specificity and sensitivity. Many researchers have attempted to exploit different detection techniques to increase the detection sensitivity.

Since few researchers have systematically studied the optical properties of cross-linked polymers [12] and my interest in designing optical sensors was based on highly-crosslinked molecularly imprinted polymers, part of my research was particularly focused on studying the optical properties (e.g., the intrinsic absorption and fluorescent properties) of the imprinted polymers, the changes of optical properties in response to the binding between the polymer and the target molecule, and building a theoretical model for the detection sensitivity. The scope of my research attempted to provide a fundamental design strategy for the optimization of a polymer-based optical sensor.

The interaction between the photon and the polymer not only may cause photon extinction and fluorescence emission, but may also initiate the polymerization process (known as photopolymerization) through the absorption of photons. This process is complicated because the optical properties of the polymers may change, which, in turn, affects the photon propagation and polymerization rate. Photo-cured polymers have been used in a wide variety of areas, such as silicon-substrate coating [13], orthopedic biomaterials [14], and dental restorations [15]. The particular advantages of photo-cured polymers used as biomaterials include the potential for *in situ* formation. This allows for the filling of irregular shaped target defects (such as tooth cavities), the spatial and temporal control of the polymerization, and rapid polymerization under physiological conditions. However, a particular problem with this method is light attenuation.

Photoinitiators are designed to absorb the initiating light and produce free radicals. This absorption leads to light attenuation especially in thick samples. Light attenuation decreases the rate of initiation, and the rate of polymerization. Consequently, the extent of polymerization (cure) may be low at great depths. Limited depth of cure may compromise the chemical stability and the physical properties of the biomaterials and lead to reduced service life. Numerous studies address the levels of irradiance and duration needed to cure polymers to varying depths [16–20]. However, these studies are empirical and provide little

insight into the relationship between the curing process and light propagation. Therefore, an additional part of my research was to understand the various interactions of light with polymers as light is transported through composite materials. Ultimately this research attempted to develop a dynamic light propagation model suitable for simulating the photo-curing of polymers and to optimize the photopolymerization process. Dental composites, due to their extensive use and importance, were the materials studied in this research.

1.1 Optical Molecularly Imprinted Polymer Sensors

1.1.1 General Introduction of Biochemical Sensors

A biochemical sensor is a device incorporating a biological recognition element with a physical or chemical transducer [21, 22]. As illustrated in Fig. 1.1, a particular biological molecule is selectively recognized by the recognition element through a reaction, specific adsorption, or other chemical process. The chemical or physical signals from the recognition element are converted into usable signals, such as electrical or optical signals, by the transducer. Ultimately the signals are sent into an amplifier and output for data acquisition and analysis.

Recognition processes involve the binding of a chemical species with a complementary structural species. Their relation can be regarded as a lock and a key. Biochemical sensing elements may be as large as the whole organism or as small as a single molecule. They may be natural or synthetic. Natural recognition elements, such as whole cells, organelles, enzymes or antibodies, have been extensively investigated [2, 23, 24]. The primary drawback of these systems is keeping these cellular or multi-cellular structures alive. Numerous techniques have been developed to replace natural receptors with smaller, more stable biochemical mimetic structures for use in harsh environments [1, 2]. Biochemical mimetic structures are artificial counterparts that mimic natural recognition processes. Molecularly imprinted polymers are one of the most remarkable mimetic structures [1].

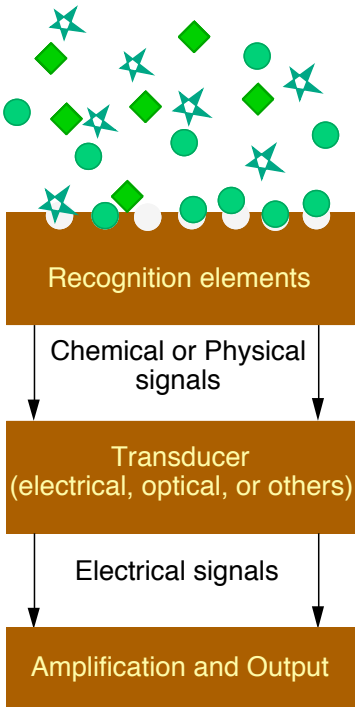

Figure 1.1: Schematic representation of a biochemical sensor [1,2] consisting of a biochemical recognition element, transducer and signal processing element. The shape-specific recognition site recognizes the analyte molecule (•) and generates the chemical or physical signals, which are detected by the transducer. The transducer converts these into electrical signals for amplification and output.

1.1.2 Biochemical Mimetic Structures – Molecularly Imprinted Polymer (MIP)

Molecular imprinting was first introduced in mid-1950s by Linus Pauling [11]. Molecularly imprinted polymers are produced by co-polymerizing functional and cross-linking monomers in the presence of the target analyte (the molecule for imprinting or the molecular template*) [1]. The schematic representation of molecular imprinting procedures is shown in Fig. 1.2. Producing MIPs begins with a polymerized template. Through self-assembly or covalent bonding with the functional monomer, a complex is formed. This

*A template is a molecule whose structure serves as a specific pattern of designated shape and size. It is like the key.

monomer-template complex is copolymerized with a cross-linker to form a highly cross-linked macroporous polymer with the imprinted molecules embedded. In the last step, the template is removed by solvent extraction or chemical cleavage. The resulting cavities, which are the recognition sites, are ready to selectively rebind with the analytes. Due to the highly cross-linked matrices, a molecularly imprinted polymer stably maintains its "memory" in extreme environments, such as in the dry state at room temperature for a long period of time [1, 25].

The majority of MIPs are based on organic polymers synthesized by radical polymerization from functional and cross-linking monomers with vinyl or acrylic groups, since rich varieties of those functional monomers are available [1]. In most cases, the polymer mixture contains an inert solvent that is required not only to dissolve all ingredients, in particular, the imprinting analytes, but also to generate a highly porous structure, which allows the elution of the imprinted analytes and access to the imprinted sites.

1.1.3 Comparison of Immunoassay and MIPs

Immunoassay is a method to distinguish related proteins using antibodies. Antibodies, also called immuno-globulins, are proteins with specific affinity for antigens. In traditional solid-phase immunoassay, the steps are 1) attaching specific antibodies to a polymer support, 2) adding the sample and washing to remove unbound proteins, and 3) adding radio-labeled second antibodies with specific binding sites for the detected proteins [26]. Although less than a nanogram of a protein can be detected with the immunoassay method, the recognition process is tedious and usually takes several days.

Replacing immunoassay with molecularly imprinted polymers would have several advantages. First, MIPs are much more stable and, unlike immunoassay, work in a wide range of temperature, pH, and humidity [27]. Second, MIPs can be created to detect analytes for which it is hard or impossible to develop antigen-antibody combinations [25]. Finally, MIPs can distinguish enantiomers which are typically difficult to separate [28, 29]. Most commonly, enantiomers react with chiral enzymes [26], which do not exist for all enantiomers.

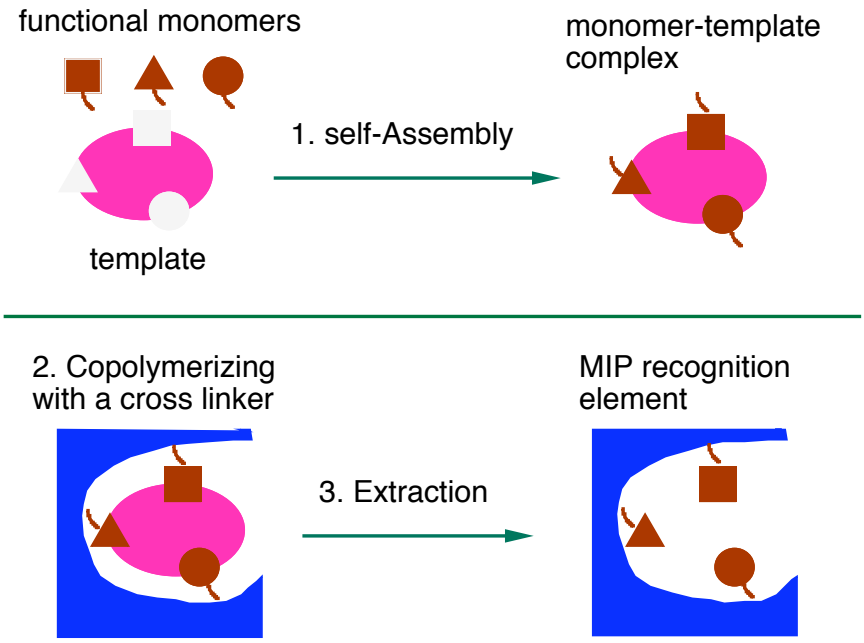

Figure 1.2: Schematic representation of the molecular imprinting production [1]. First starts with a synthesis process of polymerisable template and the self-organizing polymerization process. Then, a highly cross-linked macroporous polymer with the imprinted molecules is formed. Finally the template is removed by solvent extraction or chemical cleavage.

1.1.4 Current Development of Optical MIP Sensors

Many researchers have attempted to integrate MIPs with optical transducers [30–34]. Optical transducers typically detect changes in the optical properties of the MIPs. Although the concentration changes of analytes in the solvent could be measured directly based on their specific fluorescent spectra, the signals are weak when the analytes are dilute. For example, the detecting limitation of anthracene in a dimethylformamide solution when using the Fluorolog-3 spectrofluorometer (Model FL3-22, ISA manufacturer) is about 0.004 ppm. The role of the MIPs is to adsorb or extract the analytes and thereby concentrate them, which in turn enlarges the optical signals. The separation of the analyte from a complex mixture is a further advantage, because there are often different quenchers, like humic acids [31], that prevent direct fluorescence measurement. Some researchers have specifically measured the fluorescent properties of the analytes in the

MIPs upon binding [25,30]. A potential problem with this approach is that the entrapped imprinting molecules (those not completely extracted from the polymer) and possible fluorescent properties of the polymer itself may cause high background signals. Others have used changes of fluorescent signals generated by the polymer itself [33,35,36] by incorporating fluorescent monomers into conventional functional monomers. When the analyte binds to the imprinted site, the fluorescence of the fluorescent groups is quenched, thus allowing the analyte to be quantified.

1.1.5 Comparison of Optical Sensors with Electrical Sensors

Although the development of electrical sensors began first [37], optical methods are currently favored over electrical methods [37,38]. First, more chemicals can be identified by their spectroscopic properties than by their electric properties. Second, a light guide can transmit light with different wavelengths in different directions; therefore monitoring multiple analytes is easier with optical methods. Third, light guides are insensitive to the electric or magnetic field of the environments. Finally, with the development of microlithography techniques, the optical based thin-film recognition elements are amenable to integrated circuit-type microfabrication. Nonetheless, there are also some disadvantages of optical sensors. Optical systems are generally more expensive and bigger than electrical systems.

1.2 Photo-cured Polymers – Dental Composites

Dental composite materials have been used to restore teeth since the late 1950s and have become more and more popular due to the better esthetics of composites. Development of composite materials has proceeded from chemical curing, requiring separate pastes mixed together before applying to the prepared tooth, to photo-curing, which utilizes premixed, self-stable materials with long working time. Photocured dental materials still have several problems including (1) limited depth of cure due to light absorption by the resins and pigments and light scattering of the fillers in the composites, (2) shrinkage of the composite, (3) marginal adhesion, (4) water absorption and (5) water solubility.

Researchers continue improving the curing process (to cure faster and deeper), as well as the physical and esthetic properties of dental composites.

1.2.1 Composite components

Matrix monomer components

The majority of the monomer components consists of aromatic dimethacrylate monomer 2,2-bis[4-(2-hydroxy-3-methacryloyloxypropoxy)-phenyl] propane (BIS-GMA), and triethylene glycol dimethacrylate (TEGDMA). BIS-GMA is characterized by its large molecular size and chemical structure, which provides lower volatility, lower polymerization shrinkage, more rapid hardening and production of stronger and stiffer resin [39]. The low molecular weight TEGDMA, on the other hand, offers the following advantages: 1) low viscosity, which permits higher filler loading, 2) a high number of double bonds per unit weight, which yields greater opportunity for a high conversion of double bonds during polymerization, and 3) a high degree of crosslinking and compact molecular structure that creates a hard resin matrix.

Fillers

The filler material commonly is a ceramic oxide (such as silica or zironia) or a glass. Selection of filler types (different materials and sizes) is dependent upon compressive strength, stiffness, abrasion resistance, thermal expansion, and refractive index match with the organic monomer. Usually coarse particles provide higher strength and wear resistance while finer particles reduce polymerization contraction [39]. Currently dentists attempt to form hybrid macro and micro fillers in the range of 0.5–5 μm to combine the advantages of both.

Photosensitizers and inhibitors

The free-radical photosensitizer used in light-cured composites is usually a combination of an α-1,2 diketone such as benzil or camphoroquinone (CQ) and an accelerator (amine reducing agent) such as dimethylaminoethyl methacrylate (DMAEMA) or DMPTI [39]. Intense blue light around 470 nm wavelength is used to excite the α-diketone, thereby

initiating the photo-polymerization process. Commonly the concentration of CQ photosensitizer is in the range 0.17–1.03% of the resin by weight and that of accelerator is 0.86–1.39%.

1.2.2 Extent of Polymerization – Degree of Conversion (DC)

Many methods have been used to determine the extent of polymerization. The degree of conversion (DC) is the most commonly used and recommended [15]. The DC is the fraction of the number of carbon-carbon double bonds that are converted during the polymerization, and typically is in the range of 50–70% for dental composites [40]. The unpolymerized carbon-carbon double bonds have an absorption at $1638\,\mathrm{cm}^{-1}$, which can be measured by Fourier Transform Infrared (FTIR) spectroscopy. It is desirable to increase the DC to increase the mechanical hardness, wear resistance, and chemical stability of the composites. Typically a composite reaching 80% of the maximum DC value ($\simeq$65%) is considered adequately cured.

The DC is affected by many factors, including those related to the composite formulation: monomer composition, the composition and size distribution of fillers, photosensitizer, accelerator, and inhibitor type and concentration; the light illumination, such as the output spectra and the power of the light; and the curing environment, such as the geometry of specimen, the distance from the light source, and the color of the backing materials.

Intuitively, higher light powers should produce a higher curing extent and a greater depth of cure. Nonetheless, some researchers have found that the marginal adhesion between the teeth and the composite might have better integrity at a lower curing rate [18, 41–44]. Others have shown that reducing the curing rate produces less contraction stress within the composite [43, 45], thereby improving the marginal integrity [46]. Two ways can be used to achieve lower curing rates but still ensure maximum DC and retain the depth of cure. The first is to use longer exposures at lower irradiances [41–43, 47]. The second is to begin with low irradiance for a short duration, followed by a second exposure at higher irradiance [18, 43]. In these cases, it is important to ensure that DC is not compromised in the final materials, otherwise the hardness, wear resistance, water

absorption, and water solubility may suffer [48, 49].

1.3 Research Goals

The goals of this dissertation can be divided into three parts: initially, to design, model, and evaluate an optical MIP sensor for fluorescent analyte detection; next, to correlate optical properties with extent of polymerization; and finally, to build and verify a dynamic Monte Carlo model simulating light transport in photocuring polymers that have dynamic optical properties.

Fluorescence spectroscopy is capable of determining both the fluorescent analyte concentration in the aqueous solution and that in the recognition elements (MIPs). MIPs can adsorb the analytes to increase the analyte concentration, thereby increasing the detecting limit. However, non-specific absorption of the MIPs might decrease the signals. In addition, the fluorescent light emits in all directions, therefore the light collection efficiency of the transducer is another important factor in sensor sensitivity. Chapter 2 addresses the issues of the absorption and fluorescent properties of MIPs, the quantum yield of the fluorescent analyte in MIP matrix, and the transducer light collection efficiency in fluorescence-based MIP sensor design. A Monte Carlo model was built to predict the detection limit.

Chapter 3 develops a numerical model for the fluorescence output efficiency of a MIP-waveguide sensing system. This chapter further discusses how the optical properties of polymers affect the sensitivity of the sensor system and the sensor design strategy.

The binding between the analyte and the MIPs is further investigated using the fluorescence lifetime and anisotropy techniques in Chapter 4. Fluorescence lifetime and anisotropy reveal information about the bound analyte's local environment. This chapter discusses both the steady-state and time-resolved fluorescence anisotropy of MIPs with imprinted analytes, MIPs with the imprinted analytes extracted, MIPs with rebound analytes, non-MIPs, and non-MIPs bound with analytes. In addition, the relationship between the steady-state anisotropy of MIPs and the extent of MIP polymerization is also presented.

Chapter 5 discusses the correlation between the curing extent distribution of a photo-cured composite and the light dose distribution in the composite. In this chapter, the measurements for the absorption and scattering coefficients of uncured and cured composite are presented. A static Monte Carlo model is employed to simulate photo migration in the uncured and cured composites. Two kinetic models are used to fit the correlation curve between curing extent and radiant exposure. The fitting results are compared and used to predict the radiant exposure in a photo-curing polymer system.

The primary absorber in dental composites is the photoinitiator, which starts the photo polymerization process. Chapter 6 addresses two methods for the measurement of the quantum yield of conversion of a photoinitiator, camphorquinone (CQ). The absorption coefficient changes of resins with CQ to the radiant exposure are measured at different irradiances and fit with an exponential model. This chapter derives the relationship between the changes of CQ concentration and the absorbed photon density to solve for the quantum yield of CQ conversion.

A further investigation of the changes of the optical properties of dental composites as a function of radiant exposure is presented in Chapter 7. The scattering and absorption coefficients of a filled composite are measured at different light illumination times using two integrating spheres, together with the inverse adding-doubling technique. The refractive index changes of composites with different concentrations of the photoinitiator CQ versus the curing time are also investigated to provide the background information for the characteristics of scattering coefficient changes. The scattering and absorption coefficient changes as a function of radiant exposure are derived based on the quantum yield of CQ found in Chapter 6. The relationship is then used in the dynamic Monte Carlo model described in the following chapter.

Finally, Chapter 8 develops and verifies a three-dimensional dynamic Monte Carlo model that simulates media with dynamic optical properties. The model is first verified by comparing the simulation results with numerical models for absorbing-only media and with the results from literature for scattered media. Then, this dynamic model is used to simulate the light transport in a dental composite based on the optical property–radiant exposure relationship from Chapter 7. The total reflectance and transmittance

during curing are calculated and validated by illuminating the filled composite disks, which have exactly the same composite formulation as that in Chapter 7, with the same curing lamp. The total reflectance and transmittance of the composite are recorded through dual integrating spheres as a function of irradiation time.

Chapter 2

Fluorescence-Based Optical Sensor Design for Molecularly Imprinted Polymers

2.1 Introduction

*Biochemical sensors are used in clinical diagnostics, the pharmaceutical industry, environmental pollutant monitoring, food analysis, and detection of biological warfare agents. A biochemical sensor incorporates a biochemical recognition element along with a physical or chemical transducer. The recognition element must be specific to the target analyte and stable in a wide variety of environments. Recognition elements using immunosensors (e.g., antibodies) have excellent specificity and sensitivity [50–55], but require specific antibody synthesis, may have sterilization problems, and may suffer from stability issues [55, 56]. Various biomimetic sensors that alleviate one or more of these drawbacks have been developed [1,38,57]. In this paper, sensors based on molecularly imprinted polymers (MIPs) are examined.

The recognition properties of MIPs arise from the way they are prepared. During synthesis, functional† and crosslinking monomers are copolymerized in the presence of a target analyte (the imprinted molecule) that acts as a molecular template. The monomers are chosen for their ability to interact with the functional groups of the template molecule.

*This chapter was published in *Sensors and Actuators, B – Chemical* v. 102, p. 107–116, 2004.

† "functional" here means the monomers have the ability to bind with the analytes.

Polymerization/crosslinking yields a network polymer with the template molecules incorporated. After the extraction of template molecules, the resulting cavities retain their "memory" for the target analyte [1]. MIPs are robust, stable, and resistant to a wide range of pH, humidity, and temperature [58]. MIPs are also relatively inexpensive to produce and can be synthesized for analytes for which no natural antibody exists [59].

Several groups have integrated MIPs with optical fibers [32, 60] or waveguides [31, 61, 62]. Dickert *et al.* used a quartz planar waveguide coated with a several-micron thick layer of MIP imprinted with various fluorescent polyaromatic hydrocarbons. Fluorescence emission of trapped analytes in the polymer matrix was used to detect analyte concentrations down to several μg/L [31, 63, 64].

To create practical sensing devices, the complex interplay of the factors affecting detection needs to be understood. Some studies have attempted to build a theoretical model for the sensitivity of an optical sensor [65–67]. A ray optics model was used to calculate the detection limit of a total internal reflection fluorescence (TIRF)–sensing system [65, 66]. Although the ray optics method might provide some accuracy for TIRF spectrometry [65, 66], the equation derived was an approximation and is limited to a particular sensor design. In this work, we examined three issues that affect the sensitivity of a fluorescence-based MIP sensor: the fluorescence collection efficiency, the optical properties of the MIP, and the rebinding performance of the MIP. With further analysis, we are able to select optimal design parameters for a MIP sensor.

The optical properties of the MIP samples were measured to provide the background information for the theoretical model. The absorption coefficient, the refractive index, and the fluorescence quantum efficiency of the MIPs were measured while the original template molecules were still present in the matrix. The effects of the thickness of the MIP film, the background absorption, and the background fluorescence on the sensor sensitivity were analyzed theoretically in a Monte Carlo simulation. Finally, the rebinding capacities of the imprinted polymers were examined by extracting the original template molecules from the polymer matrix and subsequently measuring the rebound analyte concentrations when polymer samples were exposed to the analyte solutions.

2.2 Theoretical Model

Our sensor consists of a layer of MIP on a transparent substrate. Figure 2.1 illustrates the schematic representation of the light path. The excitation was perpendicular to the layer surface and the emission was collected on the same side as the excitation. The absorption coefficients of MIPs at the excitation and emission wavelength were $\mu^x_{urethane}$ and $\mu^m_{urethane}$, and the absorption coefficient of anthracene was $\mu^x_{anthracene}$ at the excitation wavelength. The refractive indices of MIPs, glass plate and air were n_{mip}, n_g and n_a, respectively. For simplicity, all elements were assumed homogeneous and isotropic.

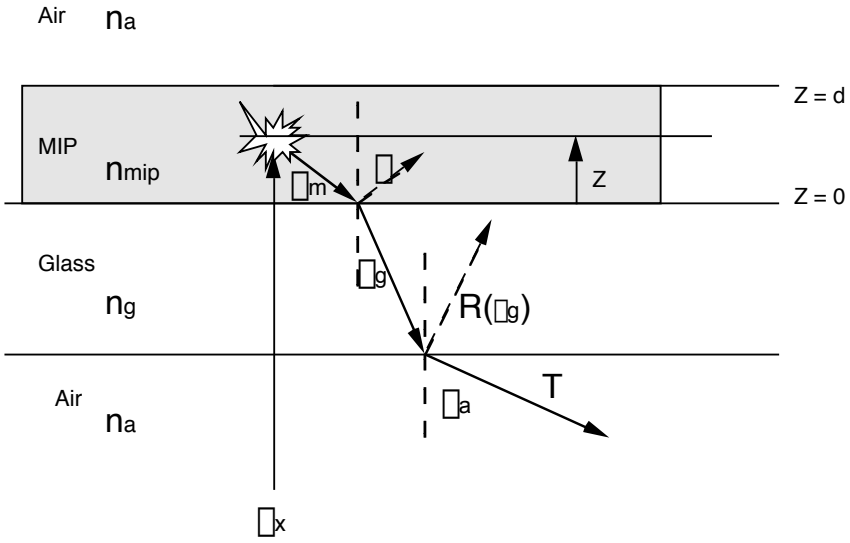

Figure 2.1: The schematic representation of light path of our sensing system consisting of MIP coated on the flat bottom of a glass vial.

In our Monte Carlo model, excitation photons were launched normally to the MIP layer. The photons were propagated according to Beer's law, a random distance S^x to the depth at which they were absorbed ($S^x = -\ln \frac{\xi}{\mu^x_{urethane}+\mu^x_{anthracene}}$, where ξ is a random number uniformly distributed between 0 and 1). The fraction of photons absorbed by the polyurethane was $\frac{\mu^x_{urethane}}{\mu^x_{urethane}+\mu^x_{anthracene}}$ and the fraction absorbed by anthracene was $\frac{\mu^x_{anthracene}}{\mu^x_{urethane}+\mu^x_{anthracene}}$. Both produced fluorescent light with different quantum yields,

$\Phi^{404}_{urethane}$ for polyurethane and $\Phi^{404}_{anthracene}$ for anthracene. Fluorescent photons were emitted uniformly in all directions. The emission photons had three possible fates: 1) to be absorbed by polyurethane, 2) to be reflected at the MIP-glass boundary, or 3) to propagate through MIPs to the glass plate. The conditions for reflection depended on the unpolarized Fresnel reflection at the particular angle of incidence [68]. Photons entering the glass were either reflected at the glass-air boundary or transmitted into the air (which again depended on the Fresnel reflection). Photon paths were corrected for refraction angles at all boundaries. Finally, those fluorescent photons transmitted from the MIPs through the glass go into the air. Only some proportion of these transmission photons can be collected by the concave mirror, reflected by the mirror, and then sent to the sensing system (see Fig. 2.2). These fractions were all counted into the geometry factor, G, since this depends on the geometry of the setup, and the relative positions of the mirrors in the fluorimeter. Fluorescent photons arising from polymer $N^m_{urethane}$ or anthracene $N^m_{anthracene}$ were recorded separately. With a total of N^x_{model} excitation photons launched in the model, the fluorescence collection efficiency E_f was

$$E_f = \frac{\Phi^{404}_{urethane} N^m_{urethane} + \Phi^{404}_{anthracene} N^m_{anthracene}}{N^x_{model}} G \tag{2.1}$$

E_f represents the ratio of the collected fluorescence photons to the input excitation photons. The value of E_f is between 0 and 1. Experimentally, E_f was equal to I^{404}_{mip}/I^x_{exp}, where I^{404}_{mip} is the emission from MIPs at 404 nm, and I^x_{exp} is the absorbed excitation light. If I^{404}_{mip}/I^x_{exp} is equal to Eq. 2.1, then

$$\frac{I^{404}_{mip}}{I^x_{exp} G} = \frac{\Phi^{404}_{urethane} N^m_{urethane} + \Phi^{404}_{anthracene} N^m_{anthracene}}{N^x_{model}} \tag{2.2}$$

Since G was unknown, and difficult to be determined accurately, we calculated the term, $I^x_{exp}G$, by comparing the result of the Monte Carlo simulation with the experimental result of the fluorescence emission of a standard anthracene cyclohexane solution. The simulation of anthracene cyclohexane solutions in a quartz cuvette was the same as the simulation described above, except we replaced MIPs by cyclohexane solutions. If N^m_{std} is the total emission photons from the standard solution and Φ_{std} is the quantum yield of the standard solution, then the theoretical fluorescence collection efficiency for the standard

solution E_{std} is $\Phi_{std}N^m_{std}G/N^x_{model}$. Again, experimentally, E_{std} is equal to I^m_{std}/I^x_{exp}, where I^m_{std} is the total emission of the standard solution measured experimentally. Therefore,

$$\frac{I^m_{std}}{I^x_{exp}G} = \frac{\Phi_{std}N^m_{std}}{N^x_{model}} \tag{2.3}$$

Since N^m_{std}/N^x_{model} can be calculated from the model, I^m_{std} can be measured from the experiment, and Φ_{std} is known, $I^x_{exp}G$ can then be calculated and substituted into Eq. 2.2.

In our simulations, the following values were used. The background absorption coefficients of cyclohexane, $\mu^x_{cyclohexane}$, and $\mu^m_{cyclohexane}$, were assumed to be $0.01\,\mathrm{cm}^{-1}$, while the absorption coefficient of MIPs was $15\,\mathrm{cm}^{-1}$ for excitation and $3.5\,\mathrm{cm}^{-1}$ for emission (see Results section). The refractive index of MIP n_{mip}, cyclohexane $n_{cyclohexane}$, the quartz cuvette n_q, and the glass vial n_g were 1.47, 1.43, 1.47, and 1.54 respectively. Two million photons were launched for each simulation set. Two free parameters, the thickness of the sensing layer t, and the concentration-dependent absorption coefficient of anthracene, $\mu^x_{anthracene}$, were varied. Finally, we compared the model results, the right hand side of Eq. 2.2, with the experimental results, the left hand side of Eq. 2.2.

2.3 Materials and Methods

2.3.1 Materials

Bisphenol A, phloroglucinol, and anthracene were purchased from Aldrich and were used as received. A mixture of p,p'-diisocyanatodiphenylmethane and 30% p,o,p'-triisocyanatodiphenylmethane was purchased from Merck-Schuchardt (Hohenbrunn, Germany) and stored under nitrogen after use. Dimethylformamide (DMF) was distilled over $MgSO_4$ under reduced pressure and was stored over 4 Å molecular sieves. Toluene was purchased from Fisher and was used as received.

2.3.2 Fabrication of MIP samples

The sensing element of our sensor was polyurethane imprinted with anthracene following the procedure of Dickert [31, 63, 69]. Imprinting solutions were made by adding anthracene to the mixture of 1.25 M solutions of monomers (0.375 mmol bisphenol A and

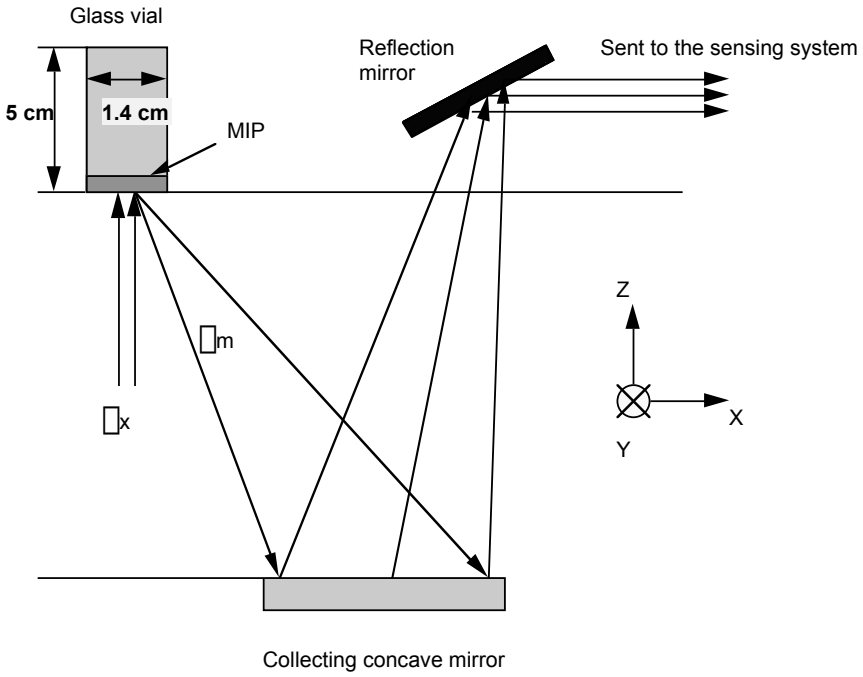

Figure 2.2: The optical setup of MIP fluorescence measurement consists of a glass container (diameter = 1.4 cm, height = 5 cm) coated with MIPs as the sensing layer on the flat bottom and a collecting concave mirror. As shown here, only some proportions of the emission λ_m can be collected by the concave mirror, reflected by the mirror, and then sent to the sensing system. These proportions are all counted into the geometry factor, G.

0.455 mmol p, p'-diisocyanatodiphenylmethane) and crosslinkers (0.250 mmol trihydroxybenzene and 0.195 mmol p, o, p'-triisocyanatodiphenylmethane) in the porogen (DMF). Control solutions were prepared in a similar manner as the imprinting solution with the absence of the template anthracene. Each mixture contained a 1:1 mole ratio of hydroxy to isocyanate functional groups and a 35 mole % of cross-linking monomers.

Polymer films with various thicknesses were formed by filling identical glass vials (1.4 cm diameter) with volumes ranging from 150 to 400 μL of the freshly prepared mixtures of the imprinting or non-imprinting solutions. Since the polymer shrinks during polymerization, about 3 μL of a catalyst (tetramethylethylene diamine) was added to each polymer sample to increase the polymerization rate and to retain the initial shape of polymers. This is because the catalyst helped the mixtures polymerize instantly while the

solvent DMF was still present in the polymers. The polymerization was completed within seconds, forming a yellow polymer on the bottom of the glass vials. All the procedures were carried out at room temperature in air. MIP samples with different thicknesses (0.15, 0.22, 0.5, 1.16, 1.45, 1.76, and 2.2 mm) and with different imprinted anthracene concentrations (0, 0.32, 0.64, 3.2, 12.8, and 25.5 mM) were synthesized.

To prepare thin films for absorbance measurements, microscope cover slips were used as spacers between two glass microscope slides. A MIP film of 150 microns was formed in the space between the glass slides. In this way, the thickness of the MIP was controlled by the height of the cover slip. Because the MIP shrank from the sides, the thickness of the MIP remained constant. To make samples for the quantum yield measurement, the polymer solution with anthracene was polymerized directly in a standard 1-cm quartz cuvette. These same samples were used to make refractive index measurements with an Abbé refractometer. After one day of polymerization, the MIPs shrank and could be removed from the cuvette.

2.3.3 Optical Characterization

The absorbance of 0.15 mm thick films of control and imprinted samples were measured with a HP–8452A Diode Array Spectrophotometer. The absorption coefficients of the MIP were obtained from the absorbance values, $\mu_a(\lambda) = A(\lambda)\ln(10)/t$, where t is the thickness of the MIP film. Since the optical properties of the polymers changed over time as the solvent evaporated, the absorption coefficients were measured daily until the solvents evaporated completely ($\sim$ 3 days for 0.15 mm-thick samples).

The refractive index of MIP bulk samples was measured using an Abbé refractometer (Model ABBE-3L). The measurement became more difficult as the polymer dried and darkened over several days. The refractive index of polyurethane bulk samples was 1.47$\pm$0.01 for the first 3 days.

2.3.4 Quantum Yield Measurement

In our characterization of the single-wavelength quantum yields of anthracene in MIPs, the excitation wavelength was 358 nm, while the emission at 404$\pm$1 nm of anthracene in

MIPs was compared to the total emission from 368 nm to 550 nm of a standard solution (0.3 g/L anthracene in cyclohexane), which has a quantum yield of 0.36 [70, 71]. Several conditions need to be satisfied following Parker's method [70]. First, to minimize the effect of variation in the intensity of the excitation light as a function of wavelength, we chose 358 nm as the excitation wavelength for all the measurements. Second, we assumed all the excitation photons were absorbed. We chose anthracene in cyclohexane with 0.3 g/L concentration as our standard solution based on Berlman's method [71]. At this concentration, the absorption coefficient is 31 cm^{-1}, which allows $<10^{-14}$ of light to be transmitted through the 1 cm-cuvette sample ($T = \exp(-31)$), thereby ensuring all light was absorbed. The total absorption coefficient for our MIP samples was the sum of the absorption coefficient of the polymers (15 cm^{-1}) and the anthracene. This high total absorption coefficient value also ensured that all light was absorbed. Third, the geometry factor of the sensing system should be the same for all the samples. The geometry factor was affected by the penetration depth of excitation light and the refractive index of solutions. Since relatively high concentrations of anthracene were used for all the measurements, the variation of penetration depth was less than 0.6 mm, for MIP samples with anthracene concentrations between 0.16 mM ($\mu_a^f = 17\,cm^{-1}$) and 25 mM ($\mu_a^f = 317\,cm^{-1}$). As for the refractive index mismatch between different solvents, an n^2 term was included in Eq. 2.4 and 2.5 [71] below.

A spectrofluorimeter (SPEX Fluorolog Model 112) was used to produce excitation light ($\lambda_x = 358 \pm 1$ nm) and to collect the emission spectra of the samples. Fluorescence of MIPs formed in quartz cuvettes and anthracene in cyclohexane were measured. Since polyurethane itself fluoresces at an excitation wavelength of 358 nm, the fluorescence from anthracene is only a fraction of the total emission. In this case, the quantum yield of polyurethane at 404±1 nm, $\Phi^{404}_{urethane}$, was calculated using Eq. 2.4 below [70]. Then, the quantum yield of anthracene in MIPs at 404±1 nm, $\Phi^{404}_{anthracene}$, was calculated using Eq. 2.5.

$$\Phi^{404}_{urethane} = \Phi_{std} \frac{I^{404}_{urethane}}{I^{total}_{std}} \left(\frac{n_{mip}}{n_{std}}\right)^2 \tag{2.4}$$

$$\frac{\mu^{404}_{anthracene}}{\mu^{404}_{anthracene}+\mu^{404}_{urethane}}\Phi^{404}_{anthracene}+\frac{\mu^{404}_{urethane}}{\mu^{404}_{anthracene}+\mu^{404}_{urethane}}\Phi^{404}_{urethane}=\Phi_{std}\frac{I^{404}_{mip}}{I^{total}_{std}}(\frac{n_{mip}}{n_{std}})^2 \tag{2.5}$$

where Φ_{std} is the quantum yield of the standard solution, $I^{404}_{urethane}$ is the emission of polyurethane alone at 404±1 nm, I^{404}_{mip} is the emission of MIPs at 404±1 nm, I^{total}_{std} is the total emission of the standard solution, $\mu^{404}_{urethane}$ and $\mu^{404}_{anthracene}$ are the absorption coefficients at 404 nm of polyurethane alone and anthracene in MIPs, and n_{std}, n_{mip} are the refractive indices of the standard solution and MIPs respectively.

2.3.5 Fluorescence Collection Efficiency Measurement

The test system consisted of a glass vial (diameter = 1.4 cm, height = 5 cm) coated with a MIP as the sensing layer on its flat bottom (Fig. 2.2). Only a fraction G (the "geometry factor" discussed earlier) of the emitted light was collected by the system. Fluorescence was measured while anthracene was still imprinted in the polymers. Different anthracene concentrations and different thickness of MIP films (those vial samples made in 2.3.2) were tested. A mechanical fixture constrained the position of the vial samples for each measurement. This fixture was adjusted so that the 0.5×10 mm rectangular excitation beam would focus on the middle of the sample. For excitation at 358 nm, the emission spectrum was recorded from 370 to 480 nm (1 nm bandpass, 2 seconds/nm). The term, $I^{404}_{mip}/I^{x}_{exp}G$, in the Eq. 2.2 could then be calculated.

2.3.6 Rebinding Characterization

To study the rebinding performance of the imprinted polymers, extraction of anthracene and subsequent rebinding experiments were performed. MIP samples imprinted with 25 mM anthracene were compared with non-imprinted samples.

The imprinted anthracene was removed by soaking the films in toluene. For better extraction, the samples were shaken continuously and the toluene was replaced every 2 days. The fluorescence signal of the toluene solution was used to check if imprinted anthracene had been extracted. Because the prepared vial-samples were thick, it took two weeks to complete most of the extraction. After extraction, the samples were placed

under vacuum to remove residual solvent. The fluorescence signal of the polymer itself was then measured using the same setup in Fig. 2.2.

Rebinding solutions were made by dissolving anthracene in DMF. Calibration curves were derived by measuring the fluorescence intensity of different concentrations (0.01 to 0.22 mM) of anthracene/DMF solutions in standard quartz cuvette using a fluorimeter (Fluorolog 112). Then, 2.5 mL of 1 mM anthracene solution was added to each of the imprinted and non-imprinted polymer samples. The vials were sealed with aluminum foil and shaken for two days. Subsequently, the rebinding solution was diluted to 1/15 of its original concentration in a standard cuvette. The fluorescence signal was measured and the anthracene concentration was derived from the calibration curve.

2.4 Results

2.4.1 Optical Characterization

Polyurethane changes its optical properties as it dries due to the evaporation of the solvent DMF, making the definition of background absorption coefficient time dependent. Figure 2.3 shows the absorption coefficients of polyurethane over three days.

The absorption coefficients of 1 mM anthracene in cyclohexane, DMF, and polyurethane on day 1 (the first day) are compared in Fig. 2.4. The absorption coefficient of anthracene in polyurethane decreased $\sim 10\%$ as the MIPs dried. The absorption coefficient was 5.1 ± 0.2 cm^{-1} at 358 nm on day 1. The spectrum of anthracene in polyurethane shows a 6 nm Stokes shift compared to the spectrum of anthracene in cyclohexane.

The single wavelength (404 ± 1 nm) quantum yield of polyurethane was calculated to be 0.00050 ± 0.00004. The single wavelength (404 ± 1 nm) quantum yield of anthracene in MIPs as a function of anthracene concentration is plotted in Fig. 2.5. As can be seen, the quantum yield decreases with increasing concentration.

2.4.2 Model Results and Experimental Verification

The simulation result (right hand side of Eq. 2.2) was compared with the experimental result (left hand side of Eq. 2.2) in Fig. 2.6. Assuming that the input excitation energy

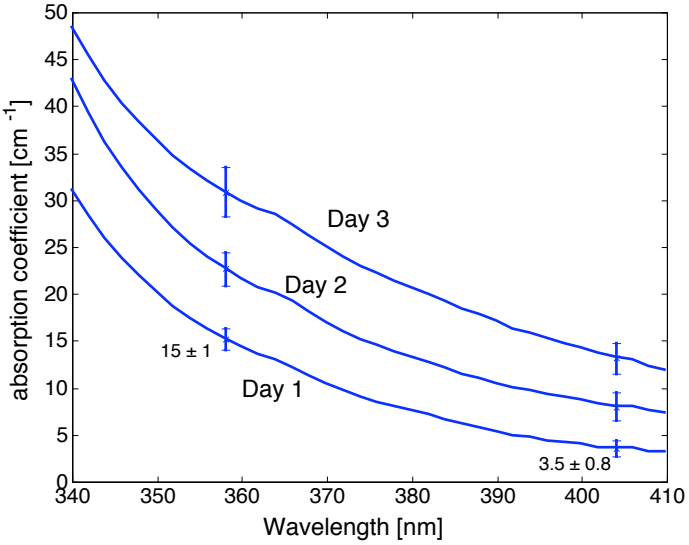

Figure 2.3: The background absorption coefficients of polyurethane as a function of wavelength over 3 days. The absorption coefficient was $15 \pm 1\,\mathrm{cm}^{-1}$ at the excitation (358 nm) wavelength of anthracene and $3.5 \pm 0.8\,\mathrm{cm}^{-1}$ at emission (404 nm) wavelength on day 1 (the first day). The error bar is the standard deviation of 5 measurements.

is 1 Joule, the output fluorescence is represented as μJoule. These measurements had a 14% standard deviation from the model.

To understand how the thickness of a MIP layer and the background absorption properties of MIPs affect anthracene fluorescence signals ($\Phi^{404}_{anthracene} N^{m}_{anthracene} / N^{x}_{model}$ in Eq. 2.2), several other simulations were constructed. Figure 2.7 shows the anthracene fluorescence energy versus the thickness of MIP films ranging from 0.01 mm to 1 mm and for anthracene concentrations ranging from 30 ppm to 3 ppb (assuming $\mu^{x}_{urethane} = \mu^{m}_{urethane} = 1\,\mathrm{cm}^{-1}$, and $\Phi^{404}_{anthracene} = 0.01$). Typically, a thicker sensing layer yields higher fluorescence signals. This prediction agrees with the observation of other researchers [63]. Observe that the fluorescence signal increases dramatically with thickness from 0 to 0.1 mm, and increases moderately above 0.3 mm. Also note that 3 ppb anthracene concentrations yield only 5 nJ fluorescence energy for 1 J excitation light.

Figure 2.8 is a simulation of anthracene fluorescence for different background absorptions, $\mu^{x}_{urethane}$ and $\mu^{m}_{urethane}$, for 4 thicknesses. Note that the background absorption has

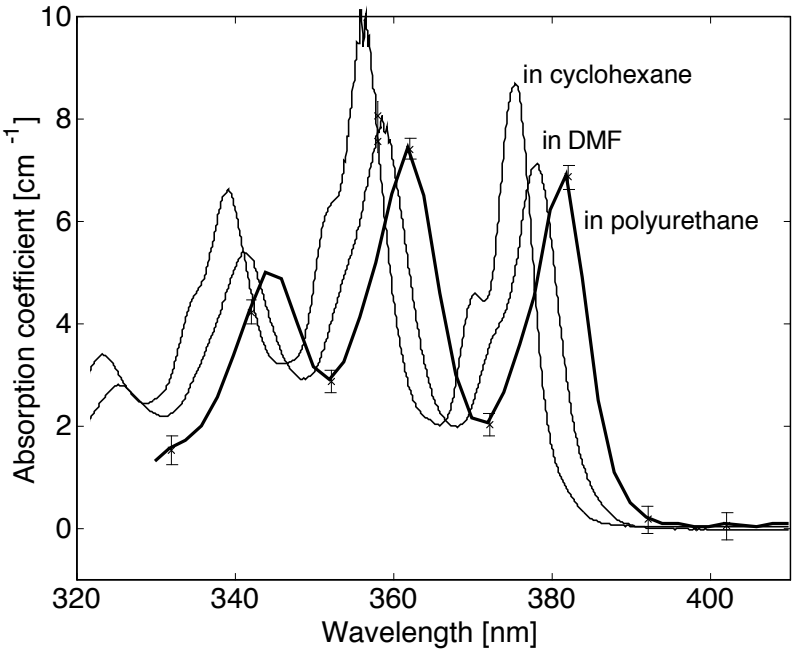

Figure 2.4: Anthracene (1 mM) absorption coefficients in cyclohexane, DMF, and polyurethane. Anthracene in polyurethane showed a 6 nm stokes shift from anthracene in cyclohexane.

greater influence on thicker MIP samples (0.5 mm and 1 mm). The fluorescence signal decreases about 50% for a 1 mm thick MIP sample and about 20% for a 0.5 mm thick sample as the background absorption increases from 1 to 10 cm^{-1}. The model also shows that the background absorption does not make much difference for thinner MIP samples ($\leq$0.2 mm). The fluorescence signal of a 0.1 mm thick, 30 ppm fluorophore concentration sample is 5 μJ for 1 J of excitation light.

2.4.3 Rebinding

Table 2.1 summarizes the results of the rebinding study on 25 mM anthracene imprinted polymer and on non-imprinted control polymer samples. Generally, the imprinted polymers showed about 6 times more rebinding than the non-imprinted control polymers. Note that samples A4b and A4c still exhibited fluorescence at 404 nm after two weeks

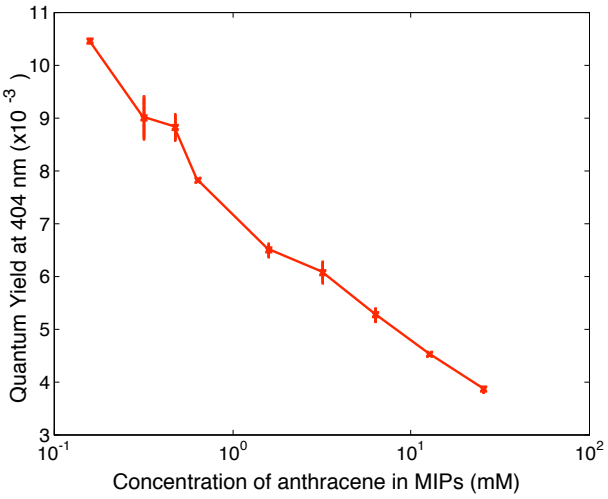

Figure 2.5: The quantum yield of anthracene in MIPs at 404±1 nm as a function of anthracene concentration.

of extraction. These two samples did not have the templated analytes extracted completely because the MIPs were adhered to the bottom of the vials. Consequently, A4b only rebound 0.66±0.01 μmole/g, while A4c would have had a negative rebinding density (because residual anthracene in the MIP would be extracted by the rebinding test solution).

2.5 Discussion

The quantum yield of anthracene in MIPs decreases as the concentration of anthracene increases from 0.1 to 25 mM. This result is possibly due to the aggregation of anthracene molecules since the concentrations we used were relatively high [31, 72–74]. A similar result was found in Rhodamine 6G and Rhodamine B at concentrations greater than 0.05 mM by Bindhu's group [72, 73]. Dickert's research group also observed that a linear relationship between the fluorescence emission and the analyte (polycyclic aromatic hydrocarbon (PAH)) concentration was only valid when the quantum yield did not change with increasing analyte concentration (up to several $\mu g L^{-1}$) in the MIP layer [74]. To check if this condition occurs in a different medium, we measured the quantum yield of

MIP sample (#)	MIP volume (μL)	Fluorescent Signal before rebinding (A.U.)	Bound Conc. (ppm)	Molecule Bound Density (μmole/g)	Bound % of theoretical imprinted sites
Ca	400	420 ± 8	4.2 ± 0.4	0.18 ± 0.02	
Cb	350	430 ± 20	3.5 ± 0.3	0.17 ± 0.01	
Cc	300	430 ± 20	2.4 ± 0.2	0.14 ± 0.01	
Cd	250	440 ± 20	1.7 ± 0.1	0.12 ± 0.01	
Ce	200	400 ± 20	1.7 ± 0.1	0.15 ± 0.01	
Cf	150	370 ± 10	1.9 ± 0.1	0.23 ± 0.01	
A4a	400	500 ± 30	28.6 ± 0.8	1.23 ± 0.03	3.7 ± 0.1
A4b	350	1070 ± 20	13.4 ± 0.2	0.66 ± 0.01	2.0 ± 0.03
A4c	300	1890 ± 60	* see caption	—	—
A4d	250	360 ± 20	17.4 ± 0.3	1.19 ± 0.02	3.6 ± 0.05
A4e	200	320 ± 5	15.2 ± 0.6	1.30 ± 0.05	3.9 ± 0.2
A4f	150	300 ± 6	12.4 ± 0.4	1.42 ± 0.04	4.3 ± 0.1

Table 2.1: Results of rebinding study. A4a – A4f represent 4-molar-percent imprinted polymers, while Ca – Cf represent non-imprinted polymers. The third column is the fluorescence signals from the MIP layer detected after extraction but before rebinding. All the errors are the standard deviation of 4 concentration measurements. *The concentration of rebinding solution for the A4c sample was 1.66 mM after the rebinding test, which was higher than the starting concentration of 1 mM. This is because the anthracene molecules were not extracted completely before the rebinding, which also agreed with the strong fluorescence signals (1890) from the MIP layer before rebinding.

anthracene in DMF. The result showed a fairly constant quantum yield when anthracene concentration ranged from 0.05 to 0.8 mM. As the concentration increased, the quantum yield decreased quickly. Moreover, the quantum yield of another fluorescent molecule, 7-carboxymethoxy-4-methyl-coumarin (in methanol), was also measured as a comparison. The quantum yield remained constant in the concentration range of 0.02 to 0.5 mM. Above 0.5 mM, the quantum yield of coumarin decreased. Another possible explanation is that the absorption coefficient may be responsible for the decrease in anthracene fluorescence and therefore lower apparent quantum yields. However, the absorption coefficient did not change over the concentration range from 0.1 to 25.5 mM.

The rebinding performance of MIPs was examined. The results of the rebinding study (Table 2.1) showed that the binding capacity was $\sim$1.2 μmol/g (about 180 ppm in MIP) for the 4 molar percent imprinted polymers, while nonspecific binding was $\sim$0.15 μmol/g for non-imprinted polymers. Although the overall rebinding capacity was moderate [75, 76], the imprinted polymers bound 6 times more than the non-imprinted polymers, indicating an imprinting effect that was comparable with other published studies [63, 64, 77]. Dickert *et al.* had about 100 times greater response from anthracene-imprinted polyurethane than control samples [63, 64]. One possible reason for our relatively low binding capacity was that the polymer films we fabricated were much thicker ($\geq$100 μm) than those prepared by Dickert (several microns). Since the rebinding of analyte molecules to the recognition sites is diffusion controlled [25], the molecules may not be able to access the sites that are buried inside the highly crosslinked polymer matrix. It is possible that only those imprinted cavities on the outer layer of the polymers were bound. However, we did not use thinner MIP films for two reasons: (1) thin films broke and had inconsistent thicknesseses, and (2) thinner MIP films have correspondingly weak fluorescence signals as shown in Fig. 2.7.

The number of fluorescent analytes trapped by a MIP can be monitored either from the loss of the fluorescence of the analyte solution or from the increase of the analyte fluorescence of the MIP. Detecting the fluorescence signals directly from the MIPs instead of the solution provides a convenient way to follow either extraction or rebinding of analytes. The following parameters affect the sensitivity of this type of MIP sensors: (1) the

thickness of a MIP sensing layer, (2) the background absorption of excitation light, and (3) the fluorescence yield of the polymers. According to our model (Fig. 2.7), a 0.2 mm thick film will maximize fluorescence signals, and the background absorption of excitation light by the polymers, $\mu^x_{urethane}$, needs to be reduced. Although our model shows that $\mu^x_{urethane}$ does not strongly influence the fluorescence emission from a 0.2 mm thick MIP (Fig. 2.8), high $\mu^x_{urethane}$ will increase the polymer self-fluorescence emission.

To further examine the effect of polymer background absorption on the fluorescence signals ($\Phi^{404}_{anthracene}N^m_{anthracene}/N^x_{model}$, and $\Phi^{404}_{urethane}N^m_{urethane}/N^x_{model}$ in Eq. 2.2), another simulation was constructed as shown in Fig. 2.9. In this simulation, the MIP thickness was 0.2 mm, the anthracene absorption coefficient $\mu^x_{anthracene}$ was 0.0002 cm^{-1}, the polyurethane absorption coefficient at emission wavelength $\mu^m_{urethane}$ was 1 cm^{-1}, and quantum yields, $\Phi^{404}_{urethane}$, and $\Phi^{404}_{anthracene}$, were 5×10^{-4}, and 0.01 respectively. Notice that as the absorption coefficient, $\mu^x_{urethane}$, increased from 0.0002 to 1 cm^{-1}, the anthracene fluorescence decreased 10 times; in contrast, the polymer fluorescence increased more than 1000 times. Also note that when $\mu^x_{urethane}$ is greater than 0.005 cm^{-1}, the polyurethane self-fluorescence exceeds the anthracene fluorescence. This suggests that to detect 3 ppb anthracene concentration with signal (anthracene fluorescence) to noise (polymer fluorescence) ratio of 10:1, the polymer should have an absorption coefficient less than 0.001 cm^{-1} (assuming the quantum yields remain the same over the concentration ranges). An alternative is to imprint a different PAH molecule that fluoresces at longer wavelengths to minimize the background absorption and emission by the polymers. Tetracene has fluorescence ranging from 480 to 580 nm, yet polyurethane still has absorption up to 0.5 cm^{-1} at 550 nm and has fluorescence emission in this wavelength range as well. An additional problem with imprinting tetracene was that the imprinting capacity of this molecule was lower than that of imprinting with anthracene due to the lower solubility of tetracene in DMF.

Alternatively, reducing the quantum yield of polymer can decrease the noise from polymer self-fluorescence. According to Fig. 2.9, polymers have about 5,000 times the fluorescence signal of anathracene at $\mu^x_{urethane} = 1\,\mathrm{cm}^{-1}$. To reach a signal to noise ratio of 10:1, the quantum yield of the polymer must be reduced by a factor of 50,000 assuming

$\mu^x_{anthracene}$ remains constant. This means the ratio of the quantum yield of fluorescence analyte to the quantum yield of polymers at the detection wavelength needs to be about 100,000.

Although our model shows that this particular polyurethane imprinted system may not be optimal for optical sensors, polyurethane can be incorporated with a quartz crystal microbalance (QCM) device for better quantitative measurements as originally studied by the Dickert group [31]. To optimize a fluorescence-based MIP sensor, one should use polymers that have lower background absorption and fluorescence emission.

2.6 Conclusions

We have developed a theoretical model for the fluorescence collection efficiency of a MIP sensor that consists of a MIP sensing layer on a transparent substrate. This model may be used to analyze the sensitivity and detection limit of an optical system and to provide an optimization strategy for the sensor design. This simulation method can be modified easily to accommodate various optical sensor designs. We have evaluated one MIP design by varying the thickness of MIP sensing layers, background absorptions, background fluorescence, and rebinding performance. We found that thicker MIP sensing layers tend to be more sensitive. To improve signal-to-noise, both background polymer absorption and fluorescence need to be reduced. Our model may be used to improve the sensitivity of other sensor designs.

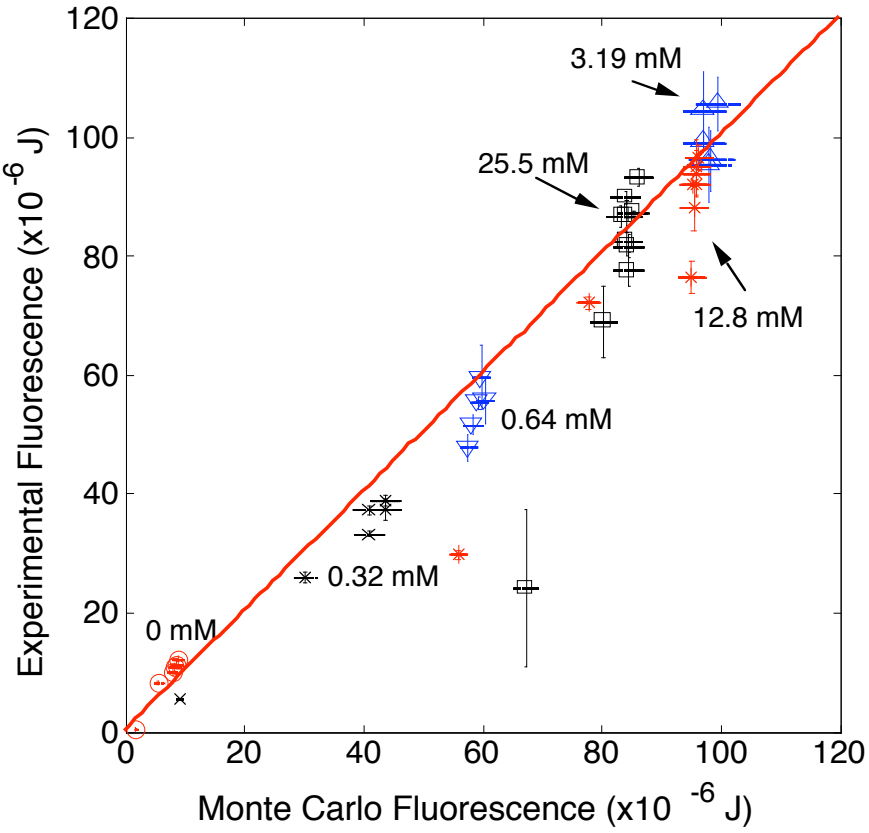

Figure 2.6: The experimental results versus the Monte Carlo Simulation. Error in experimental values are the standard deviation of 5 sample measurements. Errors in Monte Carlo values are the standard deviation of 3 simulations and the quantum yield. Markers with the same shape represent the same concentration group of anthracene in MIPs. For the same concentration group, each marker represents different thickness of MIP films. These measurements showed 14% standard deviation in the model.

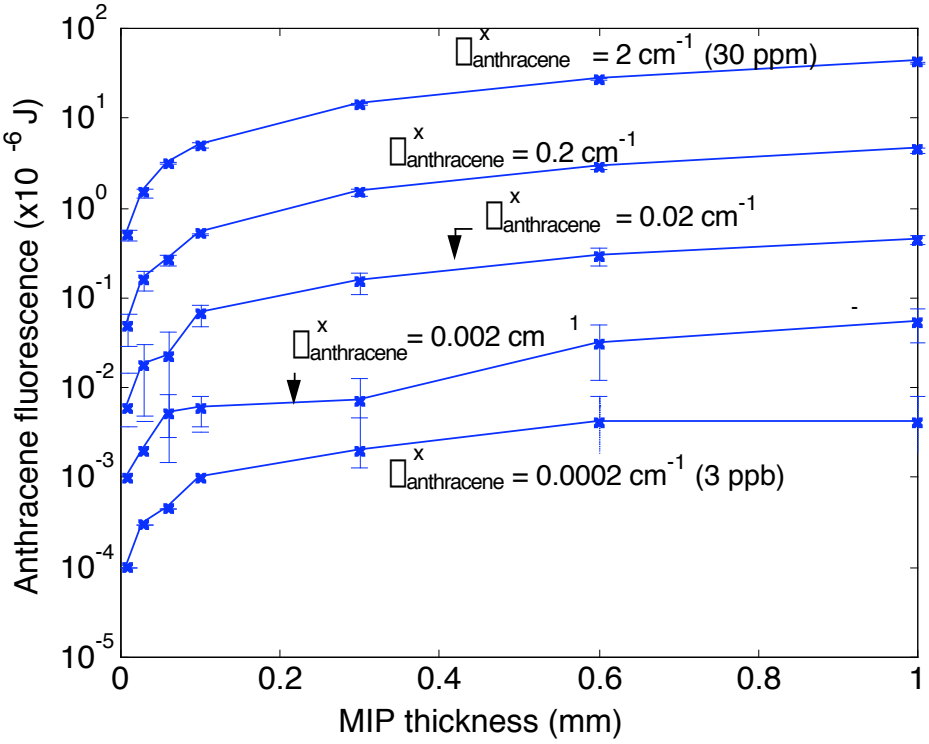

Figure 2.7: Simulation result of the fluorescence emission versus MIP thickness at different anthracene concentrations for a background absorption $\mu_{urethane}$ of $1\,\mathrm{cm}^{-1}$ and input energy of 1 J.

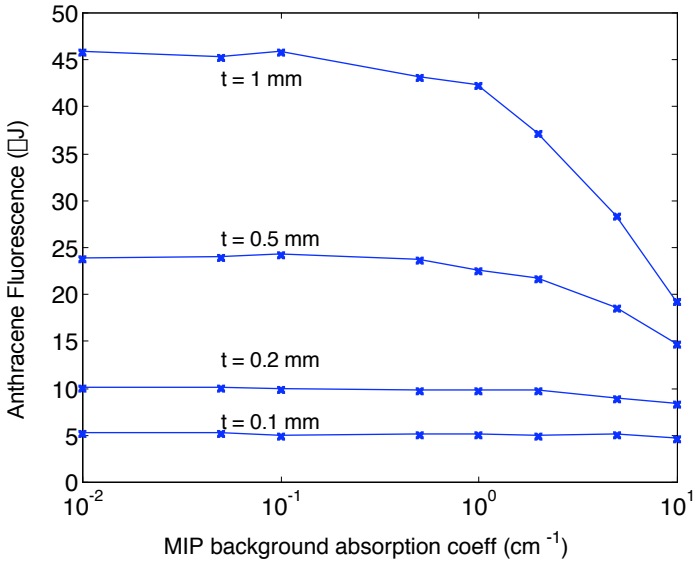

Figure 2.8: Simulation result of the fluorescence emission versus MIP background absorption, $\mu^x_{urethane}$ and $\mu^m_{urethane}$, for MIP thickness = 1, 0.5, 0.2, and 0.1 mm at fluorophore concentration of 30 ppm ($\mu^x_{anthracene} = 2\,\mathrm{cm}^{-1}$).

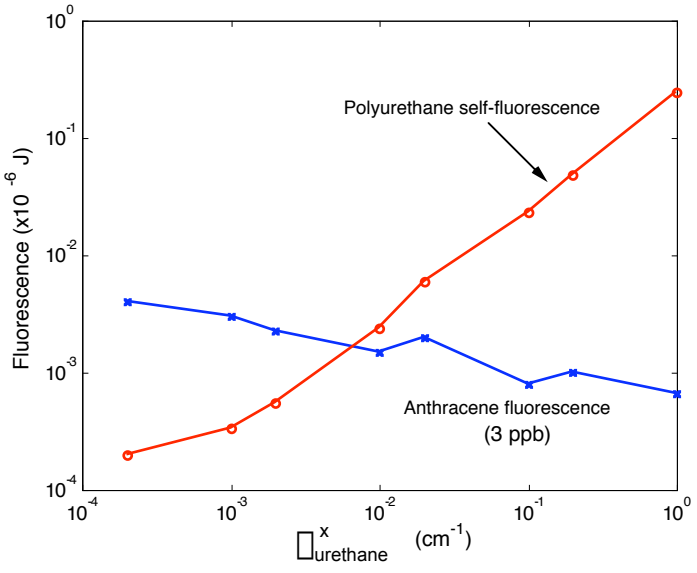

Figure 2.9: Simulation of the fluorescence emission at 404±1 nm from polyurethane, and anthracene versus polyurethane absorption coefficient $\mu^x_{urethane}$ at excitation wavelength 358 nm.

Chapter 3

Evaluation of Molecularly Imprinted Polyurethane as an Optical Waveguide for PAH Sensing

3.1 Introduction

*Evanescent-wave fluorescence-based fiber-optic biosensors detect the binding of an antigen to an antibody immobilized in the distal end of an optical fiber [78–81]. Detected refractive index changes caused by binding of an antigen and an antibody are limited to the evanescent sensing region (typically less than 1 μm thick). For immunoassay recognition elements, this is an advantage because fluorophores outside the evanescent field don't contribute to the emission signal. Molecularly imprinted polymer techniques allow much greater detection volumes that may capture more analytes. For instance, a 600 μm fiber coated for 5 cm with MIP with an active sensing depth of 1 μm will have a detecting volume of $\sim 10^{-2}$ mm^3. On the other hand, if the fiber itself is a MIP, which acts as both a detecting element and a waveguide, a 100 μm$\times$100 μm$\times$1 cm long MIP waveguide will have 10 times more detecting volume than an evanescent-wave sensor. Another advantage is that the light intensity inside a MIP waveguide that directly excites the analytes is stronger than that in the evanescent field (which decays exponentially). Yet another advantage is that a greater proportion of the fluorescence signal, generated inside the MIP, will be guided directly to the output. A potential problem of a MIP waveguide, however, is the

*This chapter was published in *Proceedings of SPIE, Optics East 2004: Nanosensing: Materials and Devices Symposium* paper 5593-108.

attenuation of the signals due to the background absorption of polymers, and an increase in the equilibrium time of the analytes and MIP.

The concept of using the biochemical sensing layer itself as an optical waveguide was presented by Hisamoto *et al.* [82]. They used an "active polymer-waveguide platform" where the sensing layer also acted as the guiding layer. The poly(vinylchloride) membrane was used both as a sensing layer and as the evanescent-wave waveguide core layer. The absorbance signal was measured, and the sensitivity of such a system was shown to be greater than that in the evanescent-wave sensing mode. Although optical sensors based on molecularly imprinted polymers have been constructed [30–34], few publications have used MIPs directly as an optical waveguide [83]. For biochemical sensing use, the attenuation of light may not be as critical as an optical fiber for optical communications. We developed a theoretical model for the fluorescence output efficiency of a MIP waveguide. A MIP system, polyurethane imprinted with polycyclic aromatic hydrocarbon (PAH) molecule, was evaluated based on the polymer's optical properties. Based on this theoretical model, the optimal optical properties of MIP was suggested to increase the sensitivity of MIP used as an optical waveguide.

3.2 Theory

3.2.1 Theoretical Model of Output signals of a MIP Waveguide

In this model, the analytes are assumed to be homogeneously distributed within the MIP; reabsorption and scattering events are neglected. The analyte and the polymer have absorption at excitation wavelength λ_x and fluorescence at wavelength λ_m. The background (polymer) absorption coefficient at λ_x is μ_a^x, the absorption coefficient of the analytes is μ_a^f, and the background absorption coefficient of emitted fluorescence light λ_m is μ_a^m. The schematic representation of this model is shown in Fig. 3.1.

If the incident irradiance is I_0 at the input end, the irradiance at a distance x from the input end becomes

$$I(x) = I_0 e^{-(\mu_a^x + \mu_a^f)x} \quad .$$

Assuming the irradiance of the emitted fluorescence light λ_m at x is $I_f(x)$, the irradiance

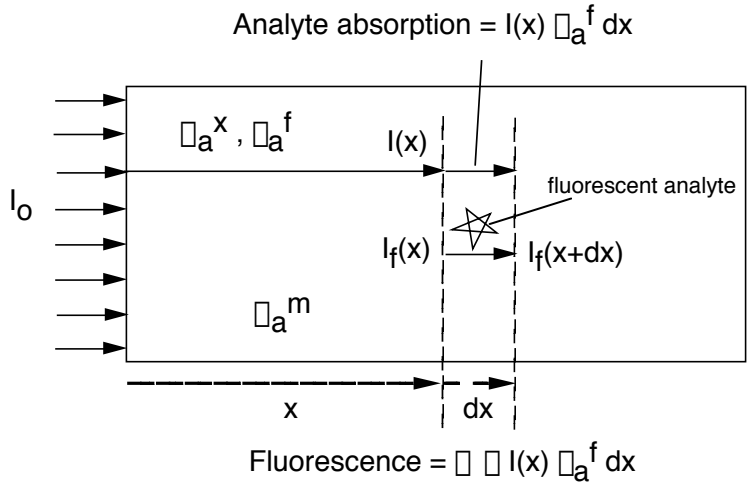

Figure 3.1: The schematic representation of MIP-waveguide model.

drops to $I_f(x)\mu_a^m\,dx$ at $x + dx$ because of the background absorption. Since both the analyte and the polymer fluoresce, assume the fluorescence quantum yield is Φ_a for analyte and Φ_p for polymer and the fluorescence irradiance from the analyte is I_f and from the polymer is I_p. We consider the fluorescence from the analytes first. The irradiance absorbed by the analytes for fluorescence in dx distance is $I(x)\mu_a^f\,dx$. Analytes release a portion (the quantum Yield, Φ_a) of the absorbed energy as fluorescent light λ_m, and only some fraction (η) will propagate to the output end of fiber, so the newly fluorescent light from the analyte added to $I_f(x+dx)$ is $\eta\Phi_a I(x)\mu_a^f\,dx$. Therefore, the analyte fluorescence irradiance at position $(x + dx)$ becomes

$$I_f(x + dx) = I_f(x) - I_f(x)\mu_a^m\,dx + \eta\Phi_a I(x)\mu_a^f\,dx.$$

Solving this equation for $I_f(x)$ with an initial condition $I_f(0) = 0$, we get the output irradiance relative to the input irradiance I_0 for fluorescence from the analytes (called "relative output efficiency" Q_a) as

$$Q_a = \frac{I_f(x)}{I_0} = A\left[e^{-\mu_a^m x} - e^{-\left(\mu_a^x+\mu_a^f\right)x}\right] \quad , \tag{3.1}$$

where

$$A = \frac{\eta\Phi_a\mu_a^f}{\mu_a^x + \mu_a^f - \mu_a^m} \quad .$$

Similarly, the relative output efficiency for background fluorescence (from the polymer itself) (Q_p) is derived as

$$Q_p = \frac{I_p(x)}{I_0} = A\left[e^{-\mu_a^m x} - e^{-(2\mu_a^x)x}\right] \quad , \tag{3.2}$$

where

$$A = \frac{\eta\Phi_p\mu_a^x}{2\mu_a^x - \mu_a^m} \quad .$$

The equation can also be expressed as "the attenuation loss", α (dB km^{-1}), which is defined as

$$\alpha = -\frac{10}{x}\log(\frac{I_f}{I_0}) \quad .$$

An alternative way to derive the equation is to integrate the fluoresence signal from the light-input end to the other end:

$$I_f(x) = \eta\Phi\int_0^x I_0\mu_a^f e^{-(\mu_a^x+\mu_a^f)x'}e^{-\mu_a^m(x-x')}dx' \quad .$$

3.3 Materials and Methods

3.3.1 Materials

Polyurethane imprinted with anthracene, a polycyclic aromatic hydrocarbon molecule, was made from a mixture of 1.25 M solutions of monomers composed of 0.375 mmol bisphenol A (Aldrich) and 0.455 mmol p,p′-diisocyanatodiphenylmethane (Merck-Schuchardt, Hohenbrunn, Germany); crosslinkers composed of 0.250 mmol trihydroxybenzene and 0.195 mmol p,o,p′-triisocyanatodiphenylmethane (Merck-Schuchardt, Hohenbrunn, Germany) in dimethylformamide (DMF) [69, 84]; and the imprint molecule anthracene (Aldrich) at 25 mM in dimethylformamide (DMF).

3.3.2 MIP waveguide preparation

Waveguides were fabricated using the technique of micromolding in capillaries (MIMIC) as shown in Fig. 3.2 [69]. A silicon master pattern made up of lines (50 μm in height by 50 μm in width and 7.5 cm in length) was fabricated through conventional photolithography using SU-8 photoresist (Microchem Corporation, Newton, MA). The PDMS mixture

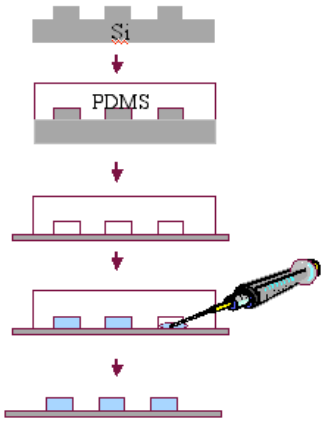

Figure 3.2: The micromolding in capillaries technique steps are to (1) creat master mold, (2) pour and cure PDMS, (3) remove PDMS and place PDMS on silicon wafer with thin coat of PDMS, (4) fill channels with MIP and allow to polymerize, and (5) peel PDMS away.

was poured over this master pattern and allowed to cure at 70°C for 4 hours. The PDMS stamp was then peeled off; thereby creating a negative image of the original pattern. The ends of the stamp were then carefully cut with a razor blade to open up the channels and each stamp was cleaned via sonication in ethanol. When placed on a silicon wafer, the stamp formed small microchannels that were filled with an imprinting solution by capillary action. The silicon wafers were previously cleaned in piranha solution (3:1 v/v, conc. H_2SO_4 / 30% H_2O_2) and were silanized with 3-aminopropyl trimethoxysilane in order to ensure covalent attachment of the polymer to the substrate [85]. Subsequent overnight polymerization under ambient conditions and stamp removal left behind imprinted filaments attached to the wafer support. Filaments were visually inspected via an optical microscope (Olympus BHM).

3.3.3 Light coupling and relative transmission measurements

A quartz lens with a focal length of 2 cm was used to focus the light from the deuterium lamp into the waveguide. Coupling was verified when the distal end of the waveguide lit up. The waveguide was rotated to an angle of approximately 30° relative to the optical

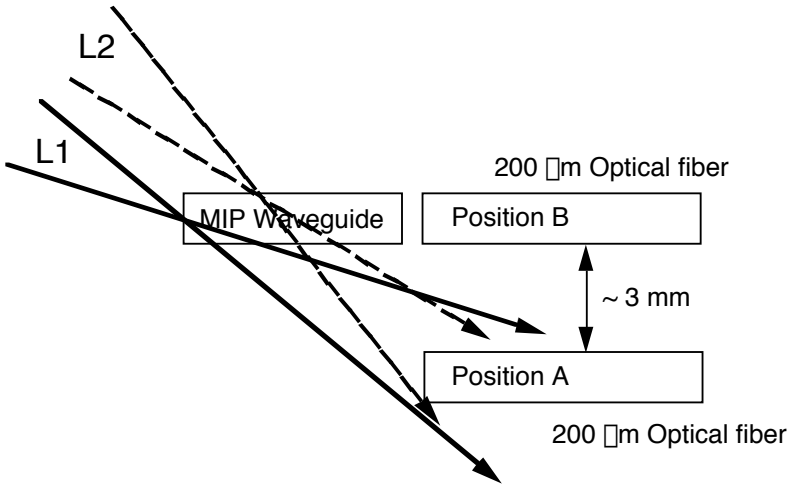

Figure 3.3: The relative four positions of the focus of the light and the optical fiber. Two positions of the focus of light: position L1: the focus of the light is at the tip of the MIP waveguide; position L2: the focus of the light was moved to focus to the side of the MIP waveguide. Two positions of the optical fiber: position A: the collecting optical fiber was put in the position where the light was directly emitted from the lens, approximately 3 mm away from the tip of the MIP waveguide; position B: the optical fiber was at the tip of the MIP waveguide to collect the light coming out from the MIP waveguide.

axis such that the direction of the light emitted from the fiber was distinct from the illumination light. The light coming out from the distal end of the MIP waveguide was then coupled into a 400 μm optical fiber and recorded by a Fluorolog-3 spectrofluorimeter. The relative four positions of the focus of the light and the optical fiber are illustrated in Fig. 3.3. First, the focus of the light is at the tip of the MIP waveguide, position L1. The collecting optical fiber was then put in position A where the light was directly emitted from the lens (approximately 3 mm away from the tip of the MIP waveguide). This served as the reference background signal. Second, the optical fiber was moved to position B to collect the light coming out from the MIP waveguide. Third, the focus of the light was moved to focus to the side of the MIP waveguide, position L2, but the angle remained the same. The optical fiber remained in position B. Finally, the optical fiber was moved to position A again.

1. The ratio of transmission of light through the MIP waveguide to the background:

$$T_{mip} = \frac{\text{light focus at L1 and fiber collect at B}}{\text{light focus at L1 and fiber collect at A}}$$

2. The comparison data:

$$T_{side} = \frac{\text{light focus at L2 and fiber collect at B}}{\text{light focus at L1 and fiber collect at A}}$$

3. The background of focus to the tip to the background of focus to the side:

$$T_{background} = \frac{\text{light focus at L2 and fiber collect at A}}{\text{light focus at L1 and fiber collect at A}}$$

3.4 Results and Discussion

3.4.1 Light coupling and relative transmission measurements

Figure 3.4 shows the raw transmission spectra of the four measurements and their relative transmission spectra, T_{mip}, T_{side} and $T_{background}$. The L1-A and L2-A curves showed that similar background spectra were collected at position A, which is 3 mm away from the waveguide output tip, for both focusing the light to the MIP tip and focusing to the side of the MIP. The transmission at longer wavelengths, above 600 nm, is about 1.5 times higher than the wavelengths between 350 nm to 600 nm. This suggests that the light between 350 nm to 600 nm is slightly absorbed when passing through the MIP waveguide, but since the waveguide is only 100 μm thick, the amount absorbed is only $\sim 5\%$.

The T_{side} curve shows that about 10 times more light than $T_{background}$ was collected. According to Fresnel equations, no light going into the MIP from position L2 is totally internal reflected, therefore little light will be guided by the MIP waveguide. If we collected any signal, that would be the light scattered by the silicon substrate, MIP or dust.

The T_{mip} (red) curve is much higher than the other two, which demonstrates that the MIP was an effective waveguide. The total output intensity was the light guided by the MIP waveguide (since any incident angle, focused at L1 position, on the MIP waveguide will be guided due to the total internal reflection when assuming the refractive index of MIP is 1.5) plus the light scattered from the substrate, MIP or dust (the relative amount was shown by T_{side}). The T_{mip} curve shows that the transmission above 650 nm is twice

as high as that from the wavelengths below 550 nm. This means that those with shorter wavelengths are absorbed more when they propagate through MIP.

3.4.2 Numerical simulation of MIP relative output efficiency Q

In the following numerical tests, the proportion (η) of fluorescence light that propagates to the output end of the waveguide is assumed to be 0.25 since the fluorescence light is equally distributed to all direction (isotropic) and the part from solid angle $-\pi/2$ to $+\pi/2$ among 4π is assumed to propagate to the output end.

For the anthracene imprinted polyurethane MIP system, the quantum yield is 4×10^{-3} for 25 mM anthracene in MIPs, and 5×10^{-4} for polyurethane itself [84]. The optical properties of MIPs are $\mu_a^x = 30\,\mathrm{cm}^{-1}$ at 362 nm and $\mu_a^m = 12\,\mathrm{cm}^{-1}$ at 404 nm, and the absorption coefficient of 25 mM anthracene in MIPs is $\mu_a^f = 190\,\mathrm{cm}^{-1}$ at 362 nm excitation [84]. The relative output efficiency Q_a and Q_p as a function of waveguide length was plotted in Fig, 3.5. As we can see, MIP has a maximum Q_a value of 0.07% at length 0.14 mm, and Q_a drops exponentially as the length of the MIP waveguide increases due to the high background absorption of the polymers. The relative output efficiency Q_a is only 0.0002% for a 5 mm MIP waveguide. If the polymer's background absorption drops 10 times, a 0.26 mm waveguide will have a maximum Q_a of 0.09% and the Q_a only drops slightly, thus a 5 mm MIP will have Q_a up to 0.05%.

For the ratio of the background polymer fluorescence to the analyte fluorescence (S/N ratio = Q_a/Q_p), MIP has higher S/N ratio for a shorter length waveguide (Fig. 3.6). For anthracene imprinted polyurethane system, the S/N ratio drops quickly in the beginning (< 0.25 mm) and plateaus at a value around 11 for waveguides longer than 0.05 mm (the solid line, SN_1, in Fig. 3.6). If a polymer's background absorption drops 10 times (the dashed line, SN_2, in Fig. 3.6), the S/N ratio is more than 5 times higher than SN_1 for waveguides shorter than 0.02 mm. However, the SN_2 drops to a value close to SN_1 as the waveguide length increases to 0.5 mm (sub-figure in Fig. 3.6).

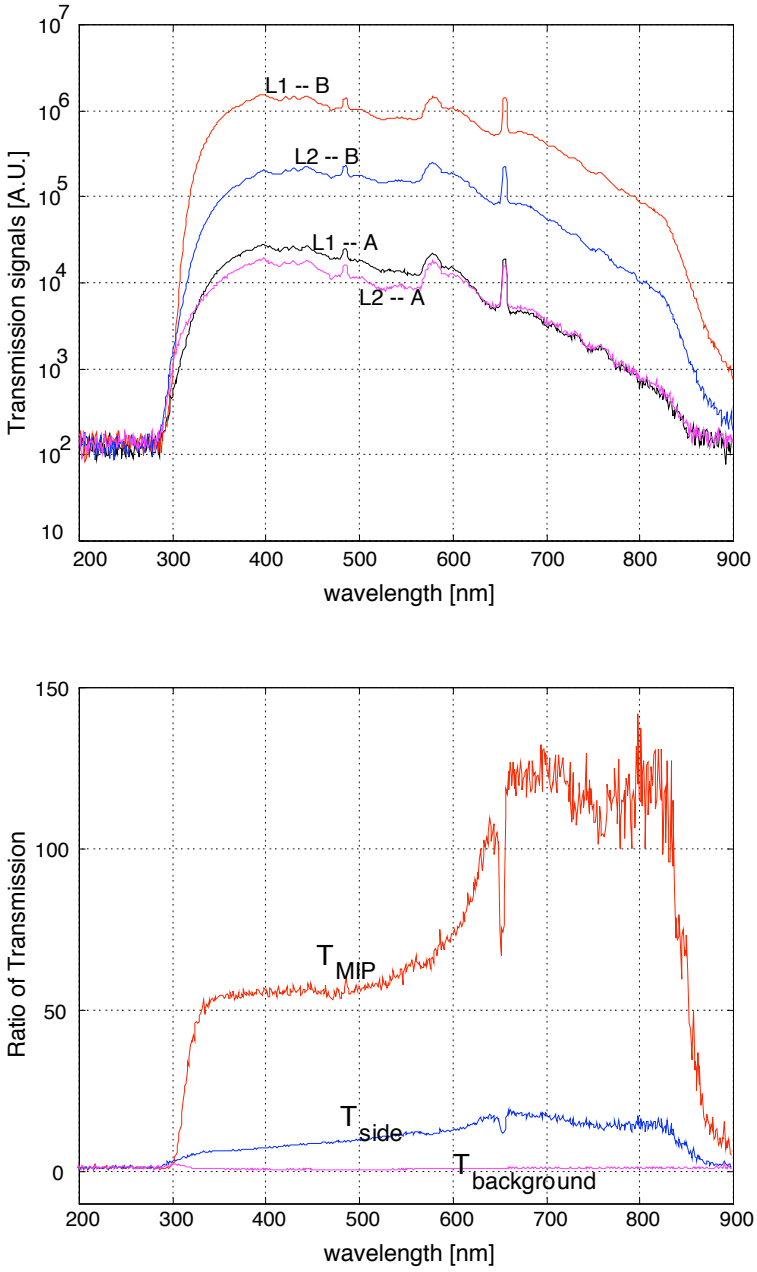

Figure 3.4: Top figure is the transmission spectra of the four measurements. Bottom figure is the ratio of the transmission spectrum. The magenta curve is $T_{background}$. The blue curve is T_{side}. The red curve is T_{MIP}.

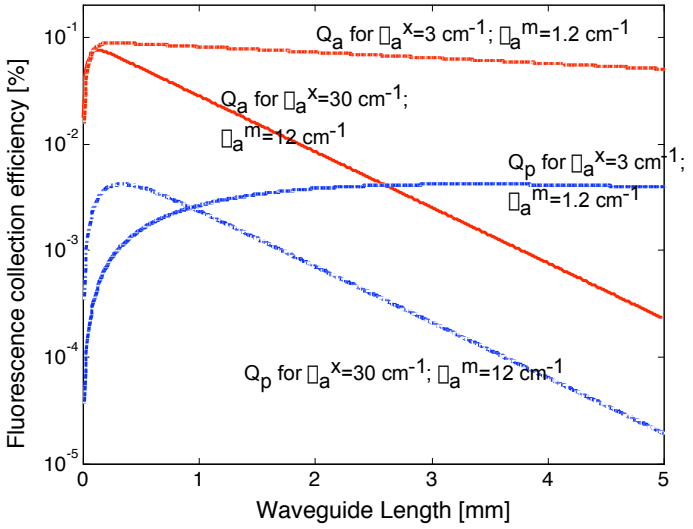

Figure 3.5: Numerical results of the relative output efficiency for analyte fluorescence Q_a and for polymer fluorescence Q_p as a function of MIP waveguide length.

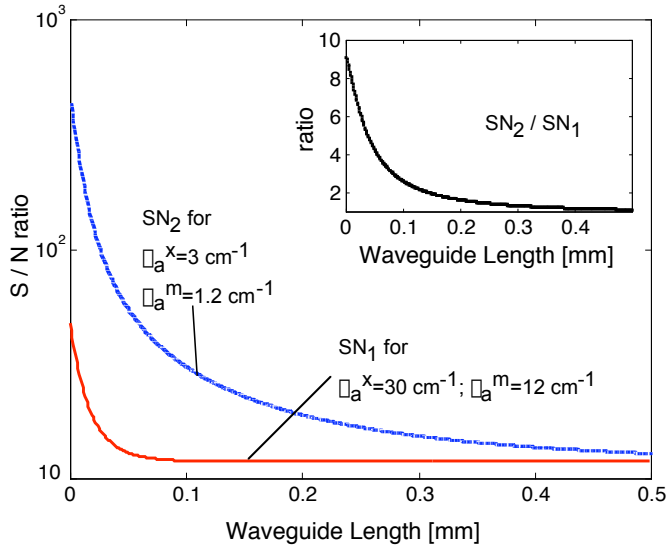

Figure 3.6: The signal to noise ratio (Q_a/Q_p) of a MIP waveguide as a function of waveguide length.

3.5 Conclusions

This study combined micromolding in capillaries (MIMIC) and MIP technique to fabricate imprinted optical waveguides for the detection of fluorescent polyaromatic hydrocarbon (PAH) molecules. Coupling of light into 5 mm long waveguide segments was verified through the comparison of relative transmission measurements. This suggests that a novel optical sensor using a MIP (as the recognition element) as an optical waveguide is possible. However, our numerical simulation shows that the relative output efficient is only 2×10^{-6} for 25 mM anthracene due to the high polymer absorption in the spectrometric regions of interest. A ten fold decrease of background absorption will increase the fluorescence output efficiency 250 times for a 5 mm waveguide segment.

Therefore, modifications in the type and purity of polymers may lead to future waveguides capable of light propagation as well as analyte detection. The emitted fluorescence from the analytes can be measured and calibrated according to analyte concentrations as long as the excitation and emission wavelength of the analytes are not at wavelengths that are strongly absorbed by the polymer. In this way, the sensing volume of MIPs can be increased, which may increase the sensitivity. Furthermore, if a single MIP waveguide can be successfully used as a biochemical sensor, by combining it with the MIMIC technique, an array of MIPs may be fabricated on a single chip to allow simultaneous analysis of multiple analytes.

Chapter 4

Fluorescence Anisotropy Studies of Molecularly Imprinted Polymers

4.1 Introduction

*Molecularly imprinted polymers (MIPs) are biomimetic materials that are used as the recognition elements in biosensors. Through host-guest interactions, imprinted polymers can exhibit recognition capabilities comparable to those of antibody-antigen systems [86]. The advantages of MIPs include their stability in a wide range of environments, their facility for sensor micro-fabrication, and their ability to detect analytes that are difficult or impossible to sense by immunoassay [58]. MIPs have been used in various separation techniques [87, 88], in drug discovery processes [89], and in biochemical sensors [90–92].

The recognition properties of MIPs arise from their synthesizing process. In this process, functional and cross-linking monomers are co-polymerized in the presence of the target analyte (the molecule for imprinting, whose structure serves as a pattern for recognition by shape and size) [1]. A good MIP system is specific to the target analytes and binds strongly with the analytes for *in situ* sensing [58, 93] or filtering [94], as well as has a high imprinting efficiency (i.e., the ratio of useful binding sites to the total number of imprinted binding sites) and uniform binding sites [77]. To examine MIP's binding performance, one often relies on the fluorescence signals of bound analytes [31] or the

*Part of this chapter was published in *Materials Research Society Proceedings 2003: Molecularly Imprinted Materials Symposium, vol. 787. p. 35-9.* Part of this chapter was submitted for publication in *Luminescence.*

polymers [36]. Steady-state fluorescence reveals the presence of analytes but lacks detailed information about the local binding environments.

Fluorescence lifetime distributions relate energy transfer of the fluorophore to the local environment because the speed of energy transfer or fluorescence quenching is a function of the distance between the fluorophore and the absorbing molecule [95]. Few research groups have studied the time-resolved fluorescence of MIPs [36, 96]. Wandelt *et al.* incorporated fluorescent monomers into cAMP-imprinted polymers and detected the quenching of fluorescence as the cAMP bound with the MIPs [36]. Their results showed different fluorescence lifetime distributions between specific and non-specific bindings; this suggests that time-resolved fluorescence measurements could possibly be used to characterize the binding specificity of MIPs.

Fluorescence anisotropy has been used to investigate fluorescent molecules in various polymer concentrations or viscosity environments [97–100], but has not yet been used to investigate the binding activity of MIPs. In this paper, we studied both the steady-state and time-resolved fluorescence and fluorescence anisotropy of MIPs. We compared the fluorescence anisotropy of MIPs with imprinted analytes present, MIPs with the imprinted analytes extracted, MIPs with rebound analytes, non-imprinted control polymers (non-MIPs), and non-MIPs bound with analytes. We also investigated changes in the steady-state anisotropy of MIPs and non-MIPs during polymerization.

4.2 Theory for Anisotropy

Assume polarized light parallel to the z-axis travels along the x-axis, and assume that I_z and I_x are the irradiances of the two polarized fluorescence lights oriented perpendicular to the y-axis (Fig. 4.1). The anisotropy (r) of a light source is defined as the ratio of the polarized component to the total irradiance [95],

$$r = \frac{I_z - I_y}{I_x + I_y + I_z} \ .$$

If $I_{\|}$ and $I_{\perp}$ are defined as the polarized irradiance parallel ($\|$) and perpendicular ($\perp$) to the direction of excitation polarization (the $x - z$ plane), then $I_z = I_{\|}$ and $I_x = I_{\perp}$. Since

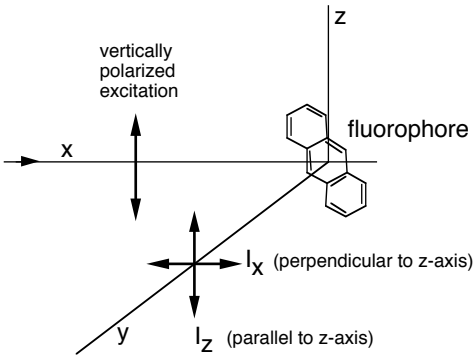

Figure 4.1: Polarization of fluorescence.

the dipole radiation from the fluorophores is symmetric around the z-axis, $I_x = I_y$. Hence,

$$r = \frac{I_{\parallel} - I_{\perp}}{I_{\parallel} + 2I_{\perp}} \ .$$

4.2.1 Steady-state anisotropy

The relationship between the steady-state anisotropy and the orientation of fluorophores can be derived by considering a single fluorophore in an isotropic solvent and in the absence of rotational diffusion. Figure 4.2 depicts a single radiating dipole oriented at an angle θ relative to the z-axis and ϕ relative to the y-axis. The radiated light from the dipole is

$$I_{\parallel}(\theta, \phi) = \cos^2\theta \ ;$$

$$I_{\perp}(\theta, \phi) = \sin^2\theta \sin^2\phi \ .$$

The population of excited fluorophores will be symmetrically distributed around the z-axis. Hence,

$$\langle \sin^2\phi \rangle = \frac{\int_0^{2\pi} \sin^2\phi d\phi}{\int_0^{2\pi} d\phi} = \frac{1}{2} \ .$$

Now if we consider all the radiating dipoles with orientation angle θ relative to the z-axis with a probability $f(\theta)$, the total polarized fluorescence intensities are

$$I_{\parallel} = \int_0^{\pi} f(\theta) \cos^2\theta d\theta \ ;$$

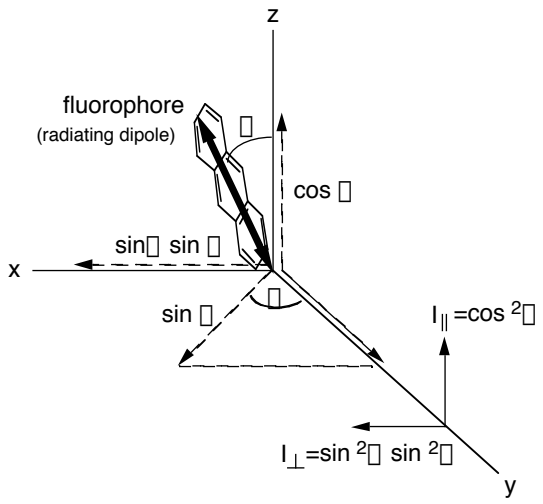

Figure 4.2: Emission intensities for a single fluorophore in a coordinate system.

$$I_\perp = \frac{1}{2}\int_0^\pi f(\theta)\sin^2\theta d\theta \ .$$

Therefore,

$$r = \frac{3\langle\cos^2\theta\rangle - 1}{2} \ , \tag{4.1}$$

where

$$\langle\cos^2\theta\rangle = \frac{\int_0^\pi f(\theta)\cos^2\theta d\theta}{\int_0^\pi f(\theta)d\theta} \ .$$

The molecules with their absorption dipoles aligned parallel to the electric vector of the polarized excitation have the highest probability of absorption (known as a photoselection phenomenon). Therefore, $f(\theta)$ is proportional to $\cos^2\theta$. Since the molecules are randomly oriented in a solution and the excitation-state population is symmetrical around the z-axis, the number of molecules radiating at an angle between θ and $\theta + d\theta$ is proportional to $\sin\theta d\theta$. As a result, the probability of molecules excited by parallelly polarized light is

$$f(\theta)d\theta = \cos^2\theta\sin\theta d\theta \ .$$

Substitution of the above equation into Eq. 4.1 yields an anisotropy of 0.4. This is the value observed when the absorption and emission dipoles are colinear, and when there are no depolarization processes.

For most fluorophores, there is an angular displacement β between the absorption-state dipole and the emission-state dipole. Hence, the observed anisotropy of fluorophores in a dilute solution is a product of the loss of anisotropy due to photoselection (=0.4) and that due to the angular displacement (β) of the absorption and emission dipoles. From a similar deviation as above,

$$r = \frac{2}{5}(\frac{3\cos^2\beta - 1}{2}) \tag{4.2}$$

Therefore, from the measured value r, one can calculate the angular displacement of the fluorophore. Note that r will lie between -0.2 and 0.4 for an isotropic solution with single-photon excitation.

4.2.2 Time-resolved anisotropy

When a fluorophore is excited with a pulse of parallelly polarized light, the decay of the difference between $I_{\parallel}(t)$ and $I_{\perp}(t)$ normalized by the total intensity is the anisotropy decay $r(t)$. Generally, $r(t)$ can be described as a multi-exponential sum,

$$r(t) = \sum_j r_j \exp(-t/\phi_j) \quad ,$$

where ϕ_j is the diffusion correlation times caused by the jth component. The limiting ansiotropy $r_0 = \sum_j r_j$ is the fluorescence anisotropy in the absence of rotational diffusion.

The multiple exponential terms are caused by different rotational diffusion rates around each x, y, or z axis for non-spherical fluorophores. In practice, one rarely resolves more than two exponentials. Generally, for small molecules, the rotational rates around the different axes are rarely different by more than a factor of 10. One can consider $r(t)$ is the combination of the fast correlation time ϕ_F and the slow correlation time ϕ_S, then

$$r(t) = r_0[\alpha \exp(-t/\phi_F) + (1-\alpha)\exp(-t/\phi_S)] \quad , \tag{4.3}$$

where α is the fraction of molecules rotating around the fast axis. Note that when α is close to 1, the anisotropy would decay with a single correlation time.

4.3 Materials and Methods

4.3.1 Materials

Polyurethane imprinted with anthracene was chosen as the MIP system [31, 84]. MIPs were made from a mixture of 0.026 mmol anthracene, monomers (0.375 mmol bisphenol A and 0.455 mmol *p,p′*-diisocyanatodiphenylmethane) and crosslinkers (0.250 mmol trihydroxybenzene and 0.195 mmol *p,o,p′*-triisocyanatodiphenylmethane) in a total of 2 mL dimethylformamide (DMF) solution. Non-imprinted polymers were prepared in a similar manner as the MIP except the template molecule anthracene was omitted from the solution.

The $1.5 \times 1.5\,\mathrm{cm}^2$ silicon wafers were first cleaned with the piranha solution (100 mL 98% H_2SO_4 with 43 mL H_2O_2). Additional silanization with an amino-silane was required to covalently attach MIPs to the wafers [85]. This was accomplished by immersing the clean wafers in 47 mL of a 1.0 mM acidic methanol solution (glacial acetic acid in methanol), 2.5 mL of MilliQ H_2O, and 500 μL of 3-aminopropyltrimethoxysilane. The reaction vessel was covered with aluminum foil and was continually flushed with nitrogen for 15 minutes. The wafer was then rinsed 3–4 times with fresh methanol to remove excess silane and subsequently heated at 120 °C for 5 minutes to promote a complete condensation reaction. The wafer was rinsed with methanol and dried under a stream of nitrogen.

Freshly prepared mixtures of the imprinting or non-imprinting solutions were spin-coated onto the silanized silicon wafers at 1000 rpm. One day after the MIPs films were formed, the imprinted anthracene was extracted by soaking the MIP-wafers in toluene. The fluorescence of the extraction solution was measured (excitation 365 nm, emission 404 nm) to monitor the extraction process. The toluene was replaced each day. It took about two days to complete the extraction process. The non-imprinted polymer samples were not treated with this procedure.

Rebinding of anthracene was conducted by soaking the extracted MIP or non-MIP samples separately in a 10 mL of 0.5 mM anthracene solution in DMF, sealed with aluminum foil and shaken for two days. Afterwards, the samples were rinsed with DMF, and

abbreviated name	sample number	Full description
anthracene in DMF	1	0.1 mM anthracene solution in DMF
non-MIPs	5	non-imprinted control polyurethane
MIPs	5	MIPs with 13 mM anthracene imprinted
extracted-MIPs	4	MIPs with imprinted anthracene extracted
rebound-MIPs	3	extracted-MIPs rebound with anthracene
rebound-non-MIPs	3	non-imprinted control polyurethane rebound with anthracene

Table 4.1: Summary of samples tested.

dried for one day.

Table 4.1 summarizes the types and the number of samples tested in our study.

4.3.2 Experimental Details

Steady-state fluorescence anisotropy measurements

The polarized fluorescence of anthracene solutions and MIP samples was measured using a fluorimeter (Fluorolog3, SPEX) with a 387 nm low-pass filter (387 AELP, Omega Optical, Inc., Brattleboro, VM, USA), two polarizers and a scrambler, as shown in Fig. 4.3. One quartz polarizer was placed at the window of the excitation monochromator; the other polarizer was located at the emission window, 90° relative to the excitation light. The 387 nm low-pass filter was placed at the excitation window immediately before the vertical polarizer to reject any possible reflected or scattered excitation light from the sample surface that might have contributed to the emission signals [95]. A polarization scrambler was inserted after the second polarizer to depolarize the light and to avoid detector bias for the two polarized states.

An anthracene solution in DMF (0.1 mM) inside a cuvette was measured at room temperature for calibration. MIP samples were placed diagonally in the cuvette chamber as shown in Fig. 4.3. The excitation scans used vertically polarized (relative to the plane of the table) excitation light from 310 to 380 nm; parallel ($I_{\parallel}$) and perpendicular ($I_{\perp}$) polarized emission at 405±2.5 nm were recorded sequentially. Emission scans used 377±2 nm vertically-polarized excitation light; both $I_{\parallel}$ and $I_{\perp}$ were scanned from 390 to 480 nm

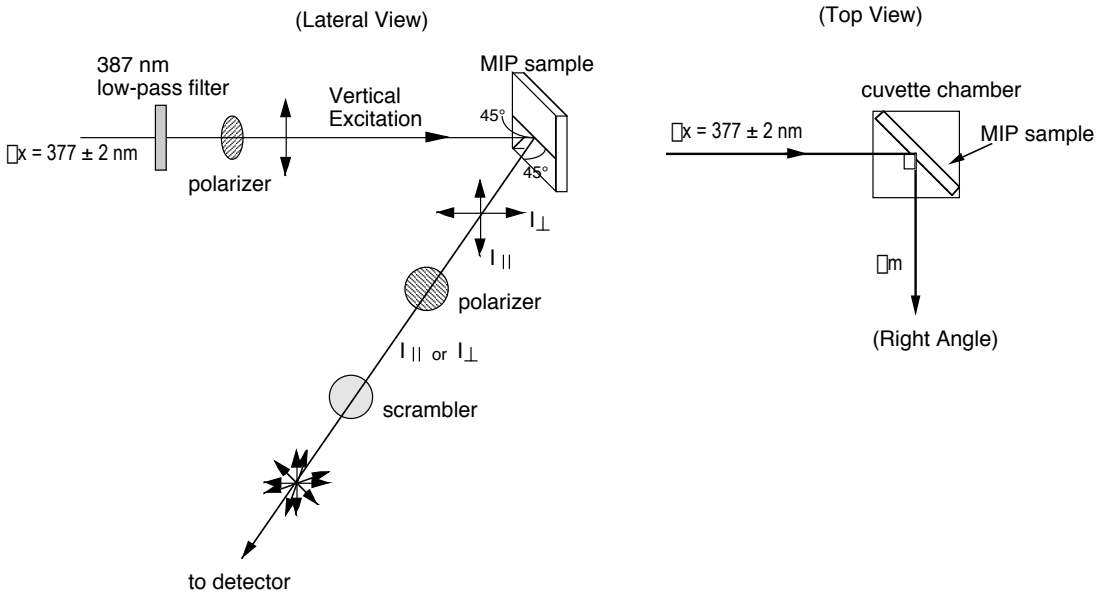

Figure 4.3: Schematic of the steady-state fluorescence anisotropy apparatus.. Excitation light was vertically polarized and incident at an angle of 45° relative to the plane of the MIP samples. Fluorescence emission was collected at an angle of 90° relative to the incident light.

sequentially.

Time-resolved fluorescence anisotropy measurements

Time-resolved fluorescence measurements were conducted using a regeneratively amplified Ti:Sapphire laser system (Clark-MXR, Inc. ORC-1000 Nd:YAG pumped TRA-1000 Ti:Sapphire laser) coupled to a Hamamatsu C5680 high-speed streak-camera equipped with a M5678 Synchronous Blanking unit and 5675 Synchronous Sweep unit (Fig. 4.4). The pulse duration of the laser was 110 femtoseconds. The instrument response was about 200 ps FWHM as determined using a standard scattering alumina suspension. The setup was similar to the steady-state measurement setup, except that a pulsed laser and a different detector were used. An extra 420±10 nm band-pass filter was placed in front of the entrance slit of the camera. A 377±5 nm pulsed laser running at 76 MHz was used to excite the MIP samples and the emitted light was recorded every 0.1 ns for 50 ns. The two

polarized states, $I_{\|}$ and $I_{\perp}$, of the emission were recorded sequentially. Two of each type of sample were measured.

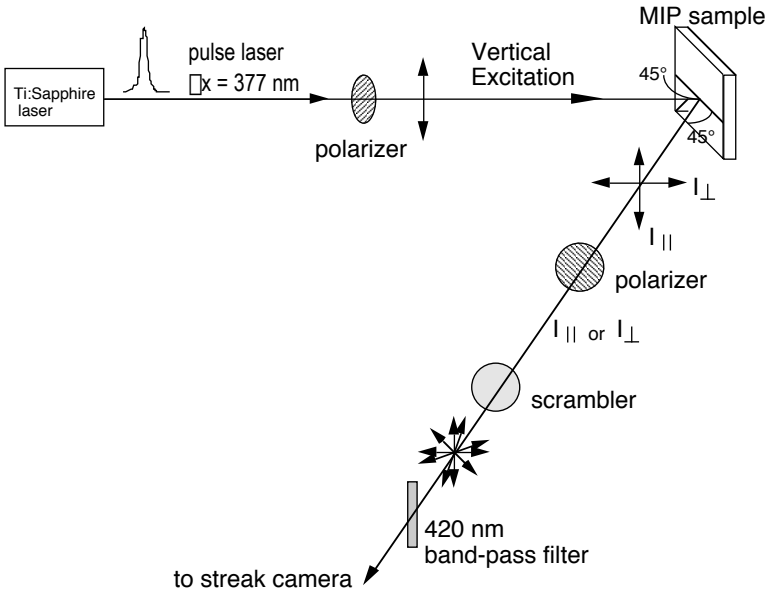

Figure 4.4: Schematic of the time-resolved fluorescence anisotropy apparatus. A 377 nm laser pulse was generated from Ti:Sapphire laser system, passed through the vertical polarizer, and sent to the MIP samples. Fluorescence emission passed through the second polarizer either vertically or horizontally, filtered by a 420 nm bandpass filter, and then collected with a streak camera.

4.3.3 Steady-state anisotropy measurements of MIP during polymerization

In this experiment, we measured the steady-state fluorescence anisotropy as a function of polymerization time of the freshly-prepared mixtures of MIPs with 5.4 mM anthracene and non-MIPs solutions in a clear quartz cuvette using the same setup as Fig. 4.3. Measurements were made every 2 minutes for the first 10 minutes, every 5 minutes for the next 20 minutes, and every 1 to 2 hours thereafter. Samples were in a gelatin form at this time. Five samples for each concentration of solution were measured.

4.4 Data Analysis

4.4.1 Time-resolved fluorescence

An exponential decay curve was used to fit the parallel-polarized fluorescence $I_{\parallel}(t)$ to calculate the fluorescence lifetime τ:

$$I_{\parallel}(t) = I_p \exp(-t/\tau) + I_0 \quad , \tag{4.4}$$

where I_p is the maximum fluorescence pulse irradiance, and I_0 is the background light irradiance which was calculated by averaging the fluorescence signals over the last 10 ns of recording time. Only one exponential time constant τ was needed because the second or higher exponential components were zero in our results.

4.4.2 Time-resolved fluorescence anisotropy

The fluorescence anisotropy r was calculated as

$$r(t) = \frac{I_{\parallel}(t) - I_{\perp}(t)}{I_{\parallel}(t) + 2I_{\perp}(t)} \quad . \tag{4.5}$$

For steady-state fluorescence anisotropy, $I_{\parallel}(t)$, $I_{\perp}(t)$, and $r(t)$ are constant over time. The time-resolved anisotropy $r(t)$ was fit to a two-component hindered-rotor model [95]:

$$\frac{r(t)}{r_{\text{limit}}} = \alpha \exp(-\frac{t}{\phi_F}) + (1-\alpha) \exp(-\frac{t}{\phi_S}) \quad , \tag{4.6}$$

where ϕ_F is a measure of rapid rotational motions with proportion α, ϕ_S measures slower rotational motions with proportion $1-\alpha$, and r_{limit} is the limiting anisotropy. All the fittings were obtained using the fmin function of Matlab.

4.4.3 Anisotropy versus polymerization time

A exponential polymerization-kinetics model [101, 102] was used to relate the anisotropy $r(t)$ as a function of the polymerization time.

$$r(t) = r_{\max} - (r_{\max} - r_0) \exp(-\frac{t}{t_{\text{polymer}}}) \quad , \tag{4.7}$$

where $r_{\max}$ is the maximum anisotropy, r_0 is the initial anisotropy, and t_{polymer} is the characteristic time for polymerization.

4.5 Results

4.5.1 Steady-state anisotropy

Figure 4.5 shows the parallel and perpendicular components of excitation and emission of MIPs and the anthracene in DMF. Fluorescence of anthracene in MIPs has a 6 nm Stoke shift relative to that in DMF. This is typical for compounds with a $S^*_{\pi\pi}$–S_0 transition in a polar solvent. Increasing the polarity of the solvent will increase the amount of red shift but typically no more than a few nanometers [103]. The parallel and perpendicular fluorescence, $I_{\parallel}^{\mathrm{DMF}}$ and $I_{\perp}^{\mathrm{DMF}}$, of anthracene in DMF should be identical since the steady-state anisotropy of anthracene molecules in a rotation-free liquid is zero. Therefore, the ratio of $I_{\parallel}^{\mathrm{DMF}}$ to $I_{\perp}^{\mathrm{DMF}}$ was used to normalize the parallel fluorescence of all other measurements. That is

$$I_{\parallel}^{\mathrm{calibrated}} = I_{\parallel}^{\mathrm{original}} \frac{I_{\perp}^{\mathrm{DMF}}}{I_{\parallel}^{\mathrm{DMF}}} \ .$$

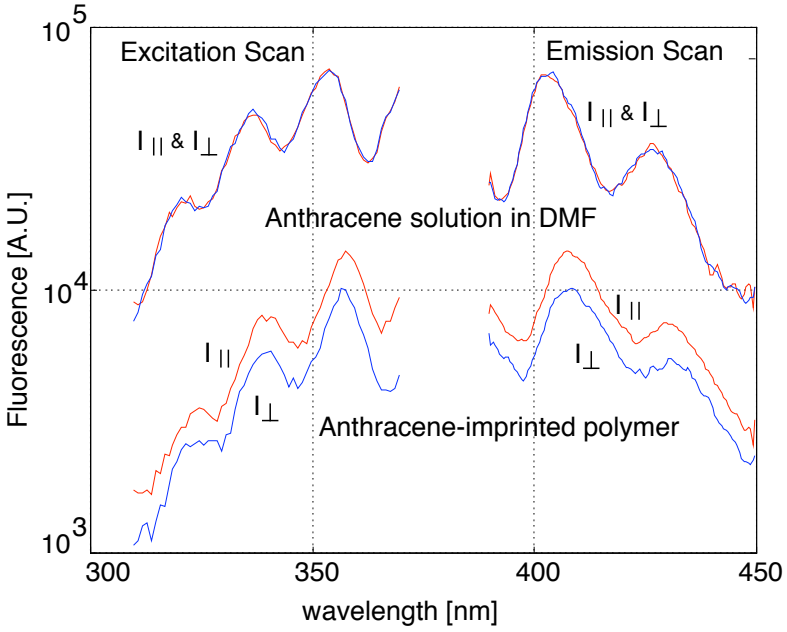

Figure 4.5: The perpendicularly $I_{\perp}$ and parallelly $I_{\parallel}$ polarized fluorescence of MIPs and anthracene in DMF for excitation scan and emission scan. The perpendicular and parallel fluorescence scans for the anthracene in DMF overlap.

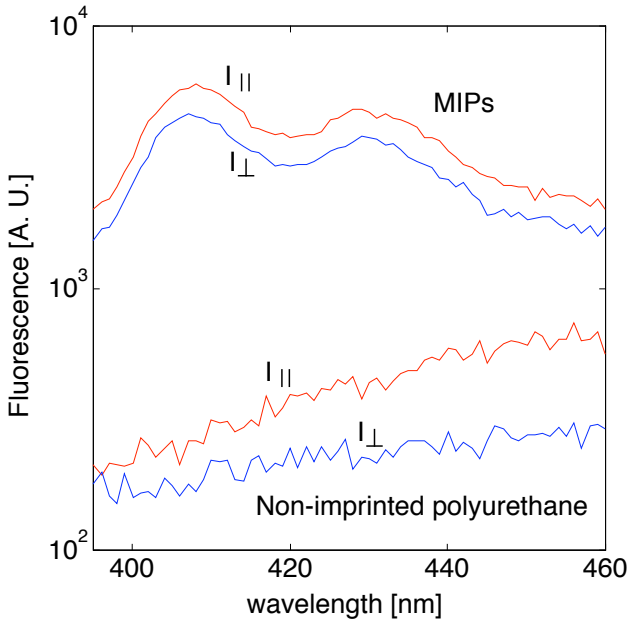

Figure 4.6: Comparison of the perpendicularly and parallelly polarized fluorescence of non-MIPs, and MIPs with 25 mM anthracene imprinted.

Non-MIPs emitted about 10 times less fluorescence than MIPs with 25 mM anthracene (Fig. 4.6). The fluorescence from a MIPs imprinted with 1 mM anthracene would drop to about the same level as a non-imprinted polyurethane.

The fluorescence anisotropy as a function of wavelength was essentially constant from 400–450 nm. The average anisotropy over the range 408±5 nm is shown in Fig. 4.7. There is no significant difference in anisotropies among all the MIPs based on ANOVA at $p = 0.05$.

4.5.2 Time-resolved fluorescence and anisotropy

Figure 4.8 shows the fluorescence at 420±10 nm as a function of time for all the samples. The fitted fluorescence lifetime τ in Eq. 4.4 for the parallel-polarized fluorescence at 420±10 nm of all the samples is listed in Table 4.2. Both rebound MIPs and rebound non-MIPs have the shortest fluorescence lifetime, while non-MIPs have the longest fluorescence lifetime (based on ANOVA at $p = 0.05$).

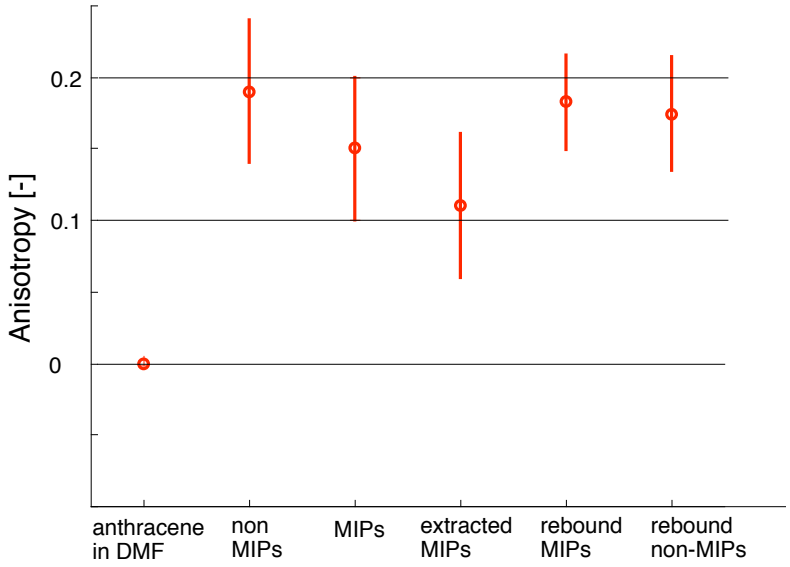

Figure 4.7: The steady-state fluorescence anisotropies of anthracene in DMF, non-MIPs, MIPs, extracted MIPs, rebound MIPs, and rebound non-MIPs.

The fitting of Eq. 4.6 to the anisotropies as a function of time $r(t)$ is listed in Table 4.2. Generally, rebound MIPs have the highest limiting anisotropy r_0 and the shortest fast-rotation correlation time ϕ_F. The non-imprinted polyurethane has the longest fast-rotation correlation time.

4.5.3 Steady-state anisotropy of MIPs during polymerization

The fluorescence anisotropy of the polymers was -0.04±0.04 when MIP or non-MIP solutions were freshly made. The anisotropy increased as the polymerization progressed, and finally reached to a stable value after the polymers solidified. Overall, the anisotropies as a function polymerization time fit Eq. 4.7 with <10% standard errors (Table 4.3).

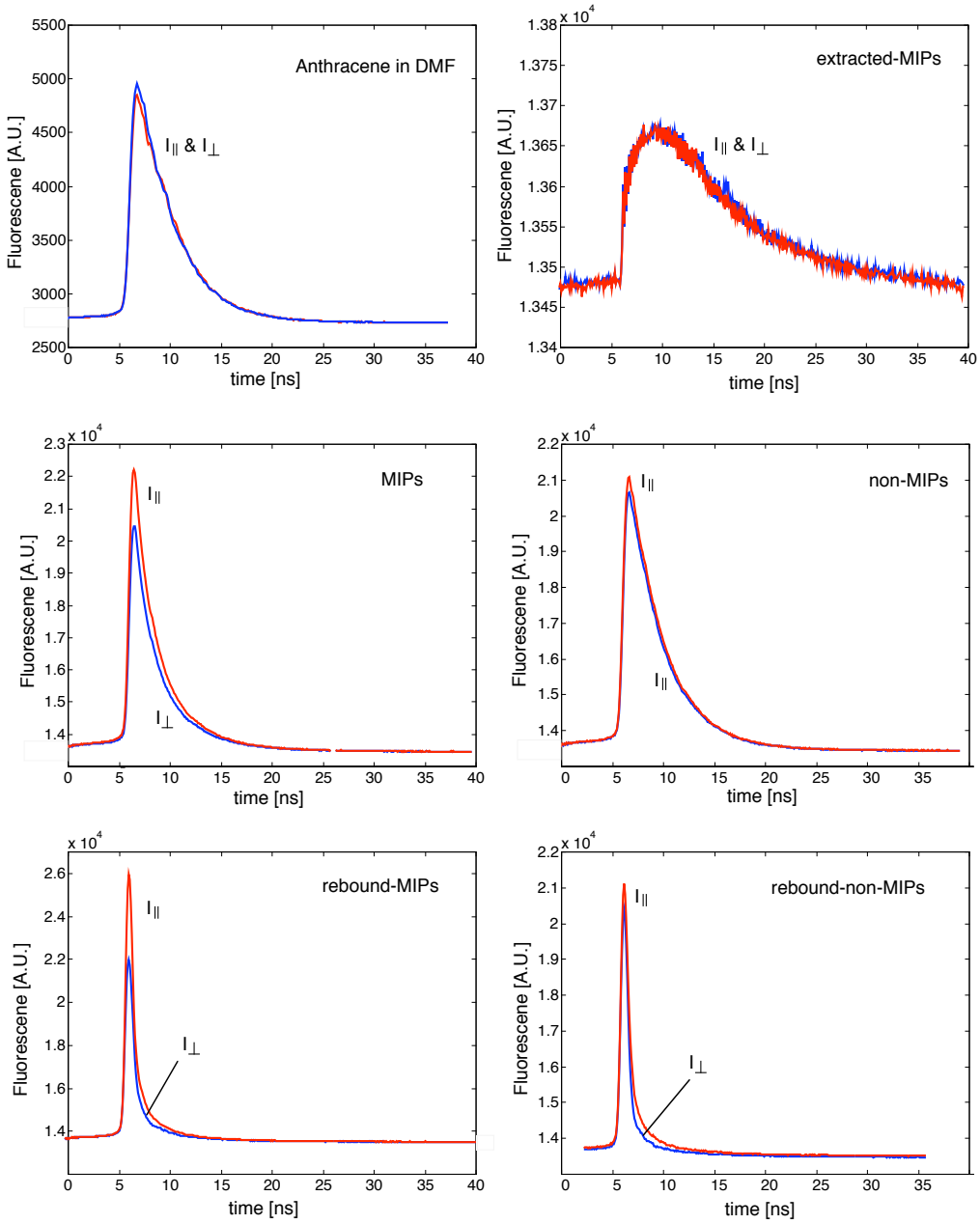

Figure 4.8: The two polarization states of the time-resolved fluorescence emission at 420±10 nm.

	τ [ns]	r_{limit} [–]	α	ϕ_F [ns]	ϕ_S [ns]
non-MIPs	3.54±0.09	0.019±0.001	0.995	3.4±0.1	350
MIPs	2.03±0.01	0.018±0.001	0.95	2.7±0.1	8.0±0.5
rebound-MIPs	0.63±0.01	0.025±0.001	0.94	1.2±0.1	11.5±0.5
rebound-non-MIPs	0.64±0.01	0.008±0.001	0.85	1.5±0.1	110±5
anthracene in DMF	4.52±0.01	0±0.0006			
extracted-MIPs	9.0±0.5	0±0.0006			

Table 4.2: Values of the fitting parameters in Eq. 4.6 and their standard errors for anisotropy decays. τ is the parallel-polarized fluorescence lifetime, ϕ_F and ϕ_S are the fast and slow rotational correlation time respectively, α and $1-\alpha$ are their proportions of contribution, and r_{limit} is the limiting anisotropy.

	r_{max}	r_0	t_{polymer} [sec]
non-MIPs	0.24±0.04	-0.05±0.02	750±150
MIPs	0.16±0.05	-0.06±0.03	1000±400

Table 4.3: Values of the fitting parameters and their standard errors for MIP polymerization kinetics (Eq. 4.7). r_{max} is the maximum anisotropy, r_0 is the initial anisotropy, and t_{polymer} is the characteristic time for polymerization.

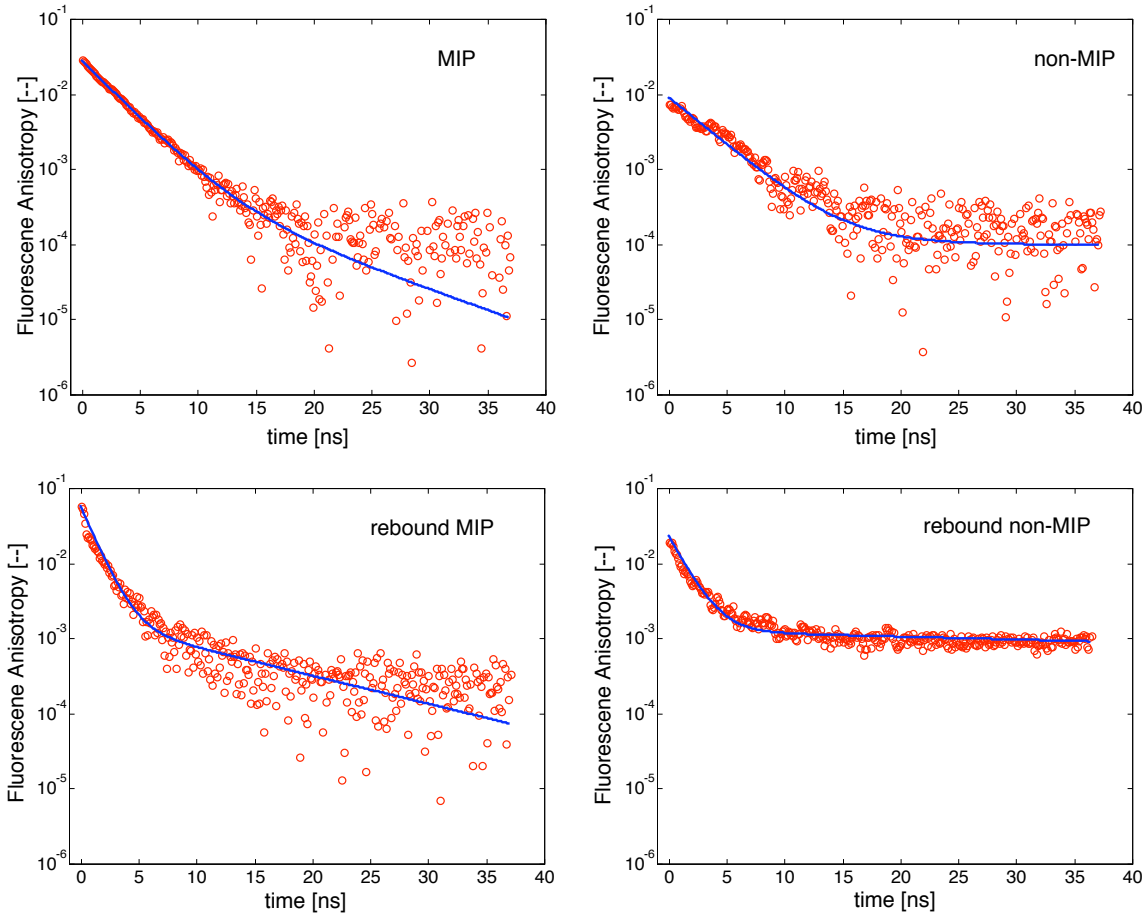

Figure 4.9: The fitting of the fluorescence anisotropy decay (circles) with two-exponential decay curve Eq. 4.6 (line). Parameters of the fitted curves are presented in Table 4.2.

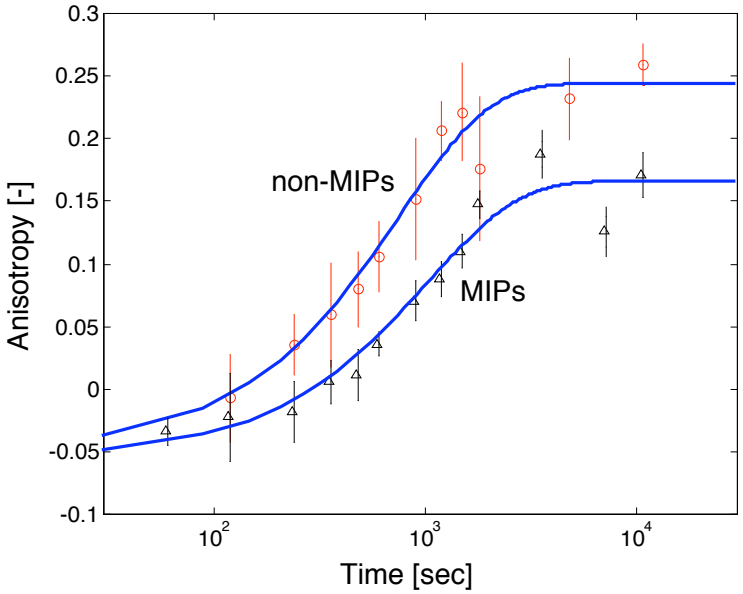

Figure 4.10: The fluorescence anisotropy of non-MIPs (circle) and MIPs (triangle) as a function of polymerization time. The solid curves are Eq. 4.7 with the fitted values of Table 4.3.

4.6 Discussion

Generally, the fluorescence anisotropy is independent of the emission wavelength because almost all emission is from the lowest singlet state [95]. The steady-state anisotropy of a fluorophore in a frozen solution without rotational diffusion is given by [95]

$$r = \frac{2}{5}\left(\frac{3\cos^2\beta - 1}{2}\right) \quad ,$$

where β is the angular displacement between the excitation dipole and emission dipole. r values slightly lower than 0.39 (corresponding to β=7.4°) are frequently reported for dilute fluorophore solutions [95]. Our anisotropy values are smaller, suggesting a larger angular displacement (an r of 0.15 corresponds to β=40°). This is probably due to radiative reabsorption between the bound anthracene and the polyurethane matrix. The large standard deviations of the anisotropy values may be caused by the inhomogeneous distribution of the distances between these fluorophore molecules.

The steady-state anisotropy values of the MIPs and non-MIPs were not zero (Fig. 4.7),

indicating that a MIP does not allow the anthracene to freely rotate. Although most DMF in MIPs will have evaporated, it is possible that the solvent exists as localized inclusions and creates micro- or nano-scale solvent cages in which the fluorophore is dissolved [104]. It is expected that the properties of such solvent inclusions are different from the bulk solvent. Most likely the viscosity of such micro-/nano-scale solvent inclusions in the MIPs would be more viscous than the bulk solvent. Therefore, a MIP acts as a highly-viscous or solid medium where rotational diffusion is constrained for bound analytes.

The fluorescence lifetime at 420 nm emission with 377 nm excitation is 4.52 ns for 0.1 mM anthracene in DMF. According to the literature [95, 105], a 1 μM solution of anthracene in degassed cyclohexane had a fluorescence lifetime 5.15$\pm$0.05 ns for emission $>$ 400 nm with 365 nm excitation, and a 5 μM, non-degassed solution has 3.99$\pm$0.03 ns lifetime at 415 nm emission with 355 nm excitation.

The fluorescence lifetime of anthracene in a polymer system was shorter than that of anthracene in DMF. Shortening of fluorescence lifetime is mostly caused by rapid resonance energy transfer [95] between the excited and ground state fluorophore molecules. This is especially likely in this imprinted polyurethane medium because the polyurethane is strongly absorbing.

According to Förster theory, the efficiency of energy transfer is proportional to d^{-6}, where d is the Förster distance between the photon donor (emission dipole) and acceptor (absorbing dipole) [95]. Therefore, the rate of fluorescence decay is sensitive to the binding distances between the dipoles. The fluorescence lifetime for rebound-MIPs or rebound non-MIPs was only 0.64 ns, much shorter than the 2.03 ns of the original MIP samples (Table 4.2). This suggests that rebound anthracene binds closely to the polymer or possibly forms localized agglomerates or aggregates on the polymer surface, causing fast energy transfer from the anthracene to the polymer or to another anthracene molecule. Further investigation is needed to quantitatively decide the distances between the fluorophores.

Anthracene in MIP environments had fast correlation times ranging from 1.2 to 2.7 ns with limiting anisotropy ranging over 0.008–0.025 (Table 4.2). Pokorná *et al.* measured a correlation time of 2.9–4.7 ns with limiting anisotropy 0.02–0.03 for anthracene in poly(methyl methacrylate) using three different solvents (chloroform, DMF, and 1,4-dioxane) [99].

Kudryasheva *et al.* studied the binding between the anthracene and luciferase and obtained a correlation time of 3.7–7.7 ns with limiting anisotropy of 0.13 for anthracene in water-ethanol solutions in the presence of luciferase [103]. In their analysis, only one correlation time was resolved.

For fluorophores in a rotationally diffusion-constrained medium, the anisotropy correlation time is expected to approach infinity. However, our result shows that anthracene bound in MIPs and non-MIPs has a fast anisotropy decay (Table 4.2), which is probably due to efficient energy transfer between the anthracene and the polyurethane. In support of this idea, the anisotropy of a different fluorophore imprinted in a different polymer system was investigated as a comparison. 1.75 mg of 9-dansyladenine was dissolved in a mixture of 50 mg polystyrene (PS) and 8.4 mg of 4-azido-2,3,5,6-tetrafluorobenzoic acid (PFPA-COOH) in 1 ml chloroform. The polymer mixture solutions were spin-coated on silicon wafers followed by UV irradiation to form a thin polymer film [13]. Polymer films with and without dansyladenine were compared. Dansyladenine-polymer film had emission fluorescence from 450 to 570 nm at an excitation of 360 nm, while the fluorescence of PS+PFPA-COOH film in the absence of 9-dansyladenine was ∼50 times weaker. Our results showed the time-resolved anisotropy of dansyladenine-polymer did not decay within 50 ns and had a limiting anisotropy of 0.2. Since polystyrene has nearly zero absorption in dansyladenine's fluorescence range, the anisotropy decay was not observed in this polymer system.

Rebound-MIPs and rebound-non-MIPs had the same fluorescence lifetime 0.64 ns and similar fast correlation times (1.2 ns and 1.5 ns). However, rebound-MIPs have much shorter slow-correlation time (11.5 ns) than the rebound-non-MIPs (110 ns). This suggests that the distances between anthracene and polyurethane molecules are similar in the MIP or non-MIP systems for most ($\geq$85%) of the molecules (Table 4.2). However, for a small proportion of the anthracene rebound in MIPs, the distance between the anthracene and the MIP backbone was shorter than that between the anthracene and non-MIPs.

One possible explanation is that the fast correlation times arise from non-specific binding. However, according to our previous rebinding study [84], the specific binding to non-specific binding was about 7 to 1 ratio and rebound-MIPs exhibited higher fluorescence

signals than rebound-non-MIPs. Therefore, the percentage of non-specific bindings in rebound-MIPs should be small. Wandelt *et al.* found a longer fluorescence lifetime for non-specific bindings, implying greater non-specific binding distances between the dipoles in their MIP system [36]. Nonetheless, different MIPs systems may have totally different binding structures. Different porosity and polarity of the MIP environment may induce different non-specific binding environments. In our MIP system, the only forces present are van der Waals force and $\pi - \pi$ stabilization forces that exist between the aromatic structures. Since both polyurethane and anthracene have aromatic structures and MIPs and non-MIPs have similar percentages of porogen (DMF) that may create similar solvent cage environments, it is highly likely that our non-MIPs had similar binding environments to MIPs for anthracene. Further investigation is needed to support this hypothesis.

The anisotropy of the polymer solutions increases during polymerization and fits a simple exponential polymerization model (Fig. 4.10). Since the viscosity increases during polymerization, this anisotropy likely reflects the viscosity of the fluorophore local environment [106]. When the polymer solutions were initially mixed, the fluorophores were still in a rotation-free environment; the initial anisotropy was close to 0. As the mixture polymerized, the crosslinking and imprinting process inhibited the fluorophores from freely rotating. As the polymerization continued, the proportion of rigidly-bound fluorophores increased, and therefore the anisotropy increased. Assume that $fI_{\|}$ and $fI_{\perp}$ is the parallel and perpendicular fluorescence from bound fluorophores, and $(1-f)I_{\|}$ and $(1-f)I_{\perp}$ is the proportion arising from unbound fluorophores. Since the unbound fluorophores are rotationally free, the emission will be independent of the plane of incidence and so

$$(1-f)I_{\|} = (1-f)I_{\perp} \ .$$

The anisotropy of partially polymerized samples becomes

$$r = \frac{fI_{\|} + (1-f)I_{\|} - fI_{\perp} - (1-f)I_{\perp}}{I_{\|} + 2I_{\perp}} = \frac{f(I_{\|} - I_{\perp})}{I_{\|} + 2I_{\perp}} \quad .$$

Thus as the fraction of bound fluorophores f increases so will the degree of anisotropy r.

4.7 Conclusions

We have investigated both steady-state and time-resolved fluorescence anisotropies of anthracene imprinted polyurethane. For this MIP system, we found that MIPs and non-MIPs have the same steady-state anisotropy. We observed that analytes rebound in the polymer system had a shorter fluorescence lifetime and a shorter fast rotational correlation time than that initially imprinted in polymers, suggesting a short-distance and tight binding between the analyte and the polymer when they rebound. The time-resolved fluorescence anisotropy technique can be used to study the binding distances and forces between analytes and MIPs. Finally, we observed that the steady-state anisotropy of polymer solutions increased with extent of polymerization. The steady-state anisotropy may provide an alternative method to observe the polymerization process or to measure the viscosity changes of fluorophore solutions with advantages of *in-situ* measurement. The limitation of this application will be that the observed solution needs to have fluorophores that have intrinsic anisotropy.

Chapter 5

A Photon Migration Model for Predicting Depth of Cure in Dental Composite

5.1 Introduction

*While significant advances have been made in understanding some of the limitations of dental composites, such as depth of cure, volumetric shrinkage, marginal adhesion, and color stability as well as fracture and wear resistance, there are still many unanswered fundamental questions concerning the light–activated polymerization process. The most important parameter for a light–activated dental composite system is the light–curing efficiency, which is defined as the extent of cure per delivered photon. The light–curing efficiency is affected by several factors, including those related to the composite formulation (monomer type, filler type, composition and size distribution, photosensitizer/accelerator/inhibitor type and concentration), the light source (output spectra, power, time of illumination) and the curing environment (geometry of the specimen, distance from the light source, color of the backing material). These factors affect the absorption and scattering of light, and consequently the amount of light delivered to various depths within the composite.

Many researchers have used an empirical approach to test the light–curing efficiency of composites by evaluating the curing depth for different light sources [16–20] or for

*This chapter was submitted for publication in *Dental Materials*.

different composition of composites [19, 20, 44, 107–109]. These studies are of limited general utility as new lamps or new composite formulations become available because earlier studies are specific to a particular combination of curing unit and material. To date, the exact relationship between the amount of light absorbed by the composite material and the polymerization level has not been fully elucidated. Fourier Transform Infrared (FTIR) spectroscopic analysis has perhaps been the most commonly used method to determine the degree of conversion of light–activated composites [19, 110–114]. Another popular parameter, hardness, has also been used routinely to evaluate the depth of cure [17–20, 102, 112, 115]. These methods provide an important indication of the extent of cure, but they do not directly provide information about the light–curing efficiency due to the effect of multiple light scattering.

This study used a Monte Carlo model to simulate photon migration within composite materials to predict the absorbed radiant exposure distribution. The CIE/ISO definition of radiant exposure is the total radiant energy incident on a surface-per-unit area [116]. It is equal to the integral over time of the irradiance $[W/cm^2]$ and has units of J/cm^2. This quantity is often referred to the dental literature as the energy density, which is more correctly defined as the radiant energy per unit volume $[J/cm^3]$ [116]. The radiant exposure varies from point to point in the composite and may be called the radiant exposure distribution. The product of the radiant exposure (at each wavelength) with the absorption coefficient (at the same wavelength) is the absorbed energy for that wavelength. The integral of all the wavelengths emitted by the lamp is the total absorbed energy per unit volume in the composite.

This radiant exposure distribution depends on the power, the dimensions and the position of the light source, and the optical properties and the geometry of the specimen. Based on the relationship between the radiant exposure distribution and the degree of conversion, or between the radiant exposure distribution and the hardness, one can determine the light–curing efficiency for a light–activated composite system. Ultimately, it should be possible to develop a model that can accurately predict the extent of cure of any dental composite in any type of cavity geometry when provided with these parameters.

5.2 Materials and Methods

5.2.1 Measurement of Degree of Conversion (DC) and Knoop Hardness (KHN)

The composite material used for this study was a commercially available light–cured minifill dental composite Z100 having approximately 70 volume percent of zirconia silica filler with average size less than 1 μm (3M ESPE, St. Paul, MN, USA). Composite was placed in a 21 mm diameter by 15 mm deep plastic container. A light curing unit (VIP, Bisco Inc., Schaumburg, IL, USA) with a 10 mm diameter light guide was placed 1 mm above the composite. The spectrum of the VIP light curing unit (wavelength range: 400–510 nm) shown in Fig. 5.1 was measured with a spectrofluorometer (SPEX Fluorolog-3, Jobin Yvon Inc., Edison, NJ, USA) by directly shining the light into the sample chamber.

The composite was illuminated for 60 seconds at 600 mW/cm^2. The composite was allowed to age for 24 hours at ambient temperature in the dark, and was then removed from the plastic container. The uncured, soft material was then scraped away with a knife, and the remaining specimen was embedded in slow-curing epoxy resin (Buehler epoxide, Buehler, Lake Bluff, IL, USA). The embedded composite material was sectioned longitudinally with a slow speed diamond saw (Isomet, Buehler) so that the depth versus the diameter of the cross section was exposed. Along the cross section, a grid was drawn on the surface dividing the composite into 2 mm sections across the diameter and 1 mm sections through the depth.

Hardness was measured in each 2×1 mm section with a Knoop diamond pyramid (136°). Hardness indentations (Kentron Hardness Tester, Torsion Balance Co., Clifton, NJ, USA) were made on the sectioned surface using a 100 g load and a dwell time of 10 s. Three hardness measurements were made for each grid area and an average hardness value was calculated.

The same specimens were then used for the degree of conversion (DC) analysis. Small chips of composite (20–40 μm in thickness and 100 μm in width and length) removed with a scalpel from the surface of the sectioned sample were placed on a KCl crystal for transmission FTIR (DS20/XAD microscope, Analect Instruments, Irvine, CA, USA).

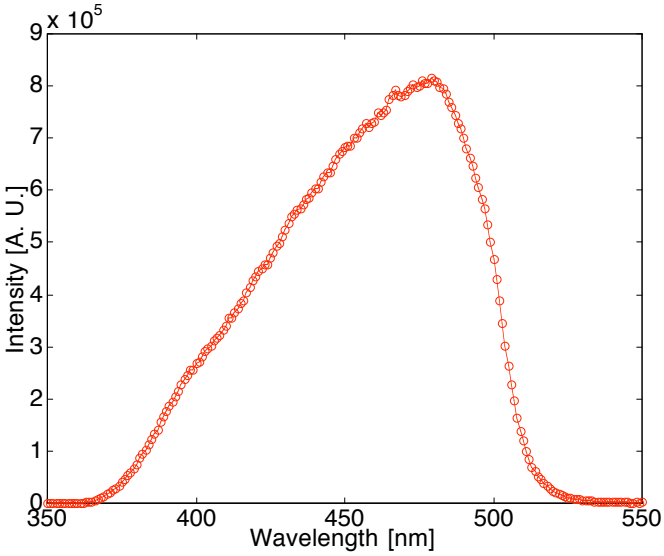

Figure 5.1: Spectrum of the VIP light curing unit.

Thirty scans were taken at $8\,\mathrm{cm}^{-1}$ resolution. The paste of the uncured composite was similarly tested. DC was calculated from the ratio of the C=C peak from the methacrylate group to that of the unchanging C...C peak from the aromatic ring for the uncured and cured specimens using standard baseline techniques (Ferracane et al., 1997 [111]). Three samples were tested for each area on the composite grid, and the results were averaged.

5.2.2 Measurement of Optical Properties

The inverse adding-doubling (IAD) method [117, 118] was used to obtain the absorption μ_a and reduced scattering coefficients μ_s' of both uncured and cured composite. A 1 mm thick sample was required for this method because the IAD method was a program simulating the possible output reflectance and transmittance at given optical properties based on a 1 mm thick sample. To obtain a disk 1 mm thick and greater than 25 mm in diameter, the uncured composite was placed on a microscope slide and pressed with another microscope slide with 1 mm spacers in between. This was done in the dark and the uncured composite disk samples were covered with aluminum foil. To obtain cured composite samples, the VIP light curing unit set to $600\,\mathrm{mW/cm}^2$ was used to cure the

disk samples. To ensure complete curing of the whole sample, both sides of the disk were illuminated for more than two minutes.

The reflection spectra of the samples were measured with an eight-inch diameter integrating sphere (IS-080, Labsphere Inc., North Sutton, NH, USA) in a reflectance mode configuration (Fig. 5.2a). A high–intensity lamp (Fiber–Lite High Intensity Illumination Series 180, Dolan–Jenner Industries, Inc., Lawrence, MA, USA) was used for illumination. Light from the lamp was conducted through a 600-μm diameter optical fiber (FT600ET, Thorlabs, Newton, NJ, USA) inserted in a stainless steel tube (painted white on the surface) and positioned 5 mm from the sample. The reflection signal was collected by a 1000-μm diameter optical fiber placed at the 0.25-inch diameter port of the sphere, guided to a spectrofluorometer (SPEX Fluorolog-3), and was recorded from 400 to 700 nm (1 nm bandpass, 0.1 second/nm). The sample was placed at the one-inch diameter port of the sphere. Reference standards with 50%, 75%, and 99% reflectance (Spectralon, Labsphere Inc., North Sutton, NH, USA), and rough-surface black paper (as 0% reflectance) were measured for the calibration of the lamp. All the measurements were done in the dark. A total of five samples were measured.

Transmission measurements were similar to the reflection measurements except that the light illumination was from outside the integrating sphere (Fig. 5.2b). For calibration, 0% and 100% transmission were measured by putting aluminum foil or nothing at the transmission port of the sphere.

The reflectance of samples was calculated using

$$R_{sample} = R_{std}\frac{M_{R(sample)} - M_{R(dark)}}{M_{R(std)} - M_{R(dark)}}$$

where R_{sample} is the reflectance of the sample, $M_{R(sample)}$ is the reflection spectrum of the composite sample, $M_{R(dark)}$ is the reflection spectrum of the rough-surface black paper, $M_{R(std)}$ is the reflection spectrum of the reflectance standard, and R_{std} is 0.99 for 99% reflectance standard, 0.75 for 75% reflectance standard, and 0.5 for 50% reflectance standard. The transmission was calculated using

$$T_{sample} = \frac{M_{T(sample)} - M_{T(Al)}}{M_{T(100)} - M_{T(Al)}}$$

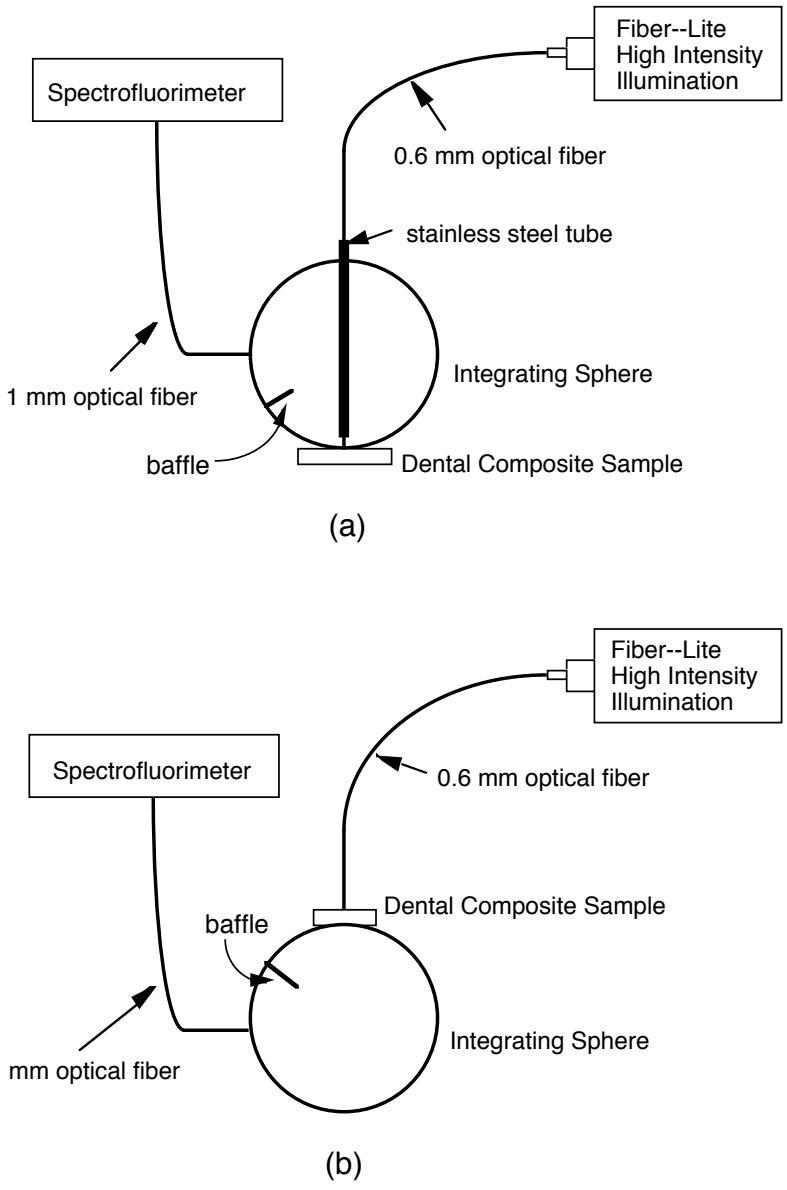

Figure 5.2: Experimental setup for optical property measurements. (a) is the configuration for measuring reflectance and (b) was used to measure transmission.

where T_{sample} is the transmittance of the sample, $M_{T(sample)}$ is the transmission spectrum of the composite sample, $M_{T(Al)}$ is the transmission spectrum of the aluminum foil, and $M_{T(100)}$ is the transmission spectrum of nothing.

The reflectance R_{sample} and transmittance T_{sample} values were then fed into the IAD software program to extract the intrinsic optical parameters for the samples. The program does this by repeatedly estimating the optical properties and comparing the expected observations with those obtained experimentally [117].

5.2.3 Monte Carlo Simulations

A Monte Carlo computer model was developed to simulate the photon migration in the composites. This Monte Carlo code was adapted from that developed by Jacques [119]. The sample was set to 20 mm wide, 20 mm long and 10 mm deep, and divided into $(1 \times 1 \times 1)\,\mathrm{mm}^3$ cubic bins to record the absorbed photon energy. The optical properties were held constant during each simulation. A 10 mm diameter collimated, flat beam was launched normal to the sample in the central position, mimicking the experimental procedure used for the DC and KHN evaluations. Photons deposited their energy into the bins based on their path of travel. If a photon hit the top surface, the photon was either transmitted to the air or was reflected back into the sample. The chance of reflection depended on the Fresnel reflection at the particular angle of incidence [68]. Photons that hit an outer boundary other than the top surface were terminated and their energy was deposited into the last bin they occupied.

In the DC and KHN experiment, the total energy of light delivered was (the irradiance) $\times$ (duration of illumination) $\times$ (the total area of light source) $= 600\,\mathrm{mW/cm^2} \times 60\,\mathrm{sec}$ $\times\ \pi(0.95/2)^2\ \mathrm{cm}^2 = 25.5\,\mathrm{J}$. The final absorbed photon count of each bin in the Monte Carlo simulation was divided by the total number of launched photons, the bin volume, and the absorption coefficient, and then multiplied by 25.5, so the final values represented the radiant exposure distribution (J/cm^2) in the composite. This distribution was then compared with the DC and KHN results.

Since the optical properties of the uncured and the cured composite were different, two sets of simulations were performed. These two simulations should bracket the range

of possible light distributions for samples whose optical properties dynamically change during curing. Since the lamp emission peak (Fig. 5.1) and the camphorquinone absorption peak [120] fall in the wavelength region of 470±5 nm, the optical properties were set as follows: $\mu_s' = 13.67\,\mathrm{cm}^{-1}$, $\mu_a = 1.06\,\mathrm{cm}^{-1}$ for uncured samples, and $\mu_s' = 12.76\,\mathrm{cm}^{-1}$, $\mu_a = 0.68\,\mathrm{cm}^{-1}$ for cured samples (see Fig. 5.3 in Results section). The refractive index was set at $n = 1.49$ for both uncured and cured samples. The exact refractive indices, which may be different between the uncured and the cured composite, were not measured. The actual index of refraction was 1.55 for BisGMA, 1.46 for TEGDMA, and 1.45 for HEMA measured by Asmussen *et al.* [121]. Since our composite was a mixture of these components and fillers, a value between 1.45 and 1.55 was chosen. However, in the Monte Carlo simulations, 1% of the refractive index variation affects only about 1% of the chances of reflection at the top surface. Increasing of the refractive index increases the chance of the reflection, which, in turn, increases the chance of the photons propagating in the composite.

5.2.4 Relating Monte Carlo radiant exposure with DC and KHN

The radiant exposure at each position in the sample was compared with the measured DC and KHN values. Various nonlinear models have been proposed to describe polymer curing kinetics [39, 122, 123]. In this paper, we adapted two simple models to fit the relationship between the extent of cure and the radiant exposure. One is a commonly used [101, 102, 107], one-phase, two-parameter, exponential form model ,

$$\frac{M(0) - M(t)}{M(0)} = 1 - \exp(-kt) \ ,$$

where $M(0)$ is the initial concentration of methacrylate groups, $M(t)$ the concentration of methacrylate groups at time t (the exposure time), and k is a rate parameter. Since the radiant exposure ($\mathrm{J/cm^2}$) is equal to the product of the irradiance ($\mathrm{W/cm^2}$) and the time (s), we replaced the time of light exposure t with the radiant exposure H, and replaced the fitting parameter, k, with $H_{dc}^{50\%}$ and $H_{khn}^{50\%}$ to include the concept of the curing threshold for 50% of maximum degree of conversion and Knoop hardness. Therefore, the above

equation was rewritten as (called "exponential model" in this paper)

$$DC = DC_{max}\left(1 - \exp(\ln 0.5\ \frac{H}{H_{dc}^{50\%}})\right) \quad ,$$

$$KHN = KHN_{max}\left(1 - \exp(\ln 0.5\ \frac{H}{H_{khn}^{50\%}})\right) \quad .$$

Another model proposed by Racz [122] can be expressed as

$$\frac{M(0) - M(t)}{M(0)} = \frac{kt^n}{1 + kt^n} \ ,$$

where t is the curing time, and k and n are the fitting parameters. This model allows a S-shaped curve. Similarly, we can correlate t with radiant exposure H, and k with radiant exposure threshold, $H_{dc}^{50\%}$ and $H_{khn}^{50\%}$, as 50% of the maximum curing level. Moreover, in our result, the best fit for n was about 2±0.2 for both DC and KHN data. Therefore we fixed $n = 2$ for both the uncured and cured composite. Each formula can then be rewritten as

$$DC = DC_{max}\frac{(H/H_{dc}^{50\%})^2}{1 + (H/H_{dc}^{50\%})^2} \quad ,$$

$$KHN = KHN_{max}\frac{(H/H_{khn}^{50\%})^2}{1 + (H/H_{khn}^{50\%})^2} \quad .$$

5.3 Results

5.3.1 Optical properties of dental composite

Figure 5.3a shows that the absorption coefficient μ_a of the composite decreases as the wavelength increases, and decreases upon curing, especially at wavelengths between 440 nm and 500 nm. For the wavelength region of 470±2 nm, which corresponds to the lamp emission peak and the camphorquinone absorption peak [120], the absorption coefficient is 1.06±0.02 cm^{-1} for uncured Z100, and 0.68±0.02 cm^{-1} for cured Z100.

Figure 5.3b shows the reduced scattering coefficient μ_s' of cured and uncured composites as a function of wavelength. Observe that the uncured composite has a slightly higher scattering coefficient than the cured composite in the wavelength range of 420 nm to 550 nm. The scattering coefficient for both cured and uncured composites decreases as the wavelength increases. For the wavelength region 470±2 nm, the reduced scattering coefficient is 13.67±0.05 cm^{-1} for uncured Z100, and 12.76±0.04 cm^{-1} for cured Z100.

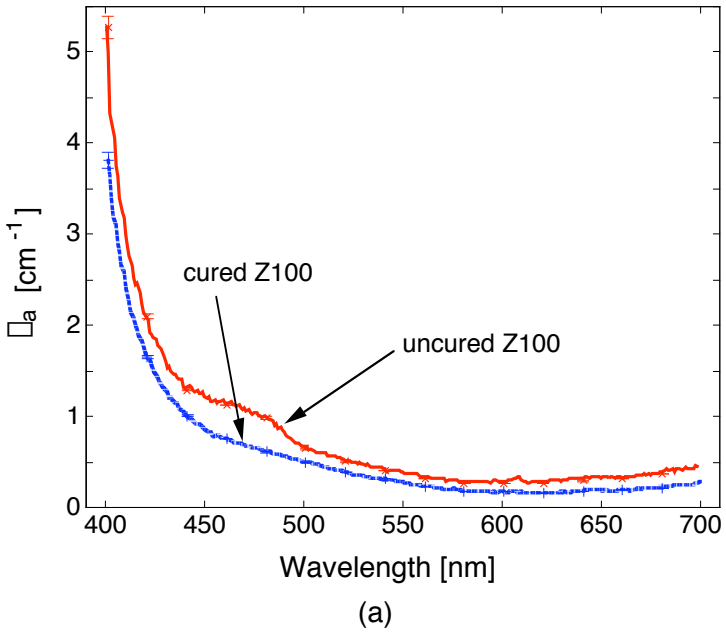

(a)

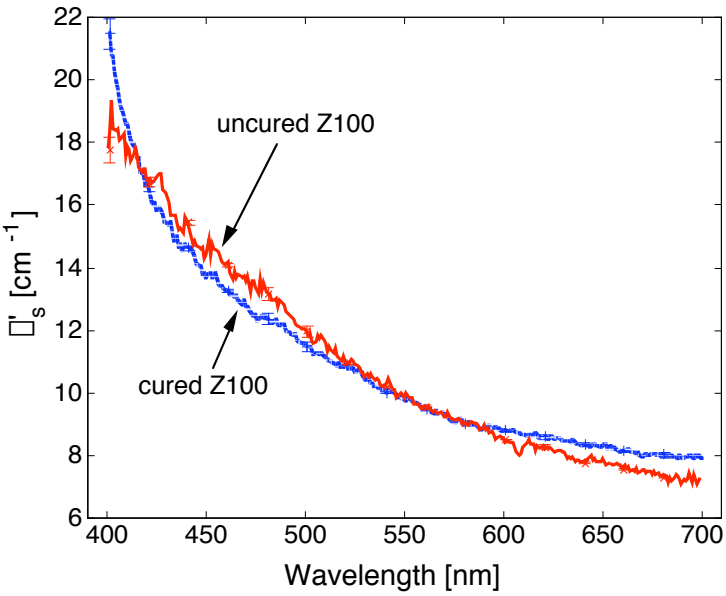

(b)

Figure 5.3: (a) is the absorption coefficient μ_a as a function of wavelength of uncured (solid) and cured (dashed) dental composite Z100. (b) is the reduced scattering coefficient μ_s' as a function of wavelength of uncured (solid) and cured (dashed) Z100.

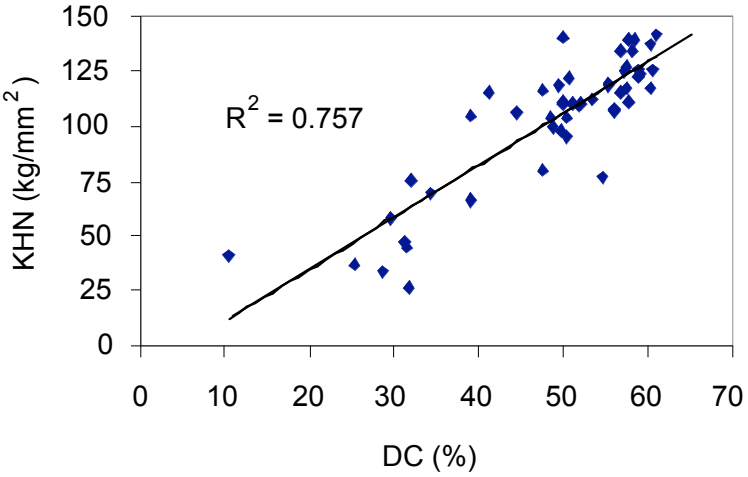

Figure 5.4: The Knoop hardness number versus the degree of conversion. The coefficient of determination R^2 between the data and the regression line is 0.757.

5.3.2 DC, KHN and Monte Carlo simulation

The hardness (the Knoop Hardness number, KHN) and the DC had a linear relationship with coefficient of determination $R^2 = 0.757$ (Fig. 5.4).

Figure 5.5 compares the measured DC and KHN values and the Monte Carlo radiant exposure across the uncured and cured sample. Note that the DC contour map shows that the composite reached the 80% curing level (DC≈50%) down to a depth of 4 mm and roughly 8 mm in radius, while the KHN contour map shows that the 80% curing level (KHN≈110 kg/mm^2) extended to slightly greater than 4 mm in depth and 6 mm in radius. The depth for 50% of the maximum DC (DC≈30%) and KHN (KHN≈70 kg/mm^2) extends down to about 6 mm.

5.3.3 Relating Monte Carlo radiant exposure to DC and KHN

The measured DC and KHN at each point in the sample was plotted against the calculated radiant exposure at that point and fitted with exponential and Racz models for an uncured composite (Fig. 5.6). The same was done for a cured composite sample (Fig. 5.7). The best fits based on the two models for $H_{dc}^{50\%}$ and $H_{khn}^{50\%}$, and the calculated radiant exposure $H_{dc}^{80\%}$ and $H_{khn}^{80\%}$ for the 80% curing level, are listed in Table 6.2. There was no

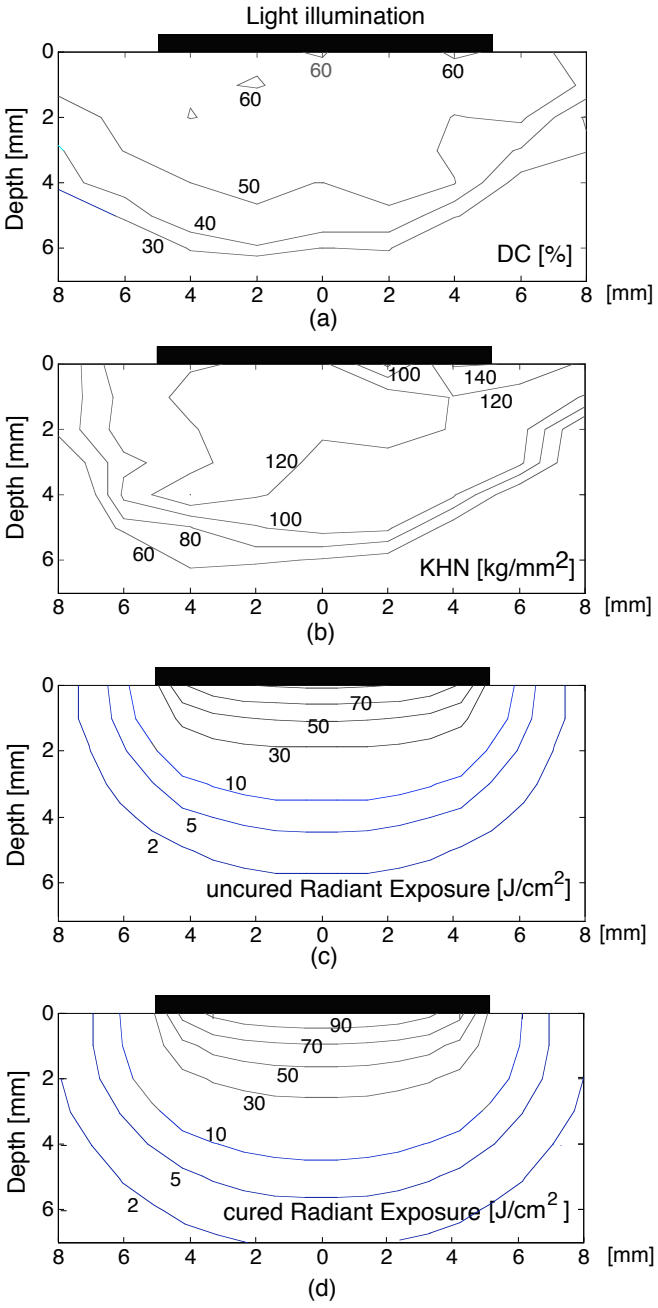

Figure 5.5: Distributions of measured DC (a), KHN (b), and calculated Monte Carlo radiant exposure for uncured (c) and cured (d) composite. The black bar above each contour map indicates the extent of the curing beam.

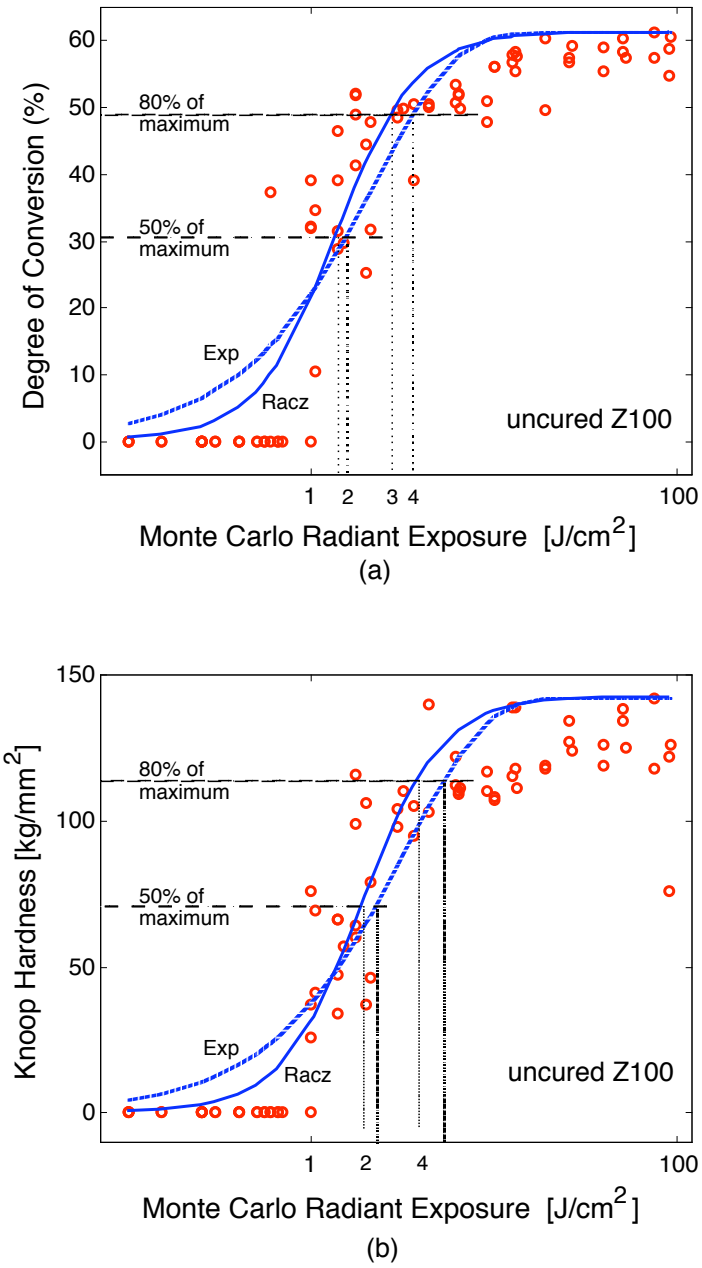

Figure 5.6: DC (a) and Knoop Hardness (b) versus Monte Carlo radiant exposure for uncured Z100. The solid curve is fitted with the Racz model, and the dashed curve is fitted with the exponential model. The coefficient of determination r^2 for the fitted curve was 0.93 for the exponential model and 0.95 for the Racz model.

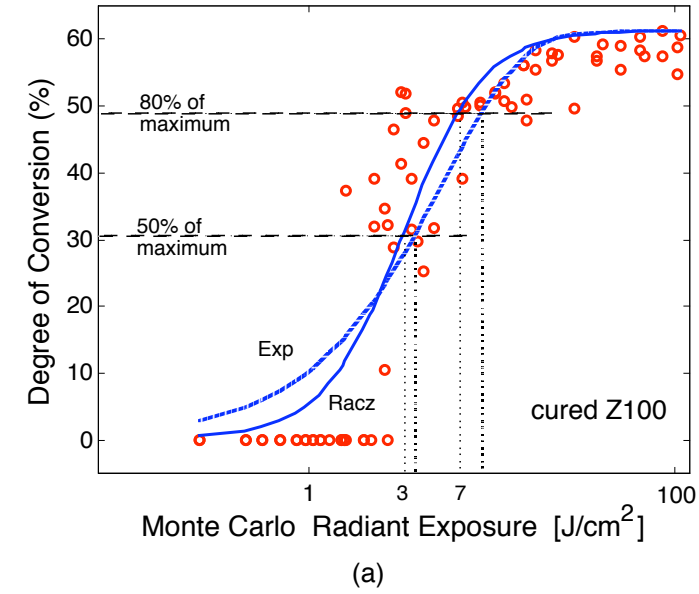

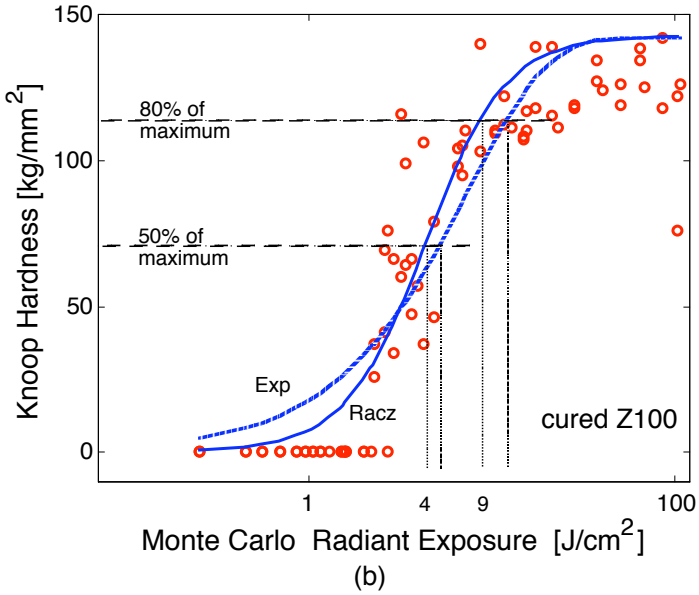

Figure 5.7: DC (a) and Knoop Hardness (b) versus Monte Carlo radiant exposure for cured Z100. The solid curve is fitted with the Racz model, and the dashed curve is fitted with the exponential model. The coefficient of determination r^2 for the fitted curve was 0.92 for the exponential model and 0.94 for the Racz model.

		uncured		cured	
		exponential	Racz	exponential	Racz
μ_a	(cm^{-1})	1.06(0.02)		0.68(0.02)	
μ_s'	(cm^{-1})	13.67(0.05)		12.76(0.04)	
$H_{dc}^{50\%}$	(J/cm^2)	1.5(0.1)	1.4(0.1)	3.8(0.3)	3.3(0.2)
$H_{khn}^{50\%}$	(J/cm^2)	2.3(0.2)	1.9(0.1)	5.2(0.4)	4.4(0.3)
$H_{dc}^{80\%}$	(J/cm^2)	3.6(0.3)	2.8(0.2)	8.7(0.7)	6.7(0.4)
$H_{khn}^{80\%}$	(J/cm^2)	5.3(0.4)	3.8(0.2)	12.0(1.0)	8.8(0.6)

Table 5.1: The optical properties used in the Monte Carlo simulation for uncured and cured Z100, and the comparison of the fitting parameters, $H_{dc}^{50\%}$ and $H_{khn}^{50\%}$, and the calculated radiant exposure thresholds, $H_{dc}^{80\%}$, and $H_{khn}^{80\%}$ using the exponential and the Racz model. Values are mean radiant exposure. The standard errors of the means are in parentheses.

significant difference between the two models for all the thresholds, $H_{dc}^{50\%}$, $H_{khn}^{50\%}$, $H_{dc}^{80\%}$, and $H_{khn}^{80\%}$, based on one-way ANOVA followed by Tukey's post-hoc multiple comparison test at $p < 0.05$.

5.4 Discussion

Few groups have studied the optical properties of dental composite. Lee et al. measured the photometric properties based on two geometries of total reflectance measurements [124]. This photometric technique was useful for evaluating the esthetic appearance of the materials, but lost detail with respect to how the composite interacts with each wavelength because it measured an integrated parameter (e.g., lumping all green wavelengths together). Taira et al. measured Kubelka-Munk optical coefficients [125]. However, it is difficult to relate these coefficients to the standard optical properties [126, 127]. In our study, we have measured the standard absorption and scattering properties of the composite before and after curing [128], because these intrinsic optical properties can be used in light propagation models.

Figure 5.5 shows that the 80% cure region was wider than the region directly illuminated by the curing light guide. This is primarily a result of scattering by the composite.

While it is possible that beam divergence may occur, our measurement showed that the beam diverged only 1 mm over a distance of 7 mm in air. Divergence would be even less in the higher index of refraction composite. To examine how the scattering and absorption coefficients affect the light distribution, another two simulations were performed with optical properties set to be the same as uncured Z100, but with doubled scattering or doubled absorption. Comparing both results (Fig. 5.8b, c) with the original uncured Z100 radiant exposure (Fig. 5.8a), one can see that a higher scattering coefficient translates to higher radiant exposures in the central direct-illumination region, while a higher absorption coefficient yields lower radiant exposures at the center. Light in both samples penetrates less deeply and less laterally, and would have less width and depth of cure. Visible light should penetrate better than UV light because Z100 has a lower scattering and absorption coefficient at longer wavelengths (Fig. 5.3).

The fit between the extent of cure (DC or KHN) and the Monte Carlo radiant exposure in Figs. 5.6 and 5.7 yielded a slightly greater regression coefficient r value (0.95 on average) using the Racz model than for the exponential model (r=0.93 on average). Cohen et al. [102] also used the exponential model and Racz's model to fit the KHN versus the exposure duration distribution, and they also found a slightly higher coefficient of determination r^2 for the Racz model than the exponential model.

Watts has described an expression for the polymerization kinetic model of light activated resin composite [39],

$$\frac{DC}{DC_{max}} = 1 - \exp[-k_p k_t^{-0.5} (\Phi I_a)^{0.5} t] \quad ,$$

where k_p and k_t are the propagation and termination rate constants, Φ is the quantum yield for initiation, I_a is the light fluence rate absorbed by the photosensitizer, and t is the exposure time. All the material dependent parameters ($k_p k_t^{-0.5} \Phi^{0.5}$) can be combined into a single constant α if assuming k_p and k_t do not change. This assumption should hold well until the end of the reaction where both propagation and termination greatly decrease due to difficulties in diffusing through a solid network. Therefore, the above equation can be rewritten as

$$\frac{DC}{DC_{max}} = 1 - \exp(-\alpha I_a^{0.5} t) \quad .$$

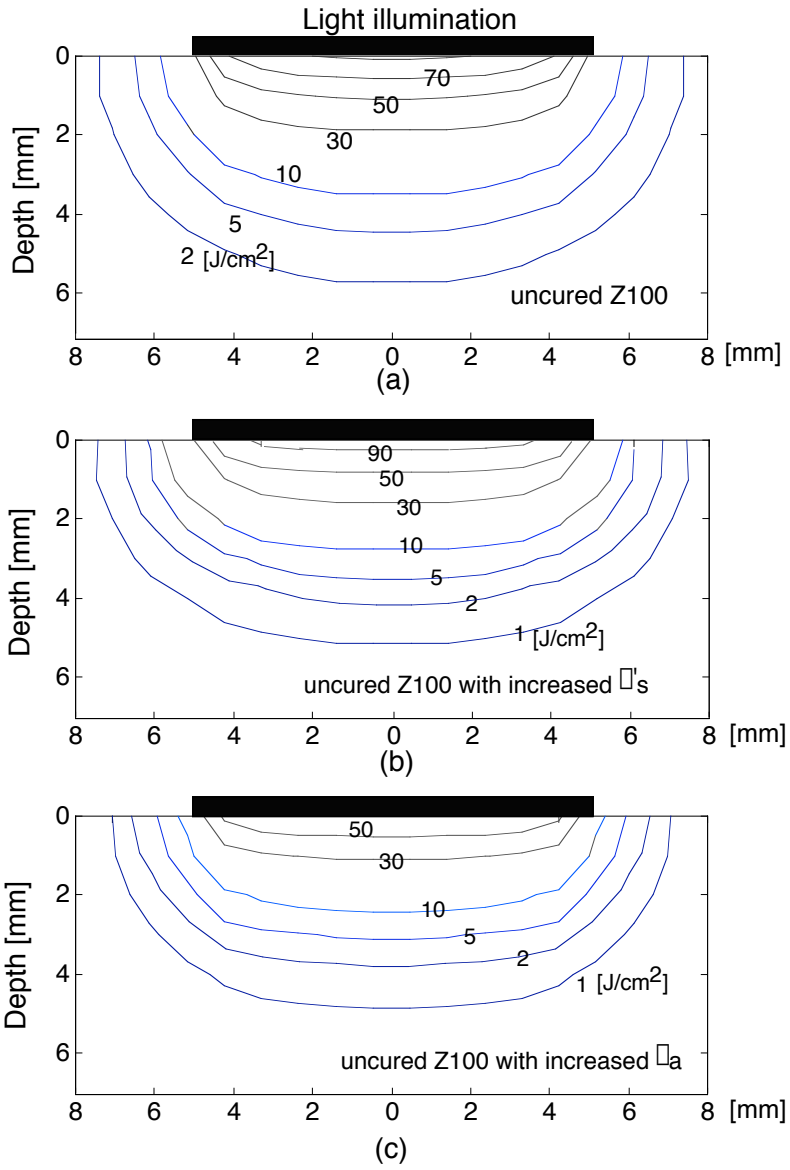

Figure 5.8: Monte Carlo radiant exposure of composites with optical properties of uncured Z100 (a), doubled scattering (b), and doubled absorption (c).

If $H = I_a t$ and we let $H_{dc}^{50\%} = -\alpha^{-2} t^{-1} (\ln 0.5)^2$, then for a constant exposure time t we obtain

$$\frac{DC}{DC_{max}} = 1 - \exp[\ln 0.5 (H/H_{dc}^{50\%})^{0.5}] \quad ,$$

where once again $H_{dc}^{50\%}$ represents the radiant exposure to reach 50% of the maximum cure. The data for the DC versus the radiant exposure distribution of uncured Z100 was fit with the above equation and $H_{dc}^{50\%}$ was shown to be 1.68 with 0.26 standard error (Fig. 5.9). The fit produced about 15% standard error, which was not as good as the other two models (7% standard error). However, it is interesting to note that the 50%-curing thresholds ($H_{dc}^{50\%}$) are equal in the three models based on one-way ANOVA followed by Tukey's post-hoc multiple comparison test at $p < 0.05$. The three fitting curves cross at DC≈28% (Fig. 5.9), but the slopes of the three curves at DC≈28% are Racz > exponential >> Watts. As a result, the estimated radiant exposure threshold for 80%-curing level ($H_{dc}^{80\%}$) in Watts model differs significantly from the $H_{dc}^{80\%}$ in the other two models (t-test: $p < 0.05$).

Including $H^{50\%}$ in the mathematical expressions for the models gives the advantages of unifying all the physical parameters (e.g., two in Racz model, and four in Watts model) into a single fitted parameter with a practical unit (J/cm^2). Moreover, the 80% curing threshold can be obtained by simply multiplying $H^{50\%}$ by 2 in the Racz model, 2.32 in the exponential model, and 5.38 in the Watts model.

We have shown a reciprocal relationship between irradiance and exposure time ($I_a \cdot t =$ constant) for Z100, instead of $I_a^{0.5} \cdot t =$ constant. The reciprocity between I_a and t also was found by other research groups [107, 108, 113, 114]. Halvorson et al. found that an equal radiant exposure ($I_a \cdot t$) gave equivalent degree of conversion for all the four materials they tested [113]. Similar results were found by Emami et al [114] and Miyazaki et al. [108] on different composites. Musanje et al. [107] examined the reciprocal relationship on four different composites based on two mechanical parameters and found that one (Z250, 3M ESPE) followed the reciprocity relationship.

The fitted thresholds differ significantly for cured and uncured optical properties (t-test: $p < 0.05$). Based on the fitting of KHN versus radiant exposure with the Racz model, one gets $H_{KHN}^{80\%} = 3.8\pm$ standard error $0.2\,\mathrm{J/cm^2}$ for uncured Z100, and $H_{KHN}^{80\%} = 8.8\pm$

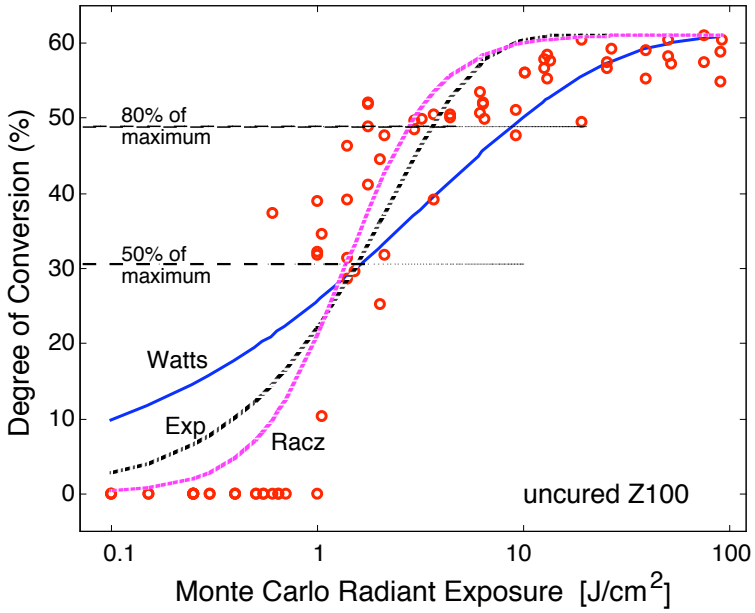

Figure 5.9: Comparison of the three models: Watts model (solid line), Racz model (dash line), and exponential model (dashdot line). The circles are the data of DC versus the Monte Carlo radiant exposure of uncured Z100.

standard error 0.6 J/cm^2 for cured Z100. Since in the actual situation the optical properties change as the composite polymerizes, the radiant exposure threshold required to produce 80% cure should reside between 3.8 and 8.8 J/cm^2. (A dynamic-optical property Monte Carlo model was not used because the relation between the number of absorbed photons and changes in optical properties is unknown.) Observe that in Fig. 5.5 the area directly under the illumination received more than ten times $H_{KHN}^{80\%}$. This implies that the center cured relatively early in the irradiation and consequently would have optical properties similar to those of cured composite. Based on this argument, one can speculate that the true 80% curing threshold will be closer to the value for the cured composite because the light will propagate through the cured material for the majority of the curing process.

In conclusion, we have shown that we can make a reasonable approximation of the radiant exposure in photo-activated dental composite materials. We have presented a simple formula for curing that is based on reciprocity of irradiance and exposure time and the concept of a threshold radiant exposure.

Chapter 6

Quantum Yield of Conversion of The Dental Photoinitiator Camphorquinone

6.1 Introduction

Photo-cured composites have been widely used in dental restorations [39]. Generally, a composite consists of a mixture of resins with photoinitiators and silane-coated, inorganic filler particles. The photoinitiator absorbs light, and is promoted to an excited state that interacts with a photoreducer (a electron or proton donor molecule) to initiate a free radical addition polymerization of the resin monomers. Camphorquinone (CQ), a blue light photoinitiator, is commonly used in dental resin formulations [129]. CQ is di-2,3-diketo-1,7,7-trimethylnorcamphane with molecular weight of 166 and has an absorption peak around 469 nm (Fig. 6.1).

The photo-curing efficiency, defined as extent of cure per delivered photon, has been by evaluated using the extent of cure (curing depth) for different composite formulations [20, 108, 130] or for different light curing units [17, 131, 132]. These studies were specific to a particular combination of curing units and materials and did not report the number of photons absorbed. Some studies [131, 132] suggested a "integrated relative curing potential" ($ICPrel$) parameter defined as

$$\mathrm{ICP_{rel}} = \int_{\lambda_1}^{\lambda_2} E(\lambda)A(\lambda)d\lambda \ , \tag{6.1}$$

where $E(\lambda)$ is the spectral irradiance of the curing unit, $A(\lambda)$ is the relative absorbance of photoinitiator, and λ_1–λ_2 is the wavelength emission range of the curing unit. In fact, if we

replace $A(\lambda)$ with the absorption coefficient $\mu_a(\lambda)$ of the photoinitiator, Eq. 6.1 represents the total absorbed energy per unit volume in the material (according to the CIE/ISO definition [116]). This parameter gives the effective photon absorption in the material. However, not all the light absorbed is equally effective at inducing polymerization. The primary absorption in resins is by the photoinitiator and the absorption drops during the curing process [133], which, in turn, may decrease the polymerization rate.

This research studied the relationship between the changes of photoinitiator absorption and the radiant exposure of the curing light. Combining this relationship with CQ's molar extinction coefficient, we were able to quantify the quantum yield Φ of CQ conversion.

$$\Phi = \frac{\text{Number of converted CQ molecules}}{\text{Number of absorbed photons}} \quad .$$

6.2 Theory

6.2.1 Irradiance of the curing illumination

The spectral power per nanometer of the wavelength λ of the lamp $P(\lambda)$ can be represented as

$$P(\lambda) = P_{\text{total}} f(\lambda) \quad ,$$

where P_{total} is the total power, and $f(\lambda)$ is the spectral probability distribution at wavelength λ, that is

$$P_{total} = \int_0^\infty P(\lambda) d\lambda \qquad \text{and} \qquad \int_0^\infty f(\lambda) d\lambda = 1 \ .$$

Since the spatial irradiance across the illumination spot has a Gaussian distribution, assume that w is the radius of the beam (where the irradiance drops 1/e), and assume $E(\lambda, r)$ is the spectral irradiance at wavelength λ and position r and has a unit of (power)/(area)/(nm), then

$$E(\lambda, r) = \frac{P(\lambda)}{\pi w^2} \exp\left(-(\frac{r^2}{w^2})\right) \quad .$$

Therefore, the average irradiance at wavelength λ over the absorbance detection area (assuming the area has a radius r_0) becomes

$$E(\lambda, r_0) = \frac{1}{\pi r_0^2} \int_0^{r_0} E(\lambda, r) 2\pi r dr = \frac{P(\lambda)}{\pi r_0^2} \left(1 - \exp(-\frac{r_0^2}{w^2})\right) \quad .$$

The total irradiance over the r_0 area is

$$E_{\text{total}}(r_0) = \frac{P_{\text{total}}}{\pi r_0^2}\left(1 - \exp(-\frac{r_0^2}{w^2})\right) \quad . \tag{6.2}$$

6.2.2 Relationship between CQ's absorption and lamp's illumination time

The absorption coefficient as a function of illumination time was assumed to be an exponential function [39, 113],

$$\mu_a(\lambda, t) = \mu_{ao}(\lambda)\exp(-t/\tau) \quad , \tag{6.3}$$

where $\mu_{ao}(\lambda)$ and τ are the fitting parameters. Physically, $\mu_{ao}(\lambda)$ is the initial absorption coefficient at wavelength λ at time 0, and the time constant τ depends on the spectral irradiance of curing lamp and CQ's quantum yield.

6.2.3 Number of photons absorbed by CQ

The number of photons delivered by the lamp per cm^2 per second as a function of wavelength $N_{\text{photon}}(\lambda, t)$ is

$$N_{\text{photon}}(\lambda, t) = \frac{E(\lambda, t)}{h\nu} = \frac{\lambda E(\lambda, t)}{hc} \quad ,$$

where $E(\lambda)$ is the irradiance at wavelength λ, h is Planck's constant, ν is frequency of light, and c is the speed of light.

The number of photons $Q(\lambda, t)$ absorbed by CQ per volume per second is $N_{\text{photon}}(\lambda, t)$ minus transmitted photons divided by the thickness of the sample, k.

$$Q(\lambda, t) = \frac{N_{\text{photon}}(\lambda, t)}{k}(1 - e^{-\mu_a(\lambda,t)k}) \quad . \tag{6.4}$$

The accumulated number of photons, $A_{\text{photon}}(t)$, absorbed by CQ per volume at time t is equal to the integration of $Q(\lambda, t)$ over all wavelengths and through time t:

$$A_{\text{photon}}(t) = \int_0^t \int_\lambda Q(\lambda, t')d\lambda dt' \quad . \tag{6.5}$$

6.2.4 Quantum yield of CQ conversion

As camphorquinone is irradiated, it bleaches and loses its absorption properties. The loss of absorption by CQ corresponds to conversion of CQ and therefore a decrease in the number of CQ molecules available for photopolymerization. The concentration $C(t)$ of CQ (number of CQ molecules/cm^3) as a function of curing time t:

$$C(t) = \left(\frac{\mu_a(\lambda, t)}{\varepsilon_\lambda \ln 10}\right)\left(\frac{N}{\text{liter}}\right)\exp(-t/\tau) \ , \tag{6.6}$$

where N is Avagado's constant. By comparing Eq. 6.5 and Eq. 6.6, the relationship of the concentration of CQ versus the accumulated number of absorbed photon density ($C(t)$ versus $A_{\text{photon}}(t)$) can be obtained. The slope of this relationship is the CQ consumption per absorbed photon, that is the quantum yield of CQ conversion.

6.3 Materials and Methods

6.3.1 Materials

The material formulation used for this study was 50:50 weight ratio of 2,2-bis[4-(2-hydroxy-3-methacryloyloxypropoxy)-phenyl] propane (BIS-GMA) to triethyleneglycol dimethacrylate (TEGDMA) (Esstech, Essington, PA), 0.35 weight% dimethylaminoethyl methacrylate (DMAEMA) (Alfa), and 0.05 weight% butylated hydroxytoluene (BHT) (Alfa) inhibitor for resin without photosensitizer. For resin with photosensitizer, 0.7 weight% of camphorquinone (CQ) (Alfa) was added.

6.3.2 CQ absorption versus CQ concentration

To measure the absorption coefficient as a function of CQ concentration, resin solutions with 5 different CQ concentrations (0, 0.26, 0.35, 0.52, and 0.7 w%) were filled into 4 mm thick cuvettes and covered with aluminum foil to avoid premature photo-activation. The absorbance of the samples was measured with a Cary 100 Bio Spectrophotometer (Varian Scientific Instruments Inc., Walnut Creek, CA) scanning from 550 down to 400 nm. This spectrophotometer is a differential system: differences in absorption of the sample and of

the reference material are measured. A 4 mm cuvette filled with water was used as the reference material for these measurements.

6.3.3 CQ absorption versus radiant exposure

Two different methods were used to measure the absorption changes as a function of radiant exposure and to count the amount of photons absorbed by the CQ molecules. In Method I, CQ's absorption coefficient was measured directly using a Cary Spectrophotometer. From these absorption spectra, the number of absorbed photons was calculated using Eq. 6.4. In Method II, the transmission of light was measured as a function of illumination time using Ocean Optics spectrometer. The lamp served as both the curing unit and as the light source for the transmission measurements.

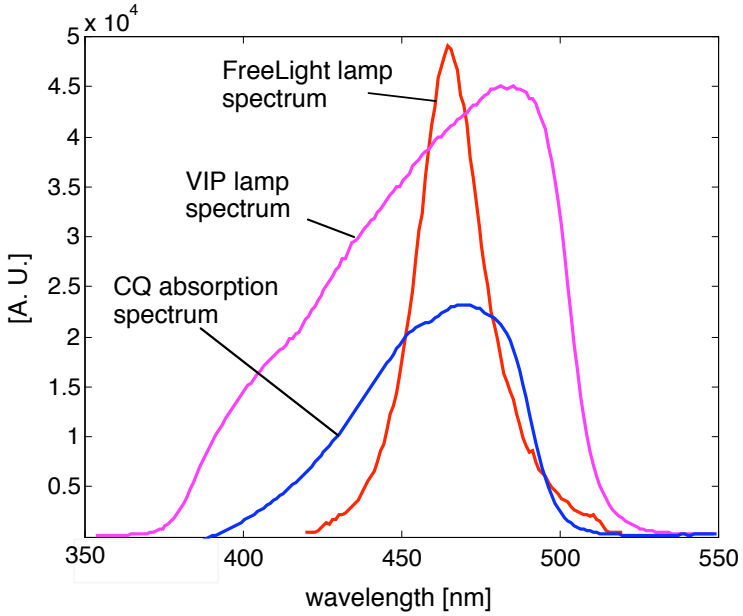

Figure 6.1: Comparison of the spectra of the 3M FreeLight LED light curing unit, VIP lamp, and CQ absorption. The peak of the spectrum is at 465 nm for 3M lamp, 482 nm for VIP lamp, and 469 nm for absorption by CQ.

Method I

We used Cary spectrophotometer to measure the absorption coefficient of resin with 0.7% CQ as a function of illumination time for three irradiances. A 3M FreeLight LED lamp (3M ESPE, Seefeld, Germany) with a 7 mm diameter illumination tip was chosen as the light curing unit. The FreeLight lamp has an illumination peak at 465 nm with narrow bandwidth (FWHM = 24 nm): this emission profile is close to the spectral absorption of CQ (Fig. 6.1). The spectrum of the lamp was measured using a spectrofluorometer (SPEX Fluorolog-3, Jobin Yvon Inc., Edison, NJ, USA). The total power of the lamp was 135±1 mW, measured with a power meter (S210A/M, Thorlabs Inc., Newton, NJ). To vary the curing irradiance, the FreeLight was placed at three different distances, 10, 15, and 27 mm, away from the surface of the sample. The FreeLight was fully charged before each irradiance measurement.

The experimental setup inside the Cary spectrophotometer chamber is shown in Fig. 6.2. To reduce the effects of non-uniform light dose through the sample (the front illumination receives more light than the back), 1 mm thick glass-slide cuvettes (bottom and side sealed with Epoxy glue) were made to contain the resin. When the thickness of the resin (1 mm) is multiplied by the maximum absorption coefficient of 0.7 wt% CQ, the bottom of the resin receives $\exp(-0.1) \approx 64\%$ of the irradiance of the top. The sample arm was resin with 0.7% CQ (called "CQ resin"). The reference arm was resin without CQ.

The power of the spectrophotometer beam was lower than the detection limit, 0.1 μW, of the power meter (LiCONiX 45PM Power Meter, Nolatek, Houma, LA). Therefore the radiant exposure for each scan was $<0.1\,\mu\mathrm{J/cm^2}$. To evaluate the curing effect from the spectrophotometer beam, the scan from 550 to 400 nm was repeated 60 times sequentially (CQ resin at the sample arm and resin without CQ at the reference arm) without any other light source on.

To minimize the effects of non-uniform irradiance (which was Gaussian) across the FreeLight illumination area, we blocked half of the spectrophotometer beams (width by height = 1×10 mm) of both channels so that only a rectangular 1×5 mm of beam reached the samples. According to our irradiance measurement, the FreeLight irradiance deviation

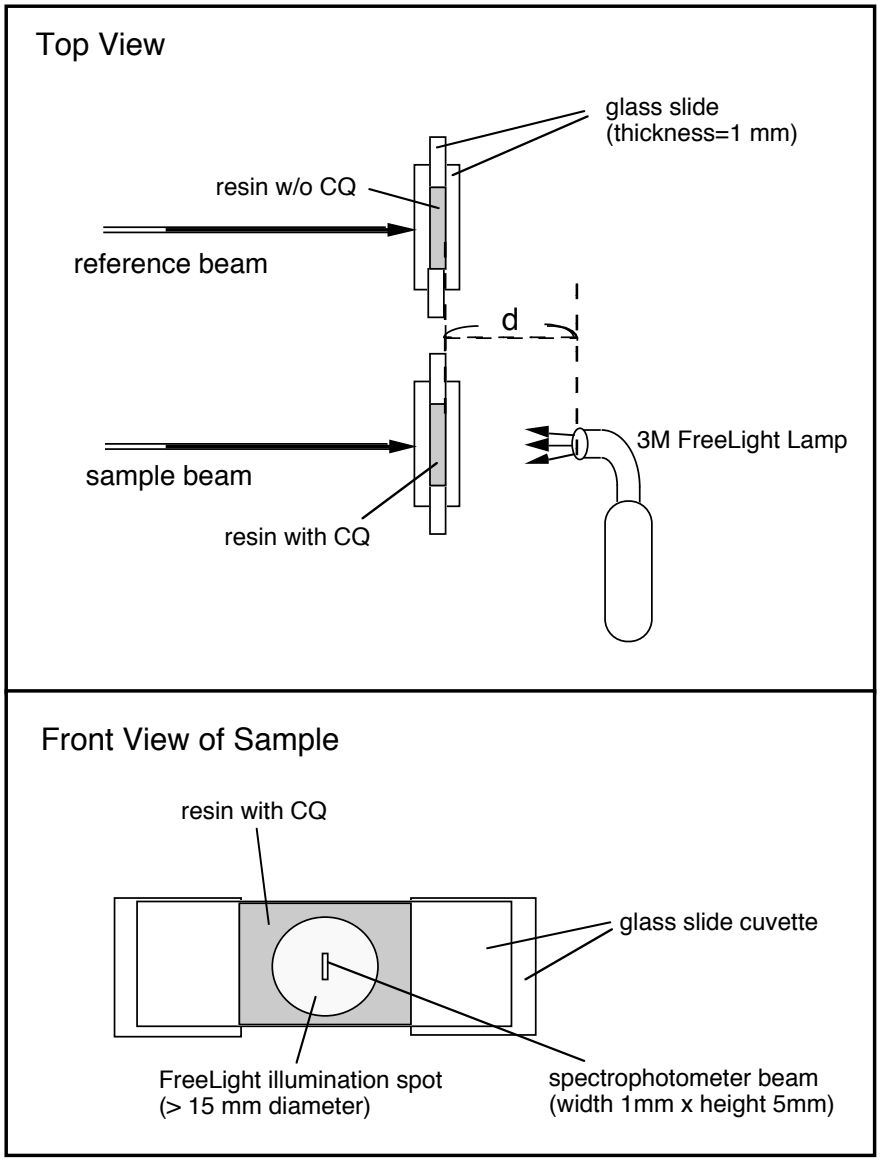

Figure 6.2: Experimental setup for dynamic absorption measurements. Top picture is a top view of the chamber of the spectrophotometer. Resin without CQ was placed at the reference arm and resin with CQ was in the sample arm. The samples were in glass-slide cuvettes with a thickness of 1 mm. The FreeLight lamp was placed in front of the sample arm at distance d=10, 15, or 27 mm to irradiate the CQ resin sample. The bottom picture is a front view of the CQ resin sample. The beam in the spectrophotometer is 1 mm wide and 5 mm high, at the center of the FreeLight illumination spot.

across that 5 mm height was less than 15% (for FreeLight positioned 10 mm away from the sample).

The illumination position of the FreeLight was adjusted such that the spectrophotometer detecting beam was situated in the center of the illumination spot (see Fig. 6.2). During the experiment, the positions of both glass-cuvette samples (the sample arm and reference arm) were fixed, thus the spectrophotometer always detected the same spot of the samples. The FreeLight was moved into a curing position to irradiate the CQ resin sample and then moved away for the subsequent absorption measurement.

The absorbance scan was from 550 to 400 nm at a speed of 0.1 s/nm. The absorbance of the CQ resin was scanned before any curing began. After this, the sample was illuminated with the FreeLight followed by a single absorbance 15 second scan. This was repeated until changes in absorbance were negligible. The FreeLight illumination was 2 seconds followed by an absorbance scan for the first 10 measurements, 5 seconds for the next 24 measurements, 10 seconds for the next ten measurements, 20 seconds for the next eight measurements, 30 seconds for the next eight measurements, and every 40 seconds for the rest of the time.

The measured absorbance $A(\lambda)$ at wavelength λ was calculated by averaging the absorbance from $\lambda - 1$ to $\lambda + 1$ nm. The absorption coefficient at wavelength λ is $\mu_a(\lambda) = A(\lambda)(\ln 10)/d$, where $d = 0.1$ cm is the thickness of the sample.

Method II

In this method, the transmission spectrum was recorded as a function of irradiation time. The experimental setup was shown in Fig. 6.3. We used a VIP lamp (VIP, Bisco Inc., Schaumburg, IL) as the light source and a spectrometer (S2000, Ocean Optics) as the detector. The Thorlabs power meter was used to measure the power for each of the 6 power settings in the VIP. The resin was filled in a glass-slide cuvette with a thickness of 1 mm. The VIP lamp was placed in front of the sample at distance $d \leq 1$ mm to irradiate the CQ resin sample. A 200 μm optical fiber was placed at the center of the VIP illumination spot to collect the transmission light. Note that, in this experiment, a stable, continuous light source is needed such that the transmitted spectrum can be recorded by the spectrometer

in real time. Therefore, the VIP lamp was chosen in this experiment as the operation time of VIP in continuous mode is 250 s (while the FreeLight only continues for 40 s maximum each time it is turned on).

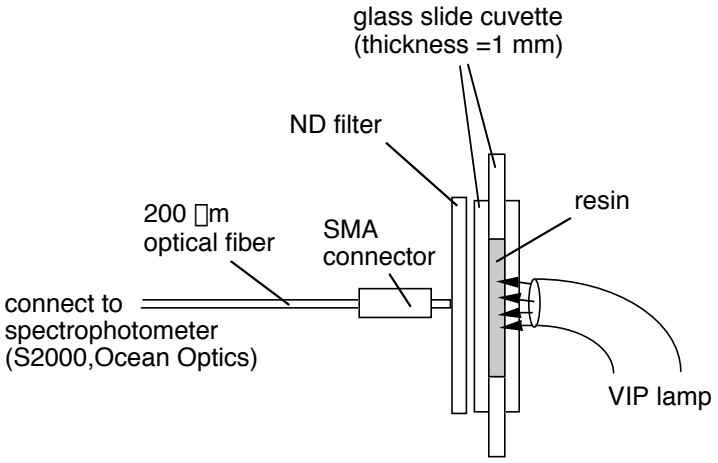

Figure 6.3: Schematic drawing of the Method II experimental setup using VIP as the light source and Ocean Optics as the detector. The resin was in a glass-slide cuvette with a thickness of 1 mm. The VIP lamp was placed in front of the sample at distance $d \leq 1$ mm to irradiate the CQ resin sample. A 200 μm optical fiber was placed at the center of the VIP illumination spot to collect the transmitted light.

Two powers (74 and 270 mW) were used for the measurements. For each power, the original lamp spectrum $E_o(\lambda)$ was measured by filling the glass-slide cuvette with resin without CQ. The spectrum was recorded every 20 seconds for a total of 10 spectra. Then, the cuvette was changed to a cuvette filled with the CQ resin. The transmitted spectrum was then recorded every 20 s for the first 600 s and every 30 s thereafter until the change in transmission was less than 5%.

Therefore, the absorbed photon density, as described in Eq. 6.4, can be calculated directly by subtracting the transmittance spectrum, $T(\lambda, t)$, from the original lamp spectrum, $E_o(\lambda)$, and converting the unit in spectrometer [count] to [number of photons per unit volume]:

$$Q(\lambda, t) = \frac{\rho}{d} \frac{\lambda}{hc} \left(E_o(\lambda) - T(\lambda, t) \right) \quad ,$$

where d is the thickness of the sample, h is Planck's constant, c is the speed of light, and

ρ is a constant to convert the unit of spectrometer [count] to the real lamp power [W].

$$\rho = \frac{\text{power}}{\int_\lambda E_o(\lambda)} \quad .$$

The absorption coefficient was calculated using

$$\mu_a(\lambda, t) = \frac{-1}{d} \ln \frac{T(\lambda, t)}{E_o(\lambda)} \quad .$$

6.3.4 Irradiance distribution over the illumination spot

For the same relative position between the sample and the FreeLight (10, 15, or 27 mm distance for the three irradiances) or the VIP, the spatial distribution of the irradiance of the illumination spot was measured by placing an optical fiber at different positions across the illumination spot (controlled by a micrometer) and detected with the spectrometer. A proper ND filter was used to attenuate the light if the signal saturated.

6.4 Results

6.4.1 Molar extinction coefficient of CQ

The absorption coefficient of unirradiated CQ increases proportionally at 469 nm with concentration (Fig. 6.4). The slope of the regression line is $105 \pm 5\,(\text{mol/L})^{-1}$, and so the molar extinction coefficient ε_{469} at 469 nm of CQ is $46 \pm 2\,\text{cm}^{-1}/(\text{mol/L})$.

6.4.2 CQ absorption versus illumination time

The absorption coefficient at 469 nm for 60 Cary spectrophotometer scans is plotted in Fig. 6.5. Figure 6.6 shows the absorption coefficient μ_a as a function of wavelength of resin with 0.7% CQ for five different illumination times with the FreeLight at irradiance E_{total}=160 mW/cm^2. There is no shift in absorption peak (always at 469$\pm$1 nm) throughout the illumination time (Fig. 6.6). For this irradiance, the absorption coefficient μ_a at five different wavelengths (410, 430, 450, 470, and 490 nm) as a function of curing time was plotted in Fig. 6.7 (dots) and fitted with Eq. 6.3. Overall, the fitting errors are less than 1%. The result fitting parameters for 8 wavelengths are listed in Table 6.1.

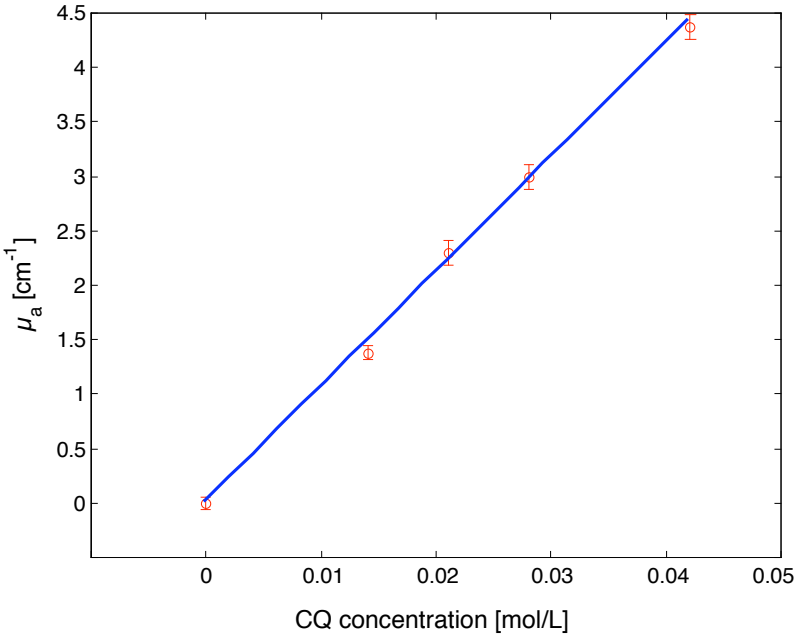

Figure 6.4: The absorption coefficient μ_a at wavelength 469±1 nm as a function of CQ molar concentration, C, (mol/L) in resin. The relationship between μ_a and C is $\mu_a = (\ln 10)\varepsilon_{469}C$, where the molar extinction coefficient ε_{469}= 46±2 cm^{-1}/(mol/L). The error bars are the standard deviations of three sample measurements.

The resin absorption coefficient at 469 nm as a function of illumination time for the FreeLight curing unit and the Cary spectrophotometer absorption detector (Method I) was plotted in Fig. 6.8; while Fig. 6.9 is the result for using VIP as the light source and Ocean Optics spectrometer as the detector (Method II). The fitting parameters in Eq. 6.3 for both figures are listed in Table 6.2. The fitting error for Fig. 6.8 is about 1% and about 5% for Fig. 6.9. Note that the first three data points were not included in the fitting. The irradiance E_{total} was calculated using Eq. 6.2 with r_0 =0.25 cm for the FreeLight lamp and r_0 =0.01 cm for the VIP lamp and P_{total}=135 mW for the FreeLight, 74 mW, and 270 mW for VIP#1 and #2. Table 6.2 shows that the radiant exposure, $H_{\text{total}} = \tau E_{\text{total}}$, (the product of the irradiance and time of illumination [116]) is the same for all the measurements (ANOVA: $p < 0.05$).

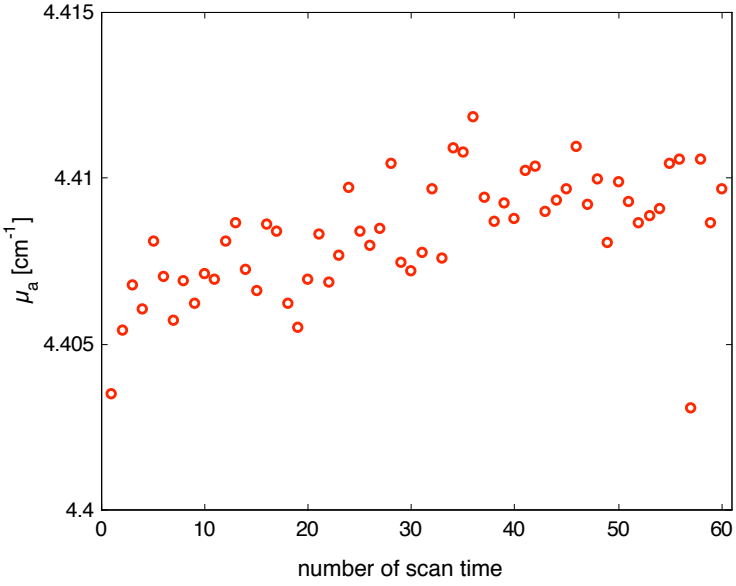

Figure 6.5: The absorption coefficient μ_a at wavelength 469±1 nm over the 60 scans with the Cary spectrophotometer. Note taht the scale in y axis is from 4.400 to 4.415 cm^{-1}.

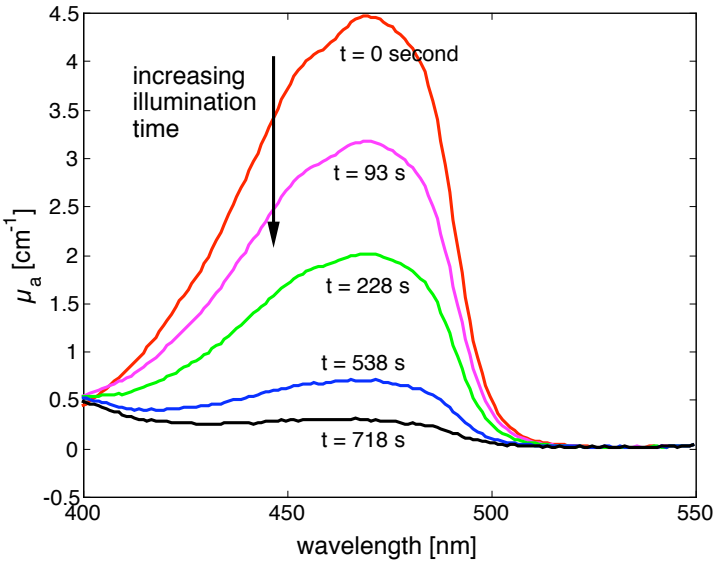

Figure 6.6: The absorption coefficient μ_a as a function of wavelength of resin with 0.7% CQ at five different illumination times for irradiance E_{total}=160 mW/cm^2. As the time of illumination increases, the absorption decreases.

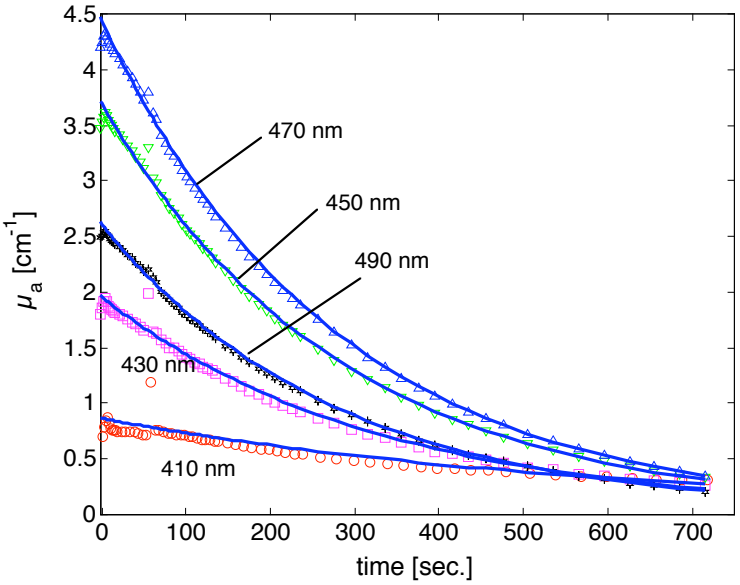

Figure 6.7: The absorption coefficient μ_a at five different wavelengths as a function of curing time for irradiance E_{total}=160 mW/cm^2. The dots are the data and the lines are the fitted exponential function. The fitted parameters are listed in Table 6.1.

	μ_{ao} (cm^{-1}) ± 0.01	τ (sec) $\pm 1\%$
400 nm	0.52	2494
410 nm	0.82	600
430 nm	1.95	326
450 nm	3.70	284
470 nm	4.45	277
490 nm	2.61	276
500 nm	0.55	300
510 nm	0.09	430

Table 6.1: μ_{ao} and τ are the fitting parameters of the exponential model (Eq. 6.3) for 8 different wavelengths.

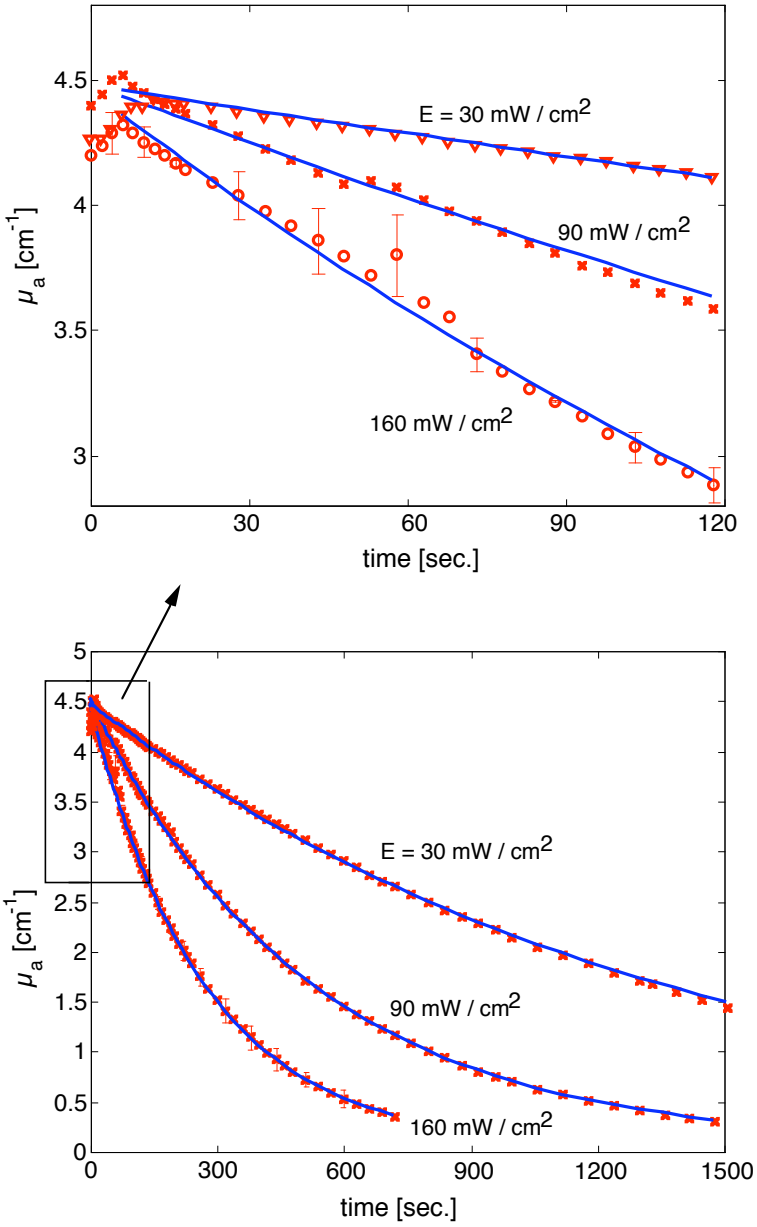

Figure 6.8: (Top) The first 120 second data of the resin absorption coefficient μ_{a469} as a function of illumination time for three different irradiances E_{total}. The error bars for 160 mW/cm^2 irradiance are the standard deviations of three sample measurements. (Bottom) Data from 0 to 1500 seconds for the three different irradiances. The dots are data and the curves are the fitted exponential function. The fitting parameters are listed in Table 6.2.

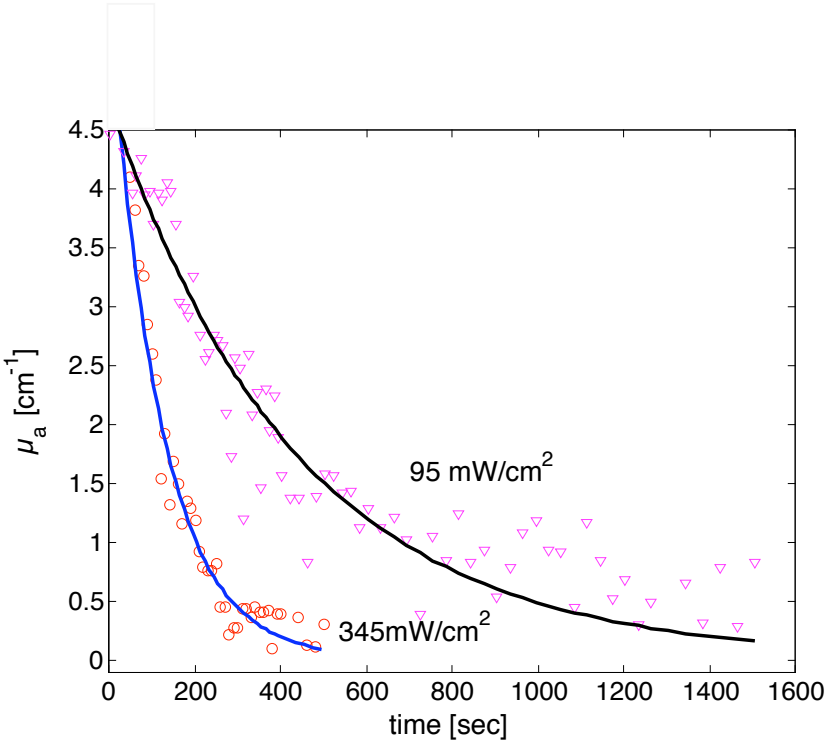

Figure 6.9: The CQ+resin absorption coefficient at 469 nm as a function of illumination time for two different irradiances using VIP as the light source. The dots are data and the curves are the fitted exponential function. The fitting parameters are listed in Table 6.2.

	w (cm)	E_{total} (mW/cm^2)	μ_{ao} (cm^{-1})	τ (sec)	τE_{total} (mJ/cm^2)	$\tau\sqrt{E_{\text{total}}}$ —	Φ —
	±0.05	±10%	±0.01	±1%	±11%		±0.002
FreeLight#1	0.5	160	4.41	280	44800	3540	0.066
FreeLight#2	0.7	90	4.51	525	47250	4980	0.065
FreeLight#3	1.2	30	4.46	1385	41550	7586	0.068
	±0.02	±5%	±0.1	±5%	±11%		±0.015
VIP#1	0.5	345	5.9	120	41400	2230	0.085
VIP#2	0.5	95	4.8	435	41325	4240	0.070

Table 6.2: List of values and their standard deviations. w is the radius of the lamp illumination spot in Eq. 6.2. The corresponding irradiance E_{total} is calculated from Eq. 6.2 for r_0 =0.25 cm for FreeLight lamp and r_0 =0.01 cm for VIP lamp. The P_{total} for FreeLight is 135 mW, 74 mW, and 270 mW for VIP#1 and #2. μ_{ao} and τ are the fitting parameters of the exponential model (Eq. 6.3). Φ is the calculated quantum yield from each experiment.

6.4.3 Photon absorption versus illumination time

Figure 6.10 depicts the number of absorbed photons per volume per second as a function of wavelength (Eq. 6.4) at five different illumination times for an irradiance E_{total}=160 mW/cm^2. As the time of illumination increases, the unit time of photon absorption decreases. The accumulated absorbed photons per volume as a function of illumination time (Eq. 6.5) is shown in Fig. 6.11.

The absorption coefficient in Fig. 6.8 (curve E=160 mW/cm^2) can be converted to a corresponding CQ concentration [number of molecules per cm^3] using Eq. 6.6. Then, the CQ concentration was plotted against the accumulated absorbed photon density in Fig. 6.12 (dots). The regression line of the dots, the quantum yield of CQ conversion, is 0.0661±0.0002. All other quantum yields for different irradiances are listed in Table 6.2.

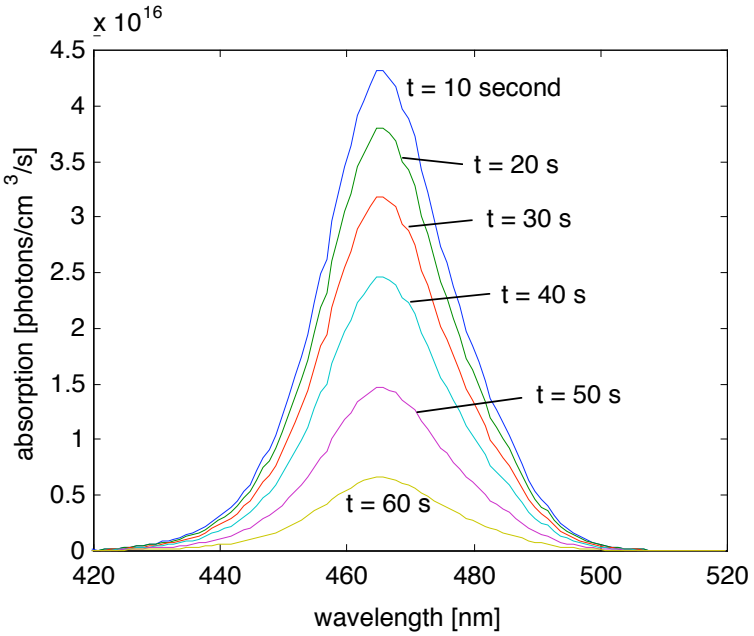

Figure 6.10: The number of photons absorbed by CQ per volume per second as a function of wavelength at five different illumination times for irradiance E_{total}=160 mW/cm^2.

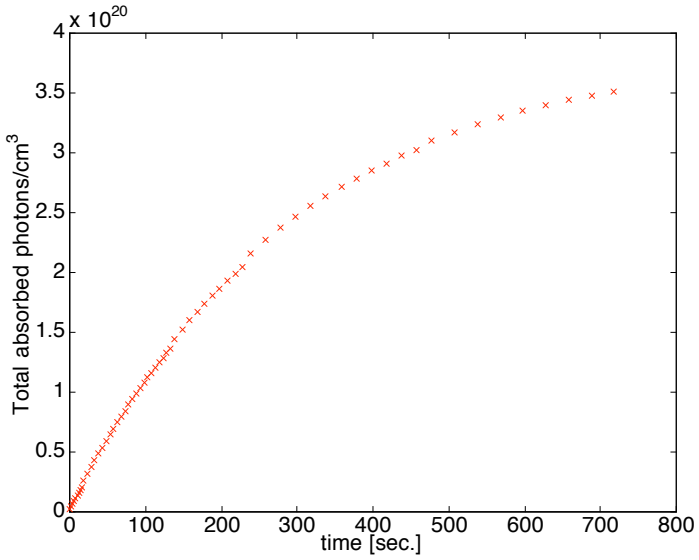

Figure 6.11: The accumulated absorbed photons, $A_{\text{photon}}(t)$, per volume as a function of illumination time.

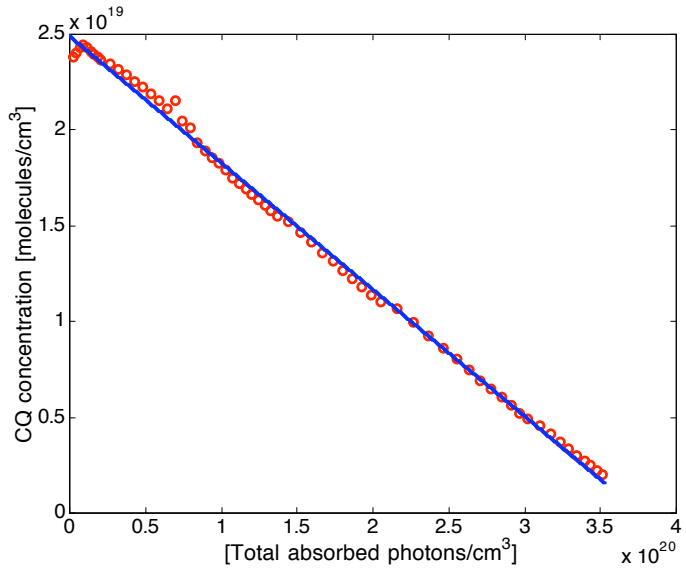

Figure 6.12: CQ concentration as a function of accumulated absorbed photons. The slope of the regression line, the quantum yield of CQ conversion, is equal to 0.0661±0.0002.

6.5 Discussion

The CQ absorption coefficient increased from 4.405 to 4.410 cm^{-1} over the 60 time sequential scans by the Cary spectrophotometer (Fig. 6.5). This increase is significant (ANOVA: $p < 0.01$) (comparison was made between the 5th scan and the 55th scan) as the standard deviation of the spectrophotometer absorbance measurements is about 0.002 cm^{-1} , but is negligible comparing to the absorption changes caused by the FreeLight illumination (Fig. 6.8).

The fact that the absorption of CQ increased during the first 8 seconds is surprising. In the Method I experiment, the absorption increased by about 0.13 cm^{-1} during the first 8 seconds for all the irradiances (Fig. 6.8). Since the absorption at 469 nm of resin without CQ is 0±0.002 (Fig. 6.4), the only component that can change the absorption at 469 nm must be related to CQ.

One possible reason is the combination of photosensitizer/reducing agent complex may have increased the absorption, but a further investigation is needed. The increase in absorption can not be attributed to specular reflectance changes at the interface between the glass slide and the resin. The index of refraction of the resin changed from 1.50 to 1.53 during curing. If the refractive index of a glass slide is 1.49, then the Fresnel reflectance at the interface will increase from 10^{-5} to 3×10^{-4}. For light going through air–glass–resin–glass–air interfaces, the transmission of the light is 92.14% before curing and 92.11% after curing. For this decrease in transmission, the expected absorption coefficient increase would be less than 0.01 cm^{-1}.

Beyond the first 8 seconds, the absorption of CQ resin decreases exponentially with curing time (Fig. 6.7, 6.6, and 6.9). The decay time constant τ in Eq. 6.3 is the same for μ_a at 450–490 nm (ANOVA: $p = 0.05$). The time constant increases as the wavelength moves further away from CQ's absorption peak (469±1 nm).

The reciprocity rule between the irradiance, E_{total}, and illumination time, t, holds for all the irradiances using two different curing units and measurements (ANOVA: $p = 0.05$) (Table 6.2). That is the radiant exposure ($H = E_{\mathrm{total}} \times t$) is a constant for all the measurements. This is consistent with some previous findings [107, 108, 113, 114, 133].

Therefore, the result gives

$$\mu_a(H) = \mu_{ao} \exp(-\frac{H}{H_{\text{total}}}) \ , \tag{6.7}$$

where μ_{ao} is $4.8\pm0.5\,\text{cm}^{-1}$ at 469 nm, and H_{total}=$43\pm4\,\text{J/cm}^2$ is the curing threshold (where CQ's concentration drops to 1/e). The curing threshold is the same for both FreeLight and VIP lamps for μ_a at 450–490 nm (ANOVA: $p = 0.05$). This means FreeLight and VIP have similar curing efficiency. Note that both μ_a and H are wavelength dependent. Lamps that have power concentrating at 450–490 nm will have lower curing threshold compared to those that have power concentrating outside the 450–490 nm region. FreeLight has ∼85% of total power at 450–490 nm region and VIP has ∼50% at 450–490 nm and 90% at 400–500 nm. Therefore, despite the fact that the FreeLight emission spectrum is narrower than CQ's absorption spectrum, it produces equal curing efficiency as the VIP whose emission spectrum covers CQ's whole absorption wavelength range.

Two different experimental methods give the same quantum yield (ANOVA at $p = 0.05$). The average quantum yield is 0.07 ± 0.01 for all the measurements. This result is the same as Nie *et al.*'s result [134]. The fact that every 14 photons absorbed convert 1 CQ may be due to reabsorption of CQs when an excited CQ returns to its ground state. Note that a different ratio of reducing agents may have a different quantum yield.

6.6 Conclusions

We have shown that CQ absorption coefficient decreases exponentially as a function of illumination time. The reciprocity relationship between the irradiance and exposure time holds for changes of CQ absorption coefficient. The FreeLight and VIP lamp yield the same curing threshold (the radiant exposure when CQ absorption drops to 1/e). The quantum yield was measured to be 0.07.

Chapter 7

Dynamic Optical Properties of Dental Composites

7.1 Introduction

While photo-cured dental composites have been widely used as direct filling restoratives due to their ease of handling and esthetic results, the optical properties of restorative composites have received little attention. Lee *et al.* measured the composite photometric properties (i.e., relating to the response of the human eye) [124, 135], which are useful for assessing the esthetic appearance but have limited utility for understanding light propagation because photometric quantities are a weighted and integrated response. Taira *et al.* measured the optical properties of two composites using the Kubelka-Munk method [125]. The Kubelka-Munk theory can predict reflectance of translucent light-scattering materials of different thicknesses on various backgrounds and has been used in dental clinics for evaluating esthetic quality [136, 137]. Unfortunately, it is difficult to relate these parameters to the standard optical properties [126, 127], that can be used in a multiple light scattering model [128]. Other groups have measured the transmission of light through composite samples [138,139]. Nonetheless, for all these measurements, the intrinsic optical properties of the materials have not been determined.

In Chapter 5, I have shown that both the absorption and scattering coefficients of the commercial composite Z100 decrease during the curing process. The decrease of Z100 absorption peak matches the photoinitiator's (camphorquinone, CQ) absorption peak.

However, the concentration of photoinitiators in this material was unknown, and therefore it was difficult to relate the changes of optical properties to the amount of light absorbed. In Chapter 6, I related the photoinitiator's absorption to the absorbed light radiant exposures for resins with known compositions. The aim of this work was to further characterize the intrinsic optical properties of dental composites and to relate the changes in the optical properties to the radiant exposure during light curing.

The changes in refractive index was considered to be the major cause for the changes in the scattering coefficient of the composite. Dudi *et al.* have used a Michelson interferometer to characterize the changes of the refractive index of a photo-cured resin [140] with half-second time resolution. In their results, the product of the light irradiance and the resin gelation time was found to be constant for different irradiances. This implies that changes in the scattering coefficient might obey a similar reciprocity for irradiance and illumination time. This reciprocity relationship has been observed in my previous studies on the degree of conversion as a function of radiant exposure (Chapter 5).

In the present study, filled composites with different concentrations of photoinitiator, CQ, were made for optical property measurements. Two integrating spheres were used to simultaneously measure the total reflection and total transmission of composites during curing. Inverse Adding-Doubling (IAD) was used to find the scattering and absorption of the composite slab samples using the measured total reflection and transmittance. The refractive indices of unfilled resins with different concentrations of CQ were also measured using an Abbé refractometer to provide background information for the scattering characteristics of the composites.

7.2 Materials and Methods

7.2.1 Materials

The resin formulation used for this study contained a 50:50 weight ratio of 2,2-bis[4-(2-hydroxy-3-methacryloyloxypropoxy)-phenyl] propane (BIS-GMA) and triethyleneglycol dimethacrylate (TEGDMA) (Esstech, Essington, PA), 0.35 weight% dimethylaminoethyl methacrylate (DMAEMA) (Alfa), and 0.05 weight% butylated hydroxytoluene (BHT)

(Alfa). For resin with photosensitizer, 0.7 weight% of camphorquinone (CQ) (Alfa) also was added. The filler material was a silane treated strontium glass obtained from a dental manufacturer (Bisco Inc., Schaumburg, IL). The composite was made by mixing 25 wt% of resin with 75 wt% of fillers in a DAC 150 speed mixer (FlackTek, Landrum, SC).

To obtain a composite slab 1 mm thick and 25 mm in diameter for the total reflectance and transmission measurement, the composite was placed on a microscope slide and pressed with another microscope slide with 1 mm spacers in between. Composite slabs with six different concentrations (0, 0.044, 0.058, 0.088, 0.116, and 0.175 wt%) of CQ were prepared. Three samples of each concentration were made.

Unfilled resins with four different concentrations (0.23, 0.35, 0.46, and 0.70 wt%) of CQ were made for refractive index measurements, as described in Chapter 5.

7.2.2 Experiments

Reflectance and Transmission Experiments

Inverse Adding-Doubling (IAD) was used to find the scattering and absorption of the composite slab samples based on total reflection and total transmission of the sample. The total reflection and total transmission (R&T) of the composite were measured with two 8-inch integrating spheres (Fig. 7.1). Total reflectance was measured in the top sphere and total transmission was measured in the bottom sphere. A 1 mm optical fiber was used to conduct the illumination light to the sample, and two 600 μm optical fibers were used to conduct the reflectance or transmission light into a dual-channel spectrometer (SD2000, Ocean Optics), which measured the light spectrum of each sphere simultaneously. The space between the ports of the two integrating spheres was slightly greater than 3 mm, which was just enough for the composite slab samples to be put in and taken out. This kept light leakage outside of the integrating sphere as small as possible.

Since the IAD method assumes homogeneous optical properties, the irradiance of the curing light over the composite needs to be as uniform as possible; thus, the point light source (from the optical fiber) used to measure the R&T is not suitable for curing the sample. Therefore, we irradiated the composite under a FreeLight LED lamp (3M ESPE, Seefeld, Germany) at about 20 mm away, then replaced the composite slab between the

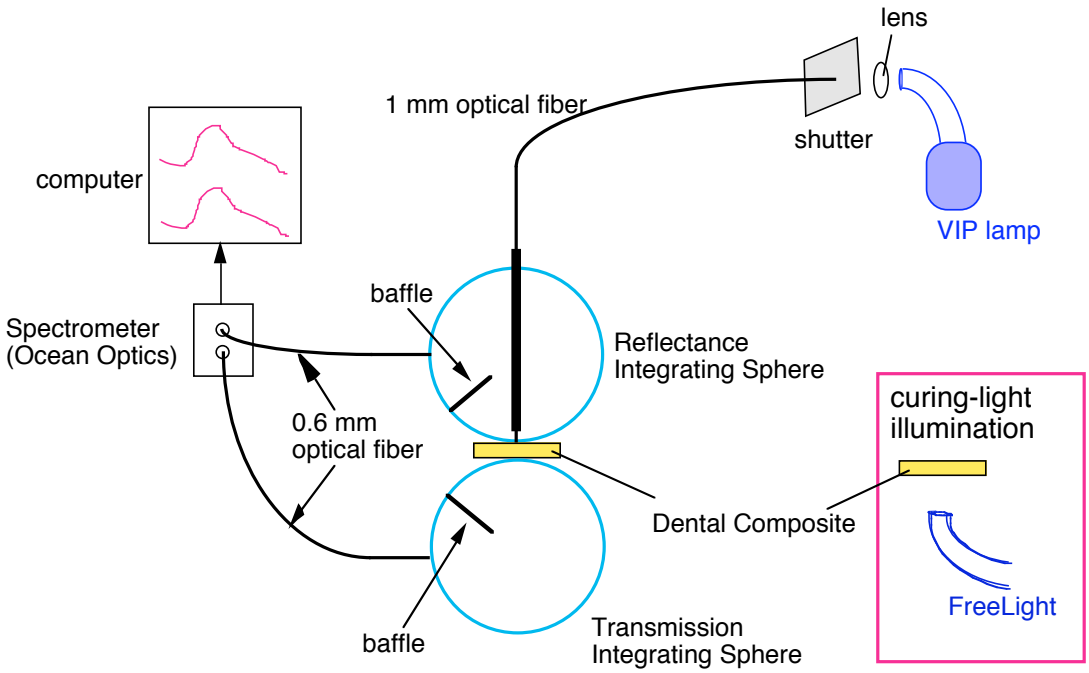

Figure 7.1: Dual 8-inch integrating spheres for total reflectance and transmission measurements. The top sphere measured the total reflectance and the bottom sphere measured the transmission. A 1 mm optical fiber conducted the illumination light from the VIP lamp to the sample, and two 600 μm optical fibers conducted the reflectance and transmission light into the spectrometers for data acquisition. The composite was cured externally with the FreeLight lamp at $\sim$20 mm away.

integrating spheres for the R&T measurement. Note that a 20 mm distance between the composite and the FreeLight was chosen such that the FWHM of the FreeLight beam was about 20 mm. The two sides of the composite slab were alternatively oriented toward the curing light to minimize the effect of inhomogeneous light dose between the top and bottom of the sample.

Since the light used to measure the R&T would cure the composite, we wanted to minimize this light exposure; in other words, the (R&T irradiance×scan time) needed to be small. However, low irradiance decreases the signal/noise for spectrometer detection, thereby increasing the integration time. Moreover, a stable, continuous light source is needed such that the spectra in the spectrometer stabilizes quickly to shorten the recording time. The VIP lamp (VIP, Bisco Inc., Schaumburg, IL) was used for the R&T measurement because the FreeLight system illuminates for only a maximum of 40 s, whereas the VIP can be operated for up to 250 s. Another advantage is that the VIP emits a broader range of wavelengths (Fig. 7.2), which allows for obtaining optical properties over a broader range of wavelengths. The VIP was operated at its lowest output power (set at 100 mW/cm^2) and in a continuous mode. At this setting, the irradiance was only about 8 mW/cm^2 at the tip of the optical fiber that was used to guide the VIP light into the integrating spheres for the R&T measurement. Each R&T measurement took about 5 s, which gives a total radiant exposure of 40 mJ/cm^2, which is less than 5% of the radiant exposure of the curing FreeLight lamp.

The R&T of the sample was recorded before any curing. Each FreeLight curing illumination was followed by a R&T measurement until changes in the R&T spectra were negligible or until the FreeLight maximum functioning time was reached (∼30 minutes). FreeLight illumination started with 3 seconds for twenty illuminations, 5 seconds for twelve illuminations, 10 seconds for twelve illuminations, 20 seconds for six illuminations, 30 seconds for ten illuminations, and 40 seconds for the rest of the time. The R&T was measured again 24 hours after curing.

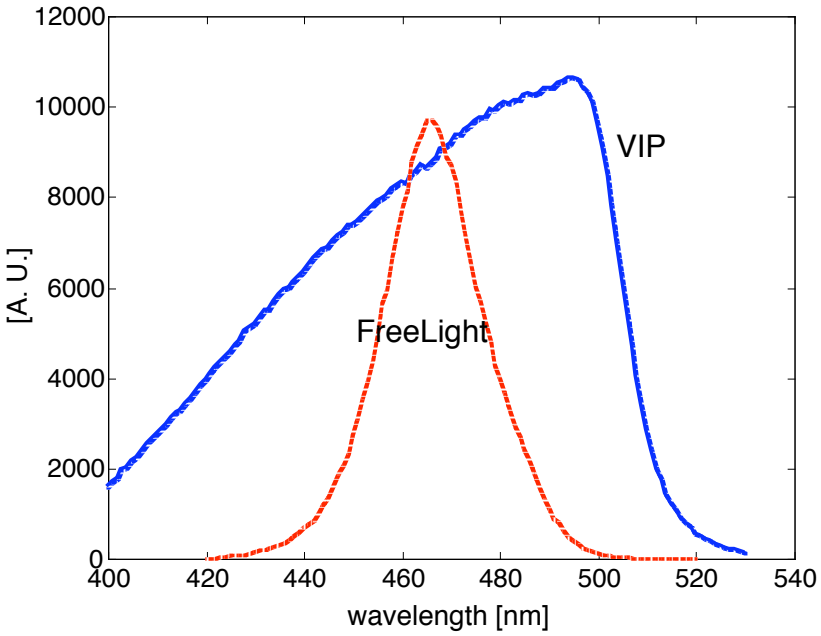

Figure 7.2: Comparison of spectra of the VIP lamp with the 3M FreeLight LED lamp.

Refractive index of unfilled resin with CQ as a function of curing time

The Abbé refractometer (Fisher Scientific, Pittsburgh, PA) was used to measure the refractive index of the resins as a function of curing time. Because the refractive index change was not large enough to be observed for at least 90 seconds when using the light source of the refractometer, the FreeLight lamp was used both to cure and to measure the refractive index change. Therefore the measured refractive indices are for the 465 nm wavelength. The refractometer lamp was kept far away from the prism window so its irradiance could be ignored.

A drop ($\sim$50 μL) of resin was used for each measurement. The FreeLight was placed in a fixed position relative to the refractometer prism (Fig. 7.3) such that the irradiance applied to the resin was kept the same for all the measurements. The total power of the lamp was measrued to be 135$\pm$1 mW (see Chapter 6). The FreeLight was set to illuminate for 10 seconds, and at the same time, the shadow-line observed through the eyepiece of the refractometer system was moved to center in the crosshairs (Fig. 7.3 Top) by turning

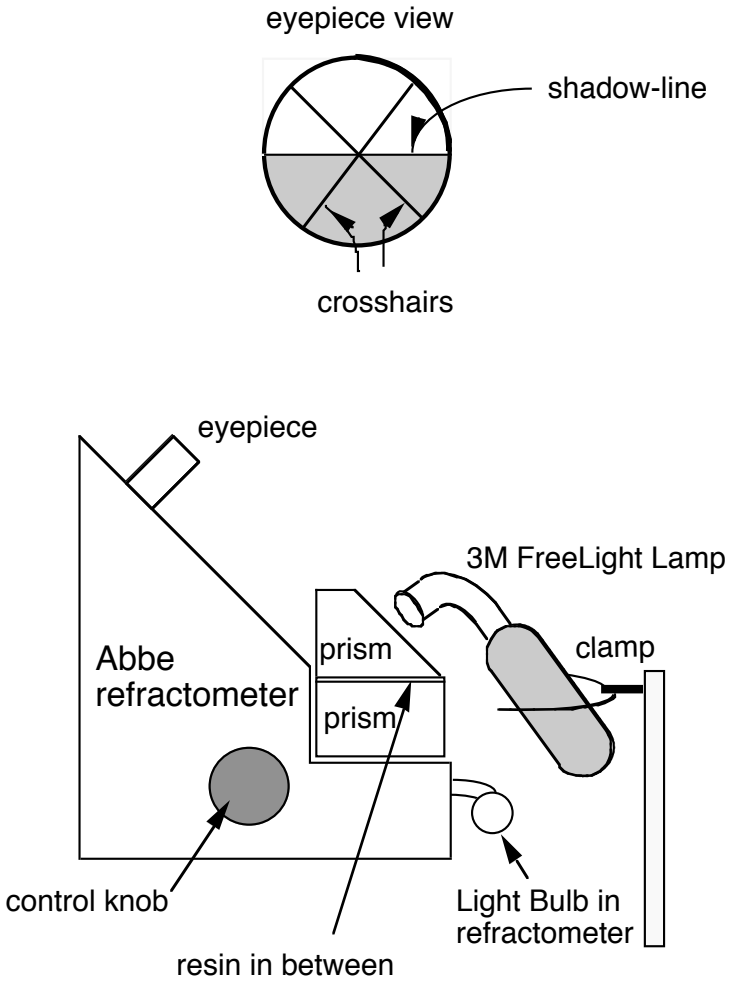

Figure 7.3: Schematic drawing of the experimental setup for the refractive index measurements of the resin. A FreeLight lamp was placed in a fixed position relative to the refractometer prism. The FreeLight served as the light source to cure the resin and to measure the refractive index change. The light source in the refractometer was kept far away from the prism. The shadow-line observed through the eyepiece can be moved to be situated at the center of the crosshairs by turning the control knob.

the control knob. After the FreeLight was turned off, the refractive index was read. This procedure was repeated until the change of refractive index was less than 0.001. The cured resin formed a 100–150 μm thick film on the top of the refractometer prism, which was easily removed with water. Each concentration of CQ resin was measured three times.

7.2.3 Data Analysis

Absorption and scattering coefficient versus radiant exposure

The absorption and scattering coefficients were obtained by iterating an adding-doubling solution of the radiative transport equation until the calculated and measured values of the reflection and transmission matched. In Chapter 6, the relationship between the CQ absorption coefficient and curing lamp radiant exposure was the same for different irradiance and fit an exponential function:

$$\mu_a(H) = \mu_{ao} \exp(-H/H_{\text{total}}) \quad , \tag{7.1}$$

where μ_{ao} is the initial absorption coefficient and $H_{\text{total}} = 43 \pm 4\,\text{J/cm}^2$ is the radiant exposure threshold where the CQ concentration drops to 1/e. Since the composites used here were formulated with the same resin mixed with filler particles, the absorption of the composite is assumed to be close to that of unfilled resin (absorption by filler particles is negligible compared to CQ). This assumption is discussed and validated in section 7.3.1.

The absorption coefficient μ_a was calculated at CQ's 469 nm absorption peak as a function of illumination time t for composites with five different concentrations of CQ and fitted with the exponential function:

$$\mu_a(t) = \mu_{ao} \exp(-t/\tau) \quad , \tag{7.2}$$

where μ_{ao} is a fitting parameter for the initial absorption coefficient at time zero and τ is another fitting parameter for the time constant. Then, the irradiance, E, for each composite measurement can be calculated as

$$E = H_{\text{total}}/\tau \quad .$$

The same irradiance E for each composite sample was also used to calculate the radiant exposure for the scattering coefficient change:

$$\mu_s'(H) = \mu_{so}' \exp(-E \cdot t / H_{s(\text{threshold})}) + \mu_{s(\text{cure})}' \ , \tag{7.3}$$

where μ_{so}' is the total decrease in scattering coefficient during curing, $H_{s(\text{threshold})}$ is the curing radiant exposure threshold, and $\mu_{s(\text{cure})}'$ is the final cured scattering coefficient.

7.3 Results and Discussion

7.3.1 Absorption and scattering coefficient spectra of composites

The absorption coefficient μ_a and scattering coefficient μ_s' spectra of uncured composites with 0.058 wt% CQ, composite without CQ, and completely cured composite are compared in Fig. 7.4. The standard deviation for three sample measurements is about 6% (not shown in the figure). The uncured composite had an absorption spectrum close to the unfilled resin absorption spectrum measured by a Cary spectrophotometer in Chapter 6. The absorption coefficient of the composite without CQ was close to zero, which also matched the absorption spectrum of unfilled resin without CQ measured by the spectrophotometer (the line was directly over the crosses in Fig. 7.4). The absorption coefficient of completely cured composite dropped to $\sim$0.1 cm^{-1}, not zero, which was probably due to residual unconverted CQ.

The scattering coefficient of the uncured composite was within 5% differences of the scattering coefficient of composite without CQ. After the composite was totally cured, the scattering coefficient dropped from approximately 30 cm^{-1} to 10 cm^{-1}. The spectrum for uncured composite appeared noisier than the other two because for the R&T measurements the VIP output power was lower and the integration time was shorter to minimize the curing effect on the sample.

7.3.2 Refractive index of unfilled CQ resin versus light illumination time

The refractive index increased with illumination time (Fig. 7.5 top). The maximum increase of the refractive index per unit time (second) was found to be at around 20 second

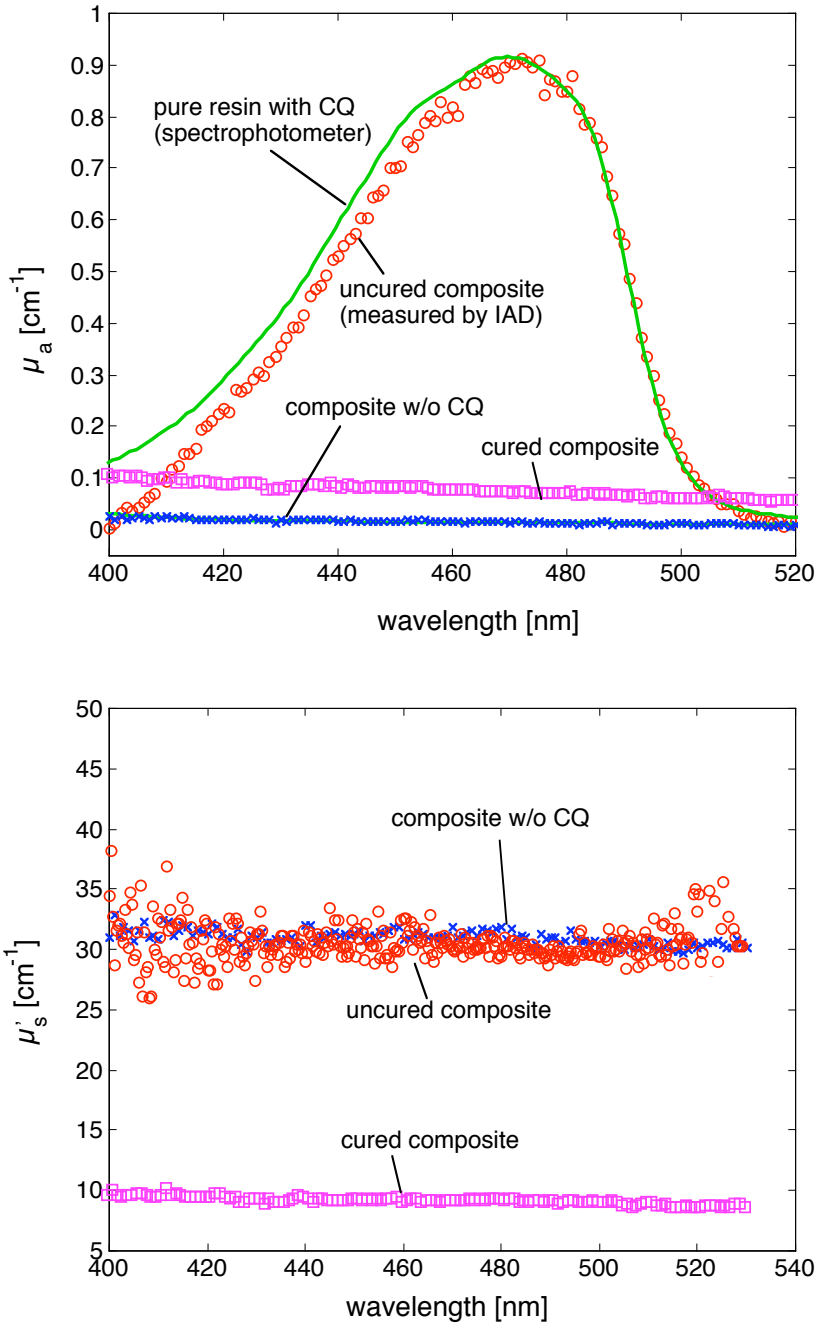

Figure 7.4: The absorption μ_a (top) and scattering μ_s' (bottom) spectra of uncured composites with 0.058 wt% CQ (circle -o-), composite without CQ (cross -x-), and completely cured composite (square). The solid line is the absorption spectrum of unfilled resin with CQ measured by a Cary spectrophotometer in Chapter 6.

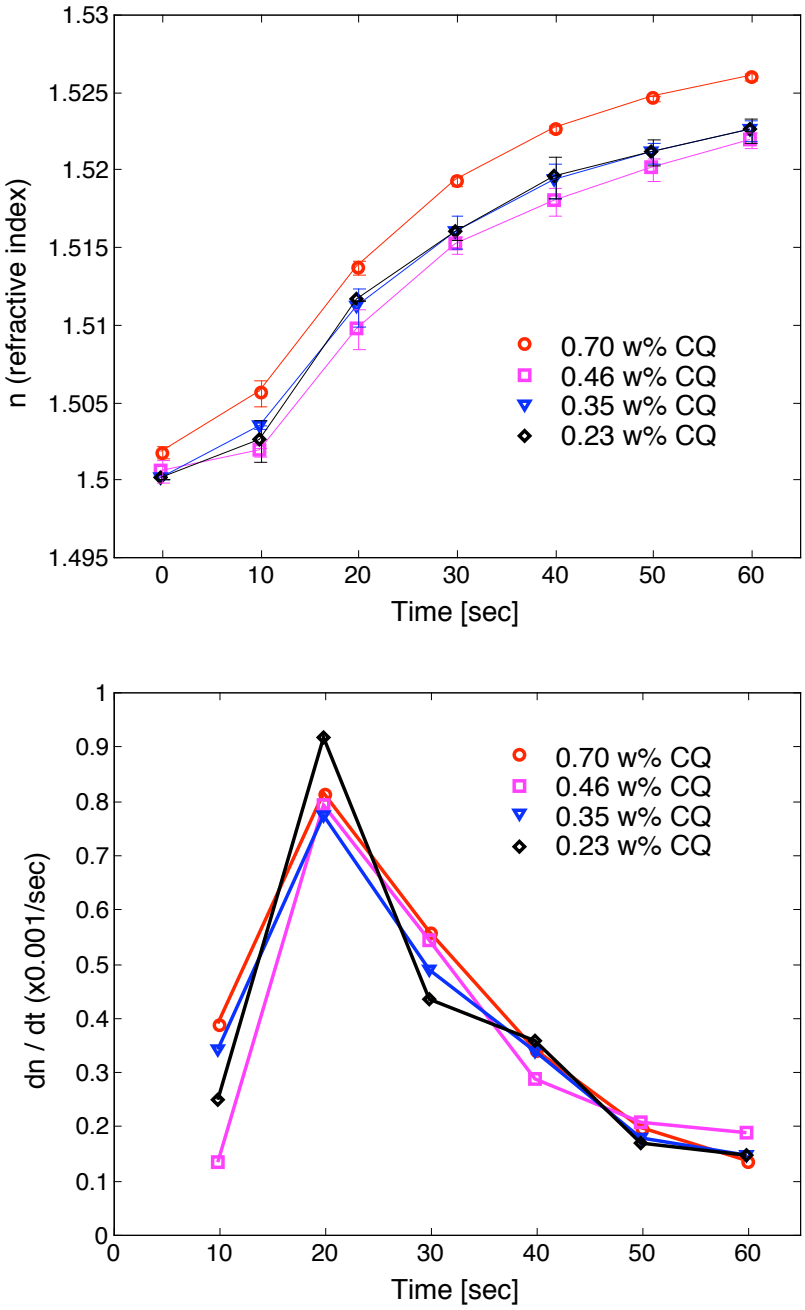

Figure 7.5: (Top) The refractive index as a function of light illumination time of unfilled resin with 4 different CQ concentrations. (Bottom) The refractive index changing rate (dn/dt) as a function of light illumination time.

(Fig. 7.5 bottom) instead of the first 10 second period. This suggests that an exponential function may not fit the first 20 seconds. This finding was consistent with Dudi *et al.*'s results [140]. The possible reason may be due to an increase in the rate of cure that was due to autoaccelaration of the curing reaction with time and a reduced inhibitor concentration with time as it gets used up. However, a further investigation is needed to support this hypothesis.

The refractive index changing rate was independent of the concentrations of the photoinitiator CQ within our observation range (0.23–0.70 wt%). It was also observed that the refractive index changing rate varied with the curing lamp irradiance (although no quantitative explanation is possible due to the unknown irradiance applied to the resin in the refractometer). According to Dudi's study [140], the irradiance and the polymer gel time obeys reciprocity, which means that the same radiant exposure will cause the same changes of the refractive index.

7.3.3 μ_a and μ_s' at 469 nm versus radiant exposure

Figure 7.6 depicts the absorption coefficient at 469 nm as a function of radiant exposure for the composites with five CQ concentrations. The standard deviation for three 0.088 wt% CQ composite measurements was less than 6%. The fit parameter for the absorption coefficient at time zero, μ_{ao}, as a function of the concentration of CQ in composite was plotted in Fig. 7.7 and fit with a regression line:

$$\mu_{ao} = 13.7 C_{\mathrm{CQ}} \quad \mathrm{cm}^{-1} \ ,$$

where C_{CQ} is the CQ weight % in the composite. From the slope and assuming the density of the composite is about $2.2\,\mathrm{g/cm^3}$, the extinction coefficient of CQ in composite was calculated to be $45 \pm 1\,\mathrm{cm}^{-1}/(\mathrm{mol/L})$, which is the same as the extinction coefficient of CQ in unfilled resin observed in Chapter 6.

The reduced scattering coefficient at 469 nm of composites with different concentrations of CQ as a function of radiant exposure was plotted in Fig. 7.8. Generally, as the radiant exposure increases, the scattering coefficient decreases. It was found that the decay of scattering coefficient was independent of the CQ concentration within the measured

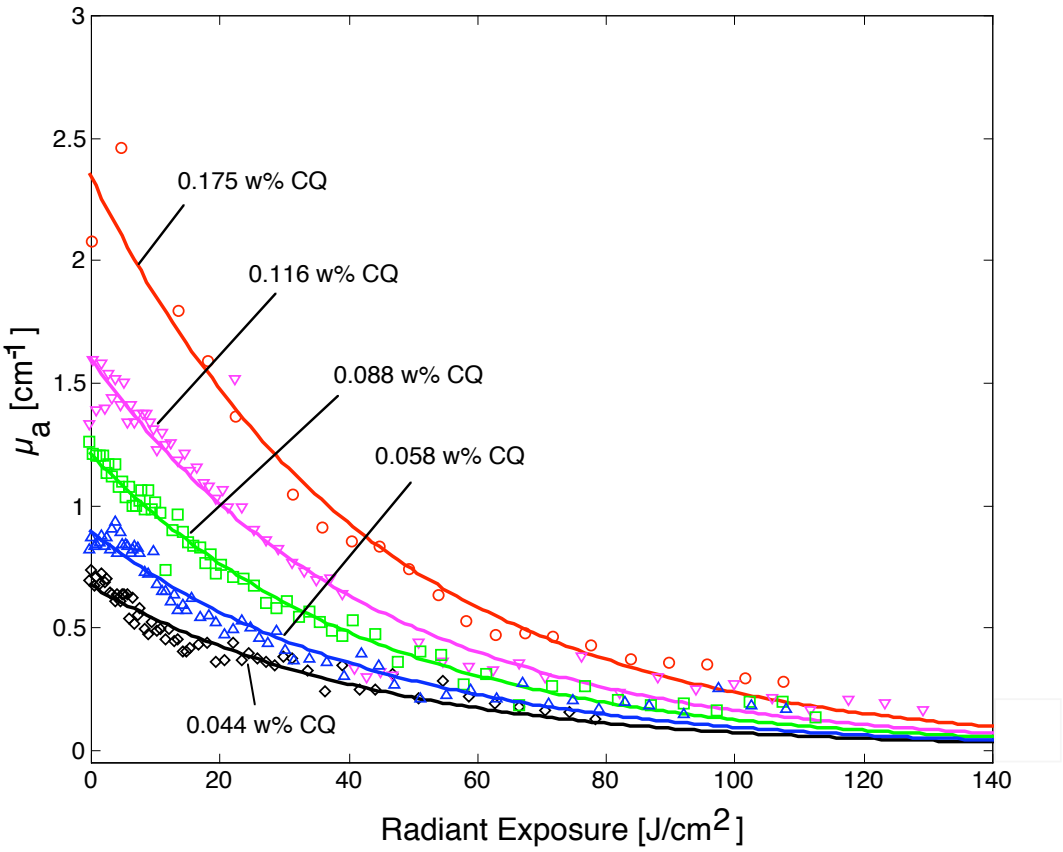

Figure 7.6: The absorption coefficient at 469 nm as a function of radiant exposure of composites with different CQ concentrations. Solid lines are the fitting curves using Eq. 7.1.

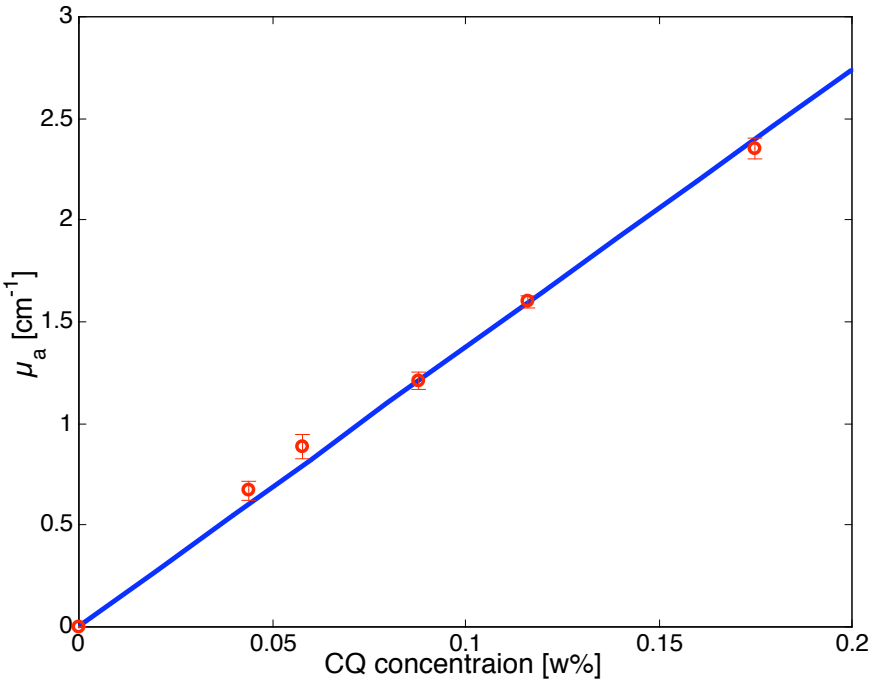

Figure 7.7: The absorption coefficient at 469 nm at time zero, the μ_{ao} in Eq. 7.2, as a function of the concentration (weight %) of CQ in composite. The slope of the regression line is 13.7±0.2 cm^{-1}/CQ wt%=45±1 cm^{-1}/(mol/L), which is CQ's extinction coefficient.

concentration range, 0.044 to 0.175 wt% and the decay rate ($d\mu_s'/dH$) was similar for all the samples with about 10% standard deviation. All the data points fit with Eq. 7.3 within a 10% standard deviation. The fitted cured scattering coefficient $\mu_{s(\text{cure})}$ is 12.5±1.0 cm^{-1}. The initial scattering coefficient of uncured composite is $\mu_{so}' + \mu_{s(\text{cure})} = 30 \pm 2\,\text{cm}^{-1}$. The fitted radiant exposure threshold $H_{s(\text{threshold})}$ is 1.4±0.2 J/cm^2. This threshold is much lower than the absorption coefficient curing threshold 43 J/cm^2. The changes of scattering coefficient may be due to the refractive index changes of the resins in the composite.

7.4 Conclusions

We found that the refractive index changing rate is independent of the CQ concentration within 0.175 wt% concentration range. Based on the quantum yield for the conversion

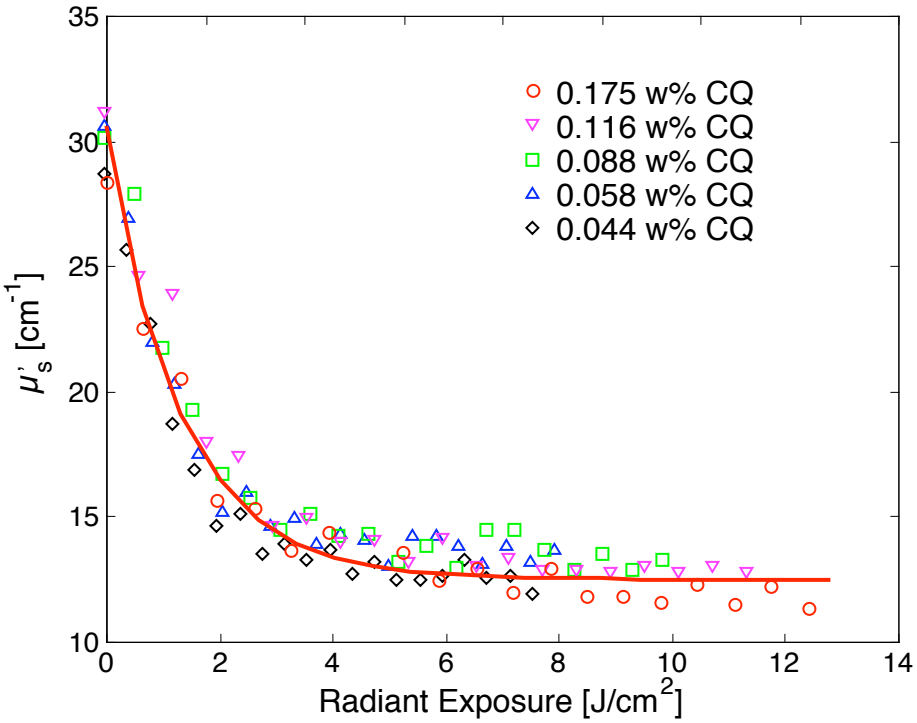

Figure 7.8: The reduced scattering coefficient at 469 nm as a function of radiant exposure for different CQ concentrations. The fitting curve is $\mu_s'(H) = 18\exp(-H/1.4) + 12.5\,[\mathrm{cm}^{-1}]$.

of CQ found in Chapter 6, one can relate the scattering coefficient changes as a function of radiant exposure. Measurement of the changes of composite scattering coefficient versus radiant exposure again confirmed the reciprocity relationship between the irradiance and exposure time.

Chapter 8

A Dynamic Monte Carlo Model for Light Transport in a Photo-cured Dental Composite

8.1 Introduction

*Photo-cured polymers have been used in a wide variety of areas, such as on UV photocurable coatings industry [141], orthopedic biomaterials [14], and dental restorations [15]. The particular advantage of a photo-cured polymer when used as a biomaterial is its potential for *in situ* formation, which allows for the filling of irregular shaped target defects (for example, cavities in the teeth), allows for spatial and temporal control of the polymerization, and allows rapid polymerization under physiological conditions. A critical feature of a photo-cured polymer is the extent of cure, which affects the mechanical or physical properties of the composite restorative, such as the hardness, the fracture toughness, or the shrinkage.

Photoinitiators are designed to absorb light and produce radicals. This absorption causes significant light attenuation (especially when polymerizing thick samples), which decreases the rate of polymerization, and causes insufficient extent of cure at deeper depths. Previous studies (Chapter 6&7) showed that during the curing process, absorption by the photoinitiator declines as the initiator is incorporated into the polymer through an addition process. The refractive index of the resin matrix also changes during the

*Part of this chapter was published in *Proceedings of SPIE, Photonics West 2005: Lasers in Dentistry XI Symposium* paper 5687-14.

polymerization [140], which in turn affects the scattering by the filler particles, thereby changing the overall scattering coefficient of the composite. Thus, the distribution of light within the composite changes as it cures.

The distribution of light in a multiply scattering medium depends on the scattering and absorption coefficients as well as on the index of refraction. In Chapter 5, I have shown that a simple Monte Carlo model can be used to simulate light transport in static optical property media to understand the light distribution in the dental composites. However, in reality, the optical properties of photo-cured dental composites change during the curing process. A more complicated dynamic Monte Carlo model that allows for the changes in optical properties as the photon is absorbed is needed to describe accurately the light distribution in the composite as it cures.

Several attempts have been made to develop Monte Carlo models that account for local changes in absorption and scattering coefficients due to laser irradiation but these models were either two-dimensional [142] or assumed a spherical geometry [143]. A three-dimensional modular adaptive grid numerical model (MAGNUM) by Pfefer *et al.* was developed to simulate the light propagation in geometrically complex biological tissues [144]. Their model allowed the optical properties to be varied within structurally complex biological tissues, but their model was not adapted for dynamic changes of optical properties during the photon deposition.

This study developed a dynamic Monte Carlo (DMC) model for heterogeneous media whose optical properties can vary with positions and can vary dynamically as photons are absorbed. The DMC model was verified with theoretical and experimental results. For absorbing-only media, we compared the model results with the values calculated by the analytical solutions. For multi-layered optical property media, we compared the results with layered Monte Carlo model developed by Prahl (Appendix A). For geometrically complex biological tissues, we compared the results with Pfefer's MAGNUM. The last step was to verify with experimental results. The DMC model results were compared with the changes of absorption coefficients of unfilled resins during curing process (measured in Chapter 6) and the optical property changes of the composites during light irradiation (Chapter 7).

8.2 Dynamic Monte Carlo (DMC) Model Methods

The DMC model is a 3-D dynamic Monte Carlo simulation program for a heterogeneous turbid medium with dynamic optical properties and for any geometry photon beam as the light source. The turbid medium is divided into many small voxels. The dimension of the voxel does not need to be "cubic", that is, the length, width, and height of the voxel *can be* different. Each voxel has its own absorption μ_a, scattering μ_s, and anisotropy g. The optical properties in each voxel can be dynamically changed as the light is absorbed. However, the index of refraction n is the same for all the voxels. The photons are either reflected or transmitted at the top or the bottom boundaries (depending on the Fresnel equation), but are absorbed at the side boundary. Outputs are the diffuse reflectance, the transmittance, the μ_a, μ_s, and the absorbed energy density in each voxel as a function of illumination time. The reflectance and transmission of the light from the medium are recorded as a array (x position versus y position). Appendix B has a detail description of the Dynamic Monte Carlo code. The parameter settings in the program are for the simulation in Section 8.4.2. The program can be easily modified to suit different situations.

8.2.1 Initialization

This Monte Carlo program uses Cartesian coordinates (x, y, z) to represent the location of the photons. The origin (0, 0, 0) is at the corner of the sample (Fig. 8.1 (a)). The dimensions of the medium and the voxel size are specified explicitly. Each voxel is the same size. Each of the Cartesian locations is converted to the voxel index based on the voxel size. Each voxel is assigned an initial set of optical properties. The trajectory of the photon is represented by the directional cosines as (u_x, u_y, u_z),

$$u_x = \cos(\theta)\cos(\varphi) \quad u_y = \cos(\theta)\sin(\varphi) \quad u_z = \sin(\theta)\ , \tag{8.1}$$

where θ is the polar angle from the z-axis and φ is the azimuthal angle in the xy-plane from the x-axis in spherical coordinate (Fig. 8.1 (b)). Each direction cosine is the cosine of the angle between the current photon direction and the respective axis.

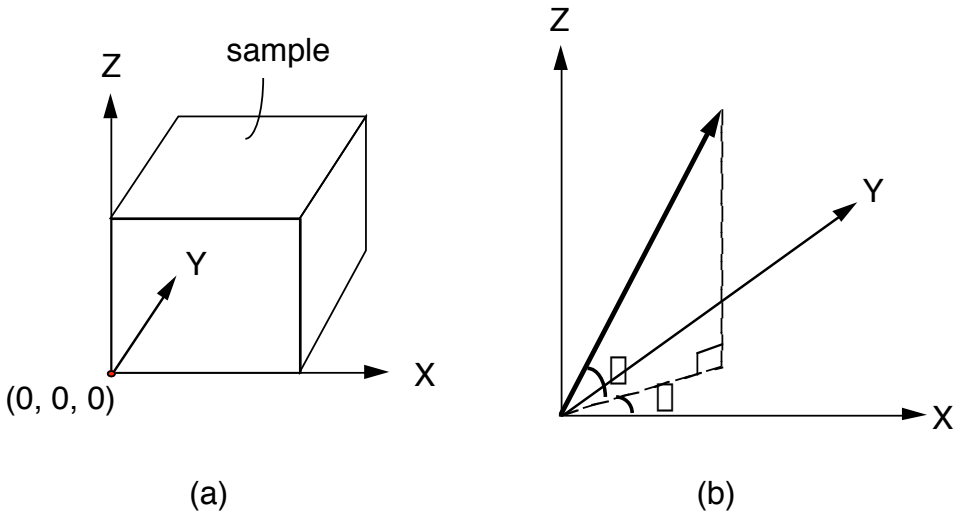

Figure 8.1: The trajectory of the photon in Cartesian coordinates.

8.2.2 Photon movement

Launching the photon: Initialization

To launch the photon, the profiles (e.g., the distribution, the size, the angle, and the center position) of the illumination beam need to be specified. The distribution of the beam can be uniformly flat, a Gaussian, or something else. In my example, a circular flat beam was launched perpendicular to the top surface and at the center of the top surface. However, this part of my code can be easily modified to fit the real characteristics of the beam. Each launched photon begins with a standard weight, one minus the specular reflection, at the surface (see section 8.2.3). As the photon moves, its weight attenuates with its path length based on the Beer's law.

Taking steps

The step size S is chosen as the distance to the next scattering event,

$$S = -\ln(\xi)/\mu_s \ ,$$

where ξ is a non-zero random number between 0 and 1, and μ_s is the scattering coefficient of the voxel which currently contains the photon. However, since the optical properties may

vary from voxel to voxel, instead of moving the photon a distance S to the next scattering event, the photon moves one voxel at a time until the accumulated (step size×scattering coefficient) matches $S \times \mu_s$ (see Fig. 8.2 for a 2-D representation). In other words,

$$-\ln(\xi) = s_1\mu_{s1} + s_2\mu_{s2} + s_3\mu_{s3} + \ldots + s_n\mu_{sn} \ ,$$

where $s_1, s_2, \ldots, s_n$ are the step sizes within each voxel, and $\mu_{s1}, \mu_{s2}, \ldots, \mu_{sn}$ are the scattering coefficients of these voxels. Note that the photon may not be able to take a full step from one voxel to another at the last step s_n. Therefore, s_n is the residual step left after the $n-1$ steps.

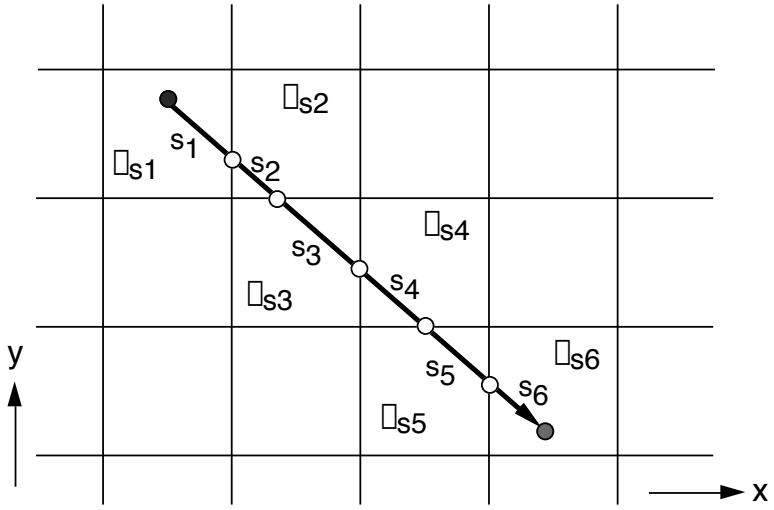

Figure 8.2: A 2-D representation of photon taking steps. The photon takes one step (s_1, s_2, ..., or s_6) at a time to cross one voxel until $-\ln(\xi) = s_1\mu_{s1} + s_2\mu_{s2} + s_3\mu_{s3} + \ldots + s_6\mu_{s6}$, where ξ is a random number between 0 and 1, and $\mu_{s1,2,\ldots,6}$ are the scattering coefficients of the voxels.

To calculate the step size $s_1, ..., s_n$, first we must find the plane (among the six planes defining a voxel) that the photon hits, then we calculate the distance from the photon's current position to the plane.

Based on the direction of the photon, three of the six planes defining a voxel can be eliminated. Like the example of a photon movement presented in Fig. 8.3 (a), the signs of u_x, u_y, and u_z tell us the photon is directed forward ($u_y > 0$) to the right ($u_x > 0$) and upwards ($u_z > 0$). Therefore, plane 1, 2, or 5 are the possible planes the photon will hit.

The distances to each of the remaining planes ($\Delta x_1, \Delta x_2, \Delta y_1, \Delta y_2, \Delta z_1$, and Δz_2) are used to calculate the angles, δ in $\vec{x}$-$\vec{y}$ plane (Fig. 8.3(b)) and α in trajectory $\vec{v}$-$\vec{z}$ plane (Fig. 8.3(c)). As shown in Fig. 8.3(b), δ is the azimuthal angle between x-axis and the segment from the photon's current position to the corner of the voxel. In this example, the photon's trajectory falls in region (I) in Fig. 8.3 (b), therefore,

$$\delta_1 = \tan^{-1}(\Delta y_1/\Delta x_1).$$

Photon's azimuthal angle φ (trajectory in the $\vec{x}$-$\vec{y}$ plane) can be calculated using the following equation:

$$\varphi = \cos^{-1} \frac{u_x}{\sqrt{u_x^2 + u_y^2}} \quad . \tag{8.2}$$

The azimuthal angles, φ and δ_1 (Fig. 8.3(b)), are compared to decide if the movement is to plane 1 or plane 2 and to calculate the moving distance Δv in $\vec{x}$-$\vec{y}$ plane. If $\varphi \leq \delta_1$, move to plane 1 and $\Delta v = \Delta x_1/\cos\varphi$; otherwise, move to plane 2 and and $\Delta v = \Delta y_1/\sin\varphi$, which is the example in Fig. 8.3(b).

Next, the photon's angle, θ, is compared with α_1 in the trajectory $\vec{v}$-$\vec{z}$ plane (Fig. 8.3(c)) to decide the movement to plane 2 or plane 5 and to calculate the step size, s_1. The angle θ can be calculated as:

$$\theta = \sin^{-1} u_z \tag{8.3}$$

In the example of Fig. 8.3(c), the angle α_1 is

$$\alpha_1 = \tan^{-1}(\Delta z_1/\Delta v).$$

If $\theta \leq \alpha_1$, move to plane 2 and $s_1 = \Delta v/\cos\theta$; otherwise, move to plane 5 and $s_1 = \Delta z_1/\sin\theta$, which is the example shown in Fig. 8.3(c).

Similarly, if the photon's trajectory in $x - y$ plane falls in region (II) like shown in Fig. 8.4, that is $u_x < 0$ and $u_y > 0$, then $\delta_2 = \tan^{-1}(\Delta y_1/\Delta x_2)$ is compared with $\pi - \varphi$. If $\pi - \varphi \leq \delta_2$, move to plane 3 and $\Delta v = \Delta x_2/\cos(\pi - \varphi)$; otherwise, move to plane 2, as shown in the figure, and $\Delta v = \Delta y_1/\sin\varphi$.

For other regions (III) and (IV), similar comparisons can be made. Please see Appendix B for the details.

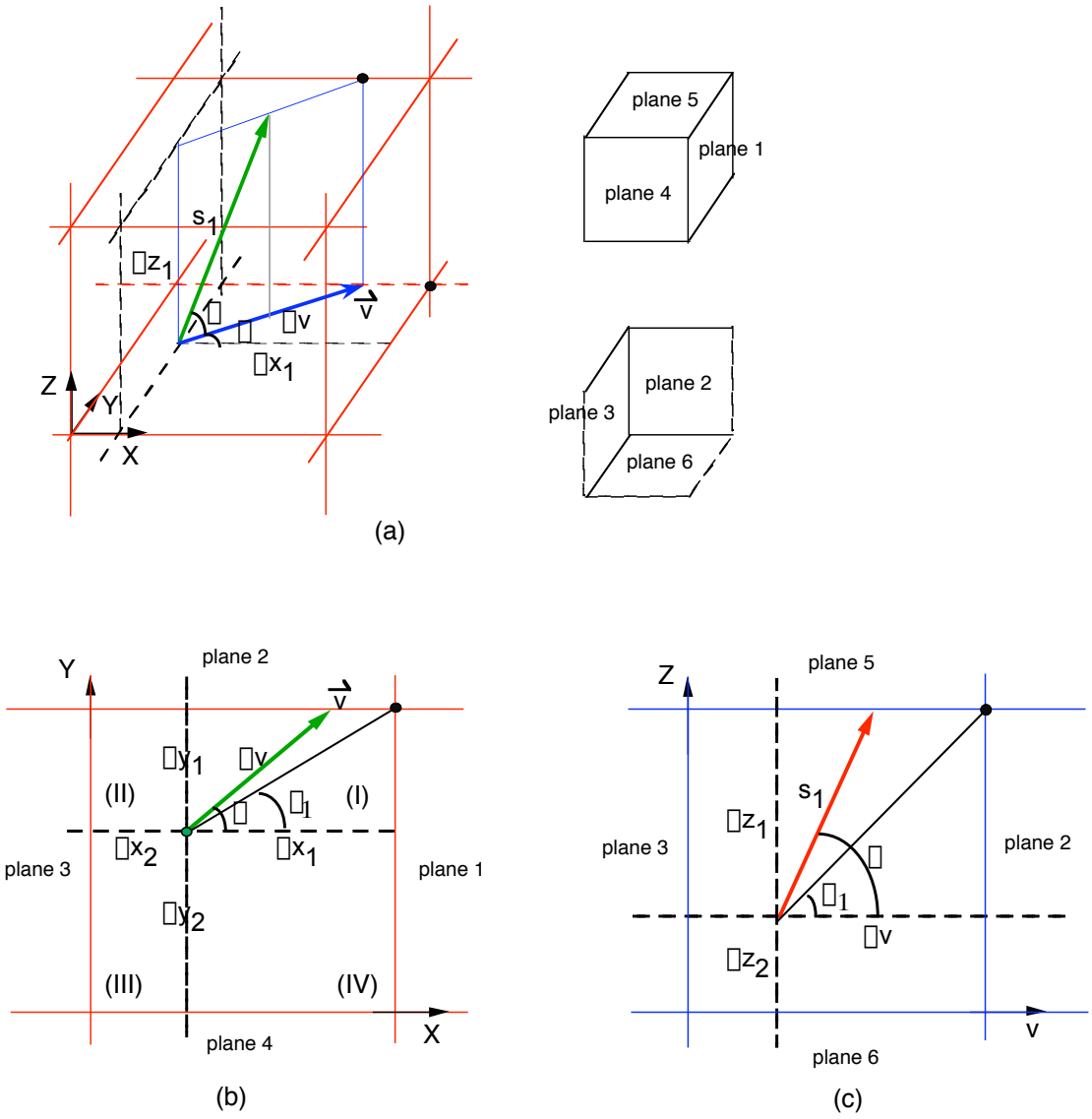

Figure 8.3: A schematic drawing of photon movement to the boundary plane of a voxel. The azimuthal angle of the trajectory is φ, and the polar angle is θ. The distances are Δx_1 to plane 1, Δx_2 to plane 3, Δy_1 to plane 2, Δy_2 to plane 4, Δz_1 to plane 5, and Δz_2 to plane 6. Figure (a) is a 3-D representation of photon movement. The projector of the trajectory in the $\vec{x}$-$\vec{y}$ plane is $\vec{v}$, and the distance to the edge of the voxel is Δv. Figure (b) is a 2-D representation of the trajectory projected in the $\vec{x}$-$\vec{y}$ plane. $\delta_1 = \tan^{-1}(\Delta y_1/\Delta x_1)$. $\Delta v = \Delta y_1/\sin\varphi$. Figure (c) is a 2-D representation of the trajectory in the trajectory $\vec{v}$-$\vec{z}$ plane. $\alpha_1 = \tan^{-1}(\Delta z_1/\Delta v)$. $s_1 = \Delta z_1/\sin\theta$.

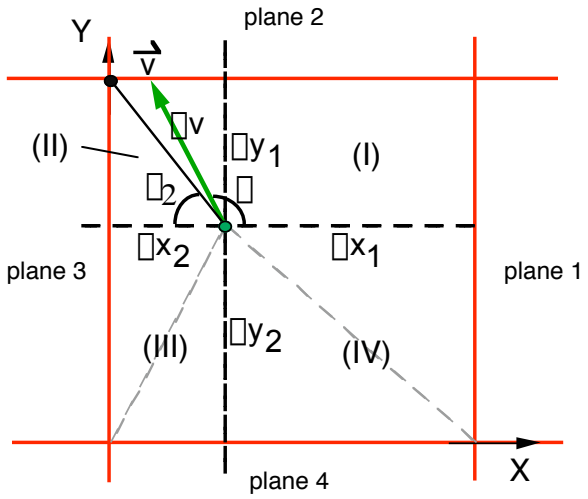

Figure 8.4: The photon's trajectory projected in the $\vec{x}$-$\vec{y}$ plane falls in region (II). The azimuthal angle of the trajectory is φ, and the angle $\delta_2 = \tan^{-1}(\Delta y_1/\Delta x_2)$.

After the step size of the photon is found, the photon position is updated from the old position (x, y, z) to a new position (x', y', z') as,

$$x' = x + s_1 u_x \,;\;\; y' = y + s_1 u_y \,;\;\; z' = z + s_1 u_z \;\; .$$

8.2.3 Drops of weight

By moving a distance of s_1, the weight of the photon (W_{new}) becomes

$$W_{new} = W_{old} \exp(-\mu_{a1} s_1) \;\; ,$$

where μ_{a1} is the absorption coefficient of the voxel that the photon crosses. The reduced weight is deposited to the local voxel that the photon is traveling through.

8.2.4 Boundary conditions

When the photon travels to the outer boundary of the medium, the photon will be terminated and any remaining weight will be dropped to the edge voxel. Note that one may need to adjust the dimensions of the medium in such a way that the chances for photons to travel to the edge of the medium are low to reduce the potential statistic errors. This may also depend on the optical properties of the medium.

When the photon travels to the top or bottom surface of the medium, there are two possible results. If the incident angle θ_i is greater than the critical angle θ_c, the photon will be totally reflected; otherwise, the photon is partially reflected back to the medium according to the Fresnel reflection. The critical angle can be calculated as

$$\theta_c = \cos^{-1}\sqrt{1 - \frac{1}{n^2}} \ ,$$

where n is the refractive index of the medium. The Fresnel reflectance R is

$$R = \frac{1}{2}(R_{\parallel} + R_{\perp}) \ , \tag{8.4}$$

where

$$R_{\parallel} = \frac{\tan^2(\theta_i - \theta_t)}{\tan^2(\theta_i + \theta_t)} \quad \text{and} \quad R_{\perp} = \frac{\sin^2(\theta_i - \theta_t)}{\sin^2(\theta_i + \theta_t)} \ ,$$

where θ_i is the incident angle and θ_t is the transmission angle calculated using Snell's law $n_i \sin\theta_i = n_t \sin\theta_t$. This R value will be added to the reflectance array if the photon is bounced back from the top or the transmission array if the photon is bounced back from the top. The weight of the photon is dropped by R.

8.2.5 Changes of optical properties

After the weight of the local voxel has been updated, the optical properties of the local voxel are updated based upon the relationship between the optical properties and radiant exposure. This relationship is material dependent. The radiant exposure H in each voxel is calculated as

$$H = \frac{W_{\text{total}}}{Nv\mu_a} \cdot EA \ ,$$

where W_{total} is the total deposited weight, N is number of photons, v is the voxel volume, μ_a is the absorption coefficient of that voxel, E is the radiant exposure of the illumination, and A is the area of the illumination beam.

8.2.6 Terminate a photon by roulette

The standard roulette method is used to terminate the photon [145]. The weight of the photon attenuates as the photon moves; however, the weight never goes to zero. Therefore, we set a weight minimum threshold, if the photon's weight becomes less than this threshold, then the photon survival is decided by the roulette method.

8.3 DMC Model Verification

Verification of the DMC model was done by comparing the DMC results with the results of (1) numerical solutions for absorption only media, (2) layered MC model developed by Prahl for multi-layered optical property media (see Appendix A), (3) the modular adaptive grid numerical model (MAGNUM) developed by Pfefer et al [144] for heterogeneous media, (4) experimental measurements of dynamic absorption coefficients of unfilled resins, and (5) the total reflectance and transmittance and the optical properties of dental composite slabs as a function of radiant exposures.

8.3.1 Absorbing-only media

Three types of absorption properties were simulated:

1. Simple, fixed absorption coefficient media:

   (a) For a 1 J beam incident on a $\mu_a = 2\,cm^{-1}$, refractive index n_m=1.5, 1 cm thick medium, the specular reflectance of the beam is

   $$\mathrm{sr} = \left(\frac{n_m - n_{air}}{n_m + n_{air}}\right)^2 \quad . \tag{8.5}$$

   So, the theoretical total reflectance R and transmission T should be

   $$R = \frac{\mathrm{sr}}{1-(1-\mathrm{sr})^2 e^{-2\mu_a \ell}} = 0.04069 \quad \text{and} \quad T = \frac{(1-\mathrm{sr})^2 e^{-\mu_a \ell}}{1-\mathrm{sr}^2 e^{-2\mu_a \ell}} = 0.12473 \quad .$$

   The DMC model generates $R = 0.04068(6)$, and $T = 0.12473(2)$ for five simulations of 200,000 photons.

   (b) For a 1 J, r=0.5 cm radius light beam launched into a $\mu_a = 1\,\mathrm{cm}^{-1}$, n_m=1 medium, the theoretical deposited energy density at the ith layer with thickness Δx =0.1 cm is

   $$W_i = \left(e^{-\mu_a (i-1)\Delta x} - e^{-\mu_a i \Delta x}\right)/V \quad , \tag{8.6}$$

   where i is the layer number 1,2,...,10, and V=$\pi r^2 \Delta x$ is the volume of the deposited unit . Figure 8.5 shows that the DMC result matches the numerical result.

2. Layered absorption coefficient media (Fig. 8.6):

   A 1 J, r=0.5 cm radius light beam was launched into a n_m=1.5 medium whose absorption increases with depth: $\mu_{a,i} = ik\,\mathrm{cm}^{-1}$, where the increasing rate k is 0.2

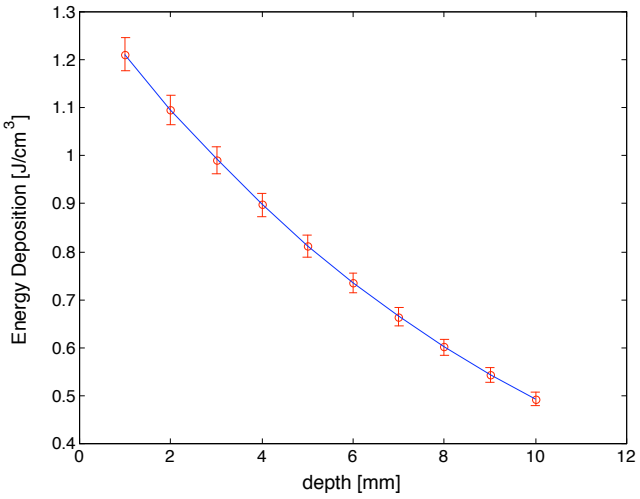

Figure 8.5: Comparison of theoretical deposited energy density Eq. 8.6 (line) and simulation results (circle) for 1 J, 1 cm diameter light beam into $\mu_a = 1\,\mathrm{cm}^{-1}$ medium with matched boundaries. Each of the error bars is the standard deviation of 5 simulations, each of which is 200,000 photons.

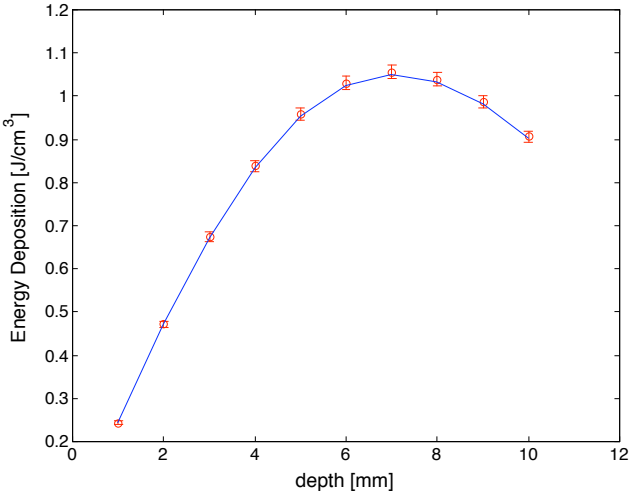

Figure 8.6: Comparison of theoretical deposited energy density Eq. 8.7 (line) and simulation results (circle) for 1 J, 1 cm diameter light beam into $\mu_{a,i} = 0.2i\,\mathrm{cm}^{-1}$ medium with specular reflection, where i is the layer number, 1, 2, ..., 10. Each layer is 0.1 cm thick. Each of the error bars is the standard deviation of 5 simulations, each of which is 200,000 photons.

and i is the layer number 1,2,...,10. Each layer is Δz=0.1 cm thick. The theoretical energy density at the ith layer is

$$W_i = \frac{1-\mathrm{sr}}{V}\left(\exp[\frac{-i(i-1)k}{2}] - \exp[\frac{-i(i+1)k}{2}]\right) \quad , \tag{8.7}$$

where sr can be calculated from Eq. 8.5 and $V = (\pi r^2 \Delta z)\,\mathrm{cm}^3$. The comparison in Fig. 8.6 shows that the DMC results match the numerical results.

3. Dynamic absorption coefficient media (Fig. 8.7 and 8.8):
   Assume an $1\,\mathrm{W/cm}^2$ light beam illuminates a medium whose absorption coefficient dynamically changes with deposited energy density:

$$\mu_{a,j}(t) = 1 - kW_j(t) \quad \mathrm{cm}^{-1} \quad , \tag{8.8}$$

   where k=0.05 and $W_j(t)$ is the jth-layer deposited energy density as a function of time t. Assume the layer thickness is Δz, then the irradiance at bottom of jth layer is

$$I_j = I_0 \prod_{i=1}^{j} \exp(-\mu_{a,i}\Delta z) \quad .$$

   Therefore,

$$W_j(t) = W_j(t-\Delta t) + \frac{\Delta t}{\Delta z} I_0 (1 - \exp(-\mu_{a,j}\Delta z)) \prod_{i=1}^{j-1} \exp(-\mu_{a,i}\Delta z) \quad .$$

   The final deposited energy density W_{DMC} in each voxel is

$$W_{\mathrm{DMC}} = w/Nv \quad [\mathrm{J/cm}^3],$$

   where w is the total weight in each voxel, $N = 4 \cdot 10^4$ photons/J, and v is the voxel volume. In all the simulations, the energy density and the absorption coefficient at each time point and each layer were recorded for comparison. Figure 8.7 compares the results of $W(t)$ and $\mu_a(t)$ at four different depths. Figure 8.8 compares the results of W_j and $\mu_{a,j}$ at five time points. The DMC results match the numerical model within 1%.

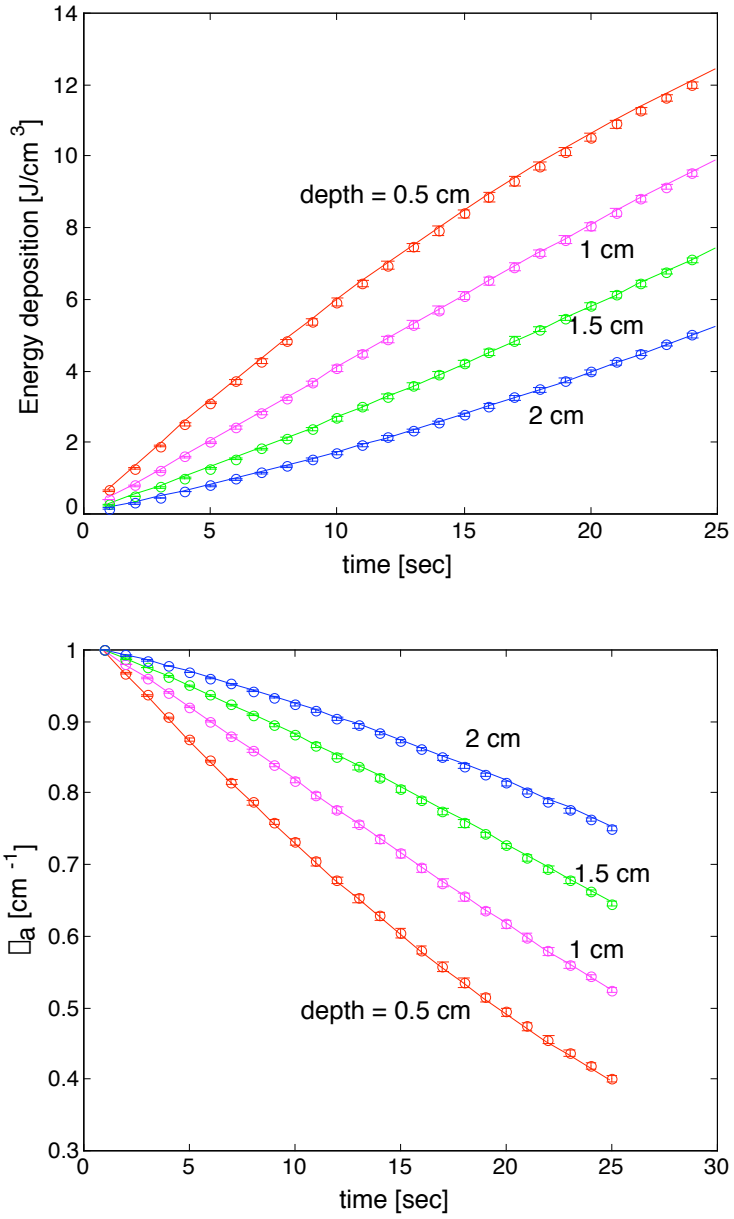

Figure 8.7: Comparison of numerical (line) and simulation results (circle) for 1 J/cm^2 light beam into dynamic absorption coefficient medium (Eq. 8.8). The top figure depicts the deposited energy density versus time at 4 different depths. The bottom figure depicts the absorption coefficients versus time at 4 depths. Each error bar is the standard deviation of 4 simulations, each of which was 1 million photons.

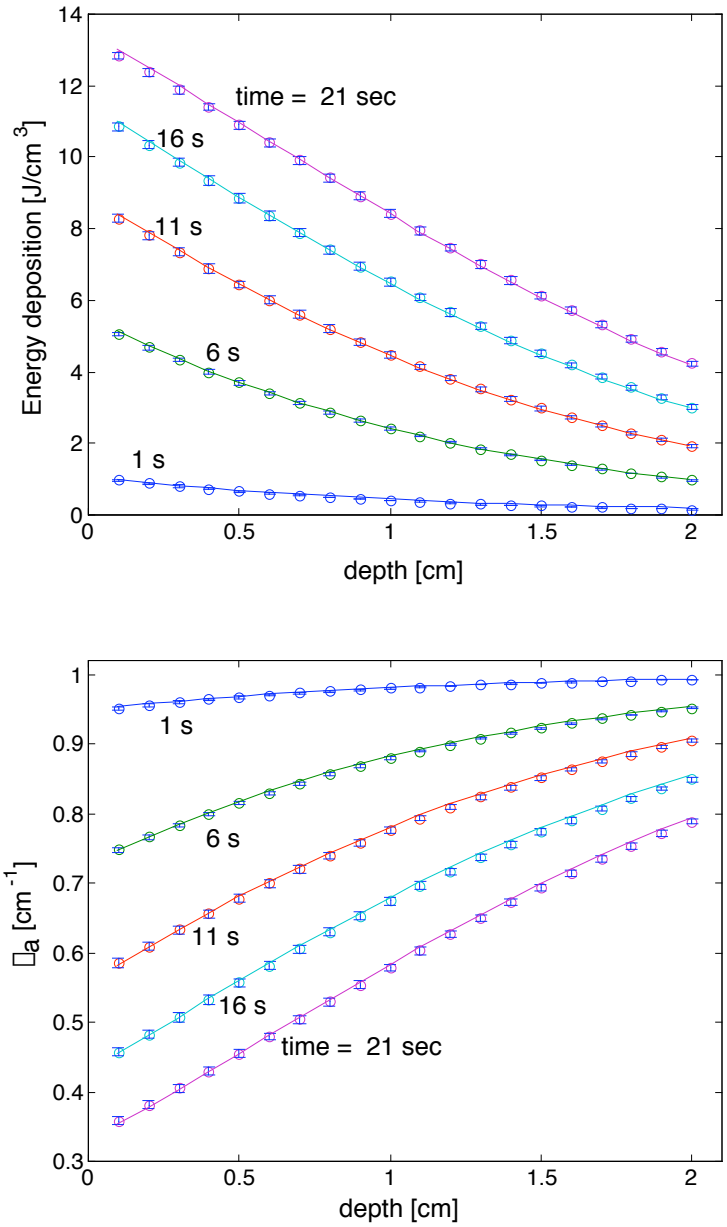

Figure 8.8: Comparison of numerical (line) and simulation results (circle) for $1\,\mathrm{W/cm^2}$ light beam into dynamic absorption coefficient medium (Eq. 8.8). The top figure depicts the deposited energy density versus depth at 5 different times. The bottom figure depicts the absorption coefficients versus depth at 5 times. Each error bar is the standard deviation of 4 simulations, each of which uses 1 million photons.

		layer 1	layer 2	Reflectance
	layer thickness	(2 mm)	(2 mm)	–
	(n, μ_a, μ_s, g)	(1, 2, 50, 0)	(1, 2, 50, 0)	
1	DMC's W	2.034±0.004	0.0745±0.0015	0.5779±0.0007
	LMC's W	2.039±0.002	0.0732±0.0013	0.5777±0.0003
	(n, μ_a, μ_s, g)	(1.5, 0.5, 50, 0.5)	(1.5, 0.5, 50, 0.5)	
2	DMC's W	1.748±0.001	0.525±0.003	0.4634±0.0002
	LMC's W	1.746±0.001	0.525±0.003	0.4626±0.0008
	(n, μ_a, μ_s, g)	(1, 2, 50, 0)	(1, 4, 50, 0)	
3	DMC's W	2.027±0.004	0.0853±0.0007	0.5777±0.0007
	LMC's W	2.027±0.003	0.0851±0.0005	0.5774±0.0007
	(n, μ_a, μ_s, g)	(1, 2, 50, 0)	(1, 2, 100, 0)	
4	DMC's W	2.051±0.006	0.0613±0.0007	0.5777±0.0012
	LMC's W	2.052±0.002	0.0610±0.0003	0.5774±0.0004

Table 8.1: This table lists four sets of simulation results of DMC and LMC models: the optical properties n, μ_a, μ_s, g of each layer, the energy deposition density W [W/cm^3] at each layer, and total reflectance. The standard errors are for five simulations, each of which uses 200,000 photons.

8.3.2 Layered optical properties μ_a and μ_s

A medium with three-layered optical properties was simulated (Table 8.1 and Fig. 8.9). A 1 W/cm^2 uniform beam was launched perpendicular to the top of the medium. The deposited energy density in each layer (W/cm^3) as well as the total reflectance were recorded. The DMC simulation results were compared with the layered Monte Carlo (LMC) model by Prahl (see Appendix A). In both simulations, 200,000 photons were launched. This was repeated five times to obtain the means and standard deviations. In all these simulations, a uniform index of refraction was assumed for all the layers.

The simulation results are listed in Table 8.1 for the deposited power density [W/cm^3] in each layer and the total reflectance. All pairs of DMC versus LMC values were also plotted against each other in Fig. 8.9.

8.3.3 Heterogeneous optical property media

To verify the DMC code for heterogeneous media, the results from the DMC model were compared with Pfefer's MAGNUM results developed for skin tissue [144] (Figure 8.10,

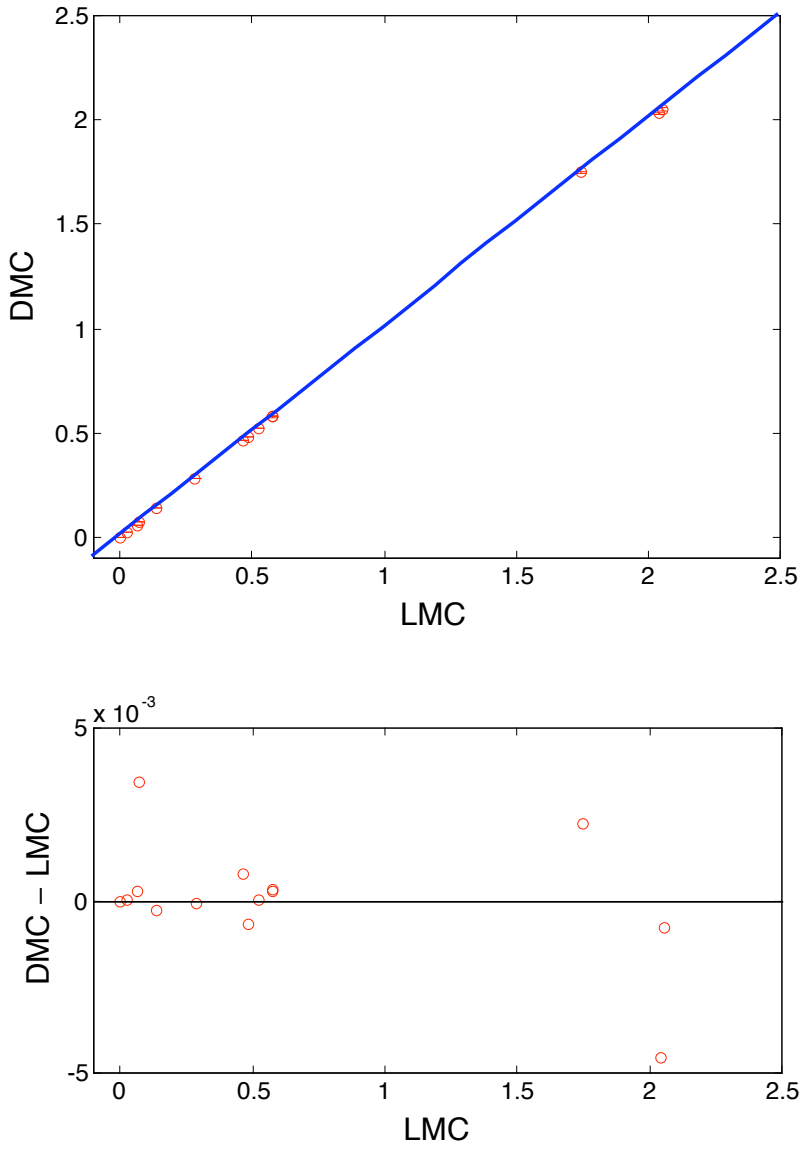

Figure 8.9: (Top) Comparison of DMC and LMC simulation values (circle). The line is a 1:1 ratio line. Each of the errorbars is the standard deviation of 5 simulations. (Bottom) The differences of DMC and LMC versus LMC values.

8.11, and 8.12). MAGNUM was written to simulate light propagation in a medium with heterogeneous optical properties, such as the absorption of blood vessels in human skin.

In the DMC simulation, the following geometry and optical properties of the medium were assumed: a 60 μm top epidermal layer ($n = 1.37, \mu_a = 470\,\mathrm{cm}^{-1}$, $\mu_s = 18\,\mathrm{cm}^{-1}$, $g = 0.79$) and 940 μm dermal layer ($n = 1.37, \mu_a = 2.2\,\mathrm{cm}^{-1}$, $\mu_s = 129\,\mathrm{cm}^{-1}$, $g = 0.79$) with one or two $120\times120\times120\,\mu\mathrm{m}^3$ "cubic" blood vessels ($n = 1.37, \mu_a = 191\,\mathrm{cm}^{-1}$, $\mu_s = 468\,\mathrm{cm}^{-1}$, $g = 0.995$) located at depth 190–310 μm or/and 440–560 μm (Fig. 8.10 Top). A fluence of $1\,\mathrm{J/cm}^2$, and a 1.0 mm diameter illumination beam centered at $x = 1000\,\mu$m, $y = 1000\,\mu$m, $z = 0\,\mu$m was assumed. The grid size was $100\times100\times10\,\mu$m.

In the MAGNUM simulation, a few differences in the geometries and optical properties of the medium were assumed: the refractive index of the blood vessels was 1.33, the blood vessel was assumed to have a "spherical" shape with a diameter of 120 μm, and the grid size was $10\times10\times10\,\mu$m (Fig. 8.10 Bottom).

The distributions of energy density in the $x-z$ plane at $y = 1$ mm for three simulations are shown in Fig. 8.11. As we can see, the two blood vessels and the top layer have high energy deposition due to their high absorption coefficients. The energy density in the column of cubes directly below the center of the beam ($x = y = 1$ mm) versus the depth is illustrated in Fig. 8.12 (colored lines) and superimposed on the top of MAGNUM result (Fig. 8.12 black lines). The dashed lines represent the simulation of the medium with upper or lower blood vessel only, while the solid lines represent the simulation of the medium with both vessels. Both DMC and MAGNUM show similar scale of energy deposition in the vessels and the shading effect on energy deposition in the vessels (much lower energy density right below the vessels).

8.4 Simulations of Dental Composites Curing Process

8.4.1 Unfilled resin with dynamic μ_a

Figure 8.13 and 8.14 show the results of this section. The changes in the absorption coefficient are based on the μ_a and radiant exposure H relationship established in Chapter

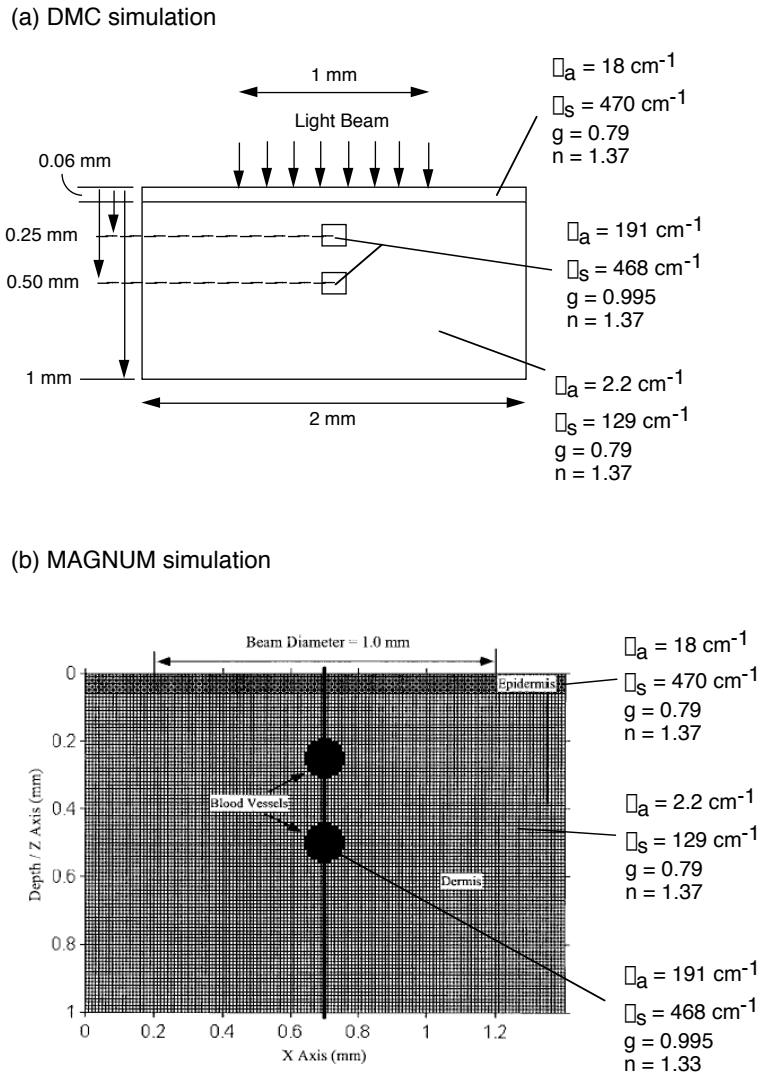

Figure 8.10: (Top) Representation of $x - z$ plane cross section of the DMC simulation. The medium consists of a 60 μm epidermal layer and a 940 μm dermal layer and two $120\times120\times120\,\mu\text{m}^3$ "cubic" blood vessels located at depth 190–310 μm or/and 440–560 μm. (Bottom) Representation of $x-z$ plane cross section of the MAGNUM simulation by Pfefer et al. The geometry is similar to the top figure except the shape of the blood vessels is spherical.

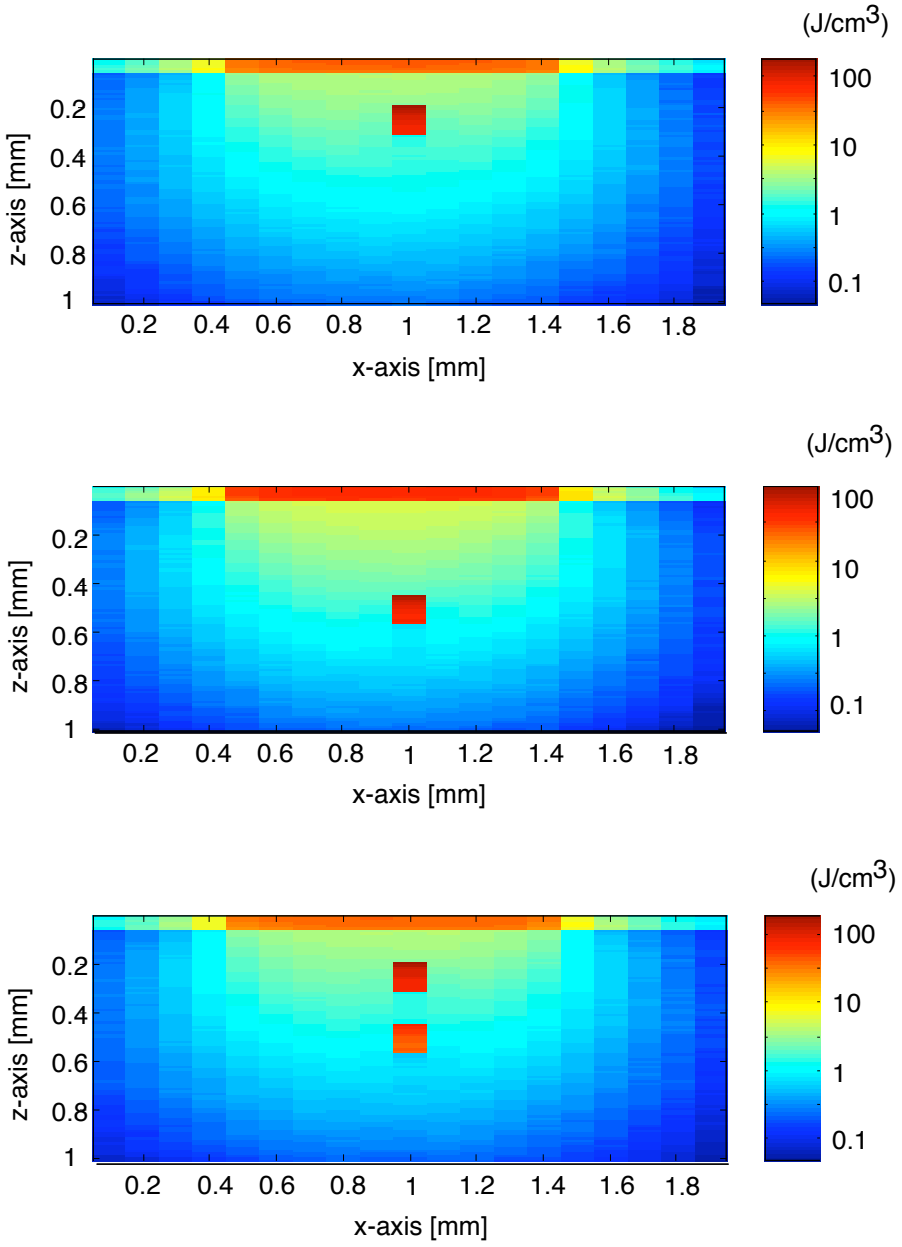

Figure 8.11: Colormap of the distribution of deposited energy density for the $x-z$ plane cross section of the simulated medium at the center of the beam (y=1 mm).

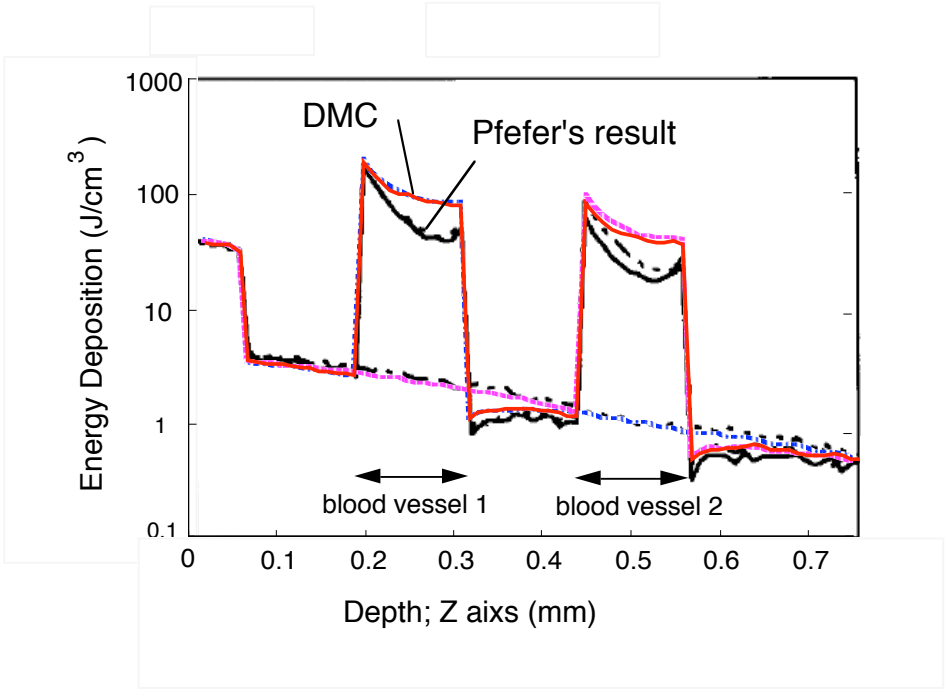

Figure 8.12: The energy deposition versus depth at the beam center of $x-z$ plane cross section for DMC simulations (colored lines) and Pfefer's MAGNUM simulations (black lines). Dotted line represents the simulation of upper blood vessel only, dashed line represents the simulation of lower blood vessel only and solid line represents the simulation of both blood vessels.

6:

$$\mu_a(H) = \mu_{ao} \exp(-H/H_{\text{total}}) \quad , \tag{8.9}$$

we simulated the μ_a of resin as a function of radiant exposure and compared the results with the experimental measurements of Chapter 6. Three simulations were performed for the three irradiances: 160, 90, and 30 mW/cm^2. The μ_{ao} was 4.46 cm^{-1} and H_{total} was 43 J/cm^2, and a thickness of 1 mm resin was assumed. The light illumination was assumed to be collimated, flat, and circular. The μ_a at different depths, the total reflectance and transmission were recorded every 10 seconds of illumination for a total of 120 seconds. Note that all the simulation parameters were assumed at 469 nm wavelength.

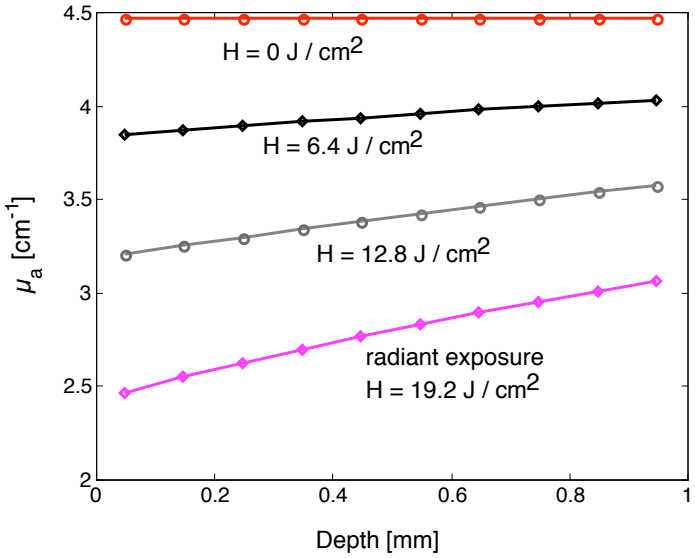

Figure 8.13: DMC model results of resin μ_a as a function of depth at different radiant exposures.

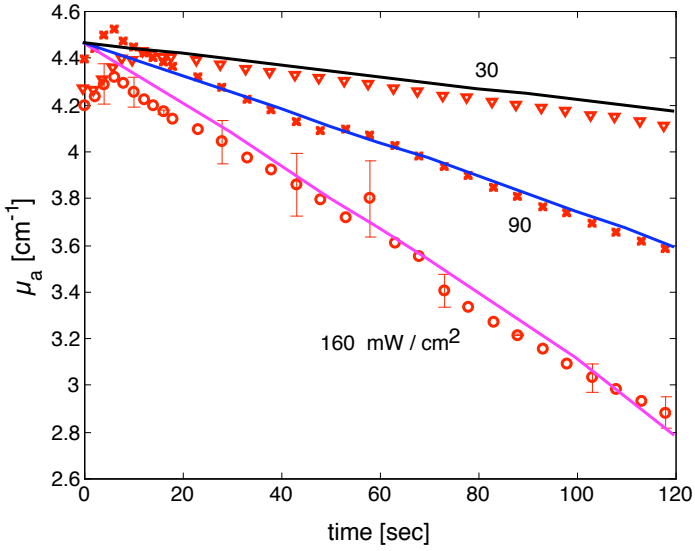

Figure 8.14: Comparison of DMC model results (lines) and the experimental results (points) from Chapter 6 for resin μ_a as a function of irradiation time for three different irradiances: 160, 90, and 30 mW/cm^2.

The change of resin μ_a as a function of depth at different radiant exposure with increments of $6.4\,\mathrm{J/cm^2}$ is shown in Fig. 8.13. Note that the radiant exposure H here is the H at the top surface, not the actual H at each depth. The μ_a of the top layer is about 30% lower than the bottom μ_a after $19\,\mathrm{J/cm^2}$ of exposure. Assume that the average of μ_a throughout the depth represents the μ_a of the whole resin. The μ_a as a function of curing time for the three irradiances is plotted in Fig. 8.14 and compared with the experimental results from Chapter 6. The overall differences between the model and experimental results were less than 5%.

8.4.2 Composites with dynamic μ_a and μ_s'

Figure 8.15, 8.16, 8.17 and 8.18 illustrate the simulation geometry and simulation results of this section. The simulation of a dental composite with dynamic μ_a and μ_s' was also based on the optical properties versus radiant exposure relationship established in Chapter 6 and 7. The $\mu_a(H)$ relationship is the same as Eq. 8.9. The dynamic reduced scattering coefficient is

$$\mu_s' = \mu_{so}' \exp(-H/H_{s(\mathrm{threshold})}) + \mu_{s(\mathrm{cure})}' \quad , \tag{8.10}$$

where μ_{so}'=$18\,\mathrm{cm^{-1}}$, $\mu_{s(\mathrm{cure})}'$=$12.5\,\mathrm{cm^{-1}}$, $H_{s(\mathrm{threshold})} = 1.4\,\mathrm{J/cm^2}$. Note that all the optical properties in the simulations were optical properties for 469 nm wavelength.

Simulations

To test the DMC model in simulating dental composites, the curing process of a 1 mm thick composite slab containing 0.175 wt% camphorquinone was simulated and the model results were compared with the experimental results of the R&T measurement in Chapter 7 (see Section 7.2.2 for experimental details). As shown in Fig. 8.15, the size of the composite was 2.8 cm by 2.8 cm by 0.1 cm in depth. The light illumination was a collimated, flat beam with power of 135 mW and diameter of 2 cm. The number of voxels is 14 in the x and y dimensions, and 5 in the z dimension.

To simulate the initial R&T for a totally uncured composite (when the radiant exposure is zero), the optical properties μ_a=$4.46\,\mathrm{cm^{-1}}$, μ_s'=$30.5\,\mathrm{cm^{-1}}$, and refractive index = 1.50

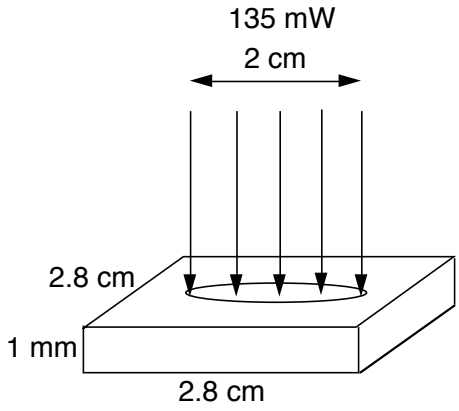

Figure 8.15: The geometry of the simulation of composites with dynamic μ_a and μ_s. The composite was 2.8 cm by 2.8 cm in width by 0.1 cm in depth. The illumination beam was circular, 135 mW in power, and 2 cm in diameter.

were assumed. In this simulation, no optical properties were changed. A total of 1,000,000 photons was launched. Then, the dynamic μ_a and μ_s' were applied in the simulation according to Eq. 8.9 and 8.10. The refractive index was assumed to be 1.53 for this simulation. The data of μ_a and μ_s' at different depths, the total reflectance (R), the total transmittance (T), and the energy deposition at different time along the central cross section were saved every 500,000 photons for a total of 15,000,000 photons.

Results

The energy deposition images along the central cross section at 10 different illumination times are plotted in Fig. 8.16. As the illumination increases, the energy deposition in the central region increases. The changes of μ_a and μ_s' as a function of radiant exposure at different depths (0.1, 0.5, and 0.9 mm) are shown in Fig. 8.17. The dots in the figure are the DMC simulation results, while the lines are Eq. 8.9 and 8.10. The radiant exposure decreases with depth, therefore the μ_a and μ_s' at the top layer (0.1 mm) drops about twice as much as that at the bottom layer (0.9 mm). Note that the radiant exposure here is the radiant exposure at the top surface, not a real radiant exposure at each layer. The real radiant exposure at different depths or voxels can be calculated by dividing the energy deposition shown in Fig. 8.16 by the μ_a of the local voxels.

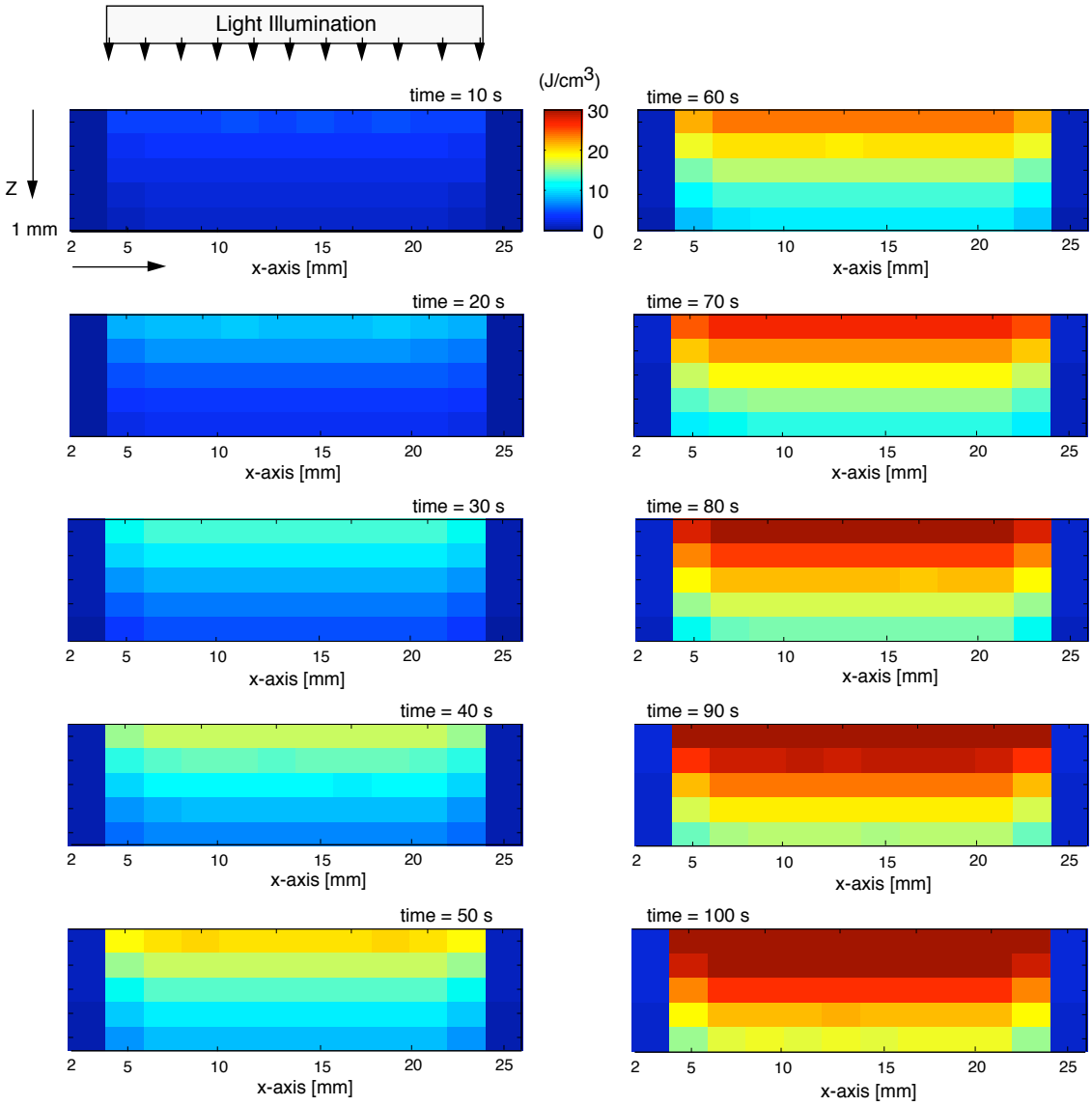

Figure 8.16: DMC model results of simulations of composites with dynamic μ_a and μ_s' (Section 8.4.2). The colormaps show the images of energy deposition (J/cm^3) of the central cross section in $x-z$ plane (at y=1.4 cm) at 10 different exposure times. The illumination beam is 135 mW in power and 2 cm in diameter.

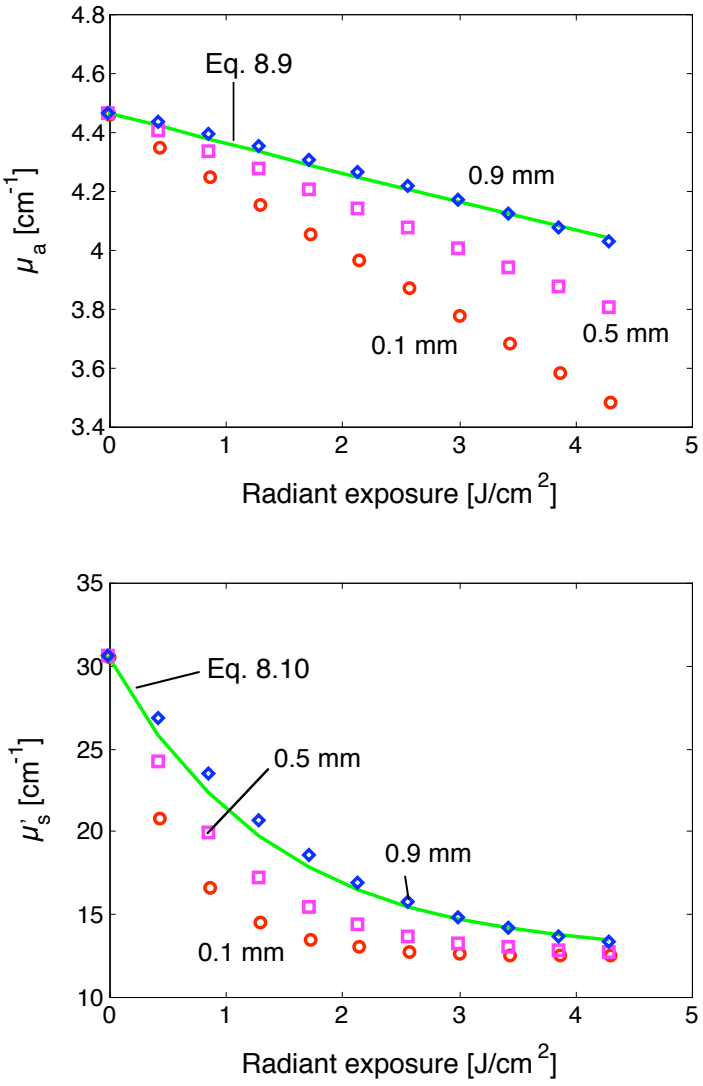

Figure 8.17: DMC model results: (Top) μ_a as a function of radiant exposure at depths 0.1, 0.5, and 0.9 mm. (Bottom) μ_s' as a function of radiant exposure at depths 0.1, 0.5, and 0.9 mm. The dots are the simulation results, while the solid lines are the equations (Eq. 8.9 and 8.10).

Figure 8.18 depicts the total reflectance R and transmittance T as a function of radiant exposure and compares the model results with the experimental results in Chapter 7. Both model and experimental results show similar trends in R and T. However, overall, the experimental R values are ~0.06 higher than the model results and the experimental T values are ~0.1 higher than the model results.

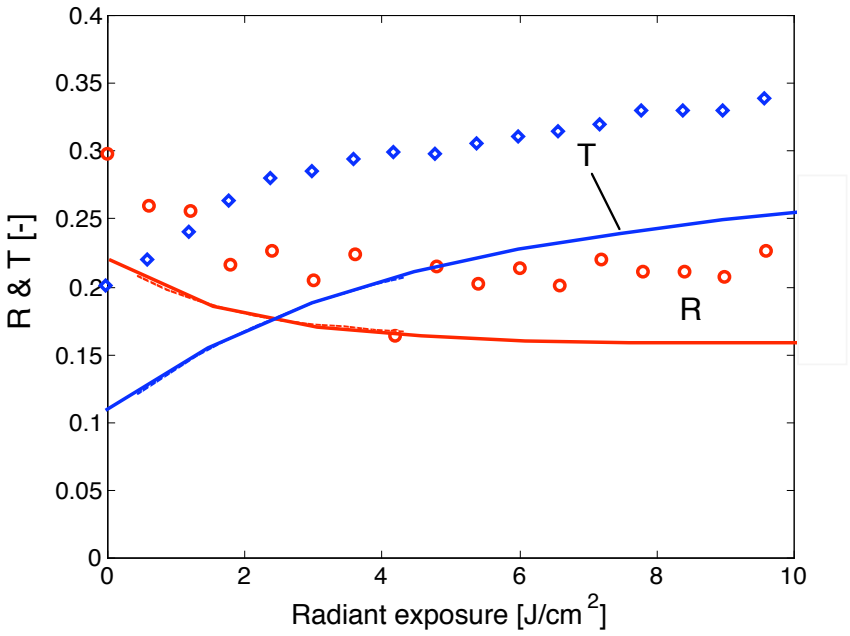

Figure 8.18: Comparison of DMC model results (lines) and experimental results (dots) of total reflectance (R) and transmittance (T) as a function of radiant exposure.

8.5 Discussion

Verification of the DMC model has been made by comparing with the analytical solutions, other research groups, and experimental results. In summary, the reflectance and transmittance results produced by the DMC for the simplified absorption only cases were within 0.05% of differences to the analytical solutions. For the simulation of dynamic absorption property media, DMC results differed within 1% from the analytical solutions (Fig. 8.7 and 8.8). The differences between my DMC model and Prahl's LMC model were within 2%, which were the combination of LMC's and DMC's statistical errors (Table 8.1

and Fig. 8.9).

The DMC model shows similar energy deposition to Pfefer's MAGNUM [144] results (Fig. 8.12), but MAGNUM showed a greater decrease in energy deposition along the depth within blood vessels and a larger shadow behind the blood vessels. This discrepancy may be because MAGNUM assumed a "spherical" shape of blood vessels while the blood vessels in my program were "cubic" in shape and had a larger volume. Since blood vessels have higher absorption and scattering coefficients, larger volumes of blood vessels might cause more photons to be captured in the blood vessels thereby yielding higher energy deposition. More photons in the blood vessels may also yield more photons transmitted to the voxels right below the vessels. Therefore, DMC has higher energy deposition behind the blood vessels than that in MAGNUM. To prove this hypothesis, future work can be done by dividing the medium into a smaller grid size ($10\times10\times10\,\mu$m) and digitally mapping the positions of the spherical vessels with voxel indices.

This DMC program was developed prior to discovering Pfefer's paper. It is interesting to compare the similarities and differences between the two models. Generally, both models were based on the standard Monte Carlo method developed for homogeneous media [119]. The standard Monte Carlo absorption (represented by weights of photons), Henyey-Greenstein scattering, and roulette termination procedures were used in both models. The concept of photon migration from the boundary of a voxel to the boundary of another voxel is similar. The major difference between our models is the method to calculate the step sizes of photon movement. My method compared the angles of the photon trajectory with the angles of the directions from the photon's position to the corner of the voxel. My code works for any dimension of voxels (i.e., the length, width, and the height of the voxel can be different). Pfefer's method compared the distances from the photon's position to each of the planes that photons would travel to. Pfefer's method only works for "cubic" voxels. However, Pfefer's code accounts for the different refractive indices among voxels. Therefore my code can be improved by adding the Snell's law and the Fresnel equation in Section 8.2.2 to account for the possible reflection or refraction at the interface between voxels.

The DMC simulation of unfilled resins during curing showed good agreement with

the experimental results with about 5% differences (Fig, 8.14). The differences are the combination of experimental standard deviations (∼3% between the measurements, see Chapter 6) and statistical errors in the model.

In the simulations of filled composite curing process (Fig. 8.17), it is interesting to see that the equations, Eq. 8.9 and 8.10, (the lines in the figure) agree with the optical properties at the bottom layer, not the top layer. This implies that the actual μ_a and μ_s' as a function of radiant exposure may decay faster than the estimations obtained in Chapter 7 using the IAD method. Since the IAD method to obtain the μ_a and μ_s' assumes the optical properties in the materials are homogeneous, it may be necessary to adjust the IAD method to take the inhomogeneity into consideration. Possibly a thinner sample should be used for the measurement. Further investigations will be needed.

The total reflectance and transmittance as a function of radiant exposures estimated by the DMC model were lower than that measured by the integrating sphere in Chapter 7 (Fig. 8.18). The discrepancy may be because the μ_a and μ_s' values used in the DMC model were higher than the actual values. In other words, lower μ_a and μ_s' values will yield higher R and T values in the model.

One may concern the statistic error caused by the boundary condition since the width of the illumination beam was close to the $x - y$ dimension of the medium. However, in reality the medium outside the composite boundary was air. The proportion for the photon to travel back to the composite medium would be the Fresnel reflectance at the composite–air boundary. This proportion will not be significant enough to bring the model R&T values close to the experimental values.

Moreover, the model can better fit the reality by adding the wavelength distribution to the profiles of the illumination beam. Only the optical properties at 469 nm was used in the model simulations while in reality, the light wavelength has a distribution from 425 to 500 nm (for FreeLight, see Chapter 6).

While the DMC model was able to simulate heterogeneous media with dynamic optical properties, the computational speed may be a consideration for using this model. The dimension of the media, the voxel sizes, the number of photons per recording time, and the absorption and scattering coefficient values all affect the simulation time. Increasing

the resolution on the grid sizes will increase the accuracy of the local energy deposition and optical property changes, but will increase statistical variations since fewer photons will be deposited in each voxel. One advantage of this DMC code is that the dimensions of the voxels can be non-symmetrical. Therefore, if the light illuminates along the z-axis, one can have finer grid sizes in the z direction and larger grid sizes in the x, y dimensions. In this way, the calculation rate can be increased. To get the simulation results shown in Fig. 8.18 using the DMC code, the propagation of a total of 5,000,000 photons required approximately 25 minutes of simulation time on a Mac G3 computer with a 500 MHz processor.

8.6 Conclusions

A dynamic Monte Carlo model has been developed to simulate the light transport in a photo-cured material that has dynamic absorption and scattering coefficients. The time-resolved energy deposition and optical property distributions in the materials, as well as the time-resolved reflectance and transmittance can be calculated during photon absorption. This model can be easily modified to accommodate different problems. This model may be used to analyze the light distribution in the dental composites to better understand the composite curing process and ultimately to predict the depth of cure. In addition, I hope this model to be applied in general laser-material or laser-tissue interaction problems. For example, this model may help understand the thermal damage in the tissues from the laser irradiation. Moreover, the model may be used to simulate the photodynamic therapy process as the absorption of the drugs in the tissue decreases during the irradiation. However, the model requires the relationship between the optical properties and the absorbed light energy (or radiant exposure). The experimental procedures to determine these can be difficult for some materials.

Chapter 9

General Discussion and Conclusions

This chapter summarizes the problems addressed and the main conclusions of this thesis.

9.1 Optical sensing with molecularly imprinted polymers

The molecularly imprinted polymer material used as the sensing element in this dissertation was polyurethane imprinted with polycyclic aromatic hydrocarbon (PAH) molecules. PAH molecules have unique fluorescence spectra that can be easily distinguished and recognized. In this study, anthracene was of particular interest as anthracene is a toxic molecule that can be found in contaminated ground water. The optical properties and fluorescence quantum yield of polyurethane imprinted with anthracene were thoroughly investigated and discussed.

9.1.1 Issues of imprinted polyurethane system

My studies on the rebinding capacity of MIPs showed that the rebinding of anthracene was about 4% of the theoretical number of imprinted binding sites and 6 times more than the non-imprinted control polyurethanes. This rebinding performance was moderate in terms of rebinding percentage but the ratio of specific to non-specific binding performance was comparable to the general performance of MIPs made by other research groups. This indicates that my polyurethane imprinted system could be used for PAH recognition but the concentration of rebound PAH might be low, thereby decreasing the detectable fluorescence signals.

Another issue of this polyurethane imprinted system was the background absorption of the polyurethane. Due to the similar chemical structure of the polyurethane to the PAH, polyurethane has a broad absorption spectrum (from 340 to 420 nm it has an absorption coefficient greater than $3\,\mathrm{cm}^{-1}$) and fluorescence (from 400 to 600 nm it has a quantum yield of 0.0005/nm) that overlaps with the fluorescence of anthracene. This was found to be the critical issue in determining sensor sensitivity.

9.1.2 Optical transducer design

Two types of sensor designs were analyzed. The first type consisted of a layer of MIPs on a transparent substrate. Excitation light was launched perpendicular to the MIP layer and the fluorescence emission was collected by a concave mirror. A Monte Carlo model was used to analyze how the background fluorescence and the thickness of MIPs affect sensitivity. The predicted behavior was verified experimentally within 15%. It was found that the MIP background absorption did not affect the sensitivity when the MIP samples were thinner than 0.2 mm. For the MIP sensor system studied, the detection limit was about 15 ppm of anthracene, which is $\sim$0.1 μmol of anthracene in 1 g of MIPs.

The second type of sensor design used the MIP itself as an optical waveguide to guide the excitation light and the fluorescence. A theoretical model of the fluorescence collection efficiency of the MIP waveguide was derived to examine how the MIP's optical properties affect the sensitivity. It was found that the fluorescence collection efficiency strongly depends on the MIP background absorption. The fluorescence output will increase 250 times and the signal to noise ratio will increase 10 fold when the background absorption decreases 10 times. The fluorescence collection efficiency is twice as great as in the first type of sensor. Other advantages over the first type of sensor include an increase in the sensing volume and the ease of MIP pattern construction for multi-analyte detection on a single chip. The advantages of the first type of sensor, on the other hand, are the ease of MIP-layer fabrication, which can be done by pipet coating or spin coating, and the increase of contact area with the analyte solutions that will accelerate the binding kinetics.

9.1.3 Fluorescence anisotropy of MIPs

Fluorescence anisotropy provides an additional method to characterize the binding performance between the analyte and MIPs. For a polyurethane imprinted system, it was found that MIPs and non-MIPs have the same steady-state anisotropy. Therefore, the attempt to use their polarization signals to distinguish the analyte signals from the polymer signals was not successful. However, differences in the time-resolved fluorescence characteristics between the rebound anthracene molecule and non-MIPs were able to help understand the binding environment of the MIP system. It was also found that the steady-state anisotropy changed during the polymerization process. This may provide an alternate way to observe the gelation process of polymers; steady-state anisotropy measurement is simple compared to other common observation methods (e.g., FTIR [19, 111], or interferometry [140]).

9.1.4 Alternative MIP systems

Improved detection limits can be achieved by imprinting a different PAH with red-shifted excitation and emission. Imprinting another PAH molecule, tetracene, that fluoresces at 480–580 nm, was tested. However, it was found that the detection limit was not dramatically increased due to polyurethane's broad fluorescence emission up to 600 nm. Another problem with imprinting tetracene was that the imprinting capacity of this molecule was one order of magnitude lower than that of imprinting with anthracene, thereby decreasing the rebinding capacity.

Another attempt was to use polymers that have low background absorption and fluorescence properties. Polyurethane synthesized from our starting materials was brown in color, which was caused by impure diisocyanate and triisocyanate mixture obtained from the commercial source. Attempts to purify the starting materials proved to be extremely difficult.

Different imprinting polymer systems such as polystyrene imprinted with 9-dansyladenine or poly(4-vinylpyridine) (PVP) imprinted with 7-carboxymethoxy4-methylcoumarin are two other possibilities. Both polystyrene and PVP are crosslinked by UV

irradiation. Polystyrene is colorless and has low absorption ($< 0.01\,\mathrm{cm}^{-1}$) at wavelengths above 290 nm. 9-dansyladenine is a fluorescent molecule that absorbs around 400 nm and fluoresces around 500 nm. PVP was found to have relatively higher absorption (∼0.5–$1\,\mathrm{cm}^{-1}$) at wavelengths between 350 and 400 nm. The absorption peak of coumarin is around 325 nm. Therefore, based on the characteristics of the optical properties of polymers and imprinted molecules, a polystyrene MIP system may have a better detection limit. The imprinting capability and rebinding capacities of both imprinting systems are currently under investigation.

9.1.5 Conclusions of MIP-optical sensing optimization

To evaluate and optimize a MIP optical sensor, the binding performance of the MIP should be examined using a fluorescence anisotropy technique in addition to the bath batch rebinding method. The fluorescence collection efficiency of the transducer should also be analyzed.

1. Guidelines for MIP design begins by characterizing the intrinsic optical properties of imprinted polymers and the analytes and using these in a Monte Carlo model to predict the fluorescence collection efficiency of the sensor. To improve signal-to-noise in fluorescence-based optical MIP sensors, both the background absorption and fluorescence quantum yield of polymers must be reduced.

2. Steady-state and time-resolved fluorescence together with fluorescence anisotropy measurements provides information on the binding distances and forces between analytes and MIPs. For the polyurethane imprinted system, analytes rebound in the polymer had a shorter fluorescence lifetime and a shorter fast rotational correlation time than those initially imprinted in polymers, suggesting a short-distance and tight binding between the analyte and the polymer when they rebound.

9.2 Photopolymerization

Photo-cured dental composites have many advantages, including esthetic appearance and the ability to cure *in situ*. However, limited light transport in the composite and

insufficient extent of cure may compromise the physical properties of the composite and reduce its service life. Chemically, the extent of cure can mean the degree of monomer conversion. Physically, the extent of cure can be represented by the relative hardness of the polymerized material. Clinically, the physical properties are most important as they directly relate to hardness and wear resistance.

A high extent of cure is desirable in dental composites, but "how much light do we need?" The most common method to evaluate photo-curing efficiency of a composite system (in terms of how effective the curing lamp cures the composite or how the composite composition affects the polymerization rate) is to measure the extent of cure of the bottom of cured composite disks with different thickness (2, 3, 4, and 5 mm) [15]. However, these studies do not directly relate the radiant exposure to the extent of cure. The radiant exposure inside the composite depends on the scattering, absorption, and index of refraction. Moreover, the absorption by the photoinitiators drops during the curing process as the initiators are photobleached. The index of refraction of the resin matrix also changes during polymerization, which in turn affects scattering by the filler particles and the overall scattering coefficient of the composite. Thus the light distribution within the composite changes during curing.

This thesis addressed these issues from the light transport theory point of view. The use of light transport theory in understanding photocuing efficiency had never been exploited by other research group. The central question of the study was *"what is the photo-curing efficiency of a photo-curing system"*, or *"what is the relationship between the amount of light and the amount of curing"*.

My study started with simple static Monte Carlo modeling to predict the radiant exposure distribution within the composite. The light distribution was compared with the curing extent distribution. It was found that the light distribution and the curing distribution were comparable and the relationship between the radiant exposure and the curing extent fitted two commonly used polymerization models. It was also found that the light distribution within the composite changed significantly during curing process and therefore it was necessary to develop a dynamic Monde Carlo model that accounts for the dynamic optical properties of the composite.

Before a dynamic Monte Carlo model could be developed, we had to know *"how much light is needed to change the optical properties"*. The major absorber in the composite was the photoinitiator. Chapter 6 demonstrated two experimental methods to measure the quantum yield of the photoinitiator conversion. Chapter 7 studied the optical property changes to the absorbed light radiant exposure. Finally, a dynamic Monte Carlo model for predicting the distribution of radiant exposure in the composite was built in Chapter 8. The photopolymerized material studied in this dissertation was a dental composite containing a photoinitiator, camphorquinone (CQ), whose absorption peak is at 469 nm. A commercial composite Z100 and an experimental composite with known material compositions were investigated. In the following sections I summarize my discoveries and discuss the ramifications of these findings.

9.2.1 How does extent of cure relate to radiant exposures? Which polymerization model works?

In Chapter 5, a static Monte Carlo model was developed to calculate the radiant exposure distribution within the composite. This was compared with the distribution of extent of cure (both DC and KHN). It was found that the relationship between the extent of cure and radiant exposure could be fitted with a simple exponential function,

$$DC = DC_{max}[1 - \exp((\ln 0.5)H/H_{dc}^{50\%})] \ ,$$

or with Racz's model,

$$DC = DC_{max}/[1 + (H/H_{dc}^{50\%})^{-2}] \ ,$$

where $H_{dc}^{50\%}$ was the only fitted parameter. This represents the radiant exposure needed to achieve 50% of maximum extent of cure.

Both models gave a S-shape curve for DC versus radiant exposure, H (Fig. 5.5). When the radiant exposure is lower than the threshold (1 J/cm^2 in Fig. 5.5), there is no DC. After the DC is initiated when $H > 1$, the DC increases dramatically with the radiant exposure. When the DC reaches 80% of the maximum value, the changing of DC with radiant exposure slows down and finally the DC reaches a maximum. It is also interesting to see that the radiant exposure needed to reach certain amount of hardness (KHN) was higher

than that needed for DC (see Table 5.1). This implies it may be more difficult to obtain adequate hardness than sufficient DC. This also indicates that the double bond conversion may not be the only factor that affects the formation of physical hardness.

It was also found that curing obeyed a reciprocity relationship for the irradiance and irradiation time, i.e., the irradiance×time = constant for the same extent of cure. This finding was consistent with that of other research groups [102,107,108,113,114]. However, this reciprocity rule conflicted with Watts' model [39],

$$\frac{DC}{DC_{max}} = 1 - \exp[-k_p k_t^{-0.5} (\Phi I_a)^{0.5} t] \quad ,$$

where k_p and k_t are the propagation and termination rate constants, Φ is the quantum yield for initiation, I_a is the light fluence rate absorbed by the photosensitizer, and t is the exposure time. The critical assumption that led the extent of cure to be dependent on the square root of irradiance, $\sqrt{I_a}$, instead of I_a was that the termination rate was assumed to be equal to the initiation rate of polymerization; thus, the concentration of polymer radicals needs to remain constant during the polymerization process. It is possible that in my experiment the polymer radicals changed during the illumination especially because the irradiance inside the composite was inhomogeneous. Different compositions of the materials and different lamp irradiances can be used to test the applicability of various polymerization models.

9.2.2 How many photoinitiators are converted per absorbed photon?

Not all the photons delivered to the composite are absorbed. Only those photons that are absorbed by the photoinitiators can possibly cause photopolymerization. Therefore, it is the effective absorbed power density (irradiance×absorption coefficient), not just the irradiance of the lamp, that matters. This value changes as the absorption coefficient changes during curing. Moreover, not all absorbed photons efficiently convert the photoinitiators. Therefore, we needed to keep tracking the concentrations of the photoinitiators.

It was found that the irradiance and irradiation time also held a reciprocity relationship

for the changes of CQ absorption coefficient.

$$\mu_a(H) = \mu_{ao} \exp(-H/H_{a(\text{threshold})}) \ ,$$

where μ_{ao} was $4.8 \pm 0.5\,\text{cm}^{-1}$, and $H_{a(\text{threshold})} = 43 \pm 4\,\text{J/cm}^2$ was the curing threshold where the concentration of CQ dropped to $1/e$. The curing threshold was the same for an LED (FreeLight, 3M ESPE) and tungsten halogen lamp (VIP, Bisco). By tracking the absorption coefficient (which relates to CQ concentration) changes to the exposure time and tracking the accumulated absorbed power density as a function of exposure time, the quantum yield of CQ conversion could be calculated. The quantum yield was measured to be 0.07±0.01, that is 14 photons must be absorbed to photobleach one CQ molecule (for 0.7 wt% CQ in the formulation of resins having specific combination of 0.35 wt% DMAEMA reducing agents and 0.05 wt% BHT inhibitors).

The efficiency of absorbed photons to convert the photoinitiator depends on many factors. Since one absorbed photon definitely creates an excited singlet state, there might be some loss in the process from the excited singlet state to the "converted" state. Although intersystem crossing to a triplet excited state is efficient (in pico second scale), it is still possible for the singlet excited state to return to a ground state (in nano second scale). Next, the triplet-state CQ needs to abstract proton and if that does not happen, it will return to the ground state. Therefore, one may optimize the proton abstraction by increasing the amine concentration. Once CQ had abstracted a proton, the CQ·H radical could give a proton back to something, again returning CQ to its ground state. Also two CQ·H radicals could react to form a CQ·H_2 alcohol and one CQ in ground state (this process would lead to two photons needed to convert one CQ). Therefore, different photoinitiators and different resin formulations may have different quantum yield values.

The photoinitiator conversion affects the absorption of the media. However, the relationship between the CQ conversion and the free radical addition (polymerization) needs further investigation to directly relate the number of absorbed photons to the amount of polymer. Therefore, the next question will be "does the absorption coefficient relate to the extent of cure?" or "do the optical properties relate to the extent of cure?".

9.2.3 How do optical properties of composites relate to radiant exposure?

The changes in the composite's optical property due to the light radiant exposure were investigated in Chapter 7. The absorption and scattering coefficients as a function of irradiation time were measured with double integrating spheres and a dual-channel spectrometer. This chapter used the information of the CQ absorption coefficient as a function of radiant exposure from Chapter 6 to figure out the radiant exposure in the composite. Then the relationship between the composite scattering coefficient and the light radiant exposure was derived.

The reduced scattering coefficient as a function of radiant exposure was

$$\mu_s'(H) = \mu_{so}' \exp(-\frac{H}{H_{s(\text{threshold})}}) + \mu_{s(cure)}' \ ,$$

where the fitting parameter $\mu_{s(\text{cure})} = 12.5\,\text{cm}^{-1}$ was the scattering coefficient of "cured" composite, $\mu_{so}' + \mu_{s(\text{cure})} = 30 \pm 2\,\text{cm}^{-1}$ was the initial scattering coefficient of uncured composite, and $H_{s(\text{threshold})} = 1.4 \pm 0.2\,\text{J/cm}^2$ was the radiant exposure threshold where the scattering dropped to $1/e$.

The refractive index changes of composites with different concentrations of the photoinitiator CQ versus the curing time were also measured. In Chapter 7 it was found that both the refractive index and the reduced scattering coefficient were independent of the concentration of CQ in the composites. Dudi *et al.* used a Michelson interferometer to measure the refractive index changes as a function of the amount of light absorbed. Further investigations could use interferometry to relate the refractive index changes to the radiant exposure. A Raleigh interferometer may be ideal for this measurement [146] as the sensitivity to changes in the refractive index may be as high as 10^{-5} for 1 mm thick sample [147]. Another advantage is that the experimental sample can be directly compared with the control sample under the same illumination beam.

The size distribution and the refractive indices of the filler particles may affect the scattering coefficients of the composites. In my study, only one filler type and one concentration were used. Further study is needed to construct a table of scattering coefficients corresponding to different filler types and sizes.

9.2.4 Do optical properties relate to extent of cure?

From Chapter 5, we obtained the relationship between extent of cure and radiant exposure (for the commercial Z100 material). From Chapter 6 and 7, we found the relationship between composite optical properties and radiant exposure (for an experimental composite). In the future, it will be interesting to compare the optical properties of composite with the extent of cure.

The threshold for a 50% change in the scattering coefficient was $1\,\mathrm{J/cm^2}$. This $H_{s(\mathrm{threshold})}$ is comparable to the threshold for changes to the degree of conversion $H_{dc}^{50\%} = 1.4\,\mathrm{J/cm^2}$ for the uncured sample simulation and $3.5\,\mathrm{J/cm^2}$ for cured sample simulation (Table 5.1). This implies that the scattering coefficient changes may be related to the degree of conversion. The threshold for the absorption coefficient to drop 50% was $H_{a(\mathrm{threshold})} = 30\,\mathrm{J/cm^2}$. These values are significantly higher than any of the thresholds for 50% degree of conversion. Therefore, it is likely that the scattering coefficient (the refractive index) is more directly related to the polymerization process. However, since the materials we used for these two sets of measurements were different, further study using exactly the same material contents is warranted.

9.2.5 How can a dynamic Monte Carlo model help optimization of photopolymerization process?

Numerical modeling of light-polymer interactions can be effective for understanding and improving photo-cured dental composites. In Chapter 5, a static Monte Carlo model estimated the radiant exposure in the composite. However, the thresholds for curing predicted by this model differed significantly when cured or uncured optical properties were used (Table 5.1). Therefore, a novel dynamic Monte Carlo model was developed in Chapter 8 to simulate light propagation in a heterogeneous medium with dynamic optical properties.

The dynamic Monte Carlo (DMC) model can help to optimize a photocured composite system in the following ways.

1. The DMC model can predict the light distribution within the composite. From

the light distribution, we can further compare with the curing distribution of the composite; consequently, the photo-curing efficiency can be obtained.

2. The DMC model can predict the depth of cure. The DMC model has the flexibility to be adapted to realistic dental composite systems (e.g., geometry of the specimen, distance from the light source, or color of the backing materials).

3. The DMC model can give insight into the curing lamp design, like the irradiance, the lamp spectrum, and the optimal irradiation time.

4. The DMC model can give constraints on composite formulations. Since the model can predict the light distribution given the optical properties of the composite, the model can provide optimal optical properties for different conditions (e.g., color of the backing materials or different light spectra). Since the scattering coefficient is correlated to the size distribution and refractive indices of the fillers, it is possible to provide a formulation design strategy.

9.2.6 What are the limitations of light transport theory on optimization of photopolymerization?

In addition to the extent of cure, shrinkage and marginal adhesion between the composite and the teeth are important issues in dental restoratives. My studies showed that the irradiance and illumination time obeyed reciprocity for (1) extent of cure, (2) the photoinitiator conversion, and (3) the optical property changes. This suggested that only the amount of light (the radiant exposure) matters to get adequate cure. Intuitively, a higher lamp power will speed up the photo-curing process. Nonetheless, some studies have found that the marginal adhesion between the composite and the teeth may have better integrity at lower curing rates [18,41–44]. Others have shown that reducing the curing rate produces less contraction stress within the composite [43,45], providing an explanation for the improved marginal integrity [46]. Other issues that may be of concern to the dentist include the temperature changes in the materials, the wear breakage issue, and the ease of staining issue, etc.

Fortunately, the DMC model is able to track the light distribution as a function of illumination time. This model can actually help with the shrinkage and marginal adhesion problem. Since the time-resolved radiant exposure can be predicted, we can predict the amount of shrinkage by integrating the information of radiant exposure – shrinkage relationship. We can even add a "dynamic" voxel size feature to the model or combine the model with the finite-element analysis technique [148] to predict the amount of shrinkage and the direction of shrinkage.

The measurements of the optical property changes to the radiant exposures can be tedious and prone to yield experimental errors. Moreover, the IAD program used to extract the absorption and scattering coefficients assumes the optical properties within the composite slab are homogenous, which is not true. This problem can be improved by measuring a thin composite sample. The DMC model can help predict the inhomogeneity thereby providing the optimal thickness for the experiment.

In conclusion, I have shown that the light transport theory can be a useful tool to study the relationship between the curing extent of a composite and the radiant exposure, to improve understanding the relationship between photo-initiated chemical reaction and the physical performance of the materials, and ultimately to suggest ways to improve the photo-curing efficiency of a composite system.

Appendix A

Layer Monte Carlo program by Prahl

This program will calculate the reflected and transmitted light from a layered medium. The total amount of light deposited in each layer is also calculated. This is a very simple implementation that should be suitable for adapting to different problems.

One important assumptions in this program are that the medium in uniform in the x and y directions. This means that the x and y coordinates of the photon do not need to be calculated. This dramatically simplies the number of calculations required to propagate a photon through a bunch of unchanging optical layers.

Output from this program can be tested using the adding-doubling method. For example, if we define the total reflected light for collimated illumination as

$$\text{UR1Layers}[\{\mu_a, \ldots\}, \{\mu_s, \ldots\}, \{g, \ldots\}, \{d, \ldots\}, n_{\text{slab}}]$$

of a layered slab with absorption coefficents $\mu_a, \ldots$, scattering coefficients $\mu_s, \ldots$, anisotropies $g, \ldots$, and thicknesses $d, \ldots$. The index of refraction of each layer in the slab is n_{slab}.

$$\begin{aligned} \text{UR1Layers}[\{1, 0.7, 1\}, \{19, 3.3, 19\}, \{0.8, 0.8, 0.8\}, \{0.01, 0.53, 0.06\}, 1.5] &= 0.09440 \\ \text{UT1Layers}[\{1, 0.7, 1\}, \{19, 3.3, 19\}, \{0.8, 0.8, 0.8\}, \{0.01, 0.53, 0.06\}, 1.5] &= 0.30962 \end{aligned}$$

Another test is

$$\begin{aligned} \text{UR1Layers}[\{1, 2, 0.1\}, \{10, 20, 20\}, \{0.8, 0.8, 0.8\}, \{0.1, 0.3, 0.6\}, 1.0] &= 0.15954 \\ \text{UT1Layers}[\{1, 2, 0.1\}, \{10, 20, 20\}, \{0.8, 0.8, 0.8\}, \{0.1, 0.3, 0.6\}, 1.0] &= 0.06949 \end{aligned}$$

```
Layered Monte Carlo by Scott Prahl (http://omlc.ogi.edu)
1 W/cm^2 Uniform Illumination of Layered Medium

Anisotropy =    0.800
Refr Index =    1.500
Photons    =  1000000

Specular Refl      =    0.04000
Backscattered Refl =    0.05438
Total Reflection   =    0.09438
Total Transmission =    0.30968

   depth    mu_a     mu_s      g       tau      Heat
   [cm]    [1/cm]   [1/cm]    [-]      [-]     [W/cm^3]
   0.010    1.000   19.000    0.800    0.200    1.550
   0.530    0.700    3.300    0.800    2.320    0.949
   0.060    1.000   19.000    0.800    3.520    1.290
```

Figure A.1: Sample output from the program.

```
char  t1[80] = "Layered Monte Carlo by Scott Prahl (http://omlc.ogi.edu)";
char  t2[80] = "1 W/cm^2 Uniform Illumination of Layered Medium";

#include <stdio.h>
#include <stdlib.h>
#include <math.h>

#define LAYERS 3
#define RANDOM random()
#define RANDOMIZE srandomdev()

long  layer, photons = 1000000;
double zeta,u,v,w,weight;
double n, rs, rd, td, bit, crit_angle, total_tau;
double heat[LAYERS], mu_a[LAYERS], mu_s[LAYERS], absorption[LAYERS];
double tau[LAYERS], thickness[LAYERS], g[LAYERS];

double random01(void)
{
    return ((double)RANDOM/(double)RAND_MAX);
}

/* Start the photon */
void launch(void)
{
    zeta = 0.0;
    u = 0.0; v = 0.0; w = 1.0;
    weight = 1.0 - rs;
}

/* Interact photon with top or bottom surface */
void bounce (void)
{
double ww;

    ww = fabs(w);
    if (ww > crit_angle) {
        double t      = sqrt(1.0-n*n*(1.0-w*w));          /* cos of exit angle */
        double temp1 = (ww - n*t)/(ww + n*t);
        double temp = (t - n*ww)/(t + n*ww);
        double exiting = (1.0-(temp1*temp1+temp*temp)/2.0) * weight; /* weight exiting */
        if (w<0) rd += exiting; else td += exiting;
        weight -= exiting;
    }
```

```
    if (w<0)  /* set bounced photon position */
        zeta = −zeta;
    else
        zeta = 2*total_tau − zeta;

    w = −w;  /* set bounced photon direction */
}

/* move photon to next scattering event */
void move(void)
{
    double d;
    long x;
    do {x=RANDOM;} while (x==0);
    d= −log((double)x/(double)RAND_MAX); /* in mfp's */

    zeta += d * w;

    while ( zeta<=0 || zeta>=total_tau ) bounce();

    /* discover which layer we are now in */
    layer=0;
    while (tau[layer]<zeta && layer<LAYERS) layer++;
}

/* absorb some of the photon packet at current location */
void absorb(void)
{
    double abs = weight * absorption[layer];
    heat[layer] += abs;
    weight      −= abs;
}

/* play roulette to terminate photon packet*/
void roulette(void)
{
    if (weight > 0.001) return;
    bit −= weight;
    if (random01() > 0.1) weight = 0; else weight /= 0.1;
    bit += weight;
}
```

```
 /* Scatter photon and establish new photon direction */
 void scatter(void)
{                                                                          90
double x1, x2, x3, t, mu, gg=g[layer];

    for(;;) {                              /*new direction*/
        x1=2.0*random01() - 1.0;
        x2=2.0*random01() - 1.0;
        if ((x3=x1*x1+x2*x2)<=1) break;
    }
    if (gg==0) { /* isotropic */
        u = 2.0 * x3 -1.0;
        v = x1 * sqrt((1-u*u)/x3);                                         100
        w = x2 * sqrt((1-u*u)/x3);
        return;
    }

    mu = (1-gg*gg)/(1-gg+2.0*gg*random01());
    mu = (1 + gg*gg-mu*mu)/2.0/gg;
    if ( fabs(w) < 0.9 ) {
        t = mu * u + sqrt((1-mu*mu)/(1-w*w)/x3) * (x1*u*w-x2*v);
        v = mu * v + sqrt((1-mu*mu)/(1-w*w)/x3) * (x1*v*w+x2*u);
        w = mu * w - sqrt((1-mu*mu)*(1-w*w)/x3) * x1;                      110
    } else {
        t = mu * u + sqrt((1-mu*mu)/(1-v*v)/x3) * (x1*u*v + x2*w);
        w = mu * w + sqrt((1-mu*mu)/(1-v*v)/x3) * (x1*v*w - x2*u);
        v = mu * v - sqrt((1-mu*mu)*(1-v*v)/x3) * x1;
    }
    u = t;
}
```

```
/* Print the results */
void print_results(void)
{
int i;
    printf("%s\n%s\n\n",t1,t2);
    printf("Anisotropy = %8.3f\nRefr Index = %8.3f\nPhotons = %8ld",g[layer],n,photons);
    printf("\n\nSpecular Refl  = %10.5f\nBackscattered Refl = %10.5f",rs,rd/(bit+photons));
    printf("\nTotal Reflection = %10.5f",rs+rd/(bit+photons));
    printf("\nTotal Transmission = %10.5f",td/(bit+photons));
    printf("\n\n depth   mu_a    mu_s     g      tau     Heat");
    printf("\n  [cm]   [1/cm]  [1/cm]   [-]     [-]    [W/cm^3]\n");

    for (i=0; i<LAYERS; i++){
        printf("%8.3f %8.3f %8.3f %8.3f", thickness[i], mu_a[i], mu_s[i], g[i]);
        printf(" %8.3f %8.3f\n", tau[i], heat[i]/thickness[i]/(bit+photons));
    }
}
```

```
int main (void)
{
long i;
                                                                        140
    RANDOMIZE;
    n=1.5;
    rs = (n−1.0)*(n−1.0)/(n+1.0)/(n+1.0); /* specular reflection */
    crit_angle = sqrt(1.0−1.0/n/n);       /* cos of critical angle */
    mu_a[0]=1.0; mu_s[0]=19.0; g[0]=0.8; thickness[0] = 0.01;
    mu_a[1]=0.7; mu_s[1]= 3.3; g[1]=0.8; thickness[1] = 0.53;
    mu_a[2]=1.0; mu_s[2]=19.0; g[2]=0.8; thickness[2] = 0.06;

    total_tau = 0;
    for(i=0; i<LAYERS; i++) {                                           150
        double t     = thickness[i]*(mu_s[i]+mu_a[i]);
        absorption[i] = mu_a[i]/(mu_s[i]+mu_a[i]);
        heat[i]       = 0;
        tau[i]        = total_tau+t;
        total_tau    += t;
    }

    for (i = 1; i <= photons; i++){
        launch ();
        while (weight > 0) {                                            160
            move ();
            absorb();
            roulette ();
            scatter ();
        }
    }
    print_results();
    return 0;
}
```

Appendix B

Dynamic Monte Carlo program by Chen

This program will calculate the time-dependent diffuse reflectance and transmittance of light from a slab medium with dynamic absorption and scattering coefficients. The time-dependent energy deposition and the absorption and scattering coefficients in each voxel are also calculated.

To start, the values of the parameters corresponding to the medium of interest need to be initialized. One can reset the values of the following parameters in the program.

1. At the program start

   The length, width, and height of the slab sample.

   The number of voxels in x, y, z dimensions.

   The profiles (power, diameter, and central position) of the illumination beam.

   The illumination time per data recording. For example, if you want to record the data every 5 seconds of light illumination, you input `period=5.0`.

   The number of times you want to record the data. For example, if you want to record the data for a total of 2 times, you input `record=2`. Note that each time is `period = 5` second.

   The number of photons for *each period of time*. Note that the total number of photons launched will be "Nphotons $\times$ record". For example, "`Nphotons = 500000`" means that every 500,000 photons the data will be recorded and this corresponds to 5 seconds of illumination if `period=5.0`. Therefore, the total number of photons launched is 1,000,000 if `record=2`.

2. In the `initialize_medium()` subroutine:

The initial optical properties (absorption and scattering coefficients and anisotropy) of each voxel can be explicitly specified here.

3. In the `change_mu()` subroutine:

   The relationship between the optical properties of the materials and the radiant exposures is specified here. In the following program, equations, Eq. 8.9 and 8.10, were used.

The photon's bin number and the boundary conditions were dealt with in `handle_boundaries()`. One may notice that the bin number was calculated by (`(int) (x*10000) / (xbin_size*10000)`). This `10000` was multiplied to avoid computational rounding errors. For positive values, the `(int)` type-case is similar to the function `(floor)`. For some values the computer encountered rounding errors: for example, `(int)0.0725/0.025` equaled to `28`, not `29`, as calculated by the computer.

Two subroutines `find_dv()` and `find_s1()` will calculate the stepsize of the photon movement. Subroutine `find_dv()` first finds out the length of the segment dv as shown in Fig. 8.3(b) or 8.4. This subroutine calculates the azimuthal angle δ between x-axis and the segment from the photon's current position to the corner of the voxel and compares photon's azimuthal angle φ and δ to find the next wall the photon can possibly reach. There are four parts (`if, else if, ....`) in this subroutine, which corresponds to the four regions: I, II, III, and IV.

Subroutine `find_s1()` will then calculate the final stepsize $s1$ of the photon movement, which corresponds to Fig. 8.3 (c). This subroutine calculates the polar angle θ between z-axis and the segment from the photon's current position to the corner of the voxel and compares photon's polar angle α and θ to find the next plane the photon will reach.

The output of this program is made in two subroutines, `print_results()` and `save()`. These two subroutines can be integrated into one `save()` subroutine if one prefers saving all the data into files. The only reason I separated them was that I preferred the data to be shown on the screen and I was interested in observing the changes of the total reflectance (`R`), the transmittance (`T`), the optical properties and the energy deposition of the medium. The time-resolved reflectance and transmission images may as well be useful

information so I saved them into files. One can easily change the format of the output to adapt to different problems.

1. `print_results()` prints data to the screen at each data recording. This subroutine prints the absorption and scattering coefficients along the depths at the center (width/2 and length/2) of the medium and the deposited energy density along the central cross section of the medium. The format of the output was designed in such a way that the data could be easily processed by a `MatLab` program.

2. `save()` saves the time-resolved reflectance and transmission arrays from the slab medium to files.

The following figure is an example of the output data on the screen (Fig. B.1). It shows the starting time of the program, simple information about the simulation, and then the data arrays: the absorption (`mua`) and scattering (`mus`) coefficients of the 5 depths at the center ($x = 1.4\,\text{cm}$ and $y = 1.4\,\text{cm}$) of the medium, the energy density `Wt` array of the 14 voxels in the y-axis versus the 5 depths at $x = 1.4\,\text{cm}$. The bin size here is $0.2\times0.2\times0.02\,[\text{cm}^3]$. Following the arrays are the total `R` and `T` for each recording. Finally it shows the total computer processing time and the time when the program was finished.

```
Mon Jan 17 15:50:08 2005

Dynamic Monte Carlo by Yin-Chu Chen
135 mW, 2 cm diameter beam on (2.8 by 2.8 by .1) cm^3 Medium
RECORD every  5 sec of illumination, starting from time = 0 sec.

 mu_a(:,1)=[    4.46    4.46    4.46    4.46    4.46    ]';     [cm^-1]
 mu_s(:,1)=[    30.50   30.50   30.50   30.50   30.50   ]';     [cm^-1]
 Wt(:,:,1)=[
0.0000  0.0000  0.0000  0.0000  0.0000  0.0000  0.0000  0.0000  0.0000  0.0000  0.0000  0.0000  0.0000  0.0000
0.0000  0.0000  0.0000  0.0000  0.0000  0.0000  0.0000  0.0000  0.0000  0.0000  0.0000  0.0000  0.0000  0.0000
0.0000  0.0000  0.0000  0.0000  0.0000  0.0000  0.0000  0.0000  0.0000  0.0000  0.0000  0.0000  0.0000  0.0000
0.0000  0.0000  0.0000  0.0000  0.0000  0.0000  0.0000  0.0000  0.0000  0.0000  0.0000  0.0000  0.0000  0.0000
0.0000  0.0000  0.0000  0.0000  0.0000  0.0000  0.0000  0.0000  0.0000  0.0000  0.0000  0.0000  0.0000  0.0000
];      [J/cm^3]
R(1)= 0.043884; T(1) = 0.000000;
 mu_a(:,2)=[    4.39    4.41    4.42    4.44    4.44    ]';     [cm^-1]
 mu_s(:,2)=[    23.67   25.22   26.56   27.83   28.50   ]';     [cm^-1]
 Wt(:,:,2)=[
0.0003  0.1184  2.7296  2.8714  2.8875  2.8331  2.9386  2.9356  2.8794  2.8821  2.8773  2.6529  0.1219  0.0004
0.0003  0.1089  1.9955  2.0672  2.1446  2.1200  2.1492  2.1414  2.1223  2.1577  2.0643  1.9254  0.0975  0.0001
0.0004  0.0945  1.3551  1.4777  1.4700  1.4709  1.4730  1.5322  1.4760  1.5061  1.4363  1.2948  0.0786  0.0002
0.0003  0.0723  0.8928  1.0061  1.0186  0.9891  0.9932  0.9963  1.0146  1.0059  0.9727  0.8797  0.0664  0.0003
0.0002  0.0572  0.5989  0.6906  0.6928  0.6874  0.6964  0.7333  0.7207  0.6901  0.6596  0.5964  0.0597  0.0004
];      [J/cm^3]
R(2)= 0.160168; T(2) = 0.080221;
 mu_a(:,3)=[    4.33    4.36    4.39    4.41    4.42    ]';     [cm^-1]
 mu_s(:,3)=[    19.78   21.63   23.50   25.39   26.54   ]';     [cm^-1]
 Wt(:,:,3)=[
0.0006  0.2279  5.1836  5.4613  5.4849  5.4046  5.4952  5.4861  5.4483  5.4622  5.4803  5.1172  0.2377  0.0005
0.0005  0.2192  3.8891  4.0923  4.1646  4.1438  4.1331  4.1465  4.1181  4.1377  4.1132  3.8061  0.2031  0.0006
0.0005  0.1918  2.7569  2.9607  2.9826  2.9433  2.9915  3.0265  2.9784  2.9999  2.9807  2.6633  0.1726  0.0008
0.0005  0.1443  1.8768  2.0675  2.1169  2.0512  2.0513  2.0633  2.0836  2.0667  2.1099  1.8363  0.1364  0.0006
0.0005  0.1191  1.2999  1.4867  1.4977  1.5027  1.4726  1.5396  1.5266  1.4760  1.4689  1.2895  0.1255  0.0007
];      [J/cm^3]
R(3)= 0.156736; T(3) = 0.089665;
---------------------------------------------------------------------
Elapsed Time  = 219.210000 s
Mon Jan 17 15:54:14 2005
```

Figure B.1: Sample output from Chen's DMC program.

```
/* DMC.c : This program was written by Yin-Chu Chen in 2004. */
/* The origin (0,0,0) is located at the corner of the sample. */

char t1[80] = "Dynamic Monte Carlo by Yin-Chu Chen";
char t2[80] = "135 mW, 2 cm diameter beam on (2.8 by 2.8 by .1) cm^3 Medium";

#include <stdio.h>
#include <stdlib.h>
#include <math.h>
#include <time.h>
#include <string.h>

#define PI 3.1415926

#define X_NBIN 14 /* number of bins in x dimension, needs to be an even number */
#define Y_NBIN 14 /* number of bins in y dimension, needs to be an even number */
#define Z_NBIN 5 /* number of bins in z dimension */
#define RECORD 2 /* number of time of recording of data */

double length=2.8, width=2.8, depth=0.10; /*dimensions of the sample [cm]*/
double bin_volume, xbin_size, ybin_size, zbin_size;

double period=5.0;       /* time of illumination for each data recording [sec]*/
double beam_power = 0.135; /* power of the illumination beam [W] */
double beam_center = 1.4;  /* center of the illumination beam [cm] */
double beam_diameter = 2; /* diameter of the beam [cm] */

/* Propagation parameters */
long   Nphotons = 500000; /* number of photons per data recording */
long   iphoton;
double x, y, z;          /* photon position */
double ux, uy, uz;       /* photon trajectory */
double w, w_extra;       /* photon weight and weight lost via roulette */
double surface_reflection; /* weight lost entering medium */
double critical_cosine;    /* cosine of the critical angle in the medium */

double absorbed[X_NBIN+1][Y_NBIN+1][Z_NBIN]; /*the extra bin is for overflow photons*/
double rb[X_NBIN+1][Y_NBIN+1];
double Rt[X_NBIN+1][Y_NBIN+1][RECORD+1];
double tm[X_NBIN+1][Y_NBIN+1];
double Tt[X_NBIN+1][Y_NBIN+1][RECORD+1];

double mu_a[X_NBIN+1][Y_NBIN+1][Z_NBIN];
double mu_s[X_NBIN+1][Y_NBIN+1][Z_NBIN];
```

```
double g[X_NBIN+1][Y_NBIN+1][Z_NBIN];
double n; /* index of refraction of the media */

double tau, dv, dz, s1, s2;   /* parameters for step sizes [cm] */
int     xbin_start, ybin_start, zbin_start;  /* indicies for photon position */
int     xbin, ybin, zbin;                    /* indicies for photon position */
int     move, moveplane;
int     nt;

int  randm(void)
{
    int   rnd = rand();
    while (rnd == 0)
        rnd = rand();
    return rnd;
}

/* initialize the medium's optical properties */
void initialize_medium(void)
{
    int     i,j,k;
    n = 1.53;
    for (i=0; i<= X_NBIN; i++)
        for (j=0; j<= Y_NBIN; j++)
            for (k=0; k< Z_NBIN; k++)
            {
                mu_a[i][j][k] = 4.46;
                mu_s[i][j][k] = 30.5;
                g[i][j][k] = 0.0;
            }
}
```

```
/*launch the photon*/
void launch(void)
{
    double tempx, tempy;

    tempx = (float) rand()/RAND_MAX - 0.5;
    tempy = (float) rand()/RAND_MAX - 0.5;

  /*photon position is between -0.5 to +0.5 cm*/
    while ( (tempx*tempx+tempy*tempy) > 0.25)
        {
        tempx = (float) rand()/RAND_MAX - 0.5;
        tempy = (float) rand()/RAND_MAX - 0.5;
        }

    /*the center of the light beam is at (0+beam_center,0+beam_center,0). */
    x = tempx*beam_diameter + beam_center; /*scale the dimension of the beam & relocate*/
    y = tempy*beam_diameter + beam_center;
    z = 0.0;

    ux = 0.0;  /*direction of the photon*/
    uy = 0.0;
    uz = 1.0;
    w = 1.0 - surface_reflection;
    dz = zbin_size;
}
```

```
/*Photons interact with top or bottom surface*/
void bounce(void)
{
    double exit_angle, temp1, temp2, rf, deposited;
    double abs_uz = fabs(uz);

    if ( abs_uz > critical_cosine)                                    110
    {   /*assume outside the boundary is air*/
        exit_angle = sqrt( 1.0 - n*n*(1.0-abs_uz*abs_uz) );
        temp1 = (abs_uz - n*exit_angle) / (abs_uz + n*exit_angle);
        temp2 = (exit_angle - n*abs_uz) / (exit_angle + n*abs_uz);
        rf = (temp1*temp1+temp2*temp2) / 2.0; /* Fresnel Reflectance */

        deposited = (1.0-rf) * w;
        if (uz < 0)
            rb[xbin_start][ybin_start] += deposited;
        else                                                          120
            tm[xbin_start][ybin_start] += deposited;

        w  -= deposited;
    }

    if (uz < 0) /* set bounced photon position */
        z = -z;
    else
        z = 2*depth - z; /*bound back from the bottom*/
                                                                      130
    uz = -uz; /* set bounced photon direction */

}
```

```
/* calculate photon's bin number and check if photon outside the boundary */
void handle_boundaries(void)
{
    xbin_start = (int)((x*10000) / (xbin_size*10000));
    ybin_start = (int)((y*10000) / (ybin_size*10000));
    zbin_start = (int)((z*10000) / (zbin_size*10000));

    /*if the photon is outside the x-y boundary, terminate the photon*/
    if (xbin_start >= X_NBIN)
    {
        xbin_start = X_NBIN;
        absorbed[xbin_start][ybin_start][zbin_start] += w;
        w = 0.0;
    }
    else if (x <= 0)
    {
        xbin_start = 0;
        absorbed[xbin_start][ybin_start][zbin_start] += w;
        w = 0.0;
    }

    if (ybin_start >= Y_NBIN)
    {
        ybin_start = Y_NBIN;
        absorbed[xbin_start][ybin_start][zbin_start] += w;
        w = 0.0;
    }
    else if (y <= 0)
    {
        ybin_start = 0;
        absorbed[xbin_start][ybin_start][zbin_start] += w;
        w = 0.0;
    }

    /*if the photon hits the top or the bottom of the boundary*/
    if (z <= 0 )
    {   zbin_start = 0;
        bounce();
    }
    else if (z >= depth)
    {
        zbin_start = Z_NBIN-1;
        bounce();
    }
}
```

```
/* calculate the segment dv as shown in Fig. 8.3(b) or Fig. 8.4 */
void find_dv(void)
{
    double dx1, dx2, dy1, dy2;
    double delta, cosphi, sinphi; /* cos(phi), sin(phi) */

    dx1 = (xbin_start+1) * xbin_size - x;
    dy1 = (ybin_start+1) * ybin_size - y;
    dx2 = x - (xbin_start) * xbin_size;
    dy2 = y - (ybin_start) * ybin_size;                                    190
    cosphi = ux / sqrt(ux*ux + uy*uy);
    sinphi = uy / sqrt(ux*ux + uy*uy);
    xbin = xbin_start;
    ybin = ybin_start;
    zbin = zbin_start;

    if (dx2 == 0)
        dx2 = xbin_size;       /* at plane 3 already */

    if (dy2 == 0)                                                          200
        dy2 = ybin_size;       /* at plane 4 already */

    if (ux == 0 && uy == 0)
        dv = 0.0;              /* moving only along z */
    else if (ux >= 0 && uy >= 0) /* if REGION I, like Fig. 8.3(b) */
    {
        delta = atan(dy1/dx1);
        if (acos(cosphi) <= delta)
        {
            dv = dx1 / cosphi;                                             210
            moveplane = 1;
        }
        else
        {
            dv = dy1 / sinphi;
            moveplane = 2;
        }
    }

    else if (ux <= 0 && uy >= 0) /* if REGION II, Fig. 8.4 */              220
    {
        delta = atan(dy1/dx2);
        if (( PI-acos(cosphi) ) <= delta)
        {
            dv = -dx2 / cosphi;
            moveplane = 3;
```

```
        }
        else
        {
            dv = dy1 / sinphi;                                          230
            moveplane = 2;
        }
        if (dx2 == xbin_size) /* move into (xbin_start-1) voxel from plane 3 */
            xbin = xbin_start−1;
    }
    else if (ux <= 0 && uy <= 0) /* if REGION III */
    {
        delta = atan(dy2/dx2);
        if (( PI−acos(cosphi) ) <= delta)
        {                                                               240
            dv = −dx2 / cosphi;
            moveplane = 3;
        }
        else
        {
            dv = −dy2 / sinphi;
            moveplane = 4;
        }
        if (dx2 == xbin_size) /* move into (xbin_start-1) voxel from plane 3 */
            xbin = xbin_start−1;                                        250
        if (dy2 == ybin_size) /* move into (ybin_start-1) voxel from plane 4 */
            ybin = ybin_start−1;

    }
    else                            /* if REGION IV */
    {
        delta = atan(dy2/dx1);
        if (( acos(cosphi) ) <= delta)
        {
            dv = dx1 / cosphi;                                          260
            moveplane = 1;
        }
        else
        {
            dv = −dy2 / sinphi;
            moveplane = 4;
        }
        if (dy2 == ybin_size) /* move into (ybin_start-1) voxel from plane 4 */
            ybin = ybin_start−1;
    }                                                                   270

}
```

```
/* calculate photon's final stepsize s1 and decide which wall of the voxel to go
   as shown in Fig. 8.3 */
void find_s1(void)
{
    if (uz == 0)       /* only move in x-y plane */
        dz = 0.0;
    else if (uz > 0)  /* move up */ /* pointing straight up to plane 5 */                    280
    {
        dz = (zbin_start+1) *zbin_size - z;
    }
    else               /* move down */
    {
        dz = z - zbin_size *(zbin_start);
        if (dz==0)     /* photon already at plane 6 */
        {   dz = zbin_size;
            zbin = zbin_start-1;         /* move into (zbin_start-1) voxel from plane 6 */
        }                                                                                   290
    }

    if (dv == 0)           /* only move in z-axis */
    {
        move = 2;          /* photon hit top or bottom wall of the voxel first */
        s1 = dz;
    }
    else if (dz==0)        /* only move in x-y plane */
    {
        move = 1;          /* photon hit side wall of the voxel first */                    300
        s1 = dv;
    }
    else
    {
        if ( asin( fabs(uz) ) < atan(dz/dv) ) /* photon hit side wall of the voxel first */
        {
            s1 = dv / cos( asin(uz) );
            move = 1;
        }
        else               /* photon hit top or bottom wall of the voxel first */          310
        {
            s1 = dz / fabs(uz);
            move = 2;
        }
    }
}
```

```
/* Roulette method to terminate the photon */
void check_status(void)
{                                                                    320
    if ( w < 0.001)
    {
        w_extra -= w;
        if (rand() > 0.1*RAND_MAX)
            w = 0;
        else
            w /= 0.1;
        w_extra += w;
    }
}                                                                    330

/* set the trajectory for next scattering event */
void spin()
{
    double x1, x2, x3, t, mu, trnd, tmp;

    x1 = 2.0 * (float) rand()/RAND_MAX - 1.0;
    x2 = 2.0 * (float) rand()/RAND_MAX - 1.0;
    x3 = x1*x1 + x2*x2;
    while (x3 > 1)                                                   340
    {   x1 = 2.0 * (float) rand()/RAND_MAX - 1.0;
        x2 = 2.0 * (float) rand()/RAND_MAX - 1.0;
        x3 = x1*x1 + x2*x2;
    }

    if (g[xbin][ybin][zbin]==0) /* isotropic */
    {   ux = 2.0 * x3 - 1.0;
        uy = x1 * sqrt( (1-ux*ux) / x3);
        uz = x2 * sqrt( (1-ux*ux) / x3);
        return;                                                      350
    }

    trnd = (float)rand()/RAND_MAX;
    mu = (1.0-g[xbin][ybin][zbin]*g[xbin][ybin][zbin]) / \
         (1.0 - g[xbin][ybin][zbin] + 2.0*g[xbin][ybin][zbin]* trnd);
    mu = (1.0 + g[xbin][ybin][zbin]*g[xbin][ybin][zbin] - mu*mu) / 2.0/g[xbin][ybin][zbin];

    if ( fabs(uz) < 0.9 )
    {
        tmp = sqrt( (1-mu*mu)/(1-uz*uz)/x3 );                        360
        t = mu*ux + tmp * (x1*ux*uz - x2*uy);
        uy = mu*uy + tmp * (x1*uy*uz + x2*ux);
        uz = mu*uz - sqrt( (1-mu*mu)*(1-uz*uz)/x3 ) * x1;
```

```
    }
    else
    {
        tmp = sqrt( (1−mu*mu)/(1−uy*uy)/x3 );
        t = mu*ux + tmp * (x1*ux*uy + x2*uz);
        uz = mu*uz + tmp * (x1*uy*uz − x2*ux);
        uy = mu*uy − sqrt( (1−mu*mu)*(1−uy*uy)/x3 ) * x1;
    }
    ux = t;
}

/* change the optical properties of the voxel */
void change_mu(void)
{
    double E = beam_power * period; /* the delivered energy per period of recording time [J]*/
    double  Hdp;

    /* convert weight to radiant exposure [J/cm2] */
    Hdp = E* absorbed[xbin][ybin][zbin]/((float)Nphotons)/bin_volume /mu_a[xbin][ybin][zbin];

    /* relationship between material's optical properties and radiant exposure */
    mu_a[xbin][ybin][zbin] = 4.46 * exp(−Hdp / 43.0);
    mu_s[xbin][ybin][zbin] = 18.0 * exp(−Hdp / 1.4) + 12.5;
}

/*save the transmission and refelctance images of the surface*/
void save(void)
{
    long in, jn, kn;
    FILE* target;

    /*save transmission as a function of illumination time into file*/
    target = fopen("t135mw.txt", "w");
    for (in=0;in<=RECORD;in++)
    {
        for (jn=0;jn<= Y_NBIN; jn++)
        {   for (kn=0; kn<= X_NBIN; kn++)
                fprintf(target,"%2.5f \t",Tt[kn][jn][in]);
            fprintf(target,"\n");
        }
        fprintf(target,"\n");
    }
    fclose(target);

    /*save reflectance as a function of illumination time into file*/
    target = fopen("r135mw.txt", "w");
```

```
    for (in=0;in<=RECORD;in++)
    {
        for (jn=0;jn<= Y_NBIN; jn++)
        {   for (kn=0; kn<= X_NBIN; kn++)
                fprintf(target,"%2.5f \t",Rt[kn][jn][in]);
            fprintf(target,"\n");
        }
        fprintf(target,"\n");
    }
    fclose(target);
}

/* print results (mua, mus, energy density, total R, T) on the screen */
void print_results(void) /* print results for each recording */
{
    int     k,l;
    double trb=0.0, ttm=0.0;
    printf("\n mu_a(:,%d)=[\t", nt+1);
    for (k=0; k< Z_NBIN; k++)
        printf("%2.2f\t", mu_a[X_NBIN/2][Y_NBIN/2][k]);
    printf("]';\t[cm^-1]");
    printf("\n mu_s(:,%d)=[\t", nt+1);
    for (k=0; k< Z_NBIN; k++)
        printf("%2.2f\t",mu_s[X_NBIN/2][Y_NBIN/2][k]);
    printf("]';\t[cm^-1]");
    printf("\n Wt(:,:,%d)=[\n", nt+1);
    for (k=0; k< Z_NBIN; k++)
    {   for (l=0; l< Y_NBIN; l++)
            printf("%2.4f\t", absorbed[X_NBIN/2][l][k]/(w_extra+Nphotons)/bin_volume * beam_power * period);
        printf("\n");
    }
    printf("];\t[J/cm^3]");
    for (k=0; k<= Y_NBIN; k++)
    {   for (l=0;l<=X_NBIN; l++)
        {   /* printf("%2.5f \t",tm[l][k]/(iphoton+1)); */
            trb += rb[l][k];
            ttm += tm[l][k];
        }
        /* printf("\n"); */
    }
    printf("\nR(%d)= %1.6f;\t",nt+1, trb/(w_extra+(iphoton+1)) + surface_reflection );
    printf("T(%d) = %1.6f; ",nt+1, ttm/(w_extra+(iphoton+1)) );
}
```

```
int main(void)
{
    double start_time, finish_time;  /* for clock() */
    time_t now;
    int     kn, jn;

    start_time = clock();                                                    460
    now = time(NULL);
    printf("%s\n", ctime(&now)); /* show clock time when program starts */

    xbin_size = length / X_NBIN;
    ybin_size = width / Y_NBIN;
    zbin_size = depth / Z_NBIN;
    bin_volume = xbin_size * ybin_size * zbin_size;

    initialize_medium();
    surface_reflection = (n - 1.0) * (n - 1.0) / (n + 1.0) / (n + 1.0); /* assume the top is air */   470
    critical_cosine = sqrt(1.0 - 1.0/n/n);
    /* srand( (unsigned)time( NULL ) ); */
    nt=0;
    printf("%s\n%s\n",t1,t2);
    printf("RECORD every %2.0f sec of illumination, starting from time = 0 sec.\n",period);

    for (iphoton=0; iphoton< (Nphotons*RECORD); iphoton++)
    {
        launch();
        /*calculate the initial position of the photon*/                       480
        xbin_start = (int)((x*10000) / (xbin_size*10000));
        ybin_start = (int)((y*10000) / (ybin_size*10000));
        zbin_start = (int)((z*10000) / (zbin_size*10000));

        if ( (iphoton % Nphotons ) == 0)
        {
            /* printf("%ld photons are launched\n",iphoton+1); */
            print_results();

            /*save the transmission image at dif. recording time into an array*/   490
            for (kn=0; kn<= X_NBIN; kn++)
                for (jn=0;jn<= Y_NBIN; jn++)
                    Tt[kn][jn][nt] = tm[kn][jn]/(w_extra+(float)(iphoton+1));

            /*save the reflectance image at dif. recording time into an array*/
            for (kn=0; kn<= X_NBIN; kn++)
                for (jn=0;jn<= Y_NBIN; jn++)
                    Rt[kn][jn][nt] = rb[kn][jn]/(w_extra+(float)(iphoton+1));
```

```
    nt += 1;                                                                    500
}

while (w > 0)
{
    double temp_w;
    tau = −log((float) randm()/RAND_MAX);
    find_dv();
    find_s1();

    while (tau > (s1 * mu_s[xbin][ybin][zbin]) && w > 0)                        510
    {
        tau −= s1 * mu_s[xbin][ybin][zbin];
        x += s1*ux;
        y += s1*uy;
        z += s1*uz;

        temp_w = w * exp( −mu_a[xbin][ybin][zbin]*s1 ) ;
        absorbed[xbin][ybin][zbin] += (w − temp_w);
        w = temp_w;
        change_mu();                                                            520

        if (move == 1) /* photon hit side wall of the voxel */
        {
            /* recalculate the position to fix the rounding error
            such that photon's position to be exactly at the edge of the voxel*/

            if (moveplane == 1 || moveplane == 3) /* photon hit plane 1 or 3 */
                x = ((int)(x/xbin_size+0.1))*xbin_size;
            else                                  /* photon hit plane 2 or 4 */
                y = ((int)(y/ybin_size+0.1))*ybin_size;                         530
        }
        else    /* photon hit top or bottom wall of the voxel */
            z = ((int)(z/zbin_size+0.1))*zbin_size;

        handle_boundaries();
        check_status();
        if (w > 0)
        {
            find_dv();
            find_s1();                                                          540
        }
    }   /* end of while (tau > (s1 * mu_s[xbin][ybin][zbin]) && w > 0) */

    /* take the residual step */
    if (w > 0)
```

```
            {
                s2 = tau / mu_s[xbin][ybin][zbin];
                x += s2*ux;
                y += s2*uy;
                z += s2*uz;                                                    550

                temp_w = w * exp( -mu_a[xbin][ybin][zbin]*s1);
                absorbed[xbin][ybin][zbin] += (w - temp_w);
                w = temp_w;
                change_mu();

                check_status();
                spin();
            }
            handle_boundaries();                                               560
        }   /*end of while (w > 0)*/

    }   /*end of for (iphoton=0; iphoton< (Nphotons*RECORD); iphoton++) */
    print_results();

    /*save the last transmission image into last array of Tt*/
    for (kn=0; kn<= X_NBIN; kn++)
        for (jn=0;jn<= Y_NBIN; jn++)
            Tt[kn][jn][RECORD] = tm[kn][jn]/(w_extra+(float)(Nphotons*RECORD));
    /*save the last reflectance image into last array of Rt*/                  570
    for (kn=0; kn<= X_NBIN; kn++)
        for (jn=0;jn<= Y_NBIN; jn++)
            Rt[kn][jn][RECORD] = rb[kn][jn]/(w_extra+(float)(Nphotons*RECORD));

    save();

    finish_time = clock();
    printf("\n---------------------------------------------------------------------\n");
    printf("Elapsed Time = %5.6f s\n", (double)(finish_time-start_time)/CLOCKS_PER_SEC);
    now = time(NULL);                                                          580
    printf("%s\n", ctime(&now)); /* show clock time when program finishes */

    return 0;
}
```

Bibliography

[1] K. Haupt and K. Mosbach, "Molecularly imprinted polymers and their use in biomimetic sensors," *Chem. Rev.*, vol. 100, pp. 2495–2504, 2000.

[2] S. M. Sze, *Semiconductor Sensors*. New York: John Wiley and Sons, Inc., 1994.

[3] M. G. Kuzyk, D. W. Garvey, B. K. Canfield, S. R. Vigil, D. J. Welker, J. Tostenrude, and C. Breckon, "Characterization of single-mode polymer optical fiber and electrooptic fiber devices," *Chem. Phys.*, vol. 245, pp. 327–340, 1999.

[4] N. Tanio and E. Koike, "What is the most transparent polymer?," *Polym. J.*, vol. 32, pp. 43–50, 2000.

[5] H. P. A. van den Boom, W. Li, P. K. van Bennekom, I. T. Monroy, and G. D. Khoe, "High-capacity transmission over polymer optical fiber," *IEEE J. Sel. Top. Quantum Electron.*, vol. 7, pp. 461–470, 2001.

[6] F. Svec and J. Frechet, "Continuous rods of macroporous polymer as high-performance liquid chromatography separation media," *Anal. Chem.*, vol. 64, pp. 820 – 822, 1992.

[7] R. H. F. R. W. Gymer, A. B. Holmes, J. H. Burroughes, R. N. Marks, C. Taliani, D. Bradley, D. A. Dos Santos, J. L. Bredas, M. Logdlund, and W. R. Salaneck, "Electroluminescence in conjugated polymers," *Nature*, vol. 397, pp. 121–128, 1999.

[8] A. Badano and J. Kanicki, "Monte carlo analysis of the spectral photon emission and extraction efficiency of organic light-emitting devices," *J. Appl. Phys.*, vol. 90, pp. 18271–1830, 2001.

[9] J. J. Shiang and A. R. Duggal, "Application of radiative transport theory to light extraction from organic light emitting diodes," *J. Appl. Phys.*, vol. 95, pp. 2880–2888, 2004.

[10] J. J. Shiang, T. J. Faircloth, and A. R. Duggal, "Experimental demonstration of increased organic light emitting device output via volumetric light scattering," *J. Appl. Phys.*, vol. 95, pp. 2889–2895, 2004.

[11] J. Janata, M. Josowicz, P. Vanysek, and D. M. DeVaney, "Chemical sensors," *Anal. Chem.*, vol. 70, pp. 179R – 208R, 1998.

[12] J. H. G. Steinke, I. R. Dunkin, and D. C. Sherrington, "Transparent macroporous polymer monoliths," *Macromolecules*, vol. 29, pp. 5826–5834, 1996.

[13] M. Yan and B. Harnish, "A simple method for the attachment of polymer films on solid substrates," *Adv. Mater.*, vol. 15, pp. 244–248, 2003.

[14] J. A. Burdick, A. J. Peterson, and K. S. Anseth, "Conversion and temperature profiles during the photoinitiated polymerization of thick orthopaedic biomaterials," *Biomaterials*, vol. 22, pp. 1779–1786, 2001.

[15] E. P. Allen, S. C. Bayne, A. H. Brodine, R. J. Cronin Jr, T. E. Donovan, J. C. Kois, and J. B. Summitt, "Annual review of selected dental literature: report of the committee on scientific investigation of the American academy of restorative dentistry," *Journal of Prosthetic Dentistry*, vol. 90, pp. 50–80, 2003.

[16] R. D. Pradhan, N. Melikechi, and F. Eichmiller, "The effects of irradiation wavelength bandwidth and spot size on the scraping depth and temperature rise in composite exposed to an argon laser or a conventional quartz-tungsten-halogen source," *Dent. Mater.*, vol. 18, pp. 221–226, 2002.

[17] K. D. Jandt, R. W. Mills, G. B. Blackwell, and S. H. Ashworth, "Depth of cure and compressive strength of dental composites cured with blue light emitting diodes (LEDs)," *Dent. Mater.*, vol. 16, pp. 41–47, 2000.

[18] J. B. Dennison, P. Yaman, R. Seir, and J. C. Hamilton, "Effect of variable light intensity on composite shrinkage," *The Journal of Prosthetic Dentistry*, vol. 84, pp. 499–505, 2000.

[19] W. D. Cook, "Factors affecting the depth of cure of UV-polymerized composites," *J Dent. Res.*, vol. 59, pp. 800–808, 1980.

[20] A. Uhl, R. W. Mills, and K. D. Jandt, "Photoinitiator dependent composite depth of cure and Knoop hardness with halogen and LED light curing units," *Biomaterials*, vol. 24, pp. 1787–1795, 2003.

[21] A. F. P. Turner, I. Karube, and G. S. Wilson, *Biosensors: Fundamentals and Applications*. Oxford University Press, 1990.

[22] D. R. Thevenot, K. Toth, R. A. Durst, and G. S. Wilson, "Electrochemical biosensors: Recommended definitions and classification - (technical report)," *Pure Appl. Chem.*, vol. 71, pp. 2333–2348, 1999.

[23] O. Sadik and G. G. Wallace, "Pulsed amperometric detection of proteins using antibody containing conducting polymers," *Anal. Chim. Acta.*, vol. 279, pp. 209–212, 1993.

[24] N. C. Foulds and C. R. Lowe, "Immobilization of glucose oxidase in ferrocene modified pyrrole polymers," *Anal. Chem.*, vol. 60, pp. 2473–2478, 1988.

[25] F. L. Dickert and O. Hayden, "Molecular fingerprints using imprinting techniques," *Adv. Mater.*, vol. 14, pp. 311–314, 2000.

[26] L. Stryer, *Biochemistry.* New York: W. H. Freeman and Company, 1995.

[27] A. A. Karyakin, M. Vuki, L. V. Lukachova, E. E. Karyakina, A. V. Orlov, G. P. Karpachova, and J. Wang, "Processable polyaniline as an advanced potentiometric PH transducers," *Anal. Chem.*, vol. 71, pp. 2534 – 2540, 1999.

[28] K. Bodenhofer, A. Hieriemann, J. Seemann, G. Gauglitz, B. Christian, B. Koppenhoefer, and W. Gopel, "Chiral discrimination in the gas phase using different transducers: thickness shear mode resonators and reflectometric interference spectroscopy," *Anal. Chem.*, vol. 69, pp. 3058–3068, 1997.

[29] T. D. James, K. R. A. Samankumara, and S. Shinkal, "Chiral discrimination of monosaccharides using a fluorescent molecular sensor," *Nature*, vol. 374, pp. 345–347, 1995.

[30] D. Kriz, O. Ramstrom, A. Svensson, and K. Mosbach, "Introducing biomimetic sensors based on molecularly imprinted polymers as recognition elements," *Anal. Chem.*, vol. 71, pp. 4559–4563, 1999.

[31] F. L. Dickert and M. Tortschanoff, "Molecularly imprinted sensor layers for the detection of polycyclic aromatic hydrocarbons in water," *Anal. Chem.*, vol. 71, pp. 4559–4563, 1999.

[32] A. L. Jenkins, O. M. Uy, and G. M. Murray, "Polymer-based lanthanide luminescent sensor for detection of the hydrolysis product of the nerve agent soman in water," *Anal. Chem.*, vol. 71, pp. 373 – 378, 1999.

[33] P. Turkewitsch, B. Wandelt, G. D. Darling, and W. S. Powell, "Fluorescent functional recognition sites through molecular imprinting. A polymer-based fluorescent chemosensor for aqueous cAMP," *Anal. Chem.*, vol. 70, pp. 2025 – 2030, 1998.

[34] R. Levi, S. McNiven, S. A. Piletsky, S. H. Cheong, K. Yano, and I. Karube, "Optical detection of chloramphenicol using molecularly imprinted polymers," *Anal. Chem.*, vol. 69, pp. 2017 – 2021, 1997.

[35] T. Takeuchi, T. Mukawa, J. Matsui, M. Higashi, and K. D. Shimizu, "Molecularly imprinted polymers with metalloporphyrin-based molecular recognition sites coassembled with methacrylic acid," *Anal. Chem.*, vol. 73, pp. 3869–3874, 2001.

[36] B. Wandelt, P. Turkewitsch, S. Wysocki, and G. D. Darling, "Fluorescent molecularly imprinted polymer studied by time-resolved fluorescence spectroscopy," *Polymer*, vol. 43, pp. 2777–2785, 2002.

[37] M. J. Madou, *Fundamentals of Microfabrication.* New York: CRC Press, 1997.

[38] M. D. Marazuela and M. C. Moreno Bondi, "Fiber-optic biosensors - an overview," *Anal. Bioanal. Chem.*, vol. 372(5-6), pp. 664–682, 2002.

[39] D. C. Watts, *Dental Restorative Materials. In: Materials Science and Technology: A Comprehensive Treatment, Medical and Dental Materials (D. F. Williams, editor).* Weinheim: VCH Verlagsgesellschaft GmbH, 1992.

[40] A. Knezevic, Z. Tarle, A. Meniga, J. Sutalo, G. Pichler, and M. Ristic, "Degree of conversion and temperature rise during polymerization of composite resin samples with blue diodes," *J. Oral Rehabil.*, vol. 28, pp. 586–591, 2001.

[41] B. Venhoven, A. J. de Gee, and C. L. Davidson, "Light initiation of dental resins: dynamics of the polymerization," *Biomaterials*, vol. 24, pp. 1787–1795, 2003.

[42] R. L. Sakaguchi and H. X. Berge, "Reduced light energy density decrease post-gel contraction while maintaining degree of conversion in composites," *J. Dent.*, vol. 26, pp. 695–700, 1998.

[43] B. S. Lim, J. L. Ferracane, R. L. Sakaguchi, and J. R. Condon, "Reduction of polymerization contraction stress for dental composites by two-step light-activation," *Dent. Mater.*, vol. 18, pp. 436–444, 2002.

[44] T. G. Oberholzer, C. H. Pameijer, S. R. Grobler, and R. J. Rossouw, "The effects of different power densities and method of exposure on the marginal adaptation of

four light-cured dental restorative materials," *Biomaterials*, vol. 24, pp. 3593–3598, 2003.

[45] R. R. Braga, T. J. Hilton, and J. L. Ferracane, "Contraction stress of flowable composite materials and their efficacy as stress-relieving layers," *J. Am. Dent. Assoc.*, vol. 134, pp. 721–728, 2003.

[46] J. L. Ferracane, L. L. Ferracane, and R. R. Braga, "Effect of admixed high-density polyethylene (hdpe) spheres on contraction stress and properties of experimental composites," *J. Biomed. Mater. Res. Part B*, vol. 66B, pp. 318–323, 2003.

[47] N. Emami, K. M. Söderholm, and L. A. Berglund, "Effect of light power density variations on bulk curing properties of dental composites," *J. Dent.*, vol. 31, pp. 189–196, 2003.

[48] J. L. Ferracane, "Water sorption and solubility of experimental dental composites," *Abstr. Pap. Am. Chem. Soc.*, vol. 214, pp. 142–POLY, 1997.

[49] E. Asmussen and A. Peutzfeldt, "Polymer structure of a light-cured resin composite in relation to distance from the surface," *Eur. J. Oral Sci.*, vol. 111, pp. 277–279, 2003.

[50] R. C. Jorgenson and S. S. Yee, "A fiber-optic chemical sensor based on surface-plasmon resonance," *Sens. Actuators, B – Chem.*, vol. 12, pp. 213 – 220, 1993.

[51] S. Kubitschko, J. Spinke, T. Bruckner, S. Pohl, and N. Oranth, "Sensitivity enhancement of optical immunosensors with nanoparticles," *Anal. Biochem.*, vol. 253(1), pp. 112–122, 1997.

[52] L. Lyon, M. Musick, and M. Natan, "Colloidal Au-enhanced surface plasmon resonance immunosensing," *Anal. Chem.*, vol. 70, pp. 5177 – 5183, 1998.

[53] T. E. Plowman, J. D. Durstchi, H. K. Wang, D. A. Christensen, J. N. Herron, and W. M. Reichert, "Multiple-analyte fluoroimmunoassay using an integrated optical waveguide sensor," *Anal. Chem.*, vol. 71, pp. 4344 – 4352, 1999.

[54] B. H. Schneider, E. L. Dickinson, M. D. Vach, J. V. Hoijer, and L. V. Howard, "Optical chip immunoassay for hCG in human whole blood," *Biosens. Bioelectron.*, vol. 15, pp. 597–604, 2000.

[55] S. Subrahmanyam, S. A., Piletsky, and A. P. F. Turner, "Application of natural receptors in sensors and assays," *Anal. Chem.*, vol. 74, pp. 3942 – 3951, 2002.

[56] B. M. Paddle, "Biosensors for chemical and biological agents of defence interest," *Biosens. Bioelectron.*, vol. 11, pp. 1079 – 1113, 1996.

[57] R. R. Seigel, P. Harder, R. Dahint, M. Grunze, F. Josse, M. Mrksich, and G. M. Whitesides, "On-line detection of nonspecific protein adsorption at artificial surfaces," *Anal. Chem.*, vol. 69, pp. 3321–3328, 1997.

[58] D. Kriz, O. Ramstrom, and K. Mosbach, "Molecular imprinting - new possibilities for sensor technology," *Anal. Chem.*, vol. 69, pp. A345–A349, 1997.

[59] L. Sabourin, R. J. Ansell, K. Mosbach, and I. A. Nicholls, "Molecularly imprinted polymer combinatorial libraries for multiple simultaneous chiral separations," *Anal. Commun.*, vol. 35, pp. 285–287, 1998.

[60] E. H. M. Koster, C. Crescenzi, W. den Hoedt, K. Ensing, and G. J. de Jong, "Fibers coated with molecularly imprinted polymers for solid-phase microextraction," *Anal. Chem.*, vol. 10, pp. 927–928, 1995.

[61] A. Kugimiya and T. Takeuchi, "Surface plasmon resonance sensor using molecularly imprinted polymer for detection of sialic acid," *Biosens. Bioelectron.*, vol. 16, pp. 1059–1062, 2001.

[62] F. L. Dickert, O. Hayden, and K. P. Halikias, "Synthetic receptors as sensor coatings for molecules and living cells," *Analyst*, vol. 126, pp. 766–771, 2001.

[63] F. L. Dickert, H. Besenbock, and M. Tortschanoff, "Molecular imprinting through van der Waals interactions: Fluorescence detection of PAHs in water," *Adv. Mater.*, vol. 10, pp. 149–152, 1998.

[64] F. L. Dickert, P. Lieberzeit, and M. Tortschanoff, "Molecular imprints as artificial antibodies - a new generation of chemical sensors," *Sens. Actuators, B – Chem.*, vol. 65, pp. 186–189, 2000.

[65] T. E. Plowman, S. S. Saavreda, and W. M. Reichert, "Planar integrated optical methods for examining thin films and their surface adlayers," *Biomaterials*, vol. 19, pp. 341 – 355, 1998.

[66] H. P. Lehr, A. Brandengurg, and G. Sulz, "Modeling and experimental verification of the performance of TIRF-sensing systems for oligonucleotide microarrays based on bulk and integrated optical planar waveguides," *Sens. Actuators, B – Chem.*, vol. 92, pp. 303 – 314, 2003.

[67] M. N. Armenise, V. M. N. Passaro, F. D. Leonardis, and M. Armenise, "Modeling and design of a novel miniaturized integrated optical sensor for gyroscope systems," *J. Lightwave Technol.*, vol. 19, pp. 1476–1494, 2001.

[68] E. Hecht, *Optics*. New York: Addison Wesley Longman, Inc., 1998.

[69] J. J. Brazier, M. Yan, S. A. Prahl, and Y.-C. Chen, "Molecularly imprinted polymers used as optical waveguides for the detection of fluorescent analytes," in *Molecularly Imprinted Materials Sensors and Other Devices* (K. J. Shea, M. J. Roberts, and M. Yan, eds.), vol. 723, pp. 115–120, Materials Research Society Symposium Proceedings, 2002.

[70] C. A. Parker, *Photoluminescence of Solutions*. New York: Elsevier Publishing Company, 1968.

[71] I. B. Berlman, *Handbook of Fluorescence Spectra of Aromatic Molecules*. New York and London: Academic Press, Inc., 1971.

[72] C. V. Bindhu, S. S. Harilal, V. Nampoori, and C. Vallabhan, "Solvent effect on absolute fluorescence quantum yield of Rhodamine 6G determined using transient thermal lens technique," *Mod. Phys. Lett. B*, vol. 13, pp. 563–576, 1999.

[73] C. V. Bindhu and S. S. Harilal, "Effect of the excitation source on the quantum-yield measurements of Rhodamine B laser dye studied using thermal-lens technique," *Anal. Sci.*, vol. 17, pp. 141–144, 2001.

[74] F. L. Dickert, P. Achatz, and K. P. Halikias, "Double molecular imprinting – a new sensor concept for improving selectivity in the detection of polycyclic aromatic hydrocarbons (PAHs) in water," *Fresenius J. Anal. Chem.*, vol. 371, pp. 11–15, 2001.

[75] R. J. Umpleby II, S. C. Baxter, Y. Z. Chen, R. N. Shah, and K. D. Shimizu, "Characterization of molecularly imprinted polymers with the Langmuir-Freundlich isotherm," *Anal. Chem.*, vol. 73, pp. 4584–4591, 2001.

[76] R. J. Umpleby II, S. C. Baxter, M. Bode, J. K. Berch, R. N. Shah, and K. D. Shimizu, "Application of the Freundlich adsorption isotherm in the characterization of molecularly imprinted polymers," *Anal. Chim. Acta.*, vol. 435, pp. 35–42, 2001.

[77] E. Yilmaz, K. Mosbach, and K. Haupt, "Influence of functional and cross-linking monomers and the amount of template on the performance of molecularly imprinted polymers in binding assays," *Anal. Commun.*, vol. 36, pp. 167–170, 1999.

[78] U. Narange, G. P. Anderson, F. S. Ligler, and J. Burans, "Fiber optic-based biosensor for risin," *Biosens. Bioelectron.*, vol. 12, pp. 937–945, 1997.

[79] A. P. Abel, M. G. Weller, G. L. Duveneck, M. Ehrat, and H. M. Widmer, "Fiber-optic evanescent wave biosensor for the detection of oligonucleotides," *Anal. Chem.*, vol. 68, pp. 2905–2912, 1996.

[80] E. A. James, K. Schmeltzer, and F. S. Ligler, "Detection of endotoxin using an evanescent wave fiber-optic biosensor," *Appl. Biochem. Biotechnol.*, vol. 60, pp. 189–201, 1996.

[81] L. K. Cao, G. P. Anderson, F. S. Ligler, and J. Ezzell, "Detection of Yersinia pestis Fraction 1 antigen with a fiber optic biosensor," *J. Clin. Microbio.*, vol. 33, pp. 336–341, 1995.

[82] H. Hisamoto, K. H. Kim, Y. Manabe, K. Sasaki, H. Minamitani, and K. Suzuki, "Ion-sensitive and selective active waveguide optodes," *Anal. Chim. Acta*, vol. 342, pp. 31–39, 1997.

[83] M. Yan and A. Kapua, "Fabrication of molecularly imprinted polymer microstructures," *Anal. Chim. Acta*, vol. 435, pp. 163–167, 2001.

[84] Y.-C. Chen, J. J. Brazier, M. Yan, P. R. Bargo, and S. A. Prahl, "Fluorescence-based optical sensor design for molecularly imprinted polymers," *Sens. Actuators, B – Chem.*, vol. 102, pp. 107–116, 2004.

[85] D. A. Stenger, J. H. Georger, C. S. Dulcey, J. J. Hickman, A. S. Rudolph, T. B. Nielsen, S. M. McCort, and J. M. Calvert, "Coplanar molecular assemblies of aminoalkylsilane and perfluorinated alkylsilane - characterization and geometric definition of mammalian-cell adhesion and growth," *J. Am. Chem. Soc.*, vol. 114, pp. 8435–8442, 1992.

[86] G. Vlatakis, L. I. Andersson, R. Muller, and K. Mosbach, "Drug assay using antibody mimics made by molecular imprinting," *Nature*, vol. 361, pp. 645–647, 1993.

[87] Y. Watabe, K. Hosoya, N. Tanaka, T. Kubo, T. Kondo, and M. Morita, "Novel surface-modified molecularly imprinted polymer focused on the removal of interference in environmental water samples," *Chem. Lett.*, vol. 33, pp. 806–807, 2004.

[88] Y. C. Huang, C. C. Lin, and C. Y. Liu, "Preparation and evaluation of molecularly imprinted polymers based on 9-ethyladenine for the recognition of nucleotide bases in capillary electrochromatography," *J. Chromatogr. A*, vol. 25, pp. 554–561, 2004.

[89] L. Ye and K. Haupt, "Molecularly imprinted polymers as antibody and receptor mimics for assays, sensors and drug discovery," *Anal. Bioanal. Chem.*, vol. 378, pp. 1887–1897, 2004.

[90] S. Gutierrez-Fernandez, M. J. Lobo-Castanon , A. J. Miranda-Ordieres, P. Tunon-Blanco, G. A. Carriedo, F. J. Garcia-Alonso, and J. I. Fidalgo, "Molecularly imprinted polyphosphazene films as recognition element in a voltammetric rifamycin SV sensor," *Electroanal.*, vol. 13, pp. 399–1404, 2001.

[91] H. C. Huang, C. I. Lin, A. K. Joseph, and Y. D. Lee, "Photo-lithographically impregnated and molecularly imprinted polymer thin film for biosensor applications," *Electrophoresis*, vol. 1027, pp. 263–268, 2004.

[92] S. Marx, A. Zaltsman, I. Turyan, and D. Mandler, "Parathion sensor based on molecularly imprinted sol-gel films," *Anal. Chem.*, vol. 76, pp. 120–126, 2004.

[93] H. S. Guo and X. He, "Study on the binding characteristics of molecular imprinted polymer selective for cefalexin in aqueous media," *Chin. J. Anal. Chem.*, vol. 28, pp. 1214–1219, 2000.

[94] M. Quaglia, E. D. Lorenzi, C. Sulitzky, G. Massolini, and B. Sellergren, "Surface initiated molecularly imprinted polymer films: a new approach in chiral capillary electrochromatography," *Analyst*, vol. 126 (9), pp. 1495–1498, 2001.

[95] J. R. Lakowicz, *Principles of Fluorescence Spectroscopy.* New York: Kluwer Academic/Plenum Publisher, 1999.

[96] J. Anderson, J. Nelson, C. Reynolds, D. Ringelberg, G. Tepper, and D. Pestov, "Steady-state and frequency-domain lifetime measurements of an activated molecular imprinted polymer imprinted to dipicolinic acid," *J. Fluoresc.*, vol. 14, pp. 269–274, 2004.

[97] O. Przhonska, M. Bondar, J. Gallay, M. Vincent, Y. Slominsky, A. Kachkovski, and A. P. Demchenko, "Photophysics of dimethylamino-substituted polymethine dye in polymeric media," *J. Photochem. Photobiol. B: Biol.*, vol. 52, pp. 19–29, 1999.

[98] M. E. Morrison, R. C. Dorfman, W. D. Clendening, D. J. Kiserow, P. J. Rossky, and S. E. Webber, "Quenching kinetics of anthracene covalently bound to a polyelectrolyte.1. effects of ionic-strength," *J. Phys. Chem.*, vol. 98, pp. 5534–5540, 1994.

[99] V. Pokorná, D. Výprachtický, J. Pecka, and F. Mikeš, "Time-resolved emission anisotropy of anthracene fluorophore in the backbone of stereoregular poly(methyl methacrylate)," *Macromol. Chem. Phys.*, vol. 202, pp. 155–162, 2001.

[100] D. Tleugabulova, A. M. Duft, M. A. Brook, and J. D. Brennan, "Monitoring solute interactions with poly(ethylene oxide)-modified colloidal silica nanoparticles via fluorescence anisotropy decay," *Langmuir*, vol. 20, pp. 101 – 108, 2004.

[101] C. H. Lloyd, S. N. Scrimgeour, J. A. Chudek, G. Hunter, and R. L. MacKay, "The application of magnetic resonance microimaging to the visible light curing of dental resins. Part 2. Dynamic imaging by the FLASH-MOVIE pulse sequence," *Dent. Mater.*, vol. 17, pp. 170–177, 2001.

[102] M. E. Cohen, D. L. Leonard, D. G. Charlton, H. W. Roberts, and J. C. Ragain Jr, "Statistical estimation of resin composite polymerization sufficiency using microhardness," *Dent. Mater.*, vol. 20, pp. 158–166, 2004.

[103] N. S. Kudryasheva, E. V. Nemtseva, A. Visser, and A. van Hoek, "Interaction of aromatic compounds with photobacterium leiognathi luciferase: fluorescence anisotropy study," *Luminescence*, vol. 18, pp. 156–161, 2003.

[104] R. J. Sturgeon and S. G. Schulman, "Steric inhibition of conjugation in lowest excited singlet state of 9-anthramide by hydrogen bond donor solvents: role of solvent in chemical structure," *J. Pharm. Sci.*, vol. 65, pp. 1833–1835, 1976.

[105] R. A. Lampert, L. A. Chewter, D. Phillips, D. V. O'Connor, A. J. Roberts, and S. R. Meech, "Standards for nanosecond fluorescence decay time measurements," *Anal. Chem.*, vol. 55, pp. 68–73, 1983.

[106] T. A. Smith, L. M. Bajada, and D. E. Dunstan, "Fluorescence polarization measurements of the local viscosity of hydroxypropyl guar in solution," *Macromolecules*, vol. 35, pp. 2736–2742, 2002.

[107] L. Musanje and B. W. Darvell, "Polymerization of resin composite restorative materials: exposure reciprocity," *Dent. Mater.*, vol. 19, pp. 531–541, 2003.

[108] M. Miyazaki, Y. Oshida, B. K. Moore, and H. Onose, "Effect of light exposure on fracture toughness and flexural strength of light-cured composites," *Dent. Mater.*, vol. 12, pp. 328–332, 1996.

[109] L. G. Lovell, S. M. Newman, and C. N. Bowman, "The effects of light intensity, temperature, and comonomer composition on the polymerization behavior of dimethacrylate dental resins," *J. Dent. Res.*, vol. 78, pp. 1469–1476, 1999.

[110] R. R. Braga and J. L. Ferracane, "Contraction stress related to degree of conversion and reaction kinetics," *J. Dent. Res.*, vol. 81, pp. 114–118, 2002.

[111] J. L. Ferracane, J. C. Mitchem, J. R. Condon, and R. Todd, "Wear and marginal breakdown of composites with various degrees of cure," *J. Dent. Res.*, vol. 76, pp. 1508–1516, 1997.

[112] J. L. Ferracane, "Correlation between hardness and degree of conversion during the setting reaction of unfilled dental restorative resins," *Dent. Mater.*, vol. 1, pp. 11–14, 1985.

[113] R. H. Halvorson, R. L. Erickson, and C. L. Davidson, "Energy dependent polymerization of resin-based composite," *Dent. Mater.*, vol. 18, pp. 463–469, 2002.

[114] N. Emami and K. M. Söderholm, "How light irradiance and curing time affect monomer conversion in light-cured resin composites," *Eur. J. Oral Sci.*, vol. 111, pp. 536–542, 2003.

[115] D. Tantbirojn, A. Versluis, Y. Cheng, and W. H. Douglas, "Fracture toughness and microhardness of a composite: do they correlate?," *J. Dent.*, vol. 31, pp. 89–95, 2003.

[116] D. H. Sliney and M. L. Wolbarsht, *Safety With Lasers and Other Optical Sources: A Comprehensive Handbook*. New Yor: Plenum Press, 1980.

[117] S. A. Prahl, *Optical Property Measurements using the Inverse Adding-Doubling program*. http://omlc.ogi.edu/software/iad/index.html: OMLC, 1999 (reviewed in 2003).

[118] S. A. Prahl, M. J. C. Vangemert, and A. J. Welch, "Determining the optical properties of turbid media by using the adding-doubling method," *Appl. Opt.*, vol. 32, pp. 559 – 568, 1993.

[119] S. L. Jacques, "Light distributions from point, line and plane sources for photochemical reactions and fluorescence in turbid biological tissues," *Photochem. Photobiol.*, vol. 67, pp. 23–32, 1998.

[120] W. D. Cook, "Spectral distributions of dental photopolymerization sources," *J Dent. Res.*, vol. 61, pp. 1436–1438, 1982.

[121] E. A. E and S. Uno, "Solubility parameters, fractional polarities, and bond strengths of some intermediary resins used in dentin bonding," *J. Dent. Res.*, vol. 72, pp. 558–565, 1993.

[122] L. M. Racz, L. Li, and B. Abedian, "Cure kinetics of light-activated polymers," *J. Polym. Sci., Part B: Polym. Phys.*, vol. 36, pp. 2887 –2894, 1998.

[123] W. M. Johnston, R. L. Leung, and P. L. Fan, "A mathematical model for post-irradiation hardening of photoactivated composite resins.," *Dent. Mater.*, vol. 1, pp. 191–194, 1985.

[124] Y. K. Lee, B. S. Lim, and C. W. Kim, "Effect of surface conditions on the color of dental resin composites," *J. Biomed. Mater. Res.*, vol. 63, pp. 657–663, 2002.

[125] M. Taira, M. Okazaki, and J. Takahashi, "Studies on optical properties of two commercial visible-light-cured composite resins by diffuse reflectance measurements," *J Oral Rehabil*, vol. 26, pp. 329–37, 1999.

[126] A. Ishimaru, *Wave propagation and scattering in random media.* New York: Academic Press, 1978.

[127] B. Hapke, *Theory of Reflectance and Emittance Spectroscopy (Topics in Remote Sensing).* New York: Cambridge University, 1993.

[128] A. J. Welch and M. van Gemert, *Optical-Thermal Response of Laser Irradiated Tissue.* Plenum Press, 1995.

[129] Q. Yu, S. Nauman, J. P. Santerre, and S. Zhu, "UV photopolymerization behavior of dimethacrylate oligomers with camphorquinone/amine initiator system," *J. Appl. Polym. Sci.*, vol. 82, pp. 1107–1117, 2001.

[130] Z. Kucybala, M. Pietrzak, J. Paczkowski, L. A. Linden, and J. F. Rabek, "Kinetic studies of a new photoinitiator hybrid system based on camphorquinone-n-phenylglicyne derivatives for laser polymerization of dental restorative and stereolithographic (3d) formulations," *Polymer*, vol. 37, pp. 4585–4591, 1996.

[131] F. Stahl, S. H. Ashworth, and R. W. Mills, "Light-emitting diode (LED) polymerization of dental composites:flexural properties and polymerization potential," *Biomaterials*, vol. 21, pp. 1379–1385, 2000.

[132] W. Teshima, Y. Nomura, N. Tanaka, H. Urabe, M. Okazaki, and Y. Nahara, "ESR study of camphorquinone/amine photoinitiator systems using blue light-emitting diodes," *Biomaterials*, vol. 24, pp. 2097–2103, 2003.

[133] Y. C. Chen, F. L. Ferracane, and S. A. Prahl, "A photon migration model for predicting depth of cure in dental composite," *Dent. Mater.*, submitted.

[134] J. Nie, L. A. Lindén, J. F. Rabek, J. P. Fouassier, F. Morlet-Savary, F. Scigalski, A. Wrzyszczynski, and E. Andrzejewska, "A reappraisal of the photopolymerization kinetics of triethyleneglycol dimethacrylate initiated by camphorquinone-N,

N-dimethyl-p-toluidine for dental purposes," *Acta. Polymer*, vol. 49, pp. 145–161, 1998.

[135] Y. K. Lee and J. M. Powers, "Color and optical properties of resin-based composites for bleached teeth after polymerization and accelerated aging," *Am. J. Dent.*, vol. 14, pp. 349–354, 2001.

[136] P. Kubelka, "New contributions to the optics of intensely light-scattering materials Part I," *J. Opt. Soc. Am.*, vol. 38, pp. 448–457, 1948.

[137] P. Kubelka, "New contributions to the optics of intensely light-scattering materials Part II," *J. Opt. Soc. Am.*, vol. 44, pp. 330–335, 1954.

[138] J. L. Ferracane, P. Aday, H. Matsumoto, and V. A. Marker, "Relationship between shade and depth of cure for light-activated dental composite resins," *Dent. Mater.*, vol. 2, pp. 80–84, 1964.

[139] H. Engqvist, J. Loof, S. Uppstrom, M. W. Phaneuf, J. C. Jonsson, L. Hermansson, and N. O. Ahnfelt, "Transmittance of a bioceramic dental restorative material based on calcium aluminate," *J. Biomed. Mater. Res.*, vol. 69B, pp. 94–98, 2004.

[140] O. Dudi and W. T. Grubbs, "Laser interferometric technique for measuring polymer cure kinetics," *J. Appl. Polym. Sci.*, vol. 74, pp. 2133–2142, 1999.

[141] Y. B. Kim, H. K. Kim, J. K. Yoo, and J. W. Hong, "UV-curable polyurethane dispersion for cationic electrodeposition coating," *Surf. Coat. Technol.*, vol. 157, pp. 40–46, 2002.

[142] S. Rastegar, B. Kim, and S. L. Jacques, "Role of temperature dependence of optical properties in laser irradiation of biological tissue," in *Proceedings of SPIE*, vol. 1646, pp. 228–231, 1992.

[143] L. C. Chin, W. M. Whelan, and I. A. Vitkin, "Models and measurements of light intensity changes during laser interstitial thermal therapy: implications for optical monitoring of the coagulation boundary location," *Phys. Med. Biol.*, vol. 48, pp. 543–559, 2003.

[144] T. J. Pfefer, J. K. Barton, E. K. Chan, M. G. Ducros, B. S. Sorg, T. E. Milner, J. S. Nelson, and A. J. Welch, "A three-dimensional modular adaptable grid numerical model for light propagation during laser irradiation of skin tissue," *IEEE J. Selec. Top. Quantum Electronics*, vol. 2, pp. 934–942, 1996.

[145] S. L. Jacques and S. A. Prahl, *Steady-state Monte Carlo: Terminate a photon by roulette*. http://omlc.ogi.edu/classroom/ece532/class4/ssmc/roulette.html: OMLC, 1998 (reviewed in 2001).

[146] M. Born and E. Wolf, *Principles of Optics*. Cambridge, UK: Cambridge University Press, 1999.

[147] D. Bucher, E. G. Richards, and W. D. Brown, "Modifications of the Rayleigh interferometer in the ultracentrifuge for use with Heme and other light-absorbing proteins," *Anal. Biochem.*, vol. 36, pp. 368–380, 1970.

[148] M. Tanaka, T. Naito, M. Yokota, and M. Kohno, "Finite element analysis of the possible mechanism of cervical lesion formation by occlusal force," *J. Oral Rehabil.*, vol. 30, pp. 60–67, 2003.

Biographical Note

Yin-Chu Chen was born in Chia-Yi City, Taiwan, on August 25, 1973. She entered the National Taiwan University in Taipei, Taiwan, on a full scholarship funded by National Ministry of Education and received the B. S. degree in Physics in 1995. She continued her study at the same institution and received her M.S. in Electrical Engineering in 1998. At the same time, she entered Teacher Education program and received a Secondary School Teaching Certificate. From 1997 to 1999, she was a Science teacher in senior high schools in Taipei. In 2000, she matriculated in the Electrical and Computer Engineering department at the Oregon Graduate Institute. Yin-Chu will start a postdoctoral position at the Wellman Center for Photomedicine in March, 2005.